Title
Heterogeneity of mononuclear phagocytes during photoreceptor degeneration

Author
Ronning, Kaitryn

Publication Date
2021

Peer reviewed|Thesis/dissertation

Heterogeneity of mononuclear phagocytes during photoreceptor degeneration

By

KAITRYN ELIZABETH RONNING

DISSERTATION

Submitted in partial satisfaction of the requirements for the degree of

DOCTOR OF PHILOSOPHY

in

Neuroscience

in the

OFFICE OF GRADUATE STUDIES

of the

UNIVERSITY OF CALIFORNIA

DAVIS

Approved:

Dr. Marie Burns, Chair

Dr. Anna La Torre

Dr. Athena Soulika

Dr. Alex Nord

Dr. Nicholas Marsh-Armstrong

Committee in Charge

2021

Abstract

The healthy central nervous system (CNS) contains resident macrophages, known as microglia, which constantly survey their environment, support neuronal function, and activate in response to neuronal disruption and loss. In response to damage and disease, monocytes can breach blood-CNS barriers, extravasate from the vasculature, and invade the neural parenchyma. These monocytes can then transform into monocyte-derived macrophages, which have traditionally been difficult to distinguish from microglia, due to similar morphologies and expression of common markers. However, recent technical advances have made it easier to identify these cell types as well as distinct subpopulations of these cells.

In this dissertation, I investigate microglial and monocytic cells in the retina, predominantly in a model of rapid, inducible photoreceptor degeneration, the *Arr1*$^{-/-}$ mouse. I find that monocytes rapidly invade the retina during degeneration, and then transform into microglia-like macrophages. These monocyte-derived macrophages are strongly pro-inflammatory during degeneration, and then later adopt a more resting microglia-like phenotype and take up residence alongside bona fide microglia after degeneration has ceased. Using single-cell mRNA sequencing during and after photoreceptor loss, I find that there are also distinct subpopulations of these mononuclear phagocytes. Microglia are particularly heterogeneous during photoreceptor loss, and there are also distinct subpopulations of monocytes and monocyte-derived macrophages. Differences between these subpopulations include differences in cell division, antigen presentation, inflammatory cytokines, and other macrophage activation genes. Finally, I find that these mononuclear phagocytes remain able to respond to further retinal injury following photoreceptor degeneration, although monocyte-derived macrophages appear to be less responsive than the resident microglia. Altogether, I find that there is a complex immune response during photoreceptor degeneration, and that the retinal immune state remains changed even well after photoreceptor loss is complete.

Acknowledgements

This dissertation is the culmination of my graduate studies, but high-quality science cannot be performed in a vacuum and there are many people without whom I could not have completed this dissertation. First and foremost, endless thanks to my mentor, Marie Burns. Marie, you have given me incredible freedom to explore new scientific ideas, yet always seem to know precisely when I need a nudge in the right direction or a bit of structure to guide me. Over these years I have tried to absorb your incredible scientific curiosity and passion for rigorous experimental design, which I hope to keep with me always. Your unwavering support and encouragement have meant the world to me, and I am a better scientist and person for your mentorship.

I have been incredibly fortunate to work in the Burns-Pugh lab. To Marie, Ed, Sarah, Eric, Gabriel, Emily, Camilla, Helen, and all the many other past lab members I have had the pleasure to work with: thank you all. You have all been so generous with your knowledge and time, and I could not have hoped for a more collaborative and intellectually stimulating environment. Ed, I have never met another person with your incredible ability to think through scientific puzzles so deeply, and our discussions never fail to leave me invigorated (and with a long reading list). Special thanks to Sarah and Eric, the long-standing microglia crew during my time in the lab. Eric, thank you for being a fountain of knowledge and sounding board for all my craziest ideas. Sarah, you have been an incredible rock and friend, in addition to a stellar scientist, figure designer extraordinaire, and wizard at keeping the lab moving.

I also have to thank the many people throughout the neuroscience community and beyond at UC Davis. Many thanks to my dissertation committee, Anna, Athena, Alex, and Nick, for being generous with your expertise, sharing all the invaluable feedback, and for pushing me to be the best scientist I can be. Thank you to members of the EyePod, Robert, Pengfei, Ratheesh, Mayank, and more, for supporting my work and answering my many, many questions

about imaging. Additionally, thank you to all the faculty, staff, and my fellow students in the Neuroscience Graduate Group. I have learned so much from you all, and some of my favorite memories from graduate school are from various neuroscience gatherings and events. In particular, I owe much to the wonderful people in my cohort and my other close neuroscience friends. Thank you to the LaTorre-Simo lab, Anna, Sergi, Jisoo, Adam, Mikaela, Elizabeth, Keiko, Corinne, and more, for the many Tupper celebrations and baked goods. And thank you to the UCD Symphony Orchestra for always letting me hang out in the bass section and make some music.

Finally, I will always be indebted to my family. Thank you, Mom and Greg, for your constant, unwavering support of all my passions and for instilling me with a love of learning. I love you so much. Kristen, thank you for all the wacky stories and long talks. Thank you to my father, who I know would be so proud of me. And last, but certainly not least, thank you Derek. I could not have done this without your support and ability to always make me smile.

Table of Contents

Abstract ii
Acknowledgements iii

Chapter 1: Introduction: Resident and monocyte-derived macrophages in the retina during neurodegeneration

Preface 1
Abstract 2
Introduction 2
The retina: the accessible central nervous system 3
Tissue barriers and immune privilege 4
Microglia: the resident immune cells of the CNS 6
Monocytes and monocyte-derived macrophages: immune invaders 8
In the absence of microglia: ablating microglia 11
Emerging themes in retinal macrophages during damage and disease 12
Harnessing differences between retinal disorders 14
The immune state after degeneration 15
Glial-immune interactions 16
Conclusions: looking ahead 17
Figures 19
References 23

Chapter 2: Loss of cone function without degeneration in a novel Gnat2 knock-out mouse

Preface 31
Abstract 32
Introduction 32
Methods 34
Results 38
Loss of Gnat2 expression does not produce cone dysmorphogenesis or retinal degeneration 38
Absence of cone-driven retinal signaling in the absence of Gnat2 40
Discussion 41
Comparison of *Gnat2*$^{-/-}$ mice to other common cone-silent mice 42
The contribution of rods to the normal murine ERG under mesopic intensities 43
Gnat2$^{-/-}$ mouse as a model of achromatopsia 44
Table and figures 46
References 53

Chapter 3: Molecular profiling of resident and infiltrating mononuclear phagocytes during rapid adult retinal degeneration using single-cell RNA sequencing

Preface 55
Abstract 56
Introduction 56
Methods 58
Results 62
Invasion of peripheral immune cells into the rapidly degenerating retina 62
Single cell profiling reveals four classes of CD11b+CD45+ cells 63
In silico identification of cell subtypes with different activation and proliferation states 65
Re-examining molecular heterogeneity of the immune response in the context of degeneration 67
Discussion 68
Distinguishing hallmarks of immune subpopulations in the degenerating retina 69
Understanding molecular heterogeneity is critical for potential functional analysis 70
Implications for photoreceptor degeneration and other retinal degenerative diseases 71
Figures 73
Supplemental materials 84
References 99

Chapter 4: Monocyte-derived macrophages establish residence alongside bona fide microglia in the retina after degeneration

Preface 103
Abstract 104
Background 105
Methods 106
Results 111
Ramified macrophages re-tile the retina after photoreceptor degeneration 111
Sustained increase in retinal immune cells after degeneration 113
Persistent transcriptional heterogeneity of retinal macrophages after loss of photoreceptors 114
Monocyte-derived macrophages take up residence alongside resident microglia 115
Probing the activation potential of macrophages to further retinal injury 116
Discussion 118
Dramatic increase in CD45+ cells in the retina following degeneration 118
Monocyte-derived cells remain in the retina following degeneration 118
Heterogeneous resolution of neuroinflammation across models of acute degeneration 120

Future directions: functional implications of the altered retinal immune state 121
Table and figures 123
References 134

Chapter 5: Concluding Remarks 137
References 140

Appendix: Tracking distinct microglia subpopulations with photoconvertible Dendra2 *in vivo*
Preface 142
Abstract 143
Background 143
Methods 145
Results 151
Dendra2-expressing retinal microglia can be efficiently photoconverted *in vivo* 151
Photoconverted Dendra2 to identify resident microglia during widespread retinal degeneration 154
Microglia with converted Dendra2 can be tracked during a response to localized photoreceptor damage 155
Discussion 157
Conclusion 159
Figures 160
Supplementary information 170
References 171

Chapter 1

Introduction: Resident and monocyte-derived macrophages in the retina during neurodegeneration

Preface

The following chapter is a review that I will submit for publication following the submission of this dissertation. It has been formatted to meet the guidelines of this dissertation. The authors are Kaitryn E. Ronning and Marie E. Burns. I created the figures and wrote and edited the manuscript, under the guidance of Marie E. Burns who also edited the manuscript. This review serves as the introduction for the following data chapters of this dissertation, providing an overview of mononuclear phagocytes in the retina during health and disease.

Abstract

The response and contribution of circulating immune cells to the progression of neurological and neurodegenerative diseases is of increasing interest to the field of neuroinflammation. In the retina, circulating monocytes cross the blood-retinal barrier and infiltrate the retinal parenchyma during retinal degeneration. The retina is an ideal compartment for investigating neuro-immune interactions because of the clinical importance of prevalent blinding neurodegenerative diseases like age-related macular degeneration and glaucoma, as well as the accessibility of the eye for visualization, treatment, and longitudinal assessment. Here we review some of the recent studies comparing resident microglia and monocyte-derived macrophages during retinal degeneration, highlight some of the technological advances that are critical to this work, compare findings in the retina with similar work in the brain, and touch upon some of the unanswered questions and work yet to come.

Introduction

Traditionally the central nervous system (CNS) was considered tightly immune privileged. In large part this assumption was due to knowledge of the specialized barriers between the neural tissue and the rest of the body, as well as the presence of specialized immune cells in the central nervous system known as microglia. However, more recent work has revealed that these barriers are readily breached during damage and disease, allowing circulating immune cells to extravasate from blood vessels and join the team of resident microglia in mitigating damage and restoring homeostasis. One well-studied CNS compartment for following these distinct immune cell populations is the neural retina, which like the brain is bounded by protective blood-brain (blood-retina) barriers and possesses its own complement of resident microglial cells. In this review, we discuss recent advances in understanding the unique roles of resident and invading immune cells specifically in the context of retinal degeneration.

The retina: the accessible central nervous system

The retina is the light-sensitive central nervous system tissue consisting principally of photoreceptors, bipolar cells and ganglion cells that initiate the first steps in vision. Defective signaling or loss of any of these cells can impair vision and even lead to blindness, making the retina a clinically important target. Additionally, because the retina is more physically accessible than the brain and spinal cord, it is an ideal tissue to study the neuroinflammatory response during damage and disease, including the response of resident immune cells and peripheral immune cells invading the neural parenchyma.

Many common retinal conditions and diseases trigger neuroinflammation, including retinal detachment, retinitis pigmentosa, age-related macular degeneration, and glaucoma. Our understanding of the mechanistic underpinnings of these diseases comes largely from animal studies, and the wide range of available mouse models provides researchers with a selection of types and severity of degeneration, ages of onset, and primary cause of damage. This includes several genetic models of photoreceptor degenerative disorders (Veleri et al., 2015), as well as many light-inducible models of degeneration, which vary in both intensity of light exposure required and susceptibility, in some cases due to underlying genetic mutations (C.-K. Chen et al., 1999; J. Chen et al., 1999; Chen et al., 2004; Danciger et al., 2005; LaVail et al., 1999; Sennlaub et al., 2013; Xu et al., 1997). There are other models of inducible damage, such a laser injuries (Miller et al., 2019), artificial retinal detachment (Conart et al., 2020; Kiang et al., 2018; Nakazawa et al., 2011; Wang et al., 2017), and ocular surface trauma that results in loss of retinal neurons (Cade et al., 2011; Paschalis et al., 2017). Finally, there are also a variety of genetic and inducible models of glaucoma (Harada et al., 2019; Wang et al., 2021).

Unlike other CNS tissues, the retina uniquely lies behind the transparent cornea and lens of the eye, allowing non-invasive imaging of the retina in both health and disease (Azimipour et al., 2019; Zhang et al., 2015). This ocular imaging is especially useful when studying immune cells in mouse models, as several transgenic fluorescent reporter mice have

been developed to visualize mononuclear phagocytes. While not an exhaustive list, some of the most commonly used lines include Cx3cr1-GFP (Jung et al., 2000), Ccr2-RFP (Saederup et al., 2010), Cx3cr1-CreER-YFP (Littman, 2013), and more (Eme-Scolan and Dando, 2020). A few transgenic mouse lines have been created to visualize locally-distinct subsets of mononuclear phagocytes, including Cx3cr1-Dendra which allows local photoconversion of cells of interest (Miller et al., 2021), and Cx3cr1-'Microfetti' which drives expression of four fluorophores randomly across mononuclear phagocytes (Tay et al., 2017). These transgenic mice have been important for understanding microglial activation in response to injury and disease, as well as the invasion of peripheral immune cells invasion during degeneration (Karlen et al., 2020; Reyes et al., 2017; Yu et al., 2020)(Figure 1.1 Box 1).

Despite clear fundamental differences between the retina and brain in terms of CNS compartments, there are striking similarities between the immune populations in the two, both at rest and during the response to degeneration (London et al., 2013a). Recurring themes in the immune response to retinal degeneration are discussed below (Figure 1.2), as well as how these themes are recapitulated in the central nervous system more broadly.

Tissue barriers and immune privilege

The central nervous system (CNS) has highly specialized barriers that tightly regulate the flow of ions, nutrients, other molecules, and cells between the neural tissue and the rest of the body. The majority of the vasculature of the CNS has unique properties that constitute the blood-brain barrier. Unlike vascular endothelial cells in typical vessels, vascular endothelial cells in CNS vessels adhere via tight junctions, preventing the free exchange of molecules and small solutes. Instead, these endothelial cells express a wide array of transporters to precisely regulate exchange between the CNS and blood. Furthermore, the parenchyma-facing surface of these vascular endothelial cells are wrapped by pericytes and perivascular macrophages, and

all of these cells are further ensheathed by the end feet of glia (Daneman and Prat, 2015). Together, these heterocellular, impermeable structures are called the neurovascular unit.

Other types of barriers exist in some specialized anatomical regions of the CNS. For example, while the blood-retina barrier in the inner retina consists of the neurovascular unit described above, the blood-retina barrier in the outer retina is formed by the retinal pigment epithelium (RPE) and its overlying deposit of fibrous matrix known as Bruch's Membrane (BM). Together, the RPE and BM isolate the neural retina from the fenestrated capillaries of the vascular-rich choroid. Like the vascular endothelial cells in the neurovascular unit, cells of the RPE regulate exchange between the retinal parenchyma and the choroid by adhering via tight junctions and expressing a wide range of transporters. However, unlike vascular endothelial cells, the cells of the RPE are not further enveloped by immune and glial cells, and instead have direct contact with retinal neurons, specifically the photoreceptors (Naylor et al., 2019).

In addition to regulating movement of nutrients, the presence of these specialized barriers and tight junctions are critical for regulating the immune response during neural diseases. Generally, these barriers establish the specialized compartmentalization often referred to as immune privilege, prohibiting the invasion of immune cells from the periphery during normal CNS function. The role of barrier-forming cells is especially interesting in the retina, because the RPE has been found to play an extensive and active role in immune modulation (Detrick and Hooks, 2019). Of particular interest is the immunosuppressive activity of the RPE, where RPE cells can eliminate nearby mononuclear phagocytes via TSP-1 activation of CD47 (Calippe et al., 2017).

Under normal conditions, the CNS contains microglia, the specialized resident macrophage of the nervous system, as well as a smaller population of other immune cell types such as perivascular macrophages. Due to the specialized barriers between the vasculature and CNS parenchyma, it was long assumed that the populations of immune cells in the CNS were isolated and relatively invariant during both health and neurodegeneration. However,

recently it has become clear that in many types of CNS injury and disease, including a variety of neurodegenerative disorders, the inflammatory response can cause disruptions of the tight junctions in CNS-blood barriers and circulating immune cells are able to exit the vasculature and join the resident immune populations in their response to local tissue damage and repair (Kadry et al., 2020).

Microglia: the resident immune cells of the CNS

At rest, the resident macrophages of the central nervous system include microglia and perivascular macrophages, with microglia being far more numerous and the primary resident immune responders. Microglia share many similarities with other mononuclear phagocytes, but they, like some other resident macrophage populations, have a unique ontogeny. While most macrophages arise from hematopoietic progenitors, microglia predominantly arise from yolk-sac myeloid progenitors very early in embryonic development (Ginhoux et al., 2010), although some contribution of monocytes to the microglial population later in development has been proposed (Chen et al., 2020). This unique cellular lineage may contribute to the differences between microglia and other macrophage populations throughout the body (Gautier et al., 2012), and can conveniently be harnessed to experimentally differentiate resident microglia populations from other populations of mononuclear phagocytes for functional studies (Chen et al., 2020; Ginhoux et al., 2010; O'Koren et al., 2016)(Figure 1.1 Box 2).

During development, microglia help to shape neuronal circuitry by pruning synapses (Schafer et al., 2012). Microglia continue to support neuronal function into adulthood by contributing to synaptic remodeling and playing a role in regulating neuronal excitability (Borst et al., 2021). During normal CNS function microglia throughout the CNS are highly branched with constantly moving processing, allowing them to effectively monitor the extracellular milieu and surrounding cells (Miller et al., 2019; Nimmerjahn et al., 2005; Wolf et al., 2017). They also express a wide array of receptors, which further contribute to their ability to closely monitor their

surroundings (Kettenmann et al., 2011). During normal CNS function, this quiescent state, often referred to as “resting”, is maintained in part by the neuron-derived chemokine CX3CL1 binding to the receptor CX3CR1 on microglia (Liang et al., 2009; Rashid et al., 2019; Wolf et al., 2013).

A key role of microglia is to respond to injury, infection, and degeneration in the CNS. In response to tissue damage, microglia can undergo dramatic changes in morphology and gene expression, broadly known as activation. Key features of activation include transforming from a highly ramified morphology to an ameboid state, changes in gene expression, and migration to the site of disease (Wolf et al., 2017). The ability of microglia to detect and migrate to locations of damage and disruption is particularly striking in models of focal laser damage. In both the brain and retina, after focal laser injury microglia rapidly orient towards the site of injury and within hours microglial cell bodies begin migrating (Alt and Lin, 2012; Davalos et al., 2005; Miller et al., 2019).

While these general features of activation are consistent across models, one emerging theme in the microglia literature is the dramatic degree of heterogeneity of activated microglia, between and even within models. Recent studies including those using single-cell transcriptomics have revealed that indeed microglia can adopt a wide range of phenotypes, and there can be multiple distinct populations of microglia simultaneously during damage and disease (Hammond et al., 2019; Keren-Shaul et al., 2017; O’Koren et al., 2019; Ronning et al., 2019)(Figure 1.1 Box 3). This heterogeneity is discussed further below in several models of retinal disorders.

Once at the location of damage or disease, regardless of the cause, one of the primary functions of microglia is to phagocytose debris and dead or dying cells. To some extent, this phagocytosis is beneficial, as it helps to clear the tissue and can reduce further inflammation (Brown and Neher, 2014; Silverman et al., 2019). However, uncontrolled clearance can be detrimental, with microglia phagocytosing living neurons and directly contributing to degeneration (Brown and Neher, 2014; Zhao et al., 2015). Similarly, chronic pro-inflammatory

activation of microglia can be harmful and is a common feature in neurodegenerative disorders (London et al., 2013b; Rashid et al., 2019). Experimental overexpression of CX3CL1 has been investigated as a way to counteract detrimental microglial activation, by pushing the microglia back towards a homeostatic, resting phenotype. However, likely due to the benefits of some microglia phagocytosis of debris and some neuroprotective roles microglia can adopt, increasing CX3CL1 levels does not consistently counter neuronal loss, and can in some cases be harmful (Wolf et al., 2013).

Microglia can also adopt beneficial, neuroprotective roles (Kettenmann et al., 2011; Wolf et al., 2017). For example, in some instances of retinal damage, microglia have been identified as neuroprotective (Okunuki et al., 2018; Todd et al., 2019). One way microglia can support neuronal survival and function is by releasing neurotrophic factors, such as NGF, BDNF, and GDNF, and growth factors, such as IGF-1 and FGF (Colonna and Butovsky, 2017). Modulating microglia towards helpful states, rather than harmful, to ameliorate neurodegenerative disorders is an active area of investigation (Colonna and Butovsky, 2017; Muzio et al., 2021). However, likely due to the heterogeneity of microglial activation and that the most beneficial state of microglial cells can change throughout the course of disease, we remain in the earliest stages of developing effective therapeutic interventions that modulate microglia.

Monocytes and monocyte-derived macrophages: immune invaders

In addition to a growing appreciation for the heterogeneity and many functions of microglia, studies of neuroinflammation have been further complicated as it becomes clear that a wide range of immune cells can invade the CNS. Depending on the model and compartment of the CNS, many different peripherally-derived immune cells have been detected in the CNS, ranging from T and B cells to monocytes (Baufeld et al., 2018; Evans et al., 2019; Sabatino et al., 2019). It remains unknown why some immune cell types are more prevalent in some disorders and CNS compartments than others. Curiously, in the retina work in several different

models of damage and degeneration has thus far identified monocytes as the primary immune invader from the periphery (Reyes et al., 2017), so these will be the primary peripheral immune responder discussed in this review (Figure 1.2).

Monocytes are bone-marrow-derived immune cells that, at rest, circulate through the vasculature. There are two broad classes of monocytes in circulation in the vasculature, often differentiated by their Ly6C expression. Newly born monocytes are $Ly6C^{high}$ and are the primary immune responders. If these monocytes continue to circulate, they transition to a $Ly6C^{low}$ state in which they patrol the vasculature. Alternatively, $Ly6C^{high}$ monocytes can respond to infections, damage, and disease by extravasating from the vasculature and invading the affected tissue (Shi and Pamer, 2011).

There are a variety of ways monocytes can invade the CNS general and the retina in particular. The first conclusive observations of monocytic cells in the CNS occurred after CNS barriers disruption. Bone marrow chimeras were developed to differentiate CNS resident microglia from monocytic cells, by transplanting bone marrow progenitors that would give rise to genetically labeled monocytic cells (Priller et al., 2001). Monocytic cells were observed in the CNS in these early experiments, although it was later revealed that the irradiation during the bone marrow transplantation directly disrupted CNS barriers, allowing monocytes to invade the CNS parenchyma. Indeed, when barrier damage is prevented by shielding the head of the animal from the irradiation, the same immune invasion does not occur (Mildner et al., 2007; Müther et al., 2010).

However, it has since become clear that there are instances when monocytic cells can invade the retina in the absence of experimental disruption of CNS barriers. In some cases, components of the inflammatory response itself can disrupt tight junctions in the CNS barriers, providing an avenue for monocytes to enter the CNS (Kadry et al., 2020). Disruption of retinal barriers is not sufficient for monocytes to invade the retina, however. Across tissues, the predominant way monocytes are recruited from the vasculature is via signaling of the

chemokine CCL2, expressed in the injured tissue, and the receptor CCR2, expressed by the monocytes (Shi and Pamer, 2011). Loss of CCR2 prevents monocyte invasion of the retina even after whole body irradiation (Chen et al., 2012; Mildner et al., 2007), and this CCL2-CCR2 signaling has also been strongly implicated in the recruitment of monocytes to the retina during disease (Karlen et al., 2018; Ma et al., 2017; Sennlaub et al., 2013)(Figure 1.2). However, the primary source(s) of CCL2 during disease progression remain debated. In *Cx3cr1*-deficient mice, microglia dramatically upregulate *Ccl2*, similar to CCL2+ mononuclear phagocytes observed in samples from patients with geographic atrophy, suggesting that microglia could be causal in recruiting monocytes (Sennlaub et al., 2013). Single-cell gene expression in another model also identified *Ccl2* expression in microglia (Ronning et al., 2019). However, at least in this model microglia do not appear to be the causal source of CCL2 during early monocyte invasion, as other work in that model that found that Müller glia-specific ablation of *Ccl2* was sufficient to block monocyte recruitment (Karlen et al., 2018). IL-33 expressed by Müller glia has also been implicated in monocyte recruitment, potentially via regulating CCL2 expression (Xi et al., 2016). The exact timing and primary source of CCL2 for monocyte recruitment may vary across different disease model.

After invading the tissue, monocytes differentiate into macrophages, which are antigen-presenting phagocytes that can produce an array of cytokines (Ginhoux and Jung, 2014). Like resident microglia, macrophages can adopt a wide spectrum of phenotypes, ranging from pro-inflammatory to anti-inflammatory. These pro- and anti-inflammatory states are also commonly referred to as M1 and M2 phenotypes, respectively, although this M1/M2 dichotomy does not fully reflect the wide range of functionally distinct phenotypes these cells can take. The exact phenotype a macrophage will adopt is dependent on molecular cues specific to its extracellular microenvironment (Shapouri-Moghaddam et al., 2018).

After monocytes differentiate into macrophages within the retina, they become very difficult to distinguish from retinal microglia in terms of both morphology and expression of

common makers, such as Iba1, Cx3cr1, and CD11b. These similarities are likely why monocytic cells were previously thought not to be observed in the CNS and has spurred the search for true microglia-specific markers. A few promising candidates, such as P2ry12 and Tmem119, are expressed by microglia at rest and are not expressed by monocyte-derived macrophages, allowing these subpopulations to be distinguished in healthy tissue (Bennett et al., 2016; Sasaki et al., 2003). Unfortunately, microglial activation causes downregulation of many resting, or homeostatic, genes, including *P2ry12* and *Tmem119*, so that these markers cannot be used to unambiguously differentiate macrophage subtypes during disease. To work around this complexity, recent work has shifted to developing genetically encoded lineage tracing paradigms (Chen et al., 2020; Kaiser and Feng, 2019; O'Koren et al., 2016)(Figure 1.1 Box 2). These lineage tracing techniques can conclusively differentiate microglia from monocyte-derived macrophages and will be critical in understanding the roles these unique microglial populations play during damage and disease.

In the absence of microglia: ablating microglia

A variety of transgenic and pharmacological tools have been developed to specifically ablate microglia, and these have been useful for probing microglia functions during rest and disease, as well as the state of other cells in the absence of microglia (Green et al., 2020)(Figure 1.1 Box 4). In many instances, the absence of microglia has little phenotypic or behavioral impact (Spangenberg et al., 2019). However, microglia ablation disrupts adult neurogenesis in the mouse olfactory bulb (Wallace et al., 2020). Additionally, the loss of microglia in the retina can impair synaptic transmission. In particular, loss of all retinal microglia has been linked to disruption of cone photoreceptor synapses, and specific ablation of a subset of retinal microglia results in changes to bipolar cell signaling (O'Koren et al., 2019; Wang et al., 2016). Why different methods of microglia ablation and ablation in different tissues can have differing impacts on neuronal function remains a topic of debate.

Microglia ablation experiments have also been informative for understanding the ability of non-microglial immune cells to inhabit the retina. Although peripheral immune invasion of the CNS has not been reliably observed during normal function without any intervention, the identities of immune cells in the CNS have been investigated during microglial ablation and the phase of microglial repopulation following removal of the ablating agent. In the retina, ablation and repopulation is sufficient to recruit some macrophages from the surrounding ciliary body to the retinal parenchyma (Huang et al., 2018a). These invading macrophages are most likely resident macrophages of the ciliary body and iris, rather than recently monocyte-derived macrophages (Chinnery et al., 2017). However, these ciliary macrophages are far shorter lived than microglia, and the macrophages that migrate from other ocular structures during repopulation remain morphologically distinct from the resident macrophages, suggesting some differences between the two populations despite residing in the same microenvironment. Oddly, this external source of macrophages during repopulation after microglial ablation might be a retina-specific phenomenon, as this is not observed in equivalent experiments in the brain (Huang et al., 2018b). The reason for this difference requires further studies.

Emerging themes in retinal macrophages during damage and disease

In addition to the well-established overarching changes microglia undergo during activation, there are further emerging themes in the neuroimmune response in animal models of retinal damage and disease (Figure 1.2). First, the invasion of monocytes from the periphery has been observed in many retinal disorders. Monocytes in the retinal parenchyma have been detected using a range of techniques, including immunohistochemistry, flow cytometry, single-cell mRNA sequencing, and *in vivo* retinal imaging (Karlen et al., 2020; Yu et al., 2020), and these cells appear to persist in the retina throughout the course of neuronal loss (Ma et al., 2017; Paschalis et al., 2018a).

Another common theme is sustained mislocalization of macrophages, particularly in the subretinal space. In the healthy retina, microglia are only located in the inner and outer plexiform layers and the nerve fiber layer. During damage and degeneration, microglia and monocyte-derived macrophages migrate to dying cells, which often requires movement to or through the nuclear layers. Notably, during photoreceptor degeneration, microglia migrate to the subretinal space, where they appear to accumulate (Yu et al., 2020). Subretinal macrophages have even been observed in a mouse model of glaucoma, despite the primary locus of degeneration occurring in the inner retina (Ramírez et al., 2020). Subretinal macrophages can also accumulate with age (Chinnery et al., 2012). Instances and implications of subretinal macrophages are discussed in depth in a recent review (Yu et al., 2020).

Finally, emerging across the neuroimmune response to neurodegeneration is heterogeneity. Microglia in the healthy tissue form a generally homogenous population, with the overall gene expression profile, branched morphology and putative functions being conserved across CNS regions and even across species (Dubbelaar et al., 2018; Geirsdottir et al., 2019; Hammond et al., 2019; O'Koren et al., 2019; van der Poel et al., 2019). However, injury and disease activate microglia, transforming them into a highly dynamic and heterogeneous population. Single-cell transcriptomics in models of retinal degeneration (O'Koren et al., 2019; Ronning et al., 2019; Wieghofer et al., 2021) have identified several transcriptionally distinct subpopulations of microglia, similar to the heterogeneity observed in models of Alzheimer's disease and other neurodegenerative disorders (Hammond et al., 2019; Keren-Shaul et al., 2017; Tay et al., 2018)(Figure 1.1 Box 3). Across these wide-ranging types of degenerations, a subtype of microglia identified as disease-associated microglia (DAM), first in a mouse model of Alzheimer's disease (Keren-Shaul et al., 2017), have been further differentiated into Stage 1 and Stage 2 DAM based upon single-cell transcriptomics identifying putative markers for both stages. Although the 2-stage DAM progression has not been investigated to date in the retina, similar expression of known DAM markers increase their expression in microglia during retinal

degeneration (O'Koren et al., 2019; Ronning et al., 2019; Wieghofer et al., 2021)(Figure 1.2). This suggests that there may be a core gene expression program triggered during the inflammatory response to neurodegeneration across CNS tissues and disorders.

As we continue to amass single-cell data from different species and models, it is important to note that the ability to identify subpopulations of immune cells can be difficult due to the relative scarcity of immune cells compared to the number of neurons and glia (Liddelow et al., 2020). For example, in a recent study examining transcriptional changes across the entire retina after excitotoxic injury, there were not sufficient numbers of immune cells to even statistically separate control and activated microglial populations (Todd et al., 2019). This can be overcome either by dramatically increasing the number of cells sequenced or, more commonly, enriching the number of immune cells in a given sample using fluorescence activated cell sorting or other sorting methods. Despite the need to overcome challenges in cell numbers, single-cell sequencing and other similar techniques will likely continue to be critical in improving our understanding of heterogeneous microglial activation, and in differentiating microglial and other immune responders.

Harnessing differences between retinal disorders

Despite the many shared features of microglial activation across retinal degenerative disorders, there are also clear differences that can ultimately be harnessed to further our understanding of neuroinflammation. For example, differences in the initial cause of cell death, type and extent of cell loss, and timescale of degeneration may aid our understanding of the cellular or molecular criteria that trigger monocyte invasion. Thus far the most dramatic monocyte response has been observed in models of relatively rapid retinal degeneration (Karlen et al., 2018; O'Koren et al., 2019; Paschalis et al., 2018b; Ronning et al., 2019). In another, much slower degenerative model monocytic cells were not immediately apparent, although the complete absence of monocyte-derived macrophages was not confirmed (Blank et al., 2018). Of

course speed of cell loss does not entirely determine monocyte invasion, as monocytes have been observed in animal models and human tissue samples of age related macular degeneration, a relatively slow, chronic neurodegenerative disorder (Sennlaub et al., 2013). The persistence of monocytes can also differ between types of degeneration. Unlike the transient monocyte invasion observed in a model of rapid photoreceptor degeneration (Karlen et al., 2018), persistently elevated ocular CCL2 levels have been detected in patients with age-related macular degeneration, and CCR2+ monocytes have been observed in human retinas well after the onset of age-related macular degeneration (Rezar-Dreindl et al., 2016; Sennlaub et al., 2013). Further experiments will be needed to determine if this difference is the result of continued monocyte influx or a difference in the progression of monocyte differentiation.

The precise roles monocytic cells play during retinal degeneration also remain debated and vary across models of different types of degeneration. In some cases, blocking monocyte invasion appears to be beneficial, ameliorating the loss of retinal neurons (Cruz-Guilloty et al., 2013; Guo et al., 2012; Sennlaub et al., 2013). However, in other instances of retinal damage monocytic cells have been implicated in beneficial tissue healing (London et al., 2013b, 2011). Finally, during cell-autonomous photoreceptor degeneration blocking monocyte invasion had no effect on the loss of photoreceptors (Karlen et al., 2018). Improving our understanding of the context and differences driving monocytes to these helpful or harmful states will be important both for understanding retinal degeneration and for potentially developing immunomodulatory interventions.

The immune state after degeneration

Another avenue of particular interest in retinal degenerative disorders, and photoreceptor degeneration in particular, is understanding the immune state of the retina after the completion of neuronal loss. Unlike some chronic neurodegenerative disorders, some models and human cases of photoreceptor degenerative disorders such as retinitis pigmentosa

have an end point after photoreceptor loss is complete, at which the inner retina remains intact and relatively stable for a prolonged period. There are also many groups investigating underlying causes of neuronal death with the goal of inhibiting cell loss to limit cell death, thus ceasing degeneration. This clear endpoint is an exciting avenue to design and deliver therapeutics to return some degree of sight. However, understanding the inflammatory state of the retina could be important for the effectiveness of these therapeutics.

The resolution of the immune response has recently been investigated in two distinct models of retinal injury (Ma et al., 2017; Paschalis et al., 2018a). Critically, both studies find that retinal immune cells do not fully return to a baseline resting phenotype, suggesting that loss of retinal neurons can drive long-lasting changes to the retinal immune environment. Both studies also identified that monocyte-derived macrophages can remain in the retina for prolonged periods following neuronal loss, although the implications of those cells remaining in the retina remains unclear. In another acute model of neuronal loss in the CNS, facial nerve axotomy, a small subset of microglia similarly remain persistently activated (Tay et al., 2018). Because microglial activation has been linked to retinal dysfunction, it will be important to understand if the changed retinal immune population following injury can impact the efficacy of future interventions.

Glial-immune interactions

Finally, it will be critical to put our understanding of the neuroimmune response in the larger context of all non-neuronal cells. Glial cells, which are predominantly Müller glia and a relatively small number of astrocytes in the retina, play critical roles in maintaining homeostasis, and undergo changes in response to damage and disease, generally known as reactive gliosis (Vecino et al., 2016). As discussed earlier, part of the gliotic response of Müller glia can include recruiting monocytes to the retina. These cells can also participate in the clearance of debris by phagocytosing dead and dying photoreceptors during photoreceptor degeneration (Sakami et

al., 2019). Similar to immune cells, reactive glia can adopt an array of functional states, ranging from neuroprotective to detrimental (Graca et al., 2018). Further, there is growing evidence that immune cells can directly influence glial state and vice versa (Liddelow et al., 2020, 2017), including bi-directional signaling between microglia and Müller glia (Wang et al., 2011). To what extent monocytes and monocyte-derived macrophages can similarly influence glial state remains an open question but will be important in understanding the complete neuroinflammatory response to neurodegeneration.

In addition to supporting homeostasis and responding to disruptions, in some non-mammalian species Müller glia give rise to new retinal neurons after retinal degeneration. Recent work has identified transcriptional differences between species with and without this regenerative potential (Hoang et al., 2020), and there has been significant progress in experimentally promoting Müller glia-driven regeneration in mammalian animal models (Gao et al., 2021). However, it has also become apparent that inflammation can promote regeneration, and modulating inflammation can affect retinal regeneration (Nagashima and Hitchcock, 2021). This underscores both the extent of immune-glial interactions, and the importance of fully understanding retinal immune responders. Recent work has begun to specifically investigate how immune cells change during retinal regeneration (Mitchell et al., 2019). Immune modulation may prove to be an exciting avenue for improving retinal regeneration.

Conclusions: looking ahead

Despite the heterogeneity of immune responders within models, similarities such as conserved microglial phenotypes, invasion of monocytes, and more are evident across retinal degenerative disorders, and CNS disorders more generally. Still, even after the many advances in our understanding of retinal macrophages, there is much exciting work left to be done and many questions left to answer. In addition to further study of a variety of neurodegenerative models, it will be especially important to connect precise molecular and cellular changes across

these different circumstances and place the immune response in the larger context of other non-immune CNS cells and therapeutic interventions. And, although there is much work left to be done, immune modulation is an exciting avenue for the development of future therapeutic interventions for neurodegenerative disorders.

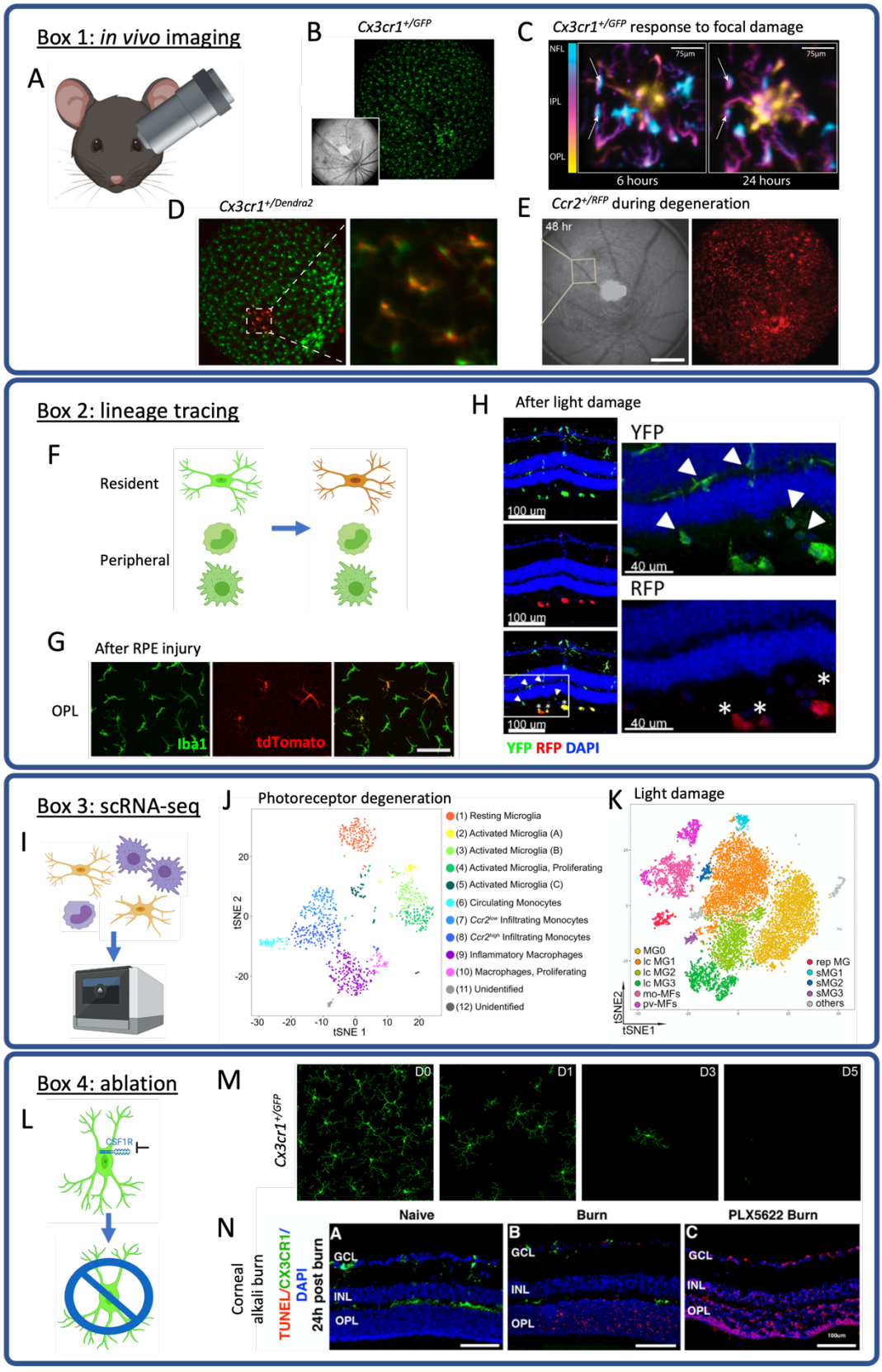
Box 1: in vivo imaging
A
B
Cx3cr1+/GFP
C
Cx3cr1+/GFP response to focal damage
NFL
IPL
OPL
75μm
6 hours
24 hours
D
Cx3cr1+/Dendra2
E
Ccr2+/RFP during degeneration
48 hr
Box 2: lineage tracing
F
Resident
Peripheral
G
After RPE injury
OPL
Iba1
tdTomato
H
After light damage
100 um
YFP
40 um
RFP
YFP RFP DAPI
Box 3: scRNA-seq
I
J
Photoreceptor degeneration
(1) Resting Microglia
(2) Activated Microglia (A)
(3) Activated Microglia (B)
(4) Activated Microglia, Proliferating
(5) Activated Microglia (C)
(6) Circulating Monocytes
(7) Ccr2low Infiltrating Monocytes
(8) Ccr2high Infiltrating Monocytes
(9) Inflammatory Macrophages
(10) Macrophages, Proliferating
(11) Unidentified
(12) Unidentified
tSNE 1
tSNE 2
K
Light damage
MG0
Ic MG1
Ic MG2
Ic MG3
mo-MFs
pv-MFs
rep MG
sMG1
sMG2
sMG3
others
tSNE1
tSNE2
Box 4: ablation
L
CSF1R
M
Cx3cr1+/GFP
D0
D1
D3
D5
N
Naive
Burn
PLX5622 Burn
Corneal alkali burn
24h post burn
TUNEL/CX3CR1/DAPI
GCL
INL
OPL
100um

Figure 1.1. Technological advances have been critical for teasing apart microglial and monocytic cells. Critical techniques include (Box 1) *in vivo* retinal imaging of fluorescently labeled immune cells, (Box 2) fluorescent lineage tracing paradigms, (Box 3) single-cell mRNA sequencing of enriched immune cells, and (Box 4) microglial ablation techniques. **(Box 1)** *In vivo* retinal imaging, schematized in (A), can be used to track immune cells in the retina. Scanning laser ophthalmoscopy (SLO) allows investigators to visualize fluorescently labeled cells (color images) and obtain structural information including the location of the vasculature by collecting back-reflected light (grayscale images in B and E). One genetically-encoded fluorescent reporter line frequently imaged in the retina is the Cx3cr1-GFP line (B-C). For example, this line has been used to visualize microglia in a healthy retina (B)(Ronning et al., 2019) and microglia responding to a focal laser injury (C)(Miller et al., 2019). (C) Use of adaptive optics can improve the depth resolution of SLO, as shown in the focal laser injury example with the cells pseudocolored by layer (Miller et al., 2019). (D) Recently the Cx3cr1-Dendra2 line was developed to label subpopulations of retinal macrophages (Miller et al., 2021). (E) The Ccr2-RFP line can be used to visualize monocyte invasion during degeneration (Karlen et al., 2018). **(Box 2)** Fluorescent lineage tracing paradigms have been critical for conclusively differentiating resident microglia from monocyte-derived cells. Frequently these paradigms involve administering tamoxifen to activate an inducible Cre recombinase and then waiting a set amount of time after tamoxifen, such that the resident cells will express different fluorophore(s) than monocytic cells, as schematized in (F). Examples of such lineage tracing paradigms include uses in a model of RPE injury (G)(Ma et al., 2017) and light-induced photoreceptor loss (H)(O'Koren et al., 2016). **(Box 3)** Retinas from healthy and diseased eyes can be dissociated, and then immune cells, enriched using techniques such as fluorescence activated cell sorting, can be used to generate single-cell mRNA libraries. One of the most frequently used systems is the Chromium 10X Genomics system (I). (J-K) Example tSNE plots of immune cells in two models of light-induced photoreceptor degeneration (O'Koren et al., 2019; Ronning et al., 2019).

(Box 4) Microglia ablation techniques have been important for identifying functional niches of microglia and how other cells change in the absence of microglia. (L) Several of the most commonly used techniques ablate microglia by inhibiting the CSF1 receptor (CSF1R). Example of microglia ablation in a healthy retina (M)(Huang et al., 2018a) and in a model of retinal ganglion cell death due to a corneal alkali burn (N)(Paschalis et al., 2019). RPE = retinal pigment epithelium; NFL = nerve fiber layer; GCL = ganglion cell layer; IPL = inner plexiform layer; INL = inner nuclear layer; OPL = outer plexiform layer. Portions of this figure were created with BioRender.com.

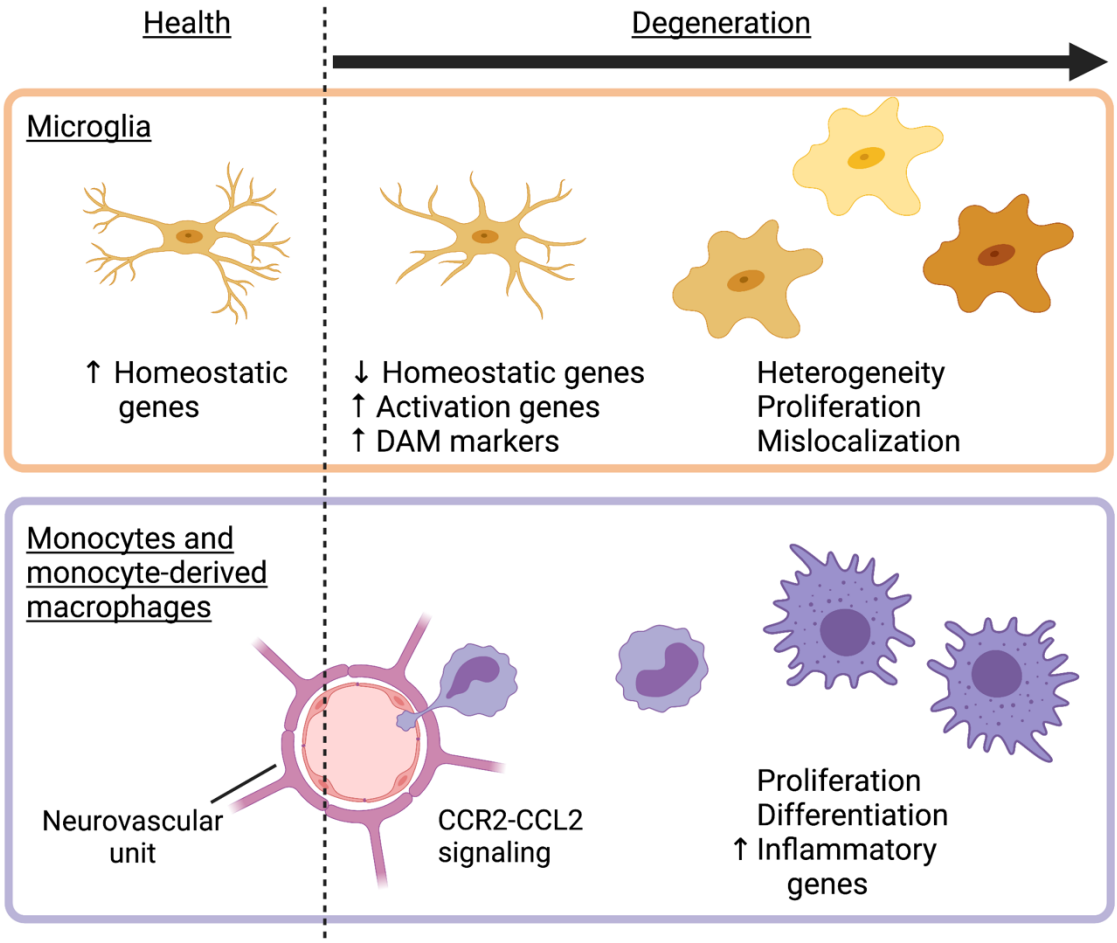

Figure 1.2. Shared features of the immune response to retinal degeneration. (Top row, yellow/orange) In response to retinal degeneration, microglia activate, which involves changes in morphology and gene expression. In addition to a shared loss of homeostatic gene expression and increase in DAM (disease associated microglia) genes, activated retinal microglia form heterogeneous subpopulations, proliferate, and migrate to retinal layers which usually do not contain immune cells during normal function. (Bottom row, purple) In addition to microglial activation, in many retinal disorders monocytes can pass the inner blood retinal barrier in a CCL2-CCR2 dependent way and invade the retinal parenchyma. After invading, monocytes can then differentiate into macrophages, which can further proliferate and increase their expression of inflammatory genes. Figure was created with BioRender.com.

References

Alt, C., Lin, C.P., 2012. In vivo quantification of microglia dynamics with a scanning laser ophthalmoscope in a mouse model of focal laser injury, in: Ophthalmic Technologies XXII. Presented at the Ophthalmic Technologies XXII, International Society for Optics and Photonics, p. 820907. https://doi.org/10.1117/12.909141

Azimipour, M., Jonnal, R.S., Werner, J.S., Zawadzki, R.J., 2019. Coextensive synchronized SLO-OCT with adaptive optics for human retinal imaging. Opt Lett 44, 4219–4222. https://doi.org/10.1364/OL.44.004219

Baufeld, C., O'Loughlin, E., Calcagno, N., Madore, C., Butovsky, O., 2018. Differential contribution of microglia and monocytes in neurodegenerative diseases. J Neural Transm 125, 809–826. https://doi.org/10.1007/s00702-017-1795-7

Bennett, M.L., Bennett, F.C., Liddelow, S.A., Ajami, B., Zamanian, J.L., Fernhoff, N.B., Mulinyawe, S.B., Bohlen, C.J., Adil, A., Tucker, A., Weissman, I.L., Chang, E.F., Li, G., Grant, G.A., Hayden Gephart, M.G., Barres, B.A., 2016. New tools for studying microglia in the mouse and human CNS. Proc Natl Acad Sci U S A 113, E1738-1746. https://doi.org/10.1073/pnas.1525528113

Blank, T., Goldmann, T., Koch, M., Amann, L., Schön, C., Bonin, M., Pang, S., Prinz, M., Burnet, M., Wagner, J.E., Biel, M., Michalakis, S., 2018. Early Microglia Activation Precedes Photoreceptor Degeneration in a Mouse Model of CNGB1-Linked Retinitis Pigmentosa. Front. Immunol. 8. https://doi.org/10.3389/fimmu.2017.01930

Borst, K., Dumas, A.A., Prinz, M., 2021. Microglia: Immune and non-immune functions. Immunity 54, 2194–2208. https://doi.org/10.1016/j.immuni.2021.09.014

Brown, G.C., Neher, J.J., 2014. Microglial phagocytosis of live neurons. Nat Rev Neurosci 15, 209–216. https://doi.org/10.1038/nrn3710

Cade, F., Grosskreutz, C.L., Tauber, A., Dohlman, C.H., 2011. Glaucoma in eyes with severe chemical burn, before and after keratoprosthesis. Cornea 30, 1322–1327. https://doi.org/10.1097/ICO.0b013e31821eead6

Calippe, B., Augustin, S., Beguier, F., Charles-Messance, H., Poupel, L., Conart, J.-B., Hu, S.J., Lavalette, S., Fauvet, A., Rayes, J., Levy, O., Raoul, W., Fitting, C., Denèfle, T., Pickering, M.C., Harris, C., Jorieux, S., Sullivan, P.M., Sahel, J.-A., Karoyan, P., Sapieha, P., Guillonneau, X., Gautier, E.L., Sennlaub, F., 2017. Complement Factor H Inhibits CD47-Mediated Resolution of Inflammation. Immunity 46, 261–272. https://doi.org/10.1016/j.immuni.2017.01.006

Chen, C.-K., Burns, M.E., Spencer, M., Niemi, G.A., Chen, J., Hurley, J.B., Baylor, D.A., Simon, M.I., 1999. Abnormal photoresponses and light-induced apoptosis in rods lacking rhodopsin kinase. PNAS 96, 3718–3722. https://doi.org/10.1073/pnas.96.7.3718

Chen, H.-R., Sun, Y.-Y., Chen, C.-W., Kuo, Y.-M., Kuan, I.S., Tiger Li, Z.-R., Short-Miller, J.C., Smucker, M.R., Kuan, C.-Y., 2020. Fate mapping via CCR2-CreER mice reveals monocyte-to-microglia transition in development and neonatal stroke. Sci Adv 6, eabb2119. https://doi.org/10.1126/sciadv.abb2119

Chen, J., Simon, M.I., Matthes, M.T., Yasumura, D., LaVail, M.M., 1999. Increased susceptibility to light damage in an arrestin knockout mouse model of Oguchi disease (stationary night blindness). Invest. Ophthalmol. Vis. Sci. 40, 2978–2982.

Chen, L., Wu, W., Dentchev, T., Zeng, Y., Wang, J., Tsui, I., Tobias, J.W., Bennett, J., Baldwin, D., Dunaief, J.L., 2004. Light damage induced changes in mouse retinal gene expression. Experimental Eye Research 79, 239–247. https://doi.org/10.1016/j.exer.2004.05.002

Chen, M., Zhao, J., Luo, C., Pandi, S.P.S., Penalva, R.G., Fitzgerald, D.C., Xu, H., 2012. Para-inflammation-mediated retinal recruitment of bone marrow-derived myeloid cells

following whole-body irradiation is CCL2 dependent. Glia 60, 833–842. https://doi.org/10.1002/glia.22315
Chinnery, H.R., McLenachan, S., Humphries, T., Kezic, J.M., Chen, X., Ruitenberg, M.J., McMenamin, P.G., 2012. Accumulation of murine subretinal macrophages: effects of age, pigmentation and CX3CR1. Neurobiology of Aging 33, 1769–1776. https://doi.org/10.1016/j.neurobiolaging.2011.03.010
Chinnery, H.R., McMenamin, P.G., Dando, S.J., 2017. Macrophage physiology in the eye. Pflugers Arch - Eur J Physiol 469, 501–515. https://doi.org/10.1007/s00424-017-1947-5
Colonna, M., Butovsky, O., 2017. Microglia Function in the Central Nervous System During Health and Neurodegeneration. Annu Rev Immunol 35, 441–468. https://doi.org/10.1146/annurev-immunol-051116-052358
Conart, J.-B., Blot, G., Augustin, S., Millet-Puel, G., Roubeix, C., Beguier, F., Charles-Messance, H., Touhami, S., Sahel, J.-A., Berrod, J.-P., Léveillard, T., Guillonneau, X., Delarasse, C., Sennlaub, F., 2020. Insulin inhibits inflammation-induced cone death in retinal detachment. J Neuroinflammation 17, 358. https://doi.org/10.1186/s12974-020-02039-1
Cruz-Guilloty, F., Saeed, A.M., Echegaray, J.J., Duffort, S., Ballmick, A., Tan, Y., Betancourt, M., Viteri, E., Ramkhellawan, G.C., Ewald, E., Feuer, W., Huang, D., Wen, R., Hong, L., Wang, H., Laird, J.M., Sene, A., Apte, R.S., Salomon, R.G., Hollyfield, J.G., Perez, V.L., 2013. Infiltration of Proinflammatory M1 Macrophages into the Outer Retina Precedes Damage in a Mouse Model of Age-Related Macular Degeneration. Int J Inflam 2013, 503725. https://doi.org/10.1155/2013/503725
Danciger, M., Yang, H., Handschumacher, L., LaVail, M.M., 2005. Constant light-induced retinal damage and the RPE65-MET450 variant: assessment of the NZW/LacJ mouse. Mol Vis 11, 374–379.
Daneman, R., Prat, A., 2015. The Blood–Brain Barrier. Cold Spring Harb Perspect Biol 7. https://doi.org/10.1101/cshperspect.a020412
Davalos, D., Grutzendler, J., Yang, G., Kim, J.V., Zuo, Y., Jung, S., Littman, D.R., Dustin, M.L., Gan, W.-B., 2005. ATP mediates rapid microglial response to local brain injury in vivo. Nature Neuroscience 8, 752–758. https://doi.org/10.1038/nn1472
Detrick, B., Hooks, J.J., 2019. The RPE Cell and the Immune System. Retinal Pigment Epithelium in Health and Disease 101–114. https://doi.org/10.1007/978-3-030-28384-1_6
Dubbelaar, M.L., Kracht, L., Eggen, B.J.L., Boddeke, E.W.G.M., 2018. The Kaleidoscope of Microglial Phenotypes. Frontiers in Immunology 9, 1753. https://doi.org/10.3389/fimmu.2018.01753
Eme-Scolan, E., Dando, S.J., 2020. Tools and Approaches for Studying Microglia In vivo. Front. Immunol. 11. https://doi.org/10.3389/fimmu.2020.583647
Evans, F.L., Dittmer, M., de la Fuente, A.G., Fitzgerald, D.C., 2019. Protective and Regenerative Roles of T Cells in Central Nervous System Disorders. Front. Immunol. 10. https://doi.org/10.3389/fimmu.2019.02171
Gao, H., A, L., Huang, X., Chen, X., Xu, H., 2021. Müller Glia-Mediated Retinal Regeneration. Mol Neurobiol 58, 2342–2361. https://doi.org/10.1007/s12035-020-02274-w
Gautier, E.L., Shay, T., Miller, J., Greter, M., Jakubzick, C., Ivanov, S., Helft, J., Chow, A., Elpek, K.G., Gordonov, S., Mazloom, A.R., Ma'ayan, A., Chua, W.-J., Hansen, T.H., Turley, S.J., Merad, M., Randolph, G.J., 2012. Gene-expression profiles and transcriptional regulatory pathways that underlie the identity and diversity of mouse tissue macrophages. Nature Immunology 13, 1118–1128. https://doi.org/10.1038/ni.2419
Geirsdottir, L., David, E., Keren-Shaul, H., Weiner, A., Bohlen, S.C., Neuber, J., Balic, A., Giladi, A., Sheban, F., Dutertre, C.-A., Pfeifle, C., Peri, F., Raffo-Romero, A., Vizioli, J., Matiasek, K., Scheiwe, C., Meckel, S., Mätz-Rensing, K., Meer, F. van der,

Thormodsson, F.R., Stadelmann, C., Zilkha, N., Kimchi, T., Ginhoux, F., Ulitsky, I., Erny, D., Amit, I., Prinz, M., 2019. Cross-Species Single-Cell Analysis Reveals Divergence of the Primate Microglia Program. Cell 179, 1609-1622.e16. https://doi.org/10.1016/j.cell.2019.11.010

Ginhoux, F., Greter, M., Leboeuf, M., Nandi, S., See, P., Gokhan, S., Mehler, M.F., Conway, S.J., Ng, L.G., Stanley, E.R., Samokhvalov, I.M., Merad, M., 2010. Fate Mapping Analysis Reveals That Adult Microglia Derive from Primitive Macrophages. Science 330, 841–845. https://doi.org/10.1126/science.1194637

Ginhoux, F., Jung, S., 2014. Monocytes and macrophages: developmental pathways and tissue homeostasis. Nature Reviews Immunology 14, 392–404. https://doi.org/10.1038/nri3671

Graca, A.B., Hippert, C., Pearson, R.A., 2018. Müller Glia Reactivity and Development of Gliosis in Response to Pathological Conditions, in: Ash, J.D., Anderson, R.E., LaVail, M.M., Bowes Rickman, C., Hollyfield, J.G., Grimm, C. (Eds.), Retinal Degenerative Diseases, Advances in Experimental Medicine and Biology. Springer International Publishing, Cham, pp. 303–308. https://doi.org/10.1007/978-3-319-75402-4_37

Green, K.N., Crapser, J.D., Hohsfield, L.A., 2020. To Kill a Microglia: A Case for CSF1R Inhibitors. Trends in Immunology, Special Issue: Microglia and Astrocytes 41, 771–784. https://doi.org/10.1016/j.it.2020.07.001

Guo, C., Otani, A., Oishi, A., Kojima, H., Makiyama, Y., Nakagawa, S., Yoshimura, N., 2012. Knockout of ccr2 alleviates photoreceptor cell death in a model of retinitis pigmentosa. Exp Eye Res 104, 39–47. https://doi.org/10.1016/j.exer.2012.08.013

Hammond, T.R., Dufort, C., Dissing-Olesen, L., Giera, S., Young, A., Wysoker, A., Walker, A.J., Gergits, F., Segel, M., Nemesh, J., Marsh, S.E., Saunders, A., Macosko, E., Ginhoux, F., Chen, J., Franklin, R.J.M., Piao, X., McCarroll, S.A., Stevens, B., 2019. Single-Cell RNA Sequencing of Microglia throughout the Mouse Lifespan and in the Injured Brain Reveals Complex Cell-State Changes. Immunity 50, 253-271.e6. https://doi.org/10.1016/j.immuni.2018.11.004

Harada, C., Kimura, A., Guo, X., Namekata, K., Harada, T., 2019. Recent advances in genetically modified animal models of glaucoma and their roles in drug repositioning. British Journal of Ophthalmology 103, 161–166. https://doi.org/10.1136/bjophthalmol-2018-312724

Hoang, T., Wang, J., Boyd, P., Wang, F., Santiago, C., Jiang, L., Yoo, S., Lahne, M., Todd, L.J., Jia, M., Saez, C., Keuthan, C., Palazzo, I., Squires, N., Campbell, W.A., Rajaii, F., Parayil, T., Trinh, V., Kim, D.W., Wang, G., Campbell, L.J., Ash, J., Fischer, A.J., Hyde, D.R., Qian, J., Blackshaw, S., 2020. Gene regulatory networks controlling vertebrate retinal regeneration. Science 370. https://doi.org/10.1126/science.abb8598

Huang, Y., Xu, Z., Xiong, S., Qin, G., Sun, F., Yang, J., Yuan, T.-F., Zhao, L., Wang, K., Liang, Y.-X., Fu, L., Wu, T., So, K.-F., Rao, Y., Peng, B., 2018a. Dual extra-retinal origins of microglia in the model of retinal microglia repopulation. Cell Discov 4, 9. https://doi.org/10.1038/s41421-018-0011-8

Huang, Y., Xu, Z., Xiong, S., Sun, F., Qin, G., Hu, G., Wang, J., Zhao, L., Liang, Y.-X., Wu, T., Lu, Z., Humayun, M.S., So, K.-F., Pan, Y., Li, N., Yuan, T.-F., Rao, Y., Peng, B., 2018b. Repopulated microglia are solely derived from the proliferation of residual microglia after acute depletion. Nature Neuroscience 21, 530–540. https://doi.org/10.1038/s41593-018-0090-8

Jung, S., Aliberti, J., Graemmel, P., Sunshine, M.J., Kreutzberg, G.W., Sher, A., Littman, D.R., 2000. Analysis of Fractalkine Receptor CX3CR1 Function by Targeted Deletion and Green Fluorescent Protein Reporter Gene Insertion. Molecular and Cellular Biology 20, 4106–4114. https://doi.org/10.1128/MCB.20.11.4106-4114.2000

Kadry, H., Noorani, B., Cucullo, L., 2020. A blood–brain barrier overview on structure, function, impairment, and biomarkers of integrity. Fluids and Barriers of the CNS 17, 69. https://doi.org/10.1186/s12987-020-00230-3
Kaiser, T., Feng, G., 2019. Tmem119-EGFP and Tmem119-CreERT2 Transgenic Mice for Labeling and Manipulating Microglia. eNeuro 6. https://doi.org/10.1523/ENEURO.0448-18.2019
Karlen, S.J., Miller, E.B., Burns, M.E., 2020. Microglia Activation and Inflammation During the Death of Mammalian Photoreceptors. Annu Rev Vis Sci 6, 149–169. https://doi.org/10.1146/annurev-vision-121219-081730
Karlen, S.J., Miller, E.B., Wang, X., Levine, E.S., Zawadzki, R.J., Burns, M.E., 2018. Monocyte infiltration rather than microglia proliferation dominates the early immune response to rapid photoreceptor degeneration. Journal of Neuroinflammation 15, 344. https://doi.org/10.1186/s12974-018-1365-4
Keren-Shaul, H., Spinrad, A., Weiner, A., Matcovitch-Natan, O., Dvir-Szternfeld, R., Ulland, T.K., David, E., Baruch, K., Lara-Astaiso, D., Toth, B., Itzkovitz, S., Colonna, M., Schwartz, M., Amit, I., 2017. A Unique Microglia Type Associated with Restricting Development of Alzheimer's Disease. Cell 169, 1276-1290.e17. https://doi.org/10.1016/j.cell.2017.05.018
Kettenmann, H., Hanisch, U.-K., Noda, M., Verkhratsky, A., 2011. Physiology of Microglia. Physiological Reviews 91, 461–553. https://doi.org/10.1152/physrev.00011.2010
Kiang, L., Ross, B.X., Yao, J., Shanmugam, S., Andrews, C.A., Hansen, S., Besirli, C.G., Zacks, D.N., Abcouwer, S.F., 2018. Vitreous Cytokine Expression and a Murine Model Suggest a Key Role of Microglia in the Inflammatory Response to Retinal Detachment. Invest Ophthalmol Vis Sci 59, 3767–3778. https://doi.org/10.1167/iovs.18-24489
LaVail, M.M., Gorrin, G.M., Yasumura, D., Matthes, M.T., 1999. Increased susceptibility to constant light in nr and pcd mice with inherited retinal degenerations. Invest Ophthalmol Vis Sci 40, 1020–1024.
Liang, K.J., Lee, J.E., Wang, Y.D., Ma, W., Fontainhas, A.M., Fariss, R.N., Wong, W.T., 2009. Regulation of dynamic behavior of retinal microglia by CX3CR1 signaling. Invest Ophthalmol Vis Sci 50, 4444–4451. https://doi.org/10.1167/iovs.08-3357
Liddelow, S.A., Guttenplan, K.A., Clarke, L.E., Bennett, F.C., Bohlen, C.J., Schirmer, L., Bennett, M.L., Münch, A.E., Chung, W.-S., Peterson, T.C., Wilton, D.K., Frouin, A., Napier, B.A., Panicker, N., Kumar, M., Buckwalter, M.S., Rowitch, D.H., Dawson, V.L., Dawson, T.M., Stevens, B., Barres, B.A., 2017. Neurotoxic reactive astrocytes are induced by activated microglia. Nature 541, 481–487. https://doi.org/10.1038/nature21029
Liddelow, S.A., Marsh, S.E., Stevens, B., 2020. Microglia and Astrocytes in Disease: Dynamic Duo or Partners in Crime? Trends in Immunology 41, 820–835. https://doi.org/10.1016/j.it.2020.07.006
Littman, D.R., 2013. An inducible cre recombinase driven by Cx3cr1. Mouse Genome Informatics J:190965.
London, A., Benhar, I., Schwartz, M., 2013a. The retina as a window to the brain-from eye research to CNS disorders. Nat Rev Neurol 9, 44–53. https://doi.org/10.1038/nrneurol.2012.227
London, A., Cohen, M., Schwartz, M., 2013b. Microglia and monocyte-derived macrophages: functionally distinct populations that act in concert in CNS plasticity and repair. Frontiers in Cellular Neuroscience 7, 34. https://doi.org/10.3389/fncel.2013.00034
London, A., Itskovich, E., Benhar, I., Kalchenko, V., Mack, M., Jung, S., Schwartz, M., 2011. Neuroprotection and progenitor cell renewal in the injured adult murine retina requires healing monocyte-derived macrophages. J Exp Med 208, 23–39. https://doi.org/10.1084/jem.20101202

Ma, W., Zhang, Y., Gao, C., Fariss, R.N., Tam, J., Wong, W.T., 2017. Monocyte infiltration and proliferation reestablish myeloid cell homeostasis in the mouse retina following retinal pigment epithelial cell injury. Sci Rep 7, 8433. https://doi.org/10.1038/s41598-017-08702-7

Mildner, A., Schmidt, H., Nitsche, M., Merkler, D., Hanisch, U.-K., Mack, M., Heikenwalder, M., Brück, W., Priller, J., Prinz, M., 2007. Microglia in the adult brain arise from Ly-6ChiCCR2+ monocytes only under defined host conditions. Nat Neurosci 10, 1544–1553. https://doi.org/10.1038/nn2015

Miller, E.B., Karlen, S.J., Ronning, K.E., Burns, M.E., 2021. Tracking distinct microglia subpopulations with photoconvertible Dendra2 in vivo. Journal of Neuroinflammation 18, 235. https://doi.org/10.1186/s12974-021-02285-x

Miller, E.B., Zhang, P., Ching, K., Pugh, E.N., Burns, M.E., 2019. In vivo imaging reveals transient microglia recruitment and functional recovery of photoreceptor signaling after injury. Proc. Natl. Acad. Sci. U.S.A. 116, 16603–16612. https://doi.org/10.1073/pnas.1903336116

Mitchell, D.M., Sun, C., Hunter, S.S., New, D.D., Stenkamp, D.L., 2019. Regeneration associated transcriptional signature of retinal microglia and macrophages. Sci Rep 9, 4768. https://doi.org/10.1038/s41598-019-41298-8

Müther, P.S., Semkova, I., Schmidt, K., Abari, E., Kuebbeler, M., Beyer, M., Abken, H., Meyer, K.L., Kociok, N., Joussen, A.M., 2010. Conditions of retinal glial and inflammatory cell activation after irradiation in a GFP-chimeric mouse model. Invest Ophthalmol Vis Sci 51, 4831–4839. https://doi.org/10.1167/iovs.09-4923

Muzio, L., Viotti, A., Martino, G., 2021. Microglia in Neuroinflammation and Neurodegeneration: From Understanding to Therapy. Frontiers in Neuroscience 15, 1205. https://doi.org/10.3389/fnins.2021.742065

Nagashima, M., Hitchcock, P.F., 2021. Inflammation Regulates the Multi-Step Process of Retinal Regeneration in Zebrafish. Cells 10, 783. https://doi.org/10.3390/cells10040783

Nakazawa, T., Kayama, M., Ryu, M., Kunikata, H., Watanabe, R., Yasuda, M., Kinugawa, J., Vavvas, D., Miller, J.W., 2011. Tumor Necrosis Factor-α Mediates Photoreceptor Death in a Rodent Model of Retinal Detachment. Invest Ophthalmol Vis Sci 52, 1384–1391. https://doi.org/10.1167/iovs.10-6509

Naylor, A., Hopkins, A., Hudson, N., Campbell, M., 2019. Tight Junctions of the Outer Blood Retina Barrier. Int J Mol Sci 21. https://doi.org/10.3390/ijms21010211

Nimmerjahn, A., Kirchhoff, F., Helmchen, F., 2005. Resting Microglial Cells Are Highly Dynamic Surveillants of Brain Parenchyma in Vivo. Science 308, 1314–1318. https://doi.org/10.1126/science.1110647

O'Koren, E.G., Mathew, R., Saban, D.R., 2016. Fate mapping reveals that microglia and recruited monocyte-derived macrophages are definitively distinguishable by phenotype in the retina. Sci Rep 6, 20636. https://doi.org/10.1038/srep20636

O'Koren, E.G., Yu, C., Klingeborn, M., Wong, A.Y.W., Prigge, C.L., Mathew, R., Kalnitsky, J., Msallam, R.A., Silvin, A., Kay, J.N., Bowes Rickman, C., Arshavsky, V.Y., Ginhoux, F., Merad, M., Saban, D.R., 2019. Microglial Function Is Distinct in Different Anatomical Locations during Retinal Homeostasis and Degeneration. Immunity 50, 723-737.e7. https://doi.org/10.1016/j.immuni.2019.02.007

Okunuki, Y., Mukai, R., Pearsall, E.A., Klokman, G., Husain, D., Park, D.-H., Korobkina, E., Weiner, H.L., Butovsky, O., Ksander, B.R., Miller, J.W., Connor, K.M., 2018. Microglia inhibit photoreceptor cell death and regulate immune cell infiltration in response to retinal detachment. Proc Natl Acad Sci U S A 115, E6264–E6273. https://doi.org/10.1073/pnas.1719601115

Paschalis, E.I., Lei, F., Zhou, C., Chen, X.N., Kapoulea, V., Hui, P.-C., Dana, R., Chodosh, J., Vavvas, D.G., Dohlman, C.H., 2019. Microglia Regulate Neuroglia Remodeling in

Various Ocular and Retinal Injuries. The Journal of Immunology 202, 539–549. https://doi.org/10.4049/jimmunol.1800982
Paschalis, E.I., Lei, F., Zhou, C., Kapoulea, V., Dana, R., Chodosh, J., Vavvas, D.G., Dohlman, C.H., 2018a. Permanent neuroglial remodeling of the retina following infiltration of CSF1R inhibition-resistant peripheral monocytes. PNAS 115, E11359–E11368. https://doi.org/10.1073/pnas.1807123115
Paschalis, E.I., Lei, F., Zhou, C., Kapoulea, V., Thanos, A., Dana, R., Vavvas, D.G., Chodosh, J., Dohlman, C.H., 2018b. The Role of Microglia and Peripheral Monocytes in Retinal Damage after Corneal Chemical Injury. The American Journal of Pathology 188, 1580–1596. https://doi.org/10.1016/j.ajpath.2018.03.005
Paschalis, E.I., Zhou, C., Lei, F., Scott, N., Kapoulea, V., Robert, M.-C., Vavvas, D., Dana, R., Chodosh, J., Dohlman, C.H., 2017. Mechanisms of Retinal Damage after Ocular Alkali Burns. The American Journal of Pathology 187, 1327–1342. https://doi.org/10.1016/j.ajpath.2017.02.005
Priller, J., Flügel, A., Wehner, T., Boentert, M., Haas, C.A., Prinz, M., Fernández-Klett, F., Prass, K., Bechmann, I., de Boer, B.A., Frotscher, M., Kreutzberg, G.W., Persons, D.A., Dirnagl, U., 2001. Targeting gene-modified hematopoietic cells to the central nervous system: Use of green fluorescent protein uncovers microglial engraftment. Nature Medicine 7, 1356–1361. https://doi.org/10.1038/nm1201-1356
Ramírez, A.I., de Hoz, R., Fernández-Albarral, J.A., Salobrar-Garcia, E., Rojas, B., Valiente-Soriano, F.J., Avilés-Trigueros, M., Villegas-Pérez, M.P., Vidal-Sanz, M., Triviño, A., Ramírez, J.M., Salazar, J.J., 2020. Time course of bilateral microglial activation in a mouse model of laser-induced glaucoma. Scientific Reports 10, 4890. https://doi.org/10.1038/s41598-020-61848-9
Rashid, K., Akhtar-Schaefer, I., Langmann, T., 2019. Microglia in Retinal Degeneration. Frontiers in Immunology 10, 1975. https://doi.org/10.3389/fimmu.2019.01975
Reyes, N.J., O'Koren, E.G., Saban, D.R., 2017. New insights into mononuclear phagocyte biology from the visual system. Nat. Rev. Immunol. 17, 322–332. https://doi.org/10.1038/nri.2017.13
Rezar-Dreindl, S., Sacu, S., Eibenberger, K., Pollreisz, A., Bühl, W., Georgopoulos, M., Krall, C., Weigert, G., Schmidt-Erfurth, U., 2016. The Intraocular Cytokine Profile and Therapeutic Response in Persistent Neovascular Age-Related Macular Degeneration. Invest Ophthalmol Vis Sci 57, 4144–4150. https://doi.org/10.1167/iovs.16-19772
Ronning, K.E., Karlen, S.J., Miller, E.B., Burns, M.E., 2019. Molecular profiling of resident and infiltrating mononuclear phagocytes during rapid adult retinal degeneration using single-cell RNA sequencing. Scientific Reports 9, 4858. https://doi.org/10.1038/s41598-019-41141-0
Sabatino, J.J., Pröbstel, A.-K., Zamvil, S.S., 2019. B cells in autoimmune and neurodegenerative central nervous system diseases. Nature Reviews Neuroscience 20, 728–745. https://doi.org/10.1038/s41583-019-0233-2
Saederup, N., Cardona, A.E., Croft, K., Mizutani, M., Cotleur, A.C., Tsou, C.-L., Ransohoff, R.M., Charo, I.F., 2010. Selective chemokine receptor usage by central nervous system myeloid cells in CCR2-red fluorescent protein knock-in mice. PLoS ONE 5, e13693. https://doi.org/10.1371/journal.pone.0013693
Sakami, S., Imanishi, Y., Palczewski, K., 2019. Müller glia phagocytose dead photoreceptor cells in a mouse model of retinal degenerative disease. FASEB J 33, 3680–3692. https://doi.org/10.1096/fj.201801662R
Sasaki, Y., Hoshi, M., Akazawa, C., Nakamura, Y., Tsuzuki, H., Inoue, K., Kohsaka, S., 2003. Selective expression of Gi/o-coupled ATP receptor P2Y12 in microglia in rat brain. Glia 44, 242–250. https://doi.org/10.1002/glia.10293

Schafer, D.P., Lehrman, E.K., Kautzman, A.G., Koyama, R., Mardinly, A.R., Yamasaki, R., Ransohoff, R.M., Greenberg, M.E., Barres, B.A., Stevens, B., 2012. Microglia Sculpt Postnatal Neural Circuits in an Activity and Complement-Dependent Manner. Neuron 74, 691–705. https://doi.org/10.1016/j.neuron.2012.03.026

Sennlaub, F., Auvynet, C., Calippe, B., Lavalette, S., Poupel, L., Hu, S.J., Dominguez, E., Camelo, S., Levy, O., Guyon, E., Saederup, N., Charo, I.F., Rooijen, N.V., Nandrot, E., Bourges, J.-L., Behar-Cohen, F., Sahel, J.-A., Guillonneau, X., Raoul, W., Combadiere, C., 2013. CCR2(+) monocytes infiltrate atrophic lesions in age-related macular disease and mediate photoreceptor degeneration in experimental subretinal inflammation in Cx3cr1 deficient mice. EMBO Mol Med 5, 1775–1793. https://doi.org/10.1002/emmm.201302692

Shapouri-Moghaddam, A., Mohammadian, S., Vazini, H., Taghadosi, M., Esmaeili, S.-A., Mardani, F., Seifi, B., Mohammadi, A., Afshari, J.T., Sahebkar, A., 2018. Macrophage plasticity, polarization, and function in health and disease. Journal of Cellular Physiology 233, 6425–6440. https://doi.org/10.1002/jcp.26429

Shi, C., Pamer, E.G., 2011. Monocyte recruitment during infection and inflammation. Nat Rev Immunol 11, 762–774. https://doi.org/10.1038/nri3070

Silverman, S.M., Ma, W., Wang, X., Zhao, L., Wong, W.T., 2019. C3- and CR3-dependent microglial clearance protects photoreceptors in retinitis pigmentosa. J Exp Med 216, 1925–1943. https://doi.org/10.1084/jem.20190009

Spangenberg, E., Severson, P.L., Hohsfield, L.A., Crapser, J., Zhang, J., Burton, E.A., Zhang, Y., Spevak, W., Lin, J., Phan, N.Y., Habets, G., Rymar, A., Tsang, G., Walters, J., Nespi, M., Singh, P., Broome, S., Ibrahim, P., Zhang, C., Bollag, G., West, B.L., Green, K.N., 2019. Sustained microglial depletion with CSF1R inhibitor impairs parenchymal plaque development in an Alzheimer's disease model. Nature Communications 10, 3758. https://doi.org/10.1038/s41467-019-11674-z

Tay, T.L., Mai, D., Dautzenberg, J., Fernández-Klett, F., Lin, G., Sagar, Datta, M., Drougard, A., Stempfl, T., Ardura-Fabregat, A., Staszewski, O., Margineanu, A., Sporbert, A., Steinmetz, L.M., Pospisilik, J.A., Jung, S., Priller, J., Grün, D., Ronneberger, O., Prinz, M., 2017. A new fate mapping system reveals context-dependent random or clonal expansion of microglia. Nature Neuroscience 20, 793–803. https://doi.org/10.1038/nn.4547

Tay, T.L., Sagar, null, Dautzenberg, J., Grün, D., Prinz, M., 2018. Unique microglia recovery population revealed by single-cell RNAseq following neurodegeneration. Acta Neuropathol Commun 6, 87. https://doi.org/10.1186/s40478-018-0584-3

Todd, L., Palazzo, I., Suarez, L., Liu, X., Volkov, L., Hoang, T.V., Campbell, W.A., Blackshaw, S., Quan, N., Fischer, A.J., 2019. Reactive microglia and IL1β/IL-1R1-signaling mediate neuroprotection in excitotoxin-damaged mouse retina. Journal of Neuroinflammation 16, 118. https://doi.org/10.1186/s12974-019-1505-5

van der Poel, M., Ulas, T., Mizee, M.R., Hsiao, C.-C., Miedema, S.S.M., Adelia, Schuurman, K.G., Helder, B., Tas, S.W., Schultze, J.L., Hamann, J., Huitinga, I., 2019. Transcriptional profiling of human microglia reveals grey–white matter heterogeneity and multiple sclerosis-associated changes. Nature Communications 10, 1139. https://doi.org/10.1038/s41467-019-08976-7

Vecino, E., Rodriguez, F.D., Ruzafa, N., Pereiro, X., Sharma, S.C., 2016. Glia–neuron interactions in the mammalian retina. Progress in Retinal and Eye Research 51, 1–40. https://doi.org/10.1016/j.preteyeres.2015.06.003

Veleri, S., Lazar, C.H., Chang, B., Sieving, P.A., Banin, E., Swaroop, A., 2015. Biology and therapy of inherited retinal degenerative disease: insights from mouse models. Dis Model Mech 8, 109–129. https://doi.org/10.1242/dmm.017913

Wallace, J., Lord, J., Dissing-Olesen, L., Stevens, B., Murthy, V.N., 2020. Microglial depletion disrupts normal functional development of adult-born neurons in the olfactory bulb. eLife 9, e50531. https://doi.org/10.7554/eLife.50531

Wang, J., Struebing, F.L., Geisert, E.E., 2021. Commonalities of optic nerve injury and glaucoma-induced neurodegeneration: Insights from transcriptome-wide studies. Experimental Eye Research 207, 108571. https://doi.org/10.1016/j.exer.2021.108571

Wang, M., Ma, W., Zhao, L., Fariss, R.N., Wong, W.T., 2011. Adaptive Müller cell responses to microglial activation mediate neuroprotection and coordinate inflammation in the retina. Journal of Neuroinflammation 8, 173. https://doi.org/10.1186/1742-2094-8-173

Wang, X., Miller, E.B., Goswami, M., Zhang, P., Ronning, K.E., Karlen, S.J., Zawadzki, R.J., Pugh, E.N., Burns, M.E., 2017. Rapid monocyte infiltration following retinal detachment is dependent on non-canonical IL6 signaling through gp130. J Neuroinflammation 14. https://doi.org/10.1186/s12974-017-0886-6

Wang, X., Zhao, L., Zhang, J., Fariss, R.N., Ma, W., Kretschmer, F., Wang, M., Qian, H. hua, Badea, T.C., Diamond, J.S., Gan, W.-B., Roger, J.E., Wong, W.T., 2016. Requirement for Microglia for the Maintenance of Synaptic Function and Integrity in the Mature Retina. J Neurosci 36, 2827–2842. https://doi.org/10.1523/JNEUROSCI.3575-15.2016

Wieghofer, P., Hagemeyer, N., Sankowski, R., Schlecht, A., Staszewski, O., Amann, L., Gruber, M., Koch, J., Hausmann, A., Zhang, P., Boneva, S., Masuda, T., Hilgendorf, I., Goldmann, T., Böttcher, C., Priller, J., Rossi, F.M., Lange, C., Prinz, M., 2021. Mapping the origin and fate of myeloid cells in distinct compartments of the eye by single-cell profiling. EMBO J 40, e105123. https://doi.org/10.15252/embj.2020105123

Wolf, S.A., Boddeke, H.W.G.M., Kettenmann, H., 2017. Microglia in Physiology and Disease. Annu. Rev. Physiol. 79, 619–643. https://doi.org/10.1146/annurev-physiol-022516-034406

Wolf, Y., Yona, S., Kim, K.-W., Jung, S., 2013. Microglia, seen from the CX3CR1 angle. Frontiers in Cellular Neuroscience 7, 26. https://doi.org/10.3389/fncel.2013.00026

Xi, H., Katschke, K.J., Jr, Li, Y., Truong, T., Lee, W.P., Diehl, L., Rangell, L., Tao, J., Arceo, R., Eastham-Anderson, J., Hackney, J.A., Iglesias, A., Cote-Sierra, J., Elstrott, J., Weimer, R.M., van Lookeren Campagne, M., 2016. IL-33 amplifies an innate immune response in the degenerating retina. Journal of Experimental Medicine 213, 189–207. https://doi.org/10.1084/jem.20150894

Xu, J., Dodd, R.L., Makino, C.L., Simon, M.I., Baylor, D.A., Chen, J., 1997. Prolonged photoresponses in transgenic mouse rods lacking arrestin. Nature 389, 505–509. https://doi.org/10.1038/39068

Yu, C., Roubeix, C., Sennlaub, F., Saban, D.R., 2020. Microglia versus Monocytes: Distinct Roles in Degenerative Diseases of the Retina. Trends in Neurosciences 43, 433–449. https://doi.org/10.1016/j.tins.2020.03.012

Zhang, P., Zam, A., Jian, Y., Wang, X., Li, Y., Lam, K.S., Burns, M.E., Sarunic, M.V., Jr, E.N.P., Zawadzki, R.J., 2015. In vivo wide-field multispectral scanning laser ophthalmoscopy–optical coherence tomography mouse retinal imager: longitudinal imaging of ganglion cells, microglia, and Müller glia, and mapping of the mouse retinal and choroidal vasculature. JBO 20, 126005. https://doi.org/10.1117/1.JBO.20.12.126005

Zhao, L., Zabel, M.K., Wang, X., Ma, W., Shah, P., Fariss, R.N., Qian, H., Parkhurst, C.N., Gan, W.-B., Wong, W.T., 2015. Microglial phagocytosis of living photoreceptors contributes to inherited retinal degeneration. EMBO Mol Med 7, 1179–1197. https://doi.org/10.15252/emmm.201505298

Chapter 2

Loss of cone function without degeneration in a novel *Gnat2* knock-out mouse

Preface

The following chapter was submitted to *Experimental Eye Research* as a manuscript titled “Loss of cone function without degeneration in a novel *Gnat2* knock-out mouse” and was accepted on February 24, 2018. The accepted version of this manuscript has been reformatted to meet the guidelines of this dissertation. The authors of the manuscript were Kaitryn E. Ronning, Gabriel Peinado Allina, Eric B. Miller, Robert J. Zawadzki, Edward N. Pugh Jr., Rolf Herrmann, and Marie E. Burns. I performed and analyzed qRT-PCR, performed and analyzed IHC, obtained some ERGs, created figures, and wrote and edited the manuscript.

Although this project is focused on cone photoreceptors rather than immune cells, it was my first project during graduate school, and it laid the foundation for my future work in immunity in the retina. As discussed in the chapter, other similar mouse lines with silent cone photoreceptors exhibit varying degrees of neuronal disruption and loss, so in this project it was critical that I examine these mice for evidence of similar neuronal disruptions. This included assessing retinal microglia and Müller glia for signs of activation, because these cells are incredibly sensitive to damage and loss of neurons. These were my first experiments examining immune cells in the retina, in this instance in healthy retinas. Further study of retinal immune cells during retinal disease then became the core of the rest of this dissertation.

Abstract

Rods and cones mediate visual perception over 9 log units of light intensities, with both photoreceptor types contributing to a middle 3-log unit range that comprises most night-time conditions. Rod function in this mesopic range has been difficult to isolate and study *in vivo* because of the paucity of mutants that abolish cone signaling without causing photoreceptor degeneration. Here we describe a novel *Gnat2* knockout mouse line (*Gnat2*$^{-/-}$) ideal for dissecting rod and cone function. In this line, loss of Gnat2 expression abolished cone phototransduction, yet there was no loss of cones, disruption of the photoreceptor mosaic, nor change in general retinal morphology up to at least 9 months of age. Retinal microglia and Müller glia, which are highly sensitive to neuronal pathophysiology, were distributed normally with morphologies indistinguishable between *Gnat2*$^{-/-}$ and wildtype adult mice. ERG recordings demonstrated complete loss of cone-driven a-waves in *Gnat2*$^{-/-}$ mice; comparison to WT controls revealed that rods of both strains continue to function at light intensities exceeding 10^4 photoisomerizations rod^{-1} s^{-1}. We conclude that the *Gnat2*$^{-/-}$ mouse is a preferred model for functional studies of rod pathways in the retina when degeneration could be an experimental confound.

Introduction

The retinal circuits that relay rod and cone photoreceptor signals to retinal ganglion cells overlap extensively in the mammalian retina. Cones form chemical synapses with cone bipolar cells, which transmit visual signals to retinal ganglion cells (Strettoi et al., 2010). Rods transmit visual information via multiple pathways, all of which involve cone bipolar cells. The primary rod pathway employs chemical synapses between rods and rod bipolar cells, which pass information to A2 amacrine cells, which in turn modulate On- and Off-cone bipolar cells. The secondary rod pathway transmits rod responses via gap junctions directly to cones, which then relay the signals synaptically to cone bipolar cells (Deans et al., 2002). In the less common

tertiary rod pathway, rods form chemical synapses directly with cone bipolar cells (Pang et al., 2010). Although convergent pathways from both photoreceptor classes are advantageous for signaling across a wide range of light intensities, such convergence also makes dissecting the functional contributions of rods and cones to the retinal circuitry challenging.

Performing experiments under scotopic or photopic conditions is a useful way to functionally isolate rod and cone signals, but only under those extreme conditions. At intermediate light levels, both rods and cones generate light responses, but the functional consequences of their individual contributions to a combined output are difficult to assess (e.g. (Naarendorp et al., 2010)). An ideal way to separate the contributions of rod and cone signaling would be to specifically render all the rods or all the cones insensitive to light without disrupting their synaptic connections and partners. Pharmacological manipulations such as superfusion with the metabotropic glutamate receptor agonist, 2-amino-4-phosphonobutyric acid (APB), are commonly used to overwhelm light-driven changes in synaptic release, but such manipulations affect all ON-bipolar cells or all Off-bipolar cells rather than all rod inputs or all cone inputs to the circuitry. Moreover, pharmacologically silencing the cone pathway downstream of cone photoreceptors necessarily eliminates some of the rod input to vision by silencing the secondary rod pathway.

Several mutant mouse lines have been created to genetically silence rod or cone light responses. For example, mice lacking the rod-specific G-protein transducin alpha subunit (*Gnat1*$^{-/-}$) lack phototransduction signaling downstream of rhodopsin and thus have no rod electrical responses to light, with no detectable concurrent photoreceptor degeneration (Calvert et al., 2000). However, mutants with defects in the cone phototransduction cascade often exhibit morphological abnormalities. One mouse line commonly used to isolate rod function is the *Gnat2*^{cpfl3} mutant, which contains a single-base pair missense mutation in the gene encoding the cone-specific G-protein transducin alpha subunit, *Gnat2* (Chang et al., 2006). In these mice, neither *Gnat2* expression nor cone function is abolished initially, but both decline through

adulthood and are finally undetectable by 9 months of age (Chang et al., 2006). Importantly, rod-driven responses in *Gnat2*^{cpfl3} mice also decline with age, with clear evidence of photoreceptor degeneration before 27 weeks of age, or approximately 6 months (Chang et al., 2006). More recently, the *Gnat2*$^{c.518A>G}$ mouse line was found to lack cone function due to an amino acid substitution that results in incorrect protein folding and ultimately a loss of Gnat2 function (Jobling et al., 2013). While the cones of *Gnat2*$^{c.518A>G}$ mice do not completely degenerate, they exhibit some structural abnormalities as early as 3 months of age, which become more pronounced and lead to Müller cell gliosis as the mice further age. These abnormalities include M-opsin mislocalization, displaced photoreceptor terminals, altered horizontal cell morphology, and altered bipolar cell morphology, suggesting significant disruption to both rod and cone pathways within the circuitry.

Here we describe a novel *Gnat2* knock-out mouse line (*Gnat2*$^{-/-}$) that exhibits a complete loss of cone function without retinal degeneration or other noticeable morphological abnormalities. Importantly, rod function in these animals appears to be completely normal throughout adulthood, revealing the upper limit of the mesopic range of rod function, and refining previous estimate for cone thresholds and the magnitude of cone signaling in the mouse.

Methods

Animals

Mice were cared for and handled in accordance with NIH and UC Davis IACUC guidelines. C57BL/6J mice were obtained from the Jackson Laboratory (Sacramento CA). To disrupt *Gnat2* expression, a 7654 base pair deletion spanning exons 2-9 of the *Gnat2* gene on chromosome 3 was achieved by inserting a lacZ/Neo cassette using homologous recombination (Figure 2.1A). ES cell clones were generated by the UC Davis Mouse Biology Program to yield *Gnat2*$^{tm1(KOMP)Vlcg}$ during targeting project VG17376, here referred to as *Gnat2*$^{-/-}$. Vector clones

and embryonic stem cells are commercially available from the UC Davis KOMP Repository (Davis, CA). *Gnat2*$^{-/-}$ ES cells were implanted into 129Sv/J host dams, and subsequently maintained on a C57BL/6J background for more than 10 generations, with at least 3 rounds of out and in-breeding *Gnat2* heterozygotes with particular attention to genotyping for and selecting against the *rd8* mutation. All mice used in this study lacked the *rd8* mutation. For specific experiments, heterozygous *Gnat2* mice were bred to generate both wild-type and knock-out littermates for direct comparisons; because wild-type littermates were phenotypically indistinguishable from C57BL/6J, the two data sets were ultimately pooled for comparisons. In each case, mice of both sexes were used.

Quantitative real time PCR

Whole retinas were isolated from 3-4-month-old *Gnat2*$^{-/-}$ and *Gnat2*$^{+/+}$ littermate control mice. RNA was isolated from whole retinas using the RNeasy Plus Mini Kit (Qiagen) and cDNA was synthesized using the RevertAid First Strand cDNA Synthesis Kit (ThermoScientific). RNA and cDNA concentrations and quality were determined using a NanoDrop (ThermoScientific). TaqMan Gene Expression Assays (ThermoFisher Scientific) were used to quantify mRNA expression of *Gnat2*, *Hprt*, and *Rho* (Mm00492394_m1, Mm03024075_m1, and Mm01184405_m1 respectively) (UC Davis Real-Time PCR Research and Diagnostics Core Facility). Relative expression of *Gnat2* and *Rhodopsin* were calculated using the comparative C_T method (also known as the $2^{-\Delta\Delta CT}$ method; (Schmittgen and Livak, 2008)). This calculation assumes that the PCR efficiency for all genes is similar, which was confirmed for these probes and conditions using multiple dilutions (not shown). Some *Gnat2*$^{-/-}$ samples did not reach C_T threshold for detection within the range of the apparatus although the wells were replicating; in such instances, the samples were assigned the maximum hypothetical C_T value of 40 (based on the cycling conditions) for relative gene expression calculations. Statistical significance was calculated after combining the comparative C_T calculations across independent experiments at a matching dilution using a two-tailed Student's t-Test.

Immunohistochemistry

Mice 6 and 9 months of age were sacrificed by carbon dioxide euthanasia before enucleation. Eyes were fixed in 4% paraformaldehyde for 25-30 minutes, and the cornea and lens were removed during fixation. To examine histology and protein localization, fixed eyecups were embedded in agarose and sliced into 150 μm thick sections on a vibratome (Leica). Sections were blocked in normal goat serum at room temperature, followed by an overnight incubation with primary antibodies at 4 °C, and then incubation with secondary antibodies for 1.5-2 hours at room temperature. To examine the number of cone photoreceptors and microglia morphology, retinal flatmounts were prepared rather than retinal slices. In brief, whole retinas were removed from the fixed posterior pole and cut to relax the curvature. Isolated retinas were incubated in 1% Triton X-100 in PBS overnight at 4 °C followed by blocking with normal goat serum for 2 hours in a 37 °C water bath. Primary antibody incubation proceeded overnight at 4 °C, followed by incubation in secondary antibodies for 1.5-2 hours in a 37 °C water bath. Both retinal sections and flat mounts were mounted on glass slides with Diamond Antifade Mountant (Life Technologies) before imaging. Primary antibodies and nuclei stains used are listed in Table 2.1, and secondary antibodies were Alexa Fluor-conjugated (Life Technologies) and used at 1:200 or 1:300 dilution. All sections and flat mounts were imaged using a Nikon A1 confocal microscope.

Cone photoreceptor density was assessed in 5 separate areas of each flat-mounted retina: superior, inferior, nasal, temporal, and central. Two squares of 150 μm x 150 μm were randomly chosen within each area of each retina, and cones were manually selected and quantified using a counting function (Nikon NES-Elements). Statistical significance was calculated using a two-tailed Student's t-Test.

Optical coherence tomography

Mice 5 and 9 months of age were anesthetized with isoflurane and the pupils dilated with tropicamide and phenylephrine. High acquisition-speed Fd-OCT (132 nm @ 855 nm broadband

light source [Superlum] and CMOS camera [Basler] operating at 100,000 A-scans/s) were used to obtain *in vivo* mouse retinal volumetric data sets as described in (Zhang et al., 2015). Images were acquired over 1.9 x 1.9 mm retinal area (51 deg FOV; see (Zhang et al., 2016)). OCT volumes were flattened using a strip-registration algorithm to align each A-scan in the data set. To measure the thickness of retinal layers, all A-scan intensity profiles were averaged from the flattened OCT volume, and evaluated using the choroid, INL, and GCL as landmarks. The distance from choroid to INL defined the outer retinal thickness and the distance from INL to GCL was defined as inner retinal thickness.

Corneal electroretinography

After dark adaptation overnight, mice were anesthetized with isoflurane and the pupils dilated with tropicamide and phenylephrine. Electroretinograms (ERGs) were recorded with a Maxwellian-view Ganzfeld ERG system (Phoenix Research Labs), equipped with two independent calibrated LED sources (365 and 510 nm). A reference electrode was inserted subcutaneously above the eye, and a ground electrode was inserted subcutaneously at the base of the tail. Combined rod and cone photoreceptor function was characterized using 1 ms flashes of 365 and 510 nm light. Assuming an end-on collecting area of 0.87 μm^2 for rods (Lyubarsky et al., 2004) and a collecting area of 1 μm^2 for cones (Daniele et al., 2005), a flash delivering 100 photons μm^{-2} suppresses an average of ~50% of the circulating current of rods (Peinado Allina et al., 2017), but less than 4% of the circulating current of cones (Nikonov et al., 2006). We thus used this flash strength to probe the scotopic ERG in Figure 2.4. In order to isolate cone photoreceptor function, a saturating probe flash (1 ms of 365 nm, $1.22x10^6$ photons/μm^2) was delivered on top of a rod-desensitizing background (5 sec of 510 nm light, delivering at least $1x10^5$ photons μm^{-2} sec^{-1}).

Dark intervals of 20-60 s were interposed between consecutive flashes to ensure complete recovery. These intervals also served to minimize oscillatory potentials that commonly develop over the course of a recording session. To measure a- and b-wave amplitudes,

oscillatory potentials were removed prior to analysis by filtering with a 5 ms boxcar filter. A-wave amplitudes were measured from the baseline to the peak of the negative deflection of the unfiltered traces, and b-wave amplitudes were measured from the peak of the unfiltered a-wave to the peak of the filtered, positive-going deflection. All traces were analyzed using IgorPro 7.06 (WaveMetrics). Statistical significance of comparisons between wild-type and *Gnat2*$^{-/-}$ mice was calculated using a two-tailed Student's *t*-Test. Mice used for ERGs were 3-5 months of age.

Results

Loss of Gnat2 expression does not produce cone dysmorphogenesis or retinal degeneration

Gnat2 expression was targeted for disruption by inserting a 7654 base pair deletion spanning exons 2-9 of the *Gnat2* gene through homologous recombination (Figure 2.1A; see Methods). Successful disruption of gene expression was first confirmed by examining *Gnat2* mRNA expression levels using quantitative real-time PCR (qRT-PCR). Gene expression was quantified using the comparative C_T method, using *Hprt* as a reference gene. *Gnat2* expression was undetectable; based on our detection limits, mRNA levels were decreased at least $6x10^4$-fold in the knock-out retinas (p-value=0.00055, Figure 2.1B). Using the same analysis methods and different primers (see Methods), rhodopsin (*Rho*) expression was likewise quantified and found to be unchanged between *Gnat2*$^{-/-}$ and WT control littermates (p-value=0.75, Figure 2.1C), consistent with normal rod photoreceptor number and outer segment rhodopsin densities in the mutant retina.

To examine Gnat2 protein expression as well as cone photoreceptor morphology, we used immunohistochemistry and peanut agglutinin (PNA) staining of cones in retinas of both knockout and wild-type littermates (Figure 2.2). Staining with PNA revealed comparable outer segment and synaptic morphologies of cones from both genotypes (Figure 2.2A). Cone synapses were never observed to be displaced to the inner or outer nuclear layers, and there were no morphological abnormalities observed in the outer plexiform layer. While

there was clear Gnat2 immunoreactivity in the cone outer segments of wild-type retinas, there was no detectable staining in the *Gnat2*$^{-/-}$ retinas, consistent with complete loss of protein expression (Figure 2.2A). DAPI staining revealed normal nuclear layers in *Gnat2*$^{-/-}$ retinas. Indeed, the outer nuclear layers of knock-out mice and wild-type litter mate controls were indistinguishable at 6 and 9 months (ONL thickness measurements, in μm: 6-month-old WT and *Gnat2*$^{-/-}$, 51.72 ± 5.84 and 52.31 ± 3.87 respectively; 9-month-old *Gnat2*$^{-/-}$ 53.79 ± 5.63; no statistically significant differences, all $p>0.05$). Additionally, staining for both M-opsin (Figure 2.2B) and S-opsin (data not shown) was comparable between control and knockout mice, with no evident opsin mislocalization. Finally, the numbers of cones per unit retinal area were counted in retinal flat mounts (Figure 2.1C), with both *Gnat2*$^{-/-}$ and wild-type littermates showing comparable cell densities (Figure 2.1D). Thus, there were no signs of degeneration of cones in the *Gnat2*$^{-/-}$ mice up to 9 months of age.

Next, we evaluated the thickness and integrity of the retina layers by *in vivo* optical coherence tomography (OCT; Figure 2.3A). OCT uses interferometry to extract depth-dependent measures of back-scattered light, and the intensity and axial distribution of this signal are useful means to quantify subtle differences in retinal structure between mice or within an individual animal over time (e.g. (Levine et al., 2014; Zhang et al., 2015)). OCT B-scans showed the retinal layers in the *Gnat2*$^{-/-}$ mice to be indistinguishable from those of wild-type mice up to 9 months of age, with all retinas showing clearly delineated nuclear and plexiform layers, transparent (non-scattering) outer nuclear layers as well as an intact external limiting membrane, all signs of healthy photoreceptors (Figure 2.3A; (Levine et al., 2014)). Measurements of outer (Figure 2.3B) and inner retina thicknesses (data not shown) revealed no differences between wild-type and knockout strains at any age examined. Thus, there were no overt signs of photoreceptor or retinal degeneration *in vivo*.

To look for more subtle changes in retinal health, we examined the morphology and localization of retinal microglia, the resident macrophages that respond to neuronal injury or

stress by changing their morphology and migrating to the site of insult. Staining both retinal section (data not shown) and flat mounts (Figure 2.3C) with the microglial marker Iba1 revealed normal ramified morphologies and normal densities of microglial cells in the outer plexiform layer with no microglial invasion into the nuclear layers. We also examined retinal sections for signs of Müller cell gliosis by immunostaining for GFAP. No difference was detectable between control or knockout retinas (Figure 2.3D). These results provide further evidence that degeneration does not occur in the *Gnat2*$^{-/-}$ retina by 9 months of age.

Absence of cone-driven retinal signaling in the absence of Gnat2

To assess retinal function in the absence of Gnat2, we used *in vivo* electroretinograms (ERGs). The ERG provides information about the electrical responses of both photoreceptors (the a-wave) and bipolar cells (the b-wave). We first probed rod signaling in dark-adapted animals by recording ERGs in response to a flash that strongly activated rods, but negligibly activated cones (100 photons μm^{-2}; see Methods section). The ERGs elicited by such a flash were indistinguishable in both amplitude and time course between *Gnat2*$^{-/-}$ and wild-type animals (Figure 2.4A), suggesting that rod function and rod-driven bipolar cell signaling were normal in *Gnat2*$^{-/-}$ mice. Strongly consistent with this hypothesis, intensity-response functions for the a-wave and b-wave amplitudes recorded from dark-adapted animals were indistinguishable between mouse strains (Figures 2.4C and 2.4D). Moreover, the ERG elicited by a stimulus calculated to saturate both rod and cone responses (1 ms flash of 2x10^6 photons μm^{-2}; Figure 2.4B) had nearly identical saturating a-wave amplitudes (WT: 1035 ± 55 μV, mean ± SEM, n=5 and *Gnat2*$^{-/-}$: 985 ± 25 μV, n=3; p-value=0.462207), consistent with the scotopic a-wave being dominated by rods. The completely normal characteristics of scotopic ERGs of the *Gnat2*$^{-/-}$ mice reveal that rod function is unperturbed by the loss of Gnat2 expression in cones.

In contrast, cone-driven ERGs were undetectable in the absence of *Gnat2* expression. In wild-type mice, a bright flash delivered in the presence of a rod-saturating background elicited a photopic ERG response with a cone-driven a-wave of approximately 60 μV in amplitude, while

no such cone-driven a-wave was detectable in *Gnat2*$^{-/-}$ mice (Figure 2.5A-B). Because *Gnat2*$^{-/-}$ mice show normal cone morphology and normal rod function but lack visual transduction in cones, this strain is ideal for dissecting the contributions of rods and cones to the ERG across a range of steady light intensities. To examine the conditions under which cone function is manifest in the ERGs of the wild-type mice, we measured the response to an intense ultraviolet flash (365 nm, 1 ms, 1.22×10^6 photons μm^{-2}) in the presence of a 510 nm backgrounds with intensities ranging over 7 $\log_{10}$ units (Figure 2.5). A UV flash was used because it strongly activates the predominant mouse cone opsin, S-opsin, which has a 360 nm λ_{max} (Lyubarsky et al., 1999). In contrast, the 510 nm backgrounds negligibly activate the S-opsin, while strongly suppressing the rod circulating current. In the presence of scotopic and mesopic backgrounds up to 1×10^4 photons μm^2 s^{-1} (~10^4 R*/rod/s), both wild-type and *Gnat2*$^{-/-}$ mice showed indistinguishable a-wave amplitudes, consistent with predominance of rod electrical responses in this intensity regime. However, as the background intensity increased above 5×10^4 photons μm^{-2} s^{-1}, *Gnat2*$^{-/-}$ mice failed to generate detectable ERG responses, whereas wild-type mice continued to show cone-driven flash responses whose maximal amplitude changed negligibly over a 1000-fold range of backgrounds (Figure 2.5, insets). These results establish the absence of phototransduction in *Gnat2*$^{-/-}$ cones, while also revealing the level of rod excitation (~10^4 R*/rod/s) at which cones become the predominant source underlying the a-wave.

Discussion

Many studies that have attempted to dissect rod and cone contributions to retinal signaling have utilized *Gnat1*$^{-/-}$ mice, whose rods are rendered completely insensitive to light by the loss of the alpha subunit of the rod G protein, transducin (Calvert et al., 2000). In contrast, the use of the analogous disruption in cone phototransduction through genetic deletion of the cone G protein, Gnat2, has been hampered by concurrent rod pathway dysfunction or degeneration (Chang et al., 2006; Jobling et al., 2013), effects that can confound conclusions

about rod function. Here we have presented evidence that cone photoreceptors can be rendered insensitive to light by abolishing Gnat2 expression without any loss of cone cell numbers or rod function. Thus, for the first time there is a genetic line of mice lacking cone function but having intact rod circuitry, and thus an opportunity to fully examine to the extent to which rods are capable of signaling under mesopic and photopic conditions. Here we summarize our findings in the context of previous efforts in this realm and then discuss the significance of rod signaling at high light intensities for future work.

Comparison of Gnat2$^{-/-}$ mice to other common cone-silent mice

The *Gnat2*$^{-/-}$ mouse line characterized here is the first example of complete loss of cone phototransduction without degeneration or other morphological abnormalities that have been observed in other mice with *Gnat2* disruption. For example, in the *Gnat2*$^{c.518A>G}$ mouse, in which a missense mutation results in the misfolding of the protein, distinct retinal remodeling is apparent as early as 3 months of age, despite a normal rod ERG. This remodeling includes disruptions in the outer plexiform and nuclear layers, most notably displaced photoreceptor synapses, horizontal cell processes, and bipolar cell dendrites into the outer nuclear layer. These disruptions then become more pronounced with age, as does Müller cell gliosis, both of which are extensive by 12 months of age (Jobling et al., 2013). Such retinal remodeling, especially the displacement of rod bipolar cells into the outer nuclear layer, suggests that rod primary and secondary pathways in the retina are likely perturbed as early as 3 months of age. Presumably, the worsening of this remodeling contributes to the decrease in the rod ERG with age in *Gnat2*$^{c.518A>G}$ mice.

Another commonly used cone phototransduction-incompetent mouse line is *Gnat2*^{cpfl3}, in which a missense mutation results in an early stop codon in the *Gnat2* gene. In this line, loss of cone function is coincident with outer nuclear layer thinning and outer segment vacuolization by 6 months. This is accompanied by a mild but clearly detectable decrease in rod-mediated ERGs with age (Chang et al., 2006), and it has been shown that the secondary rod pathway is entirely

abolished in these mice (Nusinowitz et al., 2007). Thus, while both *Gnat2*$^{c.518A>G}$ and *Gnat2*^{cpfl3} lines have allowed significant research into rod-mediated vision (e.g. (Naarendorp et al., 2010; Pahlberg et al., 2017; Umino et al., 2008)), their use has the potential to introduce significant confounds, particularly for adult or aging studies.

In contrast, at approximately the same ages, the *Gnat2*$^{-/-}$ mouse line showed no differences in retinal thickness between knockout and wild-type littermates both by OCT and standard histological measures of nuclear layer thickness, nor was there any detectable decrease in rod-mediated ERGs. Additionally, there were no differences between knockout and control retinas in Müller cell gliosis or microglial activation, both markers of retinal dysfunction and photoreceptor loss. Most importantly, loss of Gnat2 expression did not result in any detectable change in cone morphology, cell densities, opsin localizations, or rod-driven a- or b-waves. Taken together, these results suggest the *Gnat2*$^{-/-}$ line is a valuable tool for isolating rod function under mesopic conditions, such as is needed for work investigating rod secondary and tertiary retinal pathways and for behavioral studies. Future studies that rely on downstream retinal circuitry should also take care to examine more subtle features of cone synapses, such as their electrical coupling and horizontal and bipolar cell processes, to ensure that there are not as yet undetected compensatory changes resulting from the loss of Gnat2.

The contribution of rods to the normal murine ERG under mesopic intensities

Rod and cone function can be easily separated and examined at very dim and very bright light levels, respectively. However, the wide middle range of light intensities over which phototransduction drives changes in membrane currents concurrently in both rods and cones creates ambiguity both about the absolute sensitivity of cones, as well as the state of functional adaptation of rods. Some behavioral experiments using the *Gnat2*^{cpfl3} mouse line (Umino et al., 2008), have concluded that rod signaling becomes negligible at intensities greater than −2.0 log cd m^{-2} or roughly 1 photoisomerizations rod^{-1} s^{-1}. In contrast, more recent work in mouse retinal slices has found the primary rod pathway can function at light levels similar to our results,

although this work did not entirely rule out an indirect contribution of cones (Long et al., 2013). Behavioral experiments using the *Gnat2*^{cpfl3} mouse line have found sustained rod function in the presence of background illumination of 10^3 (Nathan et al., 2006) and even 10^4 photons μm^{-2} s^{-1} (Naarendorp et al., 2010), similar to the upper functional limit of rod a-waves found here (Figure 2.5A). Various states of rod degeneration may explain some of the differences between these studies, and lead to underestimating rod contributions. Future studies utilizing the *Gnat2*$^{-/-}$ mouse should be useful in sorting out these discrepancies.

The *Gnat2*$^{-/-}$ mouse will likely also be useful for investigating the influence of rod signaling pathways on light adaptation mechanisms in the retina. For example, it has been shown that the cone-driven b-wave increases in amplitude during light adaptation, yet the cause of this increase remains unclear (Alexander et al., 2006; Garon et al., 2010; Tanikawa et al., 2004). Because the *Gnat2*$^{-/-}$ mouse line does not exhibit observable deficiencies in rod signaling, it could be used to dissect the unique contributions of the rod-pathway to post-photoreceptor light adaptation.

Gnat2$^{-/-}$ *mouse as a model of achromatopsia*

Finally, the *Gnat2*$^{-/-}$ line may also be of interest to the community as a mouse model of achromatopsia, a heterogeneous disorder in which the loss of cone function results in deficits in visual acuity, nystagmus, photophobia, and other clinical symptoms. Indeed, although the most common causative achromatopsia mutations are in the cone cyclic nucleotide-gated channel, some cases of achromatopsia have also been causally linked to mutations in Gnat2 (Kohl et al., 2004). While achromatopsia is defined as a lack of cone function, human achromatopsia patients also exhibit a wide range of rod function, ranging from essentially normal to dramatic deficits (Maguire et al., 2017). Both *Gnat2*^{cpfl3} and *Gnat2*$^{c.518A>G}$ have been used as mouse models of achromatopsia, generally as models for achromatopsia cases where secondary deficiencies arise (Chang et al., 2006; Jobling et al., 2013). In contrast, this *Gnat2*$^{-/-}$ mouse line may be useful in modeling the less severe achromatopsia cases, where rod function remains

normal (Hansen, 1990; Maguire et al., 2017), or have normal scotopic ERGs yet display dramatic deficiencies in other measures of scotopic function, such as fast flicker responses (Hansen, 1990). Thus, the *Gnat2*$^{-/-}$ mouse should be a useful model for identifying where in the rod parallel pathways these specific deficiencies arise.

Table 2.1. Antibodies and stains used for immunohistochemical staining of retinal sections and flatmounts.

Target	Host Species or Name	Catalog Number	Manufacturer	RRID	Dilution
Cones	Lectin PNA, Alexa Fluor 568 conjugated	L32458	Life Technologies	NA	1:100
GFAP	Rabbit	Z0334	Dako	AB_10013382	1:1000
Gnat2	Rabbit	LS-C321680	LifeSpan Biosciences	none	1:100
Iba1	Rabbit	019-19741	Wako Pure Chem Industries, Ltd.	AB_2665520	1:1000
M-opsin	Rabbit	None	From Cheryl Craft	AB_2314755	1:100
Nuclei	NucBlue® Fixed Cell Stain	R37606	Life Technologies	NA	1 drop/mL
S-opsin	Rabbit	None	From Cheryl Craft	none	1:100

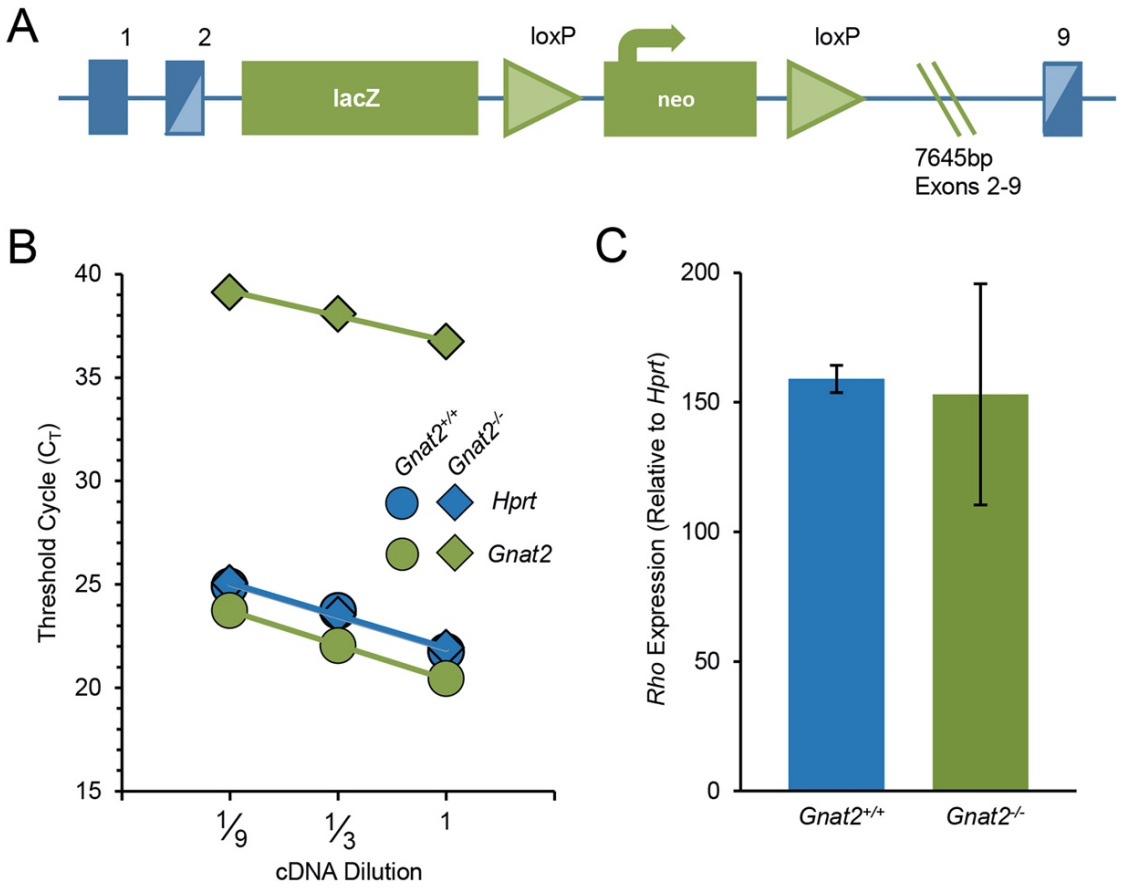

Figure 2.1. Targeted deletion of *Gnat2* decreases *Gnat2* mRNA expression while *Rho* expression remains unchanged. (A) Targeted deletion strategy used to generate the *Gnat2*$^{-/-}$ mouse line (adapted from KOMP). (B) Representative qRT-PCR results from wild-type (filled circles) and *Gnat2*$^{-/-}$ (filled diamonds) littermates 3 months of age. Threshold cycle (C_T) values are shown as a function of cDNA dilutions used for *Gnat2* (green filled) and *Hprt* (blue filled). Across 4 independent experiments, the C_T values for *Gnat2* in the knockout were dramatically increased, indicating that there was at least a 60,000-fold reduction in expression in the knockout (p-value<0.001). (C) Relative rhodopsin expression was unchanged between the knockout and control littermate (p-value=0.75; n=4-7). Bar graph shows mean $2^{-\Delta\Delta CT}$ ± SD.

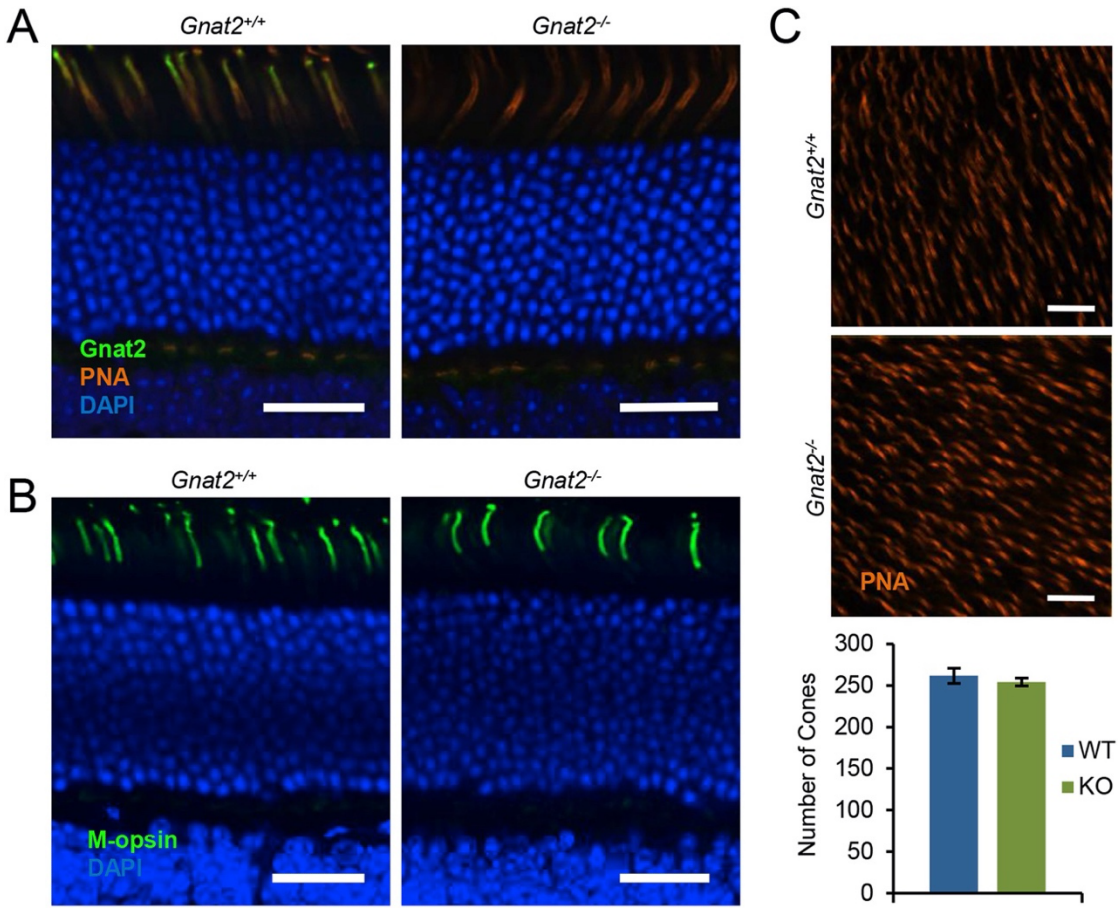

Figure 2.2. Normal cone photoreceptor morphology and number in *Gnat2*$^{-/-}$ retinas. (A) In retinal sections, PNA staining (orange) showed normal cone morphology and Gnat2 staining (green) confirmed loss of Gnat2 protein in the knockout. Shown here are representative wild-type and *Gnat2*$^{-/-}$ littermates, 5 months of age. (B) M-opsin staining (green) was the same in wild-type and knockout littermates. (C) Representative 150 µm x 150 µm areas of control and knockout littermate retinal flat mounts stained with PNA to visualize cones. Quantification revealed no difference in the number of cones per unit area (p-value=0.4817; n=5 measurements per flatmount, 4 flatmounts from each strain). All scale bars are 25 µm.

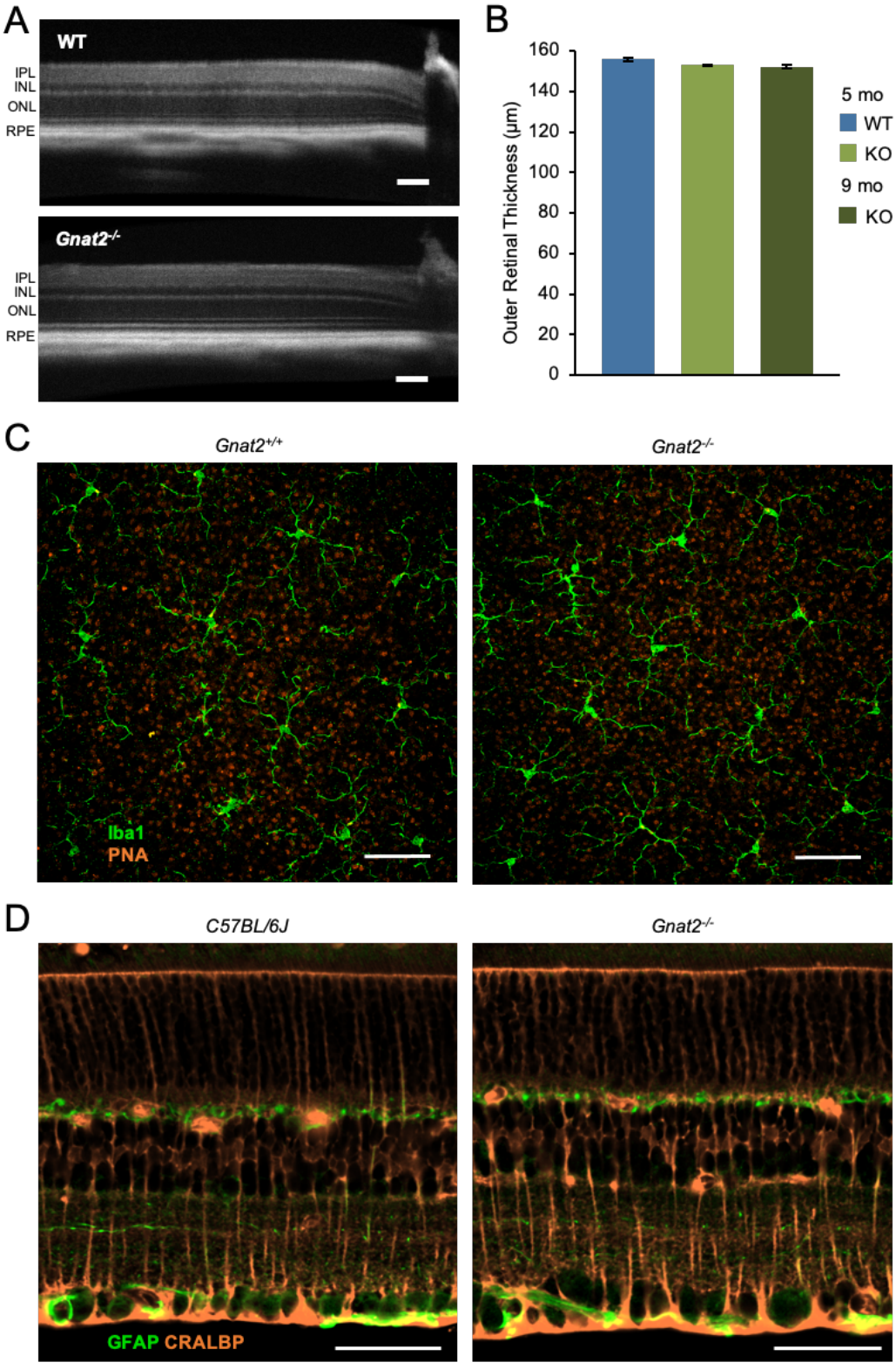

Figure 2.3. *Gnat2*$^{-/-}$ retinas do not exhibit retinal degeneration. (A) OCT B-scans through the optic nerve head show normal layering of WT and *Gnat2*$^{-/-}$ retinas. Shown here are a

representative 5-month-old WT retina (top) and a representative 9-month-old *Gnat2*$^{-/-}$ retina (bottom). The optic nerve head is located at the far right of each image. Scale bars indicate 100 μm. (B) The outer retinal thickness (choroid to INL) was on average the same in 5-month-old (5mo) WT and *Gnat2*$^{-/-}$ mice, as well as 9-month-old (9mo) *Gnat2*$^{-/-}$ mice. Data displayed are mean ± range (n=4-6 eyes for each). (C) Maximum intensity projections (through 5 μm in z) of the outer plexiform layer of *Gnat2*$^{+/+}$ and *Gnat2*$^{-/-}$ littermate flatmounts stained for Iba1 (green, microglia) and PNA (orange, cones) reveal normal ramified microglia at the photoreceptor synapses. Scale bars indicate 50 μm. (D) Representative images of retinal sections from C57BL/6J and *Gnat2*$^{-/-}$ stained for CRALBP (orange) and GFAP (green) reveal no differences in reactive gliosis. Scale bars indicate 50μm. IPL, inner plexiform layer; INL, inner nuclear layer; ONL, outer nuclear layer; RPE, retinal pigment epithelium.

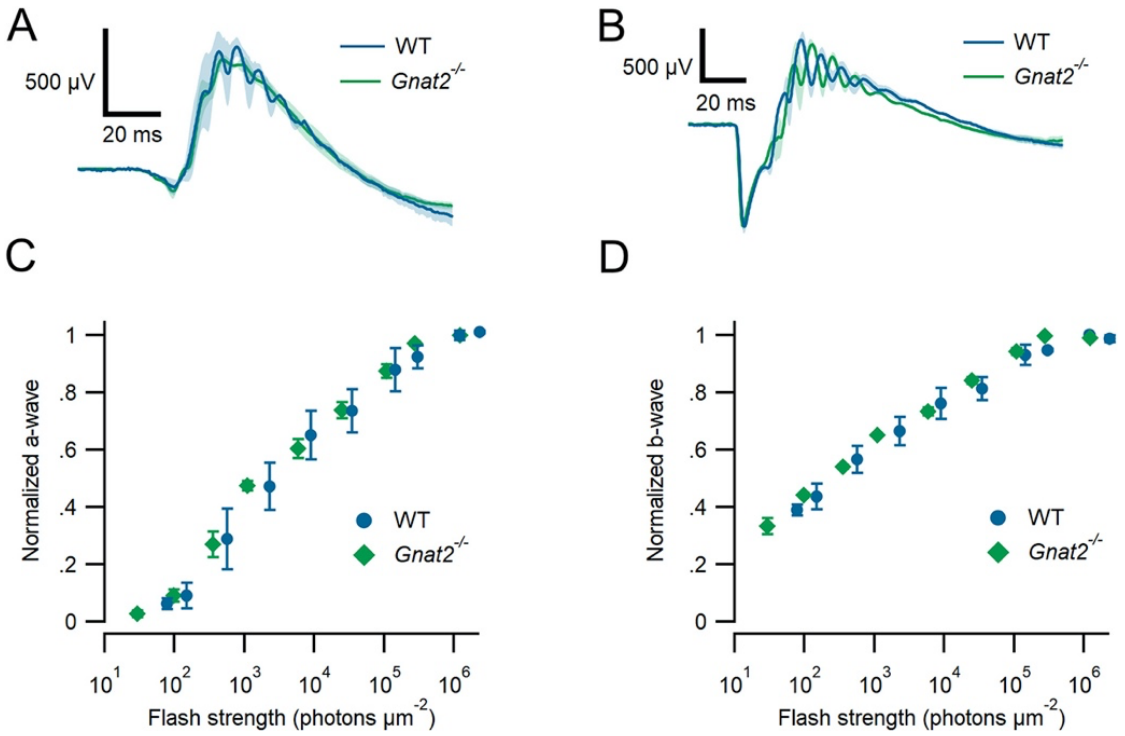

Figure 2.4. Knockout retinas display normal rod-drive a- and b-wave amplitudes. (A) Comparison of the average response of *Gnat2*$^{-/-}$ (green) and wild-type (WT, blue) animals to a flash of 100 photos µm^{-2}. (B) Average bright flash responses of *Gnat2*$^{-/-}$ and WT animals (2x10^{6} photons µm^{-2}). (C-D) Peak electroretinogram a-wave (C) and b-wave (D) amplitudes of WT (blue circles) and *Gnat2*$^{-/-}$ (green diamonds) mice in response to increasingly bright flashes of 510 nm light (32-1.22x10^{6} photons µm^{-2}).

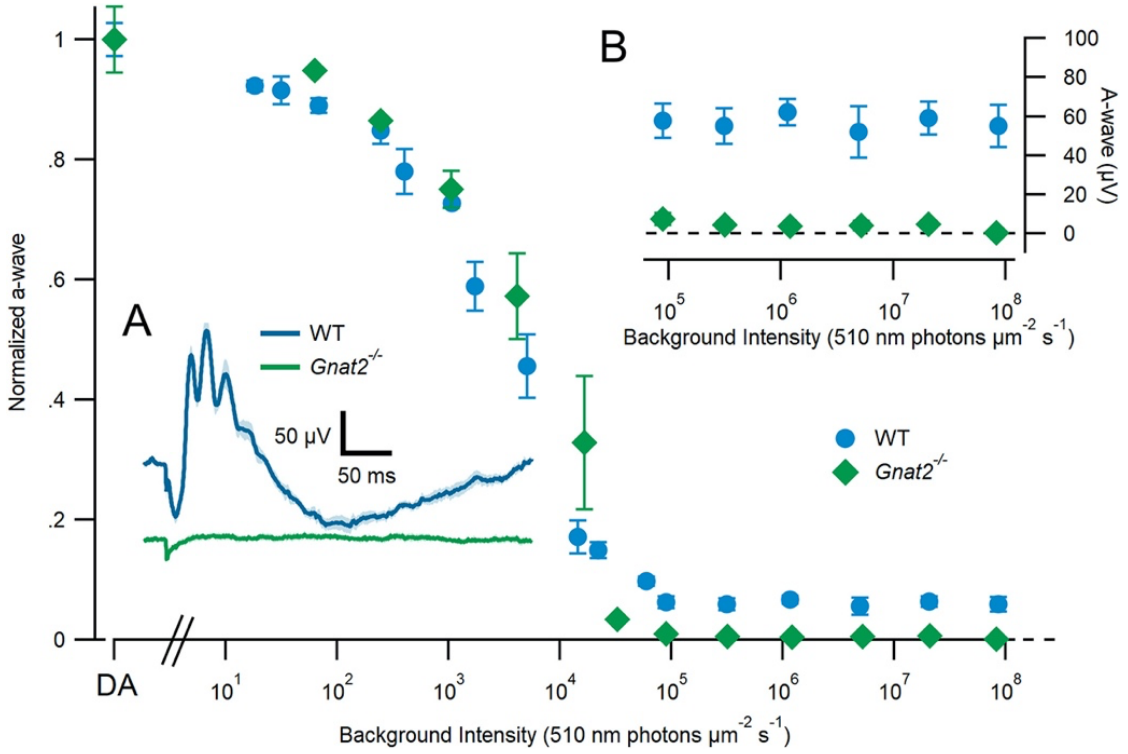

Figure 2.5. Cone-driven ERG responses are absent in *Gnat2*$^{-/-}$ mice. Electroretinogram a-wave amplitudes of WT (blue circles) and *Gnat2*$^{-/-}$ (green diamonds) mice in response to saturating flashes (365nm; 1.22x10^{6} photons µm^{-2}) delivered on increasingly intense 510nm backgrounds. Insets: (A) Average electroretinogram of WT (blue) and *Gnat2*$^{-/-}$ (green) mice in response to a 1ms saturating flash delivered on top of a rod-saturating background (510nm; 1x10^{5} photons µm^{-2}s^{-1}). The small deflection in the *Gnat2*$^{-/-}$ trace is an electrical artifact. (B) Expanded view of WT and *Gnat2*$^{-/-}$ a-wave amplitudes at the brightest background intensities. Error bars (frequently smaller than the points themselves) represent SEM.

References

Alexander, K.R., Raghuram, A., Rajagopalan, A.S., 2006. Cone phototransduction and growth of the ERG b-wave during light adaptation. Vision Research 46, 3941–3948. https://doi.org/10.1016/j.visres.2006.04.015

Calvert, P.D., Krasnoperova, N.V., Lyubarsky, A.L., Isayama, T., Nicoló, M., Kosaras, B., Wong, G., Gannon, K.S., Margolskee, R.F., Sidman, R.L., Pugh, E.N., Makino, C.L., Lem, J., 2000. Phototransduction in transgenic mice after targeted deletion of the rod transducin α-subunit. PNAS 97, 13913–13918. https://doi.org/10.1073/pnas.250478897

Chang, B., Dacey, M.S., Hawes, N.L., Hitchcock, P.F., Milam, A.H., Atmaca-Sonmez, P., Nusinowitz, S., Heckenlively, J.R., 2006. Cone Photoreceptor Function Loss-3, a Novel Mouse Model of Achromatopsia Due to a Mutation in Gnat2. Invest. Ophthalmol. Vis. Sci. 47, 5017–5021. https://doi.org/10.1167/iovs.05-1468

Daniele, L.L., Lillo, C., Lyubarsky, A.L., Nikonov, S.S., Philp, N., Mears, A.J., Swaroop, A., Williams, D.S., Pugh, E.N., 2005. Cone-like Morphological, Molecular, and Electrophysiological Features of the Photoreceptors of the Nrl Knockout Mouse. Invest. Ophthalmol. Vis. Sci. 46, 2156–2167. https://doi.org/10.1167/iovs.04-1427

Deans, M.R., Volgyi, B., Goodenough, D.A., Bloomfield, S.A., Paul, D.L., 2002. Connexin36 Is Essential for Transmission of Rod-Mediated Visual Signals in the Mammalian Retina. Neuron 36, 703–712. https://doi.org/10.1016/S0896-6273(02)01046-2

Garon, M.-L., Rufiange, M., Hamilton, R., McCulloch, D.L., Lachapelle, P., 2010. Asymmetrical growth of the photopic hill during the light adaptation effect. Doc Ophthalmol 121, 177–187. https://doi.org/10.1007/s10633-010-9243-0

Hansen, E., 1990. Clinical Aspects of Achromatopsia, in: Hess, R.F., Sharpe, L.T., Nordby, K. (Eds.), Night Vision: Basic, Clinical and Applied Aspects. Cambridge University Press, pp. 316–334.

Jobling, A.I., Vessey, K.A., Waugh, M., Mills, S.A., Fletcher, E.L., 2013. A Naturally Occurring Mouse Model of Achromatopsia: Characterization of the Mutation in Cone Transducin and Subsequent Retinal Phenotype. Invest. Ophthalmol. Vis. Sci. 54, 3350–3359. https://doi.org/10.1167/iovs.13-11831

Kohl, S., Jägle, H., Wissinger, B., Zobor, D., 2004. Achromatopsia, in: Adam, M.P., Ardinger, H.H., Pagon, R.A., Wallace, S.E., Bean, L.J., Stephens, K., Amemiya, A. (Eds.), GeneReviews®. University of Washington, Seattle, Seattle (WA).

Levine, E.S., Zam, A., Zhang, P., Pechko, A., Wang, X., FitzGerald, P., Pugh, E.N., Zawadzki, R.J., Burns, M.E., 2014. Rapid light-induced activation of retinal microglia in mice lacking Arrestin-1. Vision Res. 102, 71–79. https://doi.org/10.1016/j.visres.2014.07.011

Long, J.H., Arshavsky, V.Y., Burns, M.E., 2013. Absence of Synaptic Regulation by Phosducin in Retinal Slices. PLOS ONE 8, e83970. https://doi.org/10.1371/journal.pone.0083970

Lyubarsky, A.L., Daniele, L.L., Pugh, E.N., 2004. From candelas to photoisomerizations in the mouse eye by rhodopsin bleaching in situ and the light-rearing dependence of the major components of the mouse ERG. Vision Research, The Mouse Visual System: From Photoreceptors to Cortex 44, 3235–3251. https://doi.org/10.1016/j.visres.2004.09.019

Lyubarsky, A.L., Falsini, B., Pennesi, M.E., Valentini, P., Pugh, E.N., 1999. UV- and midwave-sensitive cone-driven retinal responses of the mouse: a possible phenotype for coexpression of cone photopigments. J. Neurosci. 19, 442–455.

Maguire, J., Parry, N.R.A., Kremers, J., Murray, I.J., McKeefry, D., 2017. The morphology of human rod ERGs obtained by silent substitution stimulation. Doc Ophthalmol 134, 11–24. https://doi.org/10.1007/s10633-017-9571-4

Naarendorp, F., Esdaille, T.M., Banden, S.M., Andrews-Labenski, J., Gross, O.P., Pugh, E.N., 2010. Dark Light, Rod Saturation, and the Absolute and Incremental Sensitivity of Mouse

Cone Vision. J. Neurosci. 30, 12495–12507. https://doi.org/10.1523/JNEUROSCI.2186-10.2010
Nathan, J., Reh, R., Ankoudinova, I., Ankoudinova, G., Chang, B., Heckenlively, J., Hurley, J.B., 2006. Scotopic and photopic visual thresholds and spatial and temporal discrimination evaluated by behavior of mice in a water maze. Photochem. Photobiol. 82, 1489–1494. https://doi.org/10.1562/2006-02-27-RA-818
Nikonov, S.S., Kholodenko, R., Lem, J., Pugh, E.N., 2006. Physiological Features of the S- and M-cone Photoreceptors of Wild-type Mice from Single-cell Recordings. J Gen Physiol 127, 359–374. https://doi.org/10.1085/jgp.200609490
Nusinowitz, S., Ridder, W.H., Ramirez, J., 2007. Temporal response properties of the primary and secondary rod-signaling pathways in normal and Gnat2 mutant mice. Experimental Eye Research 84, 1104–1114. https://doi.org/10.1016/j.exer.2007.02.009
Pahlberg, J., Frederiksen, R., Pollock, G.E., Miyagishima, K.J., Sampath, A.P., Cornwall, M.C., 2017. Voltage-sensitive conductances increase the sensitivity of rod photoresponses following pigment bleaching. The Journal of Physiology 595, 3459–3469. https://doi.org/10.1113/JP273398
Pang, J.-J., Gao, F., Lem, J., Bramblett, D.E., Paul, D.L., Wu, S.M., 2010. Direct rod input to cone BCs and direct cone input to rod BCs challenge the traditional view of mammalian BC circuitry. PNAS 107, 395–400. https://doi.org/10.1073/pnas.0907178107
Peinado Allina, G., Fortenbach, C., Naarendorp, F., Gross, O.P., Pugh, E.N., Burns, M.E., 2017. Bright flash response recovery of mammalian rods in vivo is rate limited by RGS9. J Gen Physiol 149, 443–454. https://doi.org/10.1085/jgp.201611692
Schmittgen, T.D., Livak, K.J., 2008. Analyzing real-time PCR data by the comparative C(T) method. Nat Protoc 3, 1101–1108. https://doi.org/10.1038/nprot.2008.73
Strettoi, E., Novelli, E., Mazzoni, F., Barone, I., Damiani, D., 2010. Complexity of retinal cone bipolar cells. Progress in Retinal and Eye Research 29, 272–283. https://doi.org/10.1016/j.preteyeres.2010.03.005
Tanikawa, A., Bush, R.A., Takada, Y., Mears, A.J., Swaroop, A., Sieving, P.A., 2004. Functional Rods Are Required For Photopic ERG Amplitude Increase During Light Adaptation: Study Of Nrl–/– And Rho–/– Mice. Invest. Ophthalmol. Vis. Sci. 45, 811–811.
Umino, Y., Solessio, E., Barlow, R.B., 2008. Speed, Spatial, and Temporal Tuning of Rod and Cone Vision in Mouse. J. Neurosci. 28, 189–198. https://doi.org/10.1523/JNEUROSCI.3551-07.2008
Zhang, P., Goswami, M., Zawadzki, R.J., Pugh, E.N., 2016. The Photosensitivity of Rhodopsin Bleaching and Light-Induced Increases of Fundus Reflectance in Mice Measured In Vivo With Scanning Laser Ophthalmoscopy. Invest. Ophthalmol. Vis. Sci. 57, 3650–3664. https://doi.org/10.1167/iovs.16-19393
Zhang, P., Zam, A., Jian, Y., Wang, X., Li, Y., Lam, K.S., Burns, M.E., Sarunic, M.V., Pugh, E.N., Zawadzki, R.J., 2015. In vivo wide-field multispectral scanning laser ophthalmoscopy-optical coherence tomography mouse retinal imager: longitudinal imaging of ganglion cells, microglia, and Müller glia, and mapping of the mouse retinal and choroidal vasculature. J Biomed Opt 20, 126005. https://doi.org/10.1117/1.JBO.20.12.126005

Chapter 3

Molecular profiling of resident and infiltrating mononuclear phagocytes during rapid adult retinal degeneration using single-cell RNA sequencing

Preface

The following chapter was submitted to *Scientific Reports* as a manuscript titled "Molecular profiling of resident and infiltrating mononuclear phagocytes during rapid adult retinal degeneration using single-cell RNA sequencing" and was accepted on February 27, 2019. The accepted version of this manuscript has been reformatted to meet the guidelines of this dissertation. The authors of the manuscript were Kaitryn E. Ronning, Sarah J. Karlen, Eric B. Miller, and Marie E. Burns. Marie Burns and I developed the experimental design and wrote the manuscript. Additionally, I performed the immunohistochemistry and single-cell sequencing experiments and analyses and created figures.

Abstract

Neuroinflammation commonly accompanies neurodegeneration, but the specific roles of resident and infiltrating immune cells during degeneration remains controversial. Much of the difficulty in assessing myeloid cell-specific functions during disease progression arises from the inability to clearly distinguish between activated microglia and bone marrow-derived monocytes and macrophages in various stages of differentiation and activation within the central nervous system. Using an inducible model of photoreceptor cell death, we investigated the prevalence of infiltrating monocytes and macrophage subpopulations after the initiation of degeneration in the mouse retina. *In vivo* retinal imaging revealed infiltration of $CCR2^{+}$ leukocytes across retinal vessels and into the parenchyma within 48 hours of photoreceptor degeneration. Immunohistochemistry and flow cytometry confirmed and characterized these leukocytes as $CD11b^{+}CD45^{+}$ cells. Single-cell mRNA sequencing of the entire $CD11b^{+}CD45^{+}$ population revealed the presence of resting microglia, activated microglia, monocytes, and macrophages as well as 12 distinct subpopulations within these four major cell classes. Our results demonstrate a previously immeasurable degree of molecular heterogeneity in the innate immune response to cell-autonomous degeneration within the central nervous system and highlight the necessity of unbiased high-throughput and high-dimensional molecular techniques like scRNAseq to understand the complex and changing landscape of immune responders during disease progression.

Introduction

Although the central nervous system (CNS) was once considered entirely immune-privileged, there is growing evidence that interplay between neurons, glia, and the immune system are vital to healthy synaptic function (Herz et al., 2017). Microglia, the resident macrophages of the CNS, are essential for synaptic homeostasis and plasticity and have been

implicated in many neurodevelopmental and neurodegenerative diseases (Wolf et al., 2017). In contrast, infiltration of peripheral leukocytes into the CNS is considered rare and to primarily follow physical trauma or infection (Baufeld et al., 2018; Ousman and Kubes, 2012). In the retina, infiltrating monocytes are associated with chemical or photolytic injury of the retinal pigment epithelium (RPE), which contributes to the blood-retinal barrier (Guillonneau et al., 2017; Ma et al., 2017; O'Koren et al., 2016; Reyes et al., 2017; Sennlaub et al., 2013). The differentiation of monocytes into microglia-like macrophages within the retina further challenges the ability to discern functional differences, if any, between these two distinct populations (McMenamin et al., 2019; O'Koren et al., 2016). While there are some useful expression markers to differentiate between immune cell types, particularly when used in combination for immunohistochemistry (Hickman et al., 2013) or flow cytometry (O'Koren et al., 2016), most transcriptomic and proteomic analyses are applied to entire populations, inherently averaging across subclasses and obfuscating cellular diversity.

Recent advances in single-cell RNA sequencing (scRNAseq) provide an exciting opportunity to understand the unique roles of individual cells in a high-throughput platform. Here we paired scRNAseq with a well-characterized inducible model of photoreceptor degeneration, the *Arr1*$^{-/-}$ mouse (Xu et al., 1997). Arrestin1, which is also known as retinal S-antigen (gene ID *Sag*, here referred to as *Arr1*), is a photoreceptor-specific cytosolic protein that deactivates photoexcited rhodopsin, shutting down the rod phototransduction cascade (Wilden and Kuehn, 1982). In the absence of Arr1, rods become extraordinarily sensitive (Xu et al., 1997) and degenerate upon light exposure (Chen et al., 1999; Hao et al., 2002; Karlen et al., 2018; Wang and Chen, 2014). Even relatively dim light causes rapid ultrastructural disruption of *Arr1*$^{-/-}$ photoreceptor inner segments, swelling of neighboring glia (Müller cells), and activation and migration of microglia into the photoreceptor layer within 24 hours (Levine et al., 2014). Because *Arr1* is expressed only in photoreceptors, the *Arr1*$^{-/-}$ model presents a unique opportunity to

study the heterogeneity of immune responders in a time-locked manner when a specific class of neuron begins to die.

Using *in vivo* imaging, flow cytometry, and scRNAseq, we here report profound differences in the inflammatory profiles, mitotic activity, and active phagocytosis of distinct subpopulations of microglia, monocytes, and monocyte-derived macrophages within 48 hours of the onset of rod degeneration. These results reveal a greater level of phenotypic variety than previously appreciated, adding to the complexity of understanding the role of immune cells, even at short times after the onset of neurodegeneration.

Methods

Animals

Mice were cared for and handled in accordance with the National Institutes of Health guidelines for the care and use of experimental animals and under approved protocols by the UC Davis Institutional Animal Care and Use Committee. *Arr1*$^{-/-}$ mice (Chen et al., 1999; Xu et al., 1997) were born and maintained in constant darkness before exposure to light (200 lux, 48 hours). Homozygous *Cx3cr1*$^{GFP/GFP}$ (strain 005582)(Jung et al., 2000) and *Ccr2*$^{RFP/RFP}$ (strain 017586)(Saederup et al., 2010) knock-in mice were obtained from The Jackson Laboratory, and crossed with the *Arr1*$^{-/-}$ to obtain fluorescent knock-in heterozygotes in a homozygous *Arr1*$^{-/-}$ background (*Arr1*$^{-/-}$*Cx3cr1*$^{+/GFP}$ and *Arr1*$^{-/-}$*Ccr2*$^{+/RFP}$, respectively). All mice used in this study were between 2-4 months old. Although there are reports of sex differences in microglia function and reactivity (Lenz and McCarthy, 2015), no differences were observed in immunohistochemistry or *in vivo* microglial imaging experiments (data not shown); thus, both male and female animals were used and the results combined. To avoid sex-specific differences in gene expression, only retinas from female mice were used for scRNAseq. Six littermates (3 dark-reared controls and 3 degenerating, 48 hours light-exposed mice) were used for single-cell sequencing in order to capture a sufficient number of high quality cells, ideally approximately

200 cells of any significant immune cell type (Ziegenhain et al., 2017). Female littermates were randomly divided between control and degenerating groups.

Immunohistochemistry

Immunohistochemistry was performed as previously described (Ronning et al., 2018). Briefly, mice were sacrificed by carbon dioxide euthanasia and eyes enucleated and submerged in 4% paraformaldehyde at room temperature. After 5 minutes of fixation, the cornea and lens were removed, and the eyecups were fixed for an additional 20-25 minutes. For retinal sections, fixed eyecups were embedded in agarose and sectioned on a vibratome (Leica) at a thickness of 150 µm. Sections were blocked at room temperature in normal serum, incubated in primary antibody solution at 4° C overnight, washed in PBS 3 times for 15 minutes each, and incubated in secondary antibody solution at room temperature for 1.5-2 hours before an additional 3 PBS washes and mounting with ProLong Diamond Antifade (Invitrogen). For retinal flatmounts, retinas were removed from fixed eyecups, followed by incubation in 1% Triton X-100 in PBS overnight at 4° C, and then blocked with normal serum for 2 hours at 37° C. Retinas were incubated in primary antibody solution overnight at 4° C, washed 3 times in PBT for 15-30 minutes at room temperature, and incubated in secondary antibody solution for 1.5-2 hours at 37° C before 3 PBT washes and mounting with ProLong Diamond Antifade with DAPI (Invitrogen). Tissue was stained for Ki67 using an antibody raised in rabbit (1:300; Abcam), followed by Alexa Fluor-conjugated secondary antibody (1:300 Invitrogen); rat antibodies against CD11b and MHCII (1:300 and 1:200 respectively; BioLegend) were preconjugated to Alexa Fluors and added to the secondary antibody solution; DAPI (Invitrogen) was also added to the secondary antibody solution (2 drops/mL). All sections and flat mounts were imaged using a Nikon A1 confocal microscope.

In vivo imaging with scanning laser ophthalmoscopy

A custom-built scanning laser ophthalmoscopy (SLO) system was used to image GFP^+ and RFP^+ cells within the retina, simultaneously collecting the reflectance and fluorescence

images (Zhang et al., 2015). For imaging, mice were anesthetized with 2-2.5% isoflurane and positioned on a heating pad (37°C) with a micropositioner (Bioptigen, Morrisville, NC) that allowed rotational and translational adjustment for positioning the mouse with respect to the contact lens. The pupils were dilated and cyclopleged with tropicamide and phenylephrine, and the corneal surface wetted with Gel Tears hypromellose gel (GenTeal Tears Severe, Alcon). Gel Tears helped maintain a homogeneous refractive surface between the cornea and the custom 0 diopter contact lens (Unicon Corporation, Osaka, Japan). GFP and RFP excitation was achieved with 488 nm and 561 nm lasers, respectively. Images were collected over 51° of visual angle at 43 μm per degree. In Fiji (Schindelin et al., 2012), images were registered (Thévenaz et al., 1998), averaged, background subtracted, and pseudo-colored for presentation.

Fluorescence activated cell sorting (FACS)

FACS was performed using a protocol modified from an established method (Karlen et al., 2018; O'Koren et al., 2016). After dissection, each retina was incubated in 1 mL of digestion buffer containing: Hank's Balanced Salt Solution (10-547F, Lonza), 5% Fetal Bovine Serum (FBS; 35010CV, Corning), 10mM HEPES, 0.7 mg/mL calcium chloride, 1.5 mg/mL Collagenase A (10103586001, Roche), and 0.1 mg/mL DNase I (10104159001, Roche) at 37°C for 15 minutes. Following incubation, each retina was gently dissociated, and the resulting single-cell suspension was washed, filtered through a 70 μm cell strainer, centrifuged at 350xg for 5 minutes, and resuspended in PBS. Cells were stained for viability (Zombie Viability NIR, Biolegend), and blocked with Fc light chain antibodies (eBiosciences), supplemented with normal rat serum and normal mouse serum. Cells were then incubated with anti-mouse CD11b conjugated to BV605, anti-mouse CD45 conjugated to PE, anti-mouse CCR2 conjugated to PE/Cy7, and anti-mouse AI/IE (MHCII) conjugated to BV711 (all Biolegend). Cell suspensions were washed in PBS containing 0.5% Bovine Serum Albumin (BSA), centrifuged at 350xg for 5 minutes, and resuspended in 0.5% BSA in PBS with 1:50 EDTA. All retinas were processed separately, until being combined by group (6 retinas from 3 dark-reared, control mice and 6

retinas from 3 light-exposed, degenerating mice) immediately before sorting. Cells were sorted into 40 µL of ice cold DMEM supplemented with 10% FBS using the MoFlo Astrios cell sorter (Beckman) at the UC Davis Flow Cytometry Core, gating for alive $CD11b^{+}CD45^{+}$ cells. Further analysis was performed using FlowJo.

Single-cell RNA library preparation and sequencing

Sequencing libraries were prepared from the sorted $CD11b^{+}CD45^{+}$ cells from each group (control and degenerating samples) using the 10X Genomics system (Chromium) at the UC Davis DNA Technologies and Expression Core according to manufacturer recommendations. The two resulting cDNA libraries were sequenced on a NextSeq (Illumina) system running 150 cycles of paired-end reads at the UC Davis DNA Technologies and Expression Core according to manufacturer recommendations. The transcript read lengths were 98 bp, and the sample index, cell barcode, and UMI read lengths were 8 bp, 14 bp, and 10 bp respectively. Cells were sequenced at a mean depth of 474,191 reads per cell in the control library and 225,889 reads per cell in the degenerating library. The scRNAseq dataset generated and analyzed here is available in the NCBI Gene Expression Omnibus (GEO) repository, accession number GSE121081.

scRNAseq analysis

Initial sequence processing, including barcode processing, transcript alignment, and generation of gene-barcode matrices were performed using Cell Ranger (Chromium) at the UC Davis Bioinformatics Core. Further processing and analysis was performed in R, primarily with the Seurat package unless otherwise specified (Butler et al., 2018; R Core Team, n.d.; Satija et al., 2015). Cells were examined for quality control, removing those with unique gene counts over 3,000 (to remove potential doublets from the dataset) and under 500 (to remove spurious contamination). Data were then normalized for unique molecular identifier (UMI) counts per cell and mitochondrial genes following the standard Seurat workflow. After principal components analysis, the transcript expression from the top ten principal components was used to perform *t*-

distributed stochastic neighbor embedding (tSNE) dimensional reduction. Clusters were identified using a graph-based local moving algorithm with a resolution of 1.5 (Macosko et al., 2015). This resolution was selected after trying a wide range of resolution values (0.6-1.6) and decided upon in consultation with the UC Davis Bioinformatics Core, based upon the generation of a similar number of clusters across several resolutions and reasonable numbers of differentially expressed genes between clusters. Expression of marker genes were identified using the FindMarkers function in Seurat. This function identifies genes differentially expressed in a given group (either a cluster or cloud) compared to all other cells in the dataset using a non-parametric Wilcoxon rank sum test followed by Bonferroni correction. For each cluster or cloud, p-value adjustments were based on the total number of genes expressed in at least 25% of the cells in the cluster or cloud being tested.

Results

Invasion of peripheral immune cells into the rapidly degenerating retina

The *Arr1*$^{-/-}$ mouse is a convenient, light-inducible model of widespread, cell-autonomous photoreceptor neurodegeneration (Chen et al., 1999; Karlen et al., 2018). Previous studies have shown that within 24 hours of light onset, microglia change morphology and migrate into the photoreceptor layer, and between 36 and 72 hours after light onset there is a dramatic increase in the number of Iba1^{+} cells present in the retina (Levine et al., 2014). We first aimed to investigate the source of this increase in cell number using immunohistochemistry on *Arr1*$^{-/-}$ retinas exposed to 48 hours of light. Sections of retina immunohistochemically stained for CD11b, a pan-myeloid cell marker, showed the presence of enlarged macrophage-like cells in and around the photoreceptors and subretinal space. Additionally, there were small round CD11b^{+} monocyte-like cells often visible at the vitreoretinal surface and retinal layers of light exposed mice that were never observed when the animals were maintained in darkness (Figure 3.1A).

Monocyte extravasation into the retina has been implicated in other mouse models of retinal and RPE damage known to disrupt the blood-retina barrier (for example, see (Ma et al., 2017). However, to our knowledge, leukocyte infiltration has not been previously known to occur in any models of cell-autonomous retinal neurodegeneration. To confirm the presence of infiltrating cells *in vivo*, we crossed *Arr1*$^{-/-}$ mice with *Ccr2*$^{RFP/RFP}$ knock-in mice that express RFP downstream of the *Ccr2* promoter. Using scanning laser ophthalmoscopy, we could detect very little RFP^{+} signal within the retinas of dark-reared *Arr1*$^{-/-}$ *Ccr2*$^{+/RFP}$ mice. However, when the same mouse was imaged after 48 hours of light exposure, many RFP^{+} cells were evident within the retinal parenchyma (Figure 3.1B, red), consistent with monocyte infiltration. These cells were distinct from microglial cells, which showed a different morphology and pattern of distribution at this same time point *in vivo* (*Arr1*$^{-/-}$ *Cx3CR1*$^{+/GFP}$; Figure 3.1B, green). These results suggest that there are multiple distinct populations of immune cells that rapidly respond at the onset of photoreceptor degeneration.

Single cell profiling reveals four classes of CD11b^{+}*CD45*$^{+}$ *cells*

To more precisely identify resident and peripheral immune cell classes in the retina we used single-cell RNA sequencing. Retinas of healthy dark-reared control and degenerating (light-exposed) *Arr1*$^{-/-}$ littermates were dissociated, and all live cells expressing both CD11b and CD45, which include both microglia and monocytes, were collected using FACS for single-cell RNA sequencing (Figure 3.2, black polygon). Posthoc analysis of the collected cells showed a dramatic increase in the number of CD11b^{+} CD45^{high} cells (Figure 3.2, green box), consistent with the invasion of peripheral cells seen by in vivo imaging. Interestingly, there was also an increase in the number of CD11b^{-} CD45^{high} cells during degeneration (Figure 3.2); these cells were not captured for scRNAseq and will be the subject of future study.

Single-cell mRNA libraries of CD11b^{+}CD45^{+} cells were generated and sequenced with stringent pre-processing and quality control cell filtering. The transcriptomes of all cells were compared using principal components analysis, and data were displayed in two dimensions

using a *t*-distributed stochastic neighbor embedding (tSNE) plot where the relative position of each point reflects the genetic similarity of the cell to others in the population. The majority of immune cells in the dark-reared control sample (Figure 3.3A, red) formed a well-defined cloud that did not overlap with cells from the degenerating retina. Instead, three new qualitatively distinct clouds emerged in the degenerating sample (Figure 3.3A, blue). This dissimilarity of control and degenerating samples from *Arr1*$^{-/-}$ littermates indicates that the gene expression profiles themselves were not grossly affected by tissue processing, and suggests that these four clouds represent the presence of four distinct classes of CD11b^{+}CD45^{+} cells (Figure 3.3B).

To test whether the clouds indeed correspond to distinct cell classes, we queried the expression of numerous known or proposed microglia, monocytes, and macrophages markers across all cells (at least 15 markers per group). The expression of these markers was first examined graphically, by displaying the relative expression of each gene on a tSNE plot. Cloud #1 (Figure 3.3B, orange), which was present only in control retina, expressed the highest levels of resting microglia markers, such as *P2ry12* and *Tmem119* (Figure 3.3D); Cloud #2 (Figure 3.3B, green) contained markers of microglial activation, such as *Lpl* and *Cst7* (Figure 3.3E) (Hammond et al., 2019; Keren-Shaul et al., 2017, p.). Cloud #3 (Figure 3.3B, blue) contained abundant monocyte markers such as *Ly6c2* and *Ccr2* (Figure 3.3F), and in Cloud #4 (Figure 3.3B, purple) markers of monocyte-derived macrophages like *H2-Aa* (an MHCII gene) and *Cd74* were most highly expressed (Figure 3.3G) (Yu et al., 2016). For further graphical examples of marker gene expression, see Supplemental Figure 3.1. Queries for markers of other immune and retinal cell types, including dendritic cells, neutrophils, and T and B cells, did not identify any other major cell types in the dataset, as expected since only CD11b+ cells were selected for analysis.

To independently identify differences in gene expression between these clouds, we used Seurat to generate lists of abundant transcripts differentially expressed in each Cloud relative to all other cells. These lists were rife with many known marker genes for these cell types

(Supplemental Table 3.1), including several of the markers queried in Figure 3.3 and Supplemental Figure 3.1. Thus, both candidate gene expression queries and unbiased transcriptional profiling support the conclusion that the four primary clouds of Figure 3.3B reflect: (1) Resting Microglia, (2) Activated Microglia, (3) Monocytes, and (4) Monocyte-derived Macrophages.

In silico identification of cell subtypes with different activation and proliferation states

To objectively identify transcriptionally distinct groups of, we used an unsupervised, *in silico* graph-based clustering algorithm (Macosko et al., 2015). This algorithm identified 12 distinct clusters, corresponding to 12 putative populations (Figure 3.3C). One cluster fell within the cloud deemed resting microglia (Figure 3.3C, Cluster #1); four clusters fell within the cloud of activated microglia (Clusters #2-5); three clusters fell within the cloud of monocytes (Clusters #6-8); two fell within the cloud of monocyte-derived macrophages (Clusters #9-10); and two very small clusters could not be confidently identified as any immune or retinal cell type (Clusters #11-12).

To identify potential functional differences between these putative subpopulations, we used Seurat to determine the genes most differentially expressed between clusters (Supplemental Table 3.2 for list and *p*-values). Genes associated with specific functional states like inflammation, proliferation, and phagocytosis were enriched in particular subsets of clusters (Figure 3.4). For example, expression of the inflammatory cytokines, such as *Il-1β*, was highest in monocytes and macrophages (Figure 3.4A, Clusters #6-10). Cluster #6 contained cells from both control and degenerating samples that expressed markers for peripheral immune cells like *Plac8*, suggesting that these were circulating cells captured in the vasculature at the time of dissection. The majority of cells of only two of the clusters (Clusters #4, #10) expressed genes associated with cell division, such as *Cdk1* and *Pclaf*, suggesting that these subpopulations were actively proliferating (Figure 3.4B). Finally, another small but distinct cluster contained some photoreceptor-specific transcripts involved in rod phototransduction, such as *Guca1a* and

Cngb1 (Figure 3.4D, subset of Cluster #5). We interpret this to mean that these activated microglia had phagocytosed rods containing non-degraded mRNA immediately before tissue processing.

Microglia (Clusters #1-5) expressed many complement-related genes (Supplemental Table 3.2), but the relative expression patterns between clusters were not uniformly helpful in identifying functional subpopulations. For example, C1q component genes like *C1qa* (Figure 3.4C) and some integrin subunits (data not shown) were expressed at similar levels in both control and degenerating samples, suggesting that microglia are capable of initiating the classical complement pathway in both resting and activated states. In contrast, Complement Factor H (Cfh), which inhibits the alternative complement pathway and has been linked to age-related macular degeneration (Calippe et al., 2017; McHarg et al., 2015), was decreased in the degenerating sample and did not differ much between activated microglia subpopulations (Figure 3.4C).

Since distinct subpopulations of activated microglia have been previously identified in Alzheimer's disease and ALS (Keren-Shaul et al., 2017), we examined if those previously defined activated stages were sufficient to describe the subpopulations identified here (Figure 3.4E). Keren-Shaul and colleagues suggested that microglia activation occurred in two stages, so we examined the expression of markers for both stages across all microglia clusters. Although many of the same resting microglia markers were expressed in our control sample (Cluster #1; Figure 3.4E, top row), the relative expression profiles of activated microglia clusters did not consistently align with the activation progression observed in Alzheimer's disease and ALS. For example, *Lyz2* and *Apoe*, two genes that were previously associated with stage one of activation in Alzheimer's Disease, were only enriched in one of the four activated microglia clusters (Cluster #2), yet another prominent Stage 1 marker, *Cstb*, was not similarly enriched in this cluster (Figure 3.4E, middle row). Clusters #3-5 expressed some genes associated with the second stage of activation, such as *Spp1* and *Cd63*, but there was a marked absence of others,

such as *Cst7* (Figure 3.4E, bottom row). Additionally, several of these genes and others have been identified as being differentially expressed in activated brain microglia after lysolecithin demyelination (Hammond et al., 2019). However, the relative expression and subpopulations again do not align precisely (see Supplemental Figure 3.1 for further examples of lysolecithin demyelination-related genes expression during *Arr1*$^{-/-}$ degeneration). These findings suggest that although some features of microglia activation may be conserved, the specific molecular phenotypes and subpopulations may depend on the tissue, type, and extent of neuronal degeneration.

Re-examining molecular heterogeneity of the immune response in the context of degeneration

Translating the insights garnered from the single-cell data into the framework of retinal structure and more traditional methodologies is essential for subsequently testing and manipulating immune cell function during degeneration. As a first step, we focused on MHCII, a common marker of monocyte-derived macrophages (Yang et al., 2014) that indeed showed prominent expression in those corresponding clusters (Figure 3.5A, *H2-Aa*, Clusters #9-10). FACS detection of MHCII antibody staining revealed a dramatic increase in MHCII protein levels in CD45^{+} CD11b^{+} cells from the degenerating retina (Figure 3.5C, blue box, compare control to degenerating; see Figure 3.5B for gating strategy). The same MHCII antibody when applied to immunohistochemistry stained only a fraction of CD11b^{+} cells, as best illustrated by looking at a population of cells across a large retinal area in flat mounts (Figure 3.5E). In retinal sections, MHCII^{+} cells were not localized in any particular layer but instead were distributed throughout the retina, from the vitreal surface to the outer plexiform layer (Figure 3.5D). This suggests either that the monocyte-derived macrophages did not rapidly accumulate in the photoreceptor layers or that the differentiation from monocyte to macrophage happened well before the cells arrived at their final destination. Notably, there were no clear morphological distinctions between MHCII^{+} and MHCII^{-} populations, emphasizing the inadequacy of using morphology for discriminating between activated microglia and monocyte-derived macrophages in this instance.

Through scRNAseq we also identified two subpopulations of proliferating cells in degenerating retina (Figure 3.4B, Clusters #4, 10). Utilizing IHC, we confirmed the presence of mitotically active Cd11b^{+} cells using Ki67 staining in degenerating tissue. Again, Ki67^{+} cells were not localized to a particular retinal region and instead seemed equally scarce in both inner and outer retinal layers (Figure 3.5E, example shown in outer retina). In contrast, Ki67^{+} nuclei were never observed in dark-reared control retinas, consistent with the scRNAseq findings.

In some cases, our scRNAseq data revealed cellular heterogeneity in the expression of genes commonly considered to be cell type-specific markers. For example, *Ccr2*, a common monocyte marker (e.g. (Yang et al., 2014)), was detectable in both monocyte and macrophage populations (Clouds #3 and #4; Figure 3.5A), though indeed only statistically differentially expressed in monocyte Cloud #3 (1.5-fold higher expression; p=1.35E-26; Supplemental Table 3.1). Notably, within Cloud #3 it was only differentially expressed in the inflammatory monocytes of Cluster #8 (1.8-fold higher expression, p=3.30E-29 Supplemental Table 3.2), and not the other monocyte clusters. Antibody labeling and detection using FACS showed a similar modest increase in total CCR2 staining between control and degenerating retinas (Figure 3.5C, red box). However, neither FACS nor scRNAseq results were as dramatic as the evident infiltration revealed by *in vivo* imaging of *Ccr2*$^{+/RFP}$ retinas (Figure 3.1B), possibly reflecting a difference in the lifetime of the RFP protein as compared to CCR2.

Discussion

The present study uses scRNAseq to reveal distinct subpopulations of immune responders within the retina. In combination with *in vivo* imaging, flow cytometry, and immunohistochemistry, our results show that microglial activation, monocyte infiltration, and monocyte differentiation into macrophages can occur concurrently and rapidly, within 48 hours after the onset of photoreceptor degeneration. Here we describe the distinguishing molecular

features of these subpopulations and discuss the consequences of these findings for retinal degeneration and neuroinflammation more generally.

Distinguishing hallmarks of immune subpopulations in the degenerating retina

Rigorous analysis of the scRNAseq dataset generated here revealed the presence of distinct populations and subpopulations of both invading and resident myeloid cells, consistent with *in vivo* imaging (Figure 3.1B), FACS analysis (Figures 3.2 and 3.5B-C), and immunohistochemistry (Figures 3.1A and 3.5D-E). Figure 3.6A outlines the distribution of immune subpopulations by location (retina vs. blood), condition (control vs degenerating), cloud group, and cluster number. In control retina, almost all of the immune cells were resident microglia; the majority (72.4%) of which were resting, compared to 22.8% activated. The remaining immune cells in control retina were circulating monocytes trapped in the blood stream (4.4%). Remarkably, in degenerating tissue the majority of immune cells (64%) were peripheral in origin, and at the time point investigated here were comprised roughly equally of infiltrating monocytes (35.1%) and monocyte-derived macrophages (28.8%). Only 30.7% of the immune cells in the degenerating retina were activated, resident microglia.

Statistical comparison of transcriptional profiles revealed distinct subpopulations with clear and often dramatic differences in gene expression between them. Figure 3.6B lists the top 10 significantly differentially expressed genes for each cluster and cloud, sorted by the adjusted p-value (see Supplemental Tables 3.1 and 3.2 for an extended list and all p-values) and categorized into functional groups based on gene expression in the cluster subpopulations. For example, proliferating microglia and monocytes (Clusters #4 and #10, respectively) both express significantly higher levels of *Pclaf* (*2810417H13Rik*) compared to all other cells, indicating that these cells were undergoing DNA replication and establishing their status in the proliferating functional group. Nonetheless, the molecular profile of numerous other genes within these clusters allowed us to simultaneously classify them into two distinct subpopulations of activated microglia and macrophages. Similarly, the molecular profile of Clusters #1-5 clearly

identify these as Resting (#1) and Activated (#2-5) microglia; however the more subtle differences between Clusters #2, #3, and #5 raise the question as to whether the activated microglia clusters represent stages of one continuous activation pathway or functionally distinct pathways. Finally, the key cloud genes (Figure 3.6B, bottom) emphasize commonalities in gene expression across the broader cell groups: Resting Microglia, Activated Microglia, Monocytes, and Monocyte-derived Macrophages and are derived from Supplemental Table 3.1.

Understanding molecular heterogeneity is critical for potential functional analysis

In addition to revealing subpopulations of each cell class, the scRNAseq analysis allows inference about the potential function(s) of individual subpopulations to ascertain the role they play during neurodegeneration. For example, Macrophages (Cloud #4, Clusters #9, #10) showed significantly higher levels of *H2-Aa* expression, an MHCII gene associated with antigen processing and presentation compared to all other groups (Figure 3.5A, Supplemental Tables 3.1-3.2). Retinal MHCII^{+} cells, especially in the subretinal space, have been described in models of RPE death (Ma et al., 2017), and after light injury in *Cx3cr1*$^{-/-}$ (Sennlaub et al., 2013), *RPE65*$^{Leu/Leu}$, and wild-type mice (O'Koren et al., 2016). Our immunohistochemistry revealed that MHCII+ cells were localized throughout all of the retinal layers and were not morphologically distinct from other CD11b^{+} cells. The differences in the localization and appearance of MHCII+ cells in these various models of degeneration may reflect differences in the site of infiltration, either across Bruch's membrane and RPE, or, as in the present study, across retinal vessels.

Another potential functional inference that can be drawn from the data is the role of CCL2-CCR2 signaling, which is widely known to recruit systemic immune cells during retinal degeneration. Here we found that *Ccl2* was detectable in all of the immune subgroups (Figure 3.5A), and notably not differentially increased in activated microglia, suggesting they are not the source of CCL2 to recruit infiltrating monocytes at this time point. Conversely, Monocytes (Cloud #3) and Macrophages (Cloud #4) showed expression of *Ccr2*, the CCL2 receptor (Figure 3.5A),

with considerable variability in expression between Clusters #6-10. This variability may reflect the rapid degradation of CCR2 and down regulation of *Ccr2* expression after extravasation into the retinal parenchyma. Indeed, in the *Cx3cr1*$^{-/-}$ model of age-related macular degeneration, it has been shown that monocytes down regulate *Ccr2* rapidly when differentiation into macrophages (7).

Surprisingly, we found a distinct lack of anti-inflammatory markers, such as *Il10* (Figure 3.4A), in all cells, even in the resting microglia population. Because monocytes and macrophages are capable of adopting both pro- and anti-inflammatory phenotypes (Yang et al., 2014), it is possible that anti-inflammatory cells may play a role in the response to photoreceptor degeneration at later time points, or as the rate of degeneration slows and the tissue enters a homeostatic "recovery" phase. It is also possible that anti-inflammatory signaling is more prevalent in slower models of retina degeneration.

Implications for photoreceptor degeneration and other retinal degenerative diseases

Many mouse models have been described with genetic and/or phenotypic similarities to human retinal degenerative diseases with varying ages of onset and speed of degeneration (Chang et al., 2002; Kiser and Palczewski, 2016; Levy et al., 2015). While all models involve activation of resident microglia, the potential involvement of the peripheral immune system remains unclear. In some instances, such as in cases of RPE and/or light damage, monocytes and macrophages have been detected in the degenerating retina (Guillonneau et al., 2017; O'Koren et al., 2016), though it has not been resolved whether they enter through the retinal or choroidal vasculature.

Arrestin-1 is distinctly a photoreceptor-specific protein that is not expressed in leukocytes (Heng et al., 2008; Shay and Kang, 2013) or other cells of the retina (Siegert et al., 2012). *Arr1* binds photoexcited rhodopsin (Wilden et al., 1986), quenching its ability to activate G-protein in the phototransduction cascade of vertebrate rods. Mice lacking *Arr1* have normal retinal morphology when reared in complete darkness, yet when they are exposed to light,

unrestrained rhodopsin signaling causes photoreceptors to rapidly degenerate over the course of a few days (Hao et al., 2002; Karlen et al., 2018; Xu et al., 1997) even in relatively dim light (Levine et al., 2014). Thus, the *Arr1*$^{-/-}$ mouse serves as a model for time-locked, light-induced photoreceptor degeneration, allowing the acute response of both resident and infiltrating immune cells to be followed consistently in time. The ability to chart the immune response to a time-locked degeneration onset is especially critical for studying the differentiation of monocytes into macrophages within the CNS, and how these interactions may change over time. ScRNAseq in time-locked models will be important to determine how microglia and infiltrating immune cells re-establish surveillance in degenerated retina and their immune responses to therapies and subsequent insults related to aging.

In summary, scRNAseq revealed a previously immeasurable degree of heterogeneity in the myeloid response to cell-autologous degeneration of neurons within the central nervous system, including changes in the local resident populations and an invasion of immune cells from the periphery (Figure 3.6). The complex differences between populations observed here highlight the necessity of utilizing unbiased high-throughput and high-dimensional molecular techniques like scRNAseq in combination with techniques like immunohistochemistry, *in vivo* imaging or ultimately spatial transcriptomics (Ståhl et al., 2016; Strell et al., 2019).

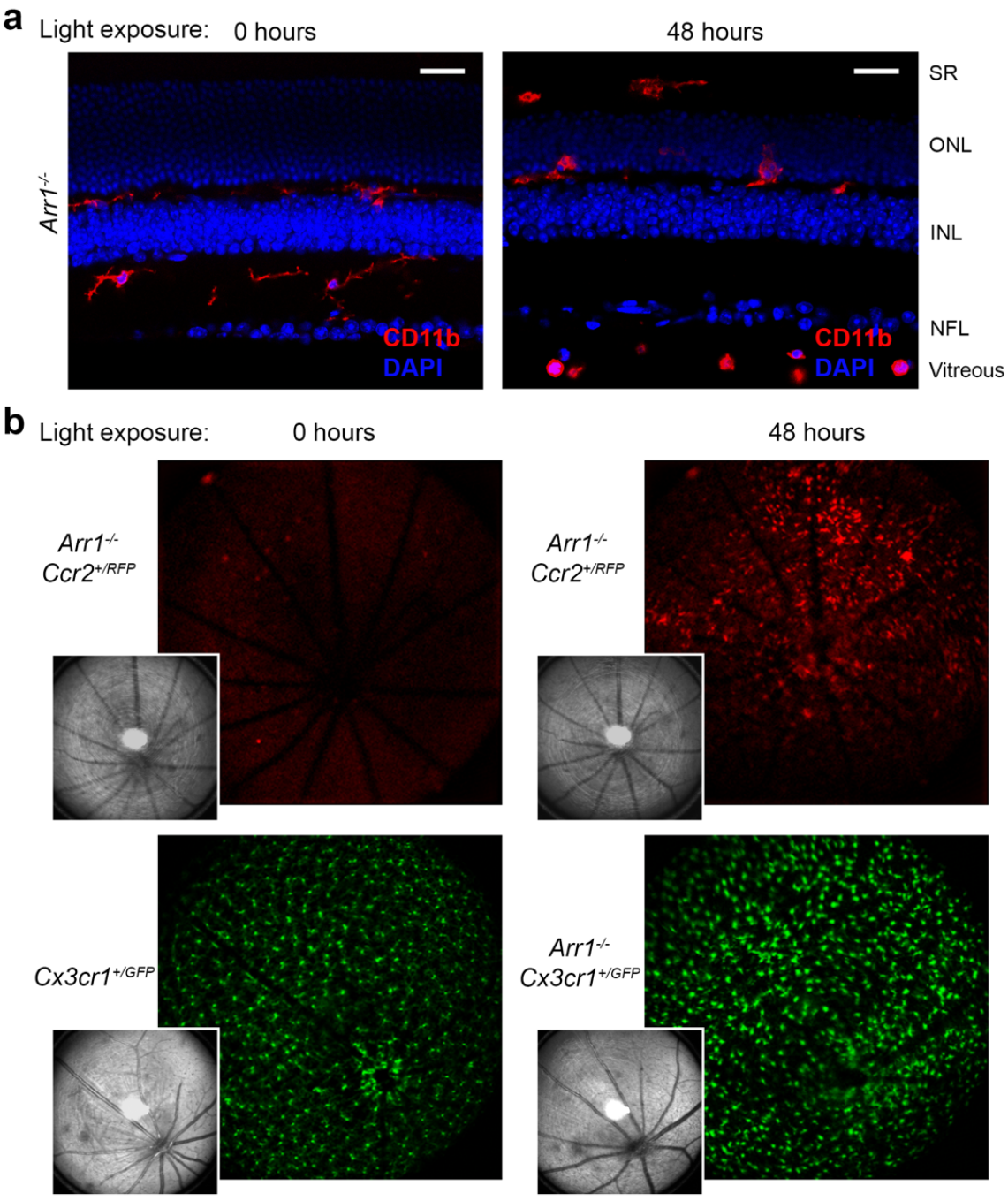

Figure 3.1. Immune cells respond to acute photoreceptor degeneration. (a) Immunohistochemical sections before and after onset of photoreceptor degeneration. After 48 hours of light exposure, CD11b^{+} cells that were round appeared in the vitreous and nerve fiber layer (NFL) near large caliber vessels while those that were ameboid were present in the

subretinal space (SR) and photoreceptor layer (outer nuclear layer, ONL). Scale bars indicate 25 μm, INL = inner nuclear layer. (b) *In vivo* retinal imaging using scanning laser ophthalmoscopy. Cells expressing RFP driven by the CCR2 promoter (putative monocytes) appeared abruptly within 48 hours of light exposure (compare 0 to 48 hours exposure taken from the same mouse), while the number of GFP expressing resident microglia have changed little. Insets show corresponding reflectance images.

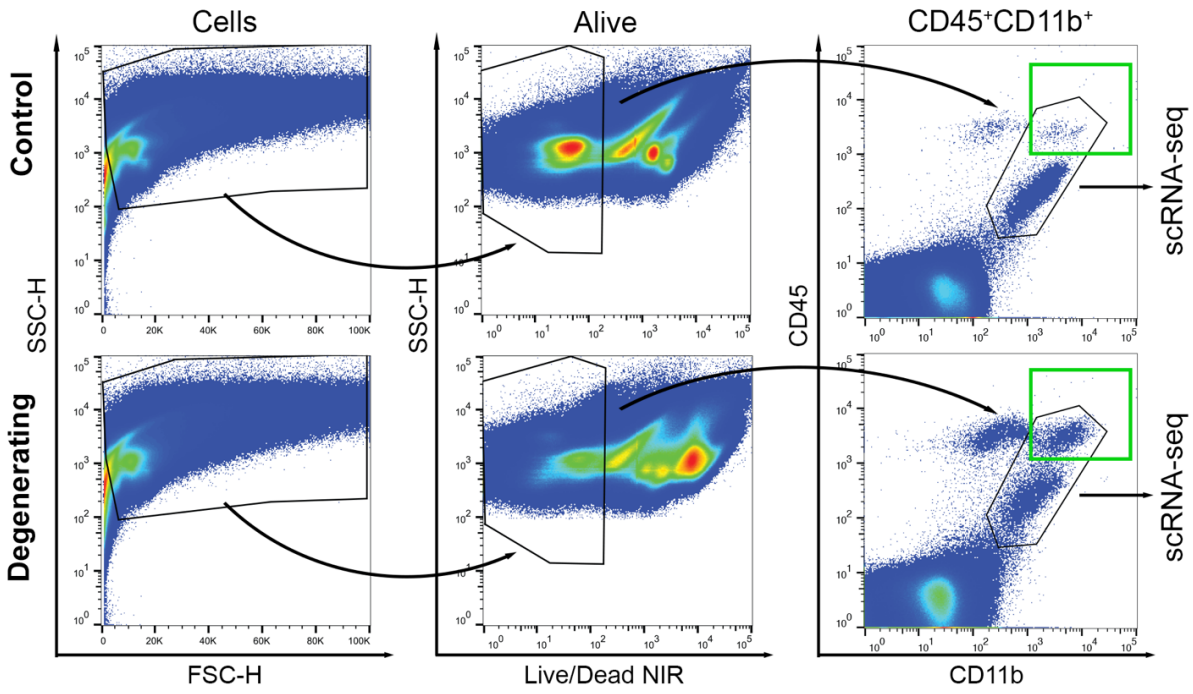

Figure 3.2. Immune response to photoreceptor degeneration can be identified and captured using FACS. After retinal dissociation, cells were detected using side scatter (SSC) and forward scatter height (FSC-H); cells that were alive (Live/Dead NIR low) and double positive for CD11b and CD45 were captured for single-cell mRNA sequencing. Green box indicated $CD11b^{+}CD45^{high}$ population, which was far larger in the degenerating sample. Black polygon encompasses cells captured for single-cell transcriptomics.

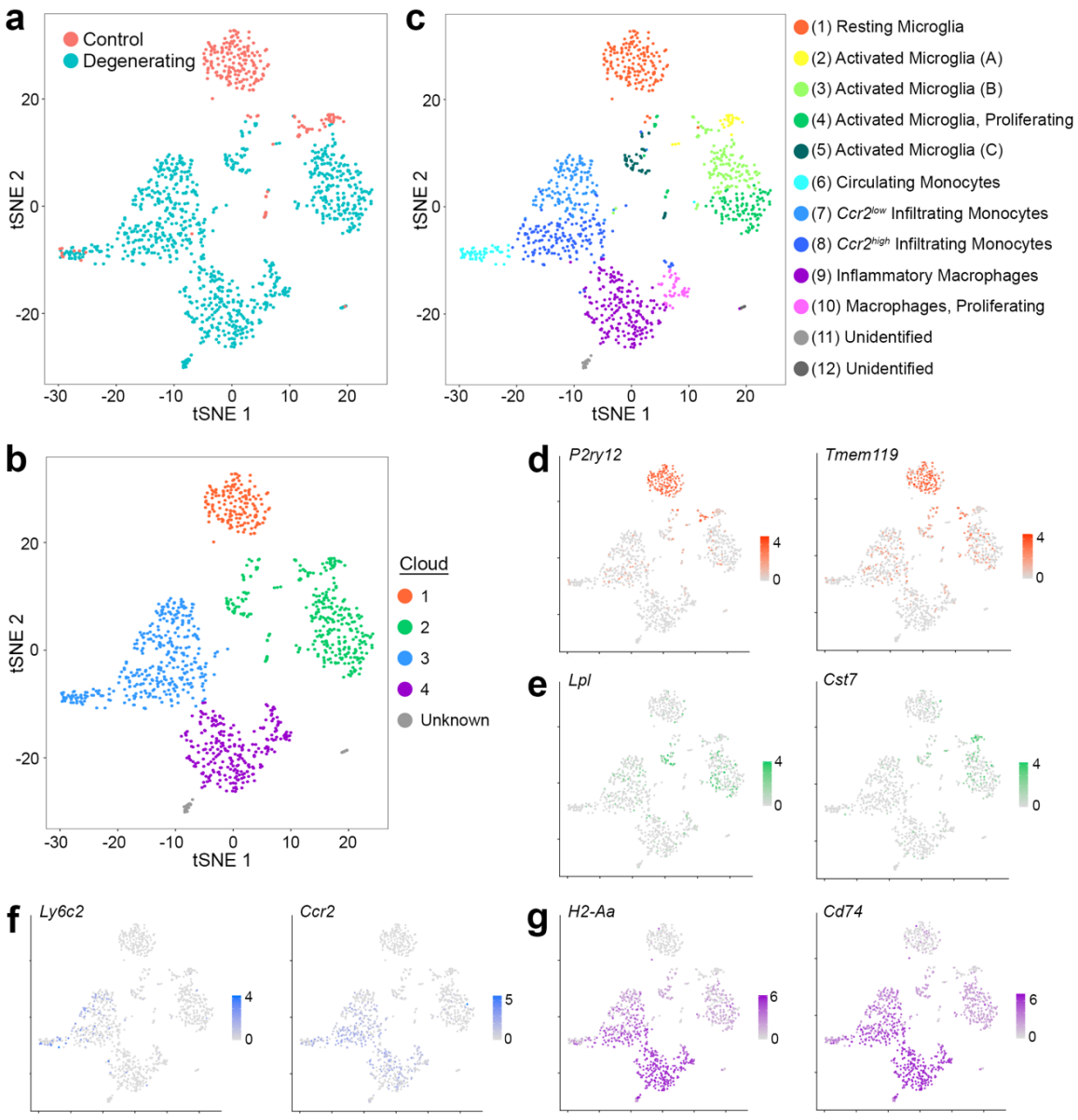

Figure 3.3. Identification of immune cells before and during retinal degeneration, displayed in tSNE plot of all cells, collapsed from a *k*-nearest neighbor comparison of all gene expression comprising the top 10 principal components. (a) Cells color-coded by sample identify, with immune cells from dark-reared control retinas in red and from degenerating retinas in blue. (b) Cells can be broadly grouped into 4 clouds, which correspond to the main 4 cells types: (1) retina microglia, (2) activated microglia, (3) monocytes, and (4) monocyte-derived macrophages. (c) Cells color-coded by cluster, identified by an unsupervised graph-

based algorithm, and assigned cell identity using relative abundance of established markers. (d-g) Example marker gene expression of genes associated with resting microglia (d), activated microglia (e), monocytes (f), and monocyte-derived macrophages (g). Scales in (d-g) indicate relative expression (log TPM values), with grey indicating no expression and saturated color indicating highest expression.

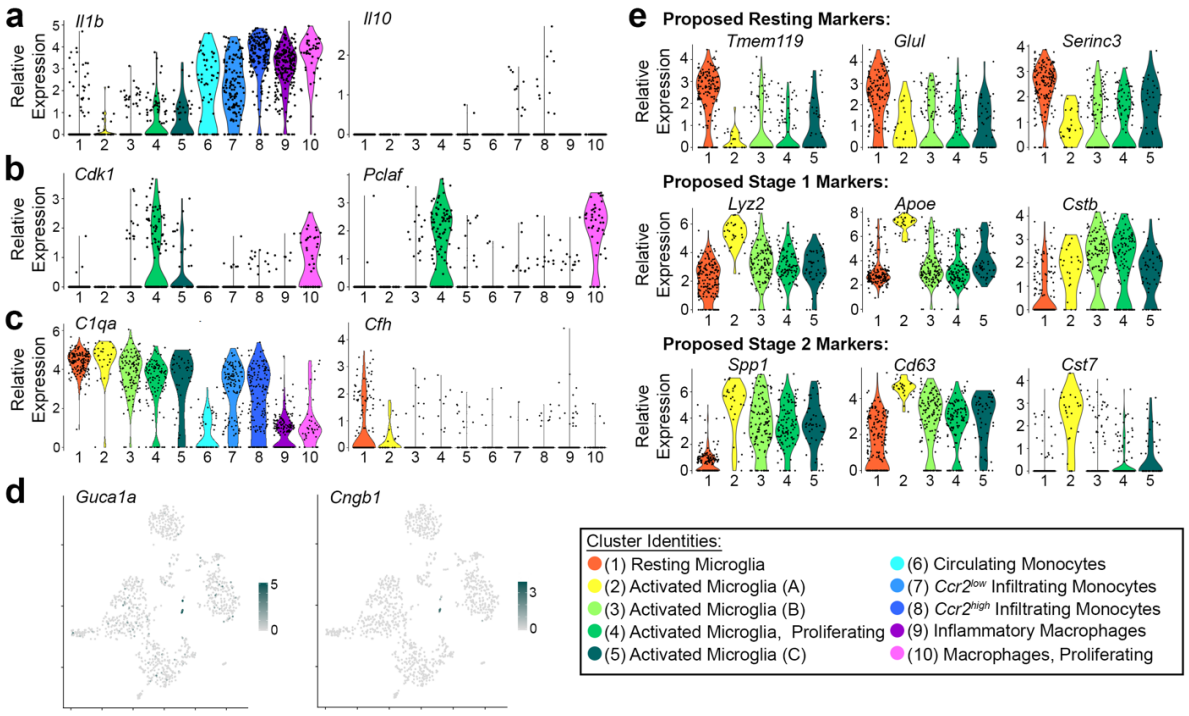

Figure 3.4. Differential gene expression between subtypes. (a) Representative inflammatory cytokine (*Il1b*) and anti-inflammatory cytokine (*Il10*) expression across identified clusters. (b) Identification of proliferative populations by expression of mitotic genes *Cdk1* and *Pclaf* (*2810417H13Rik*). (c) Expression of representative complement genes (*C1qa* and *Cfh*) across clusters. (d) Rod photoreceptor transcripts, including *Guca1a* and *Cngb1*, are found in a subset of activated microglia, particularly in several cells from Cluster #5 (activated microglia C). (e) Expression of disease activated (DA) microglia markers from Keren-Shaul *et al.* 2017, which suggested: *Tmem119*, *Glul*, and *Serinc3* are downregulated in DA microglia (i.e., are markers of resting microglia); *Lyz2*, *Apoe*, and *Cstb* are upregulated during Stage 1 of disease-related activation; *Spp1*, *Cd63*, and *Cst7* are upregulated in Stage 2 activation. None of the 5 microglia clusters in the present study completely align with these previously defined activation stages. For example, *Cst7* expression is low in activated microglia Clusters #3-5, despite the expression of other Stage 2 markers. Additionally, activated microglia Cluster #2 has lower expression of *Cstb* despite otherwise strong expression of several Stage 1 and Stage 2 markers. In (a-c,e),

the color corresponds to the cluster identity and the extruded shape represents the distribution of cells with the corresponding expression levels.

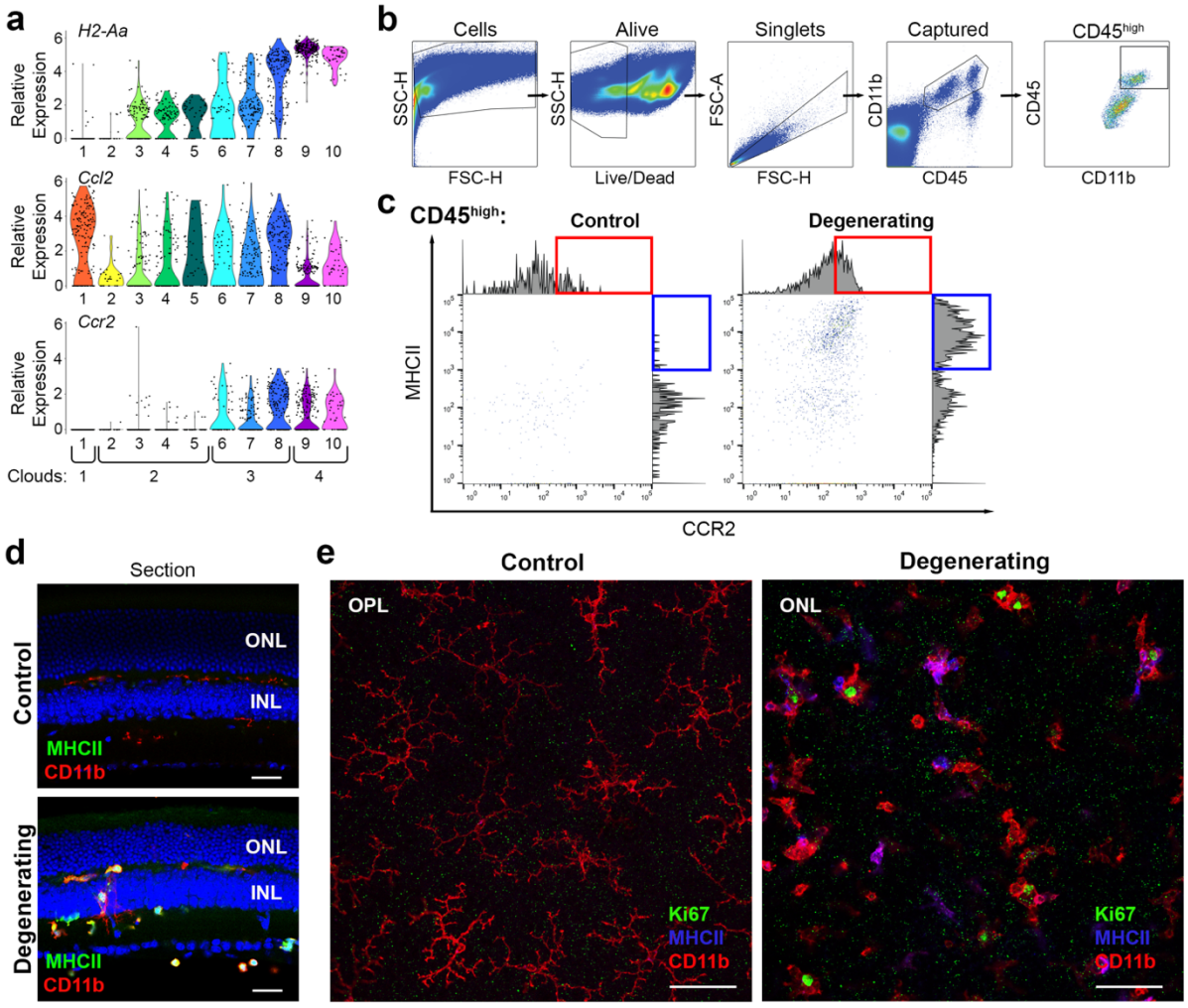

Figure 3.5. Utilizing traditional techniques in combination with scRNAseq to understand the response of immune cell populations during acute photoreceptor degeneration. (a) Relative expression of *H2-Aa*, *Ccr2*, and *Ccl2* across clusters. (b) Complete gating strategy for identifying alive, single, captured CD11b^{+}CD45^{high} cells. The gating strategy is shown here on the degenerating sample. (c) MHCII and CCR2 protein expression on CD11b^{+}CD45^{high} cells gated for scRNAseq. There was an increase in MHCII^{high} events (blue box) and CCR2 (red box) in degenerating tissue. Histograms on the edge of plots show the distribution of events across fluorescence intensities of MHCII and CCR2. (d,e) During degeneration a subset of macrophage-like CD11b^{+} cells express MHCII. No MHCII expression is regularly detected in control *Arr1*$^{-/-}$ retinas. In retinal sections, (d) MHCII^{+} cells can be seen in multiple retinal layers.

Retinal flatmounts (e) clearly reveal that some, but not all, macrophage-like cells express MHCII during degeneration, and there are no clear morphological distinctions between $MHCII^+$ and $MHCII^-$ macrophage-like cells. Additionally, during degeneration proliferating macrophage-like $CD11b^+$ cells can be identified in the retina by nuclear Ki67 staining. $Ki67^+$ nuclei are not observed in dark-reared control retinas, likely due to the very low levels of microglia turnover at rest. Both $MHCII^+$ (magenta, due to overlap of red and blue) and $MHCII^-$ (red) $CD11b^+$ cells with $Ki67^+$ nuclei (green) can be observed in degenerating retinas. Scale bars in retinal sections indicate 25 μm; scale bars in flat mounts indicate 50 μm. ONL = outer nuclear layer; OPL = outer plexiform layer; INL = inner nuclear layer.

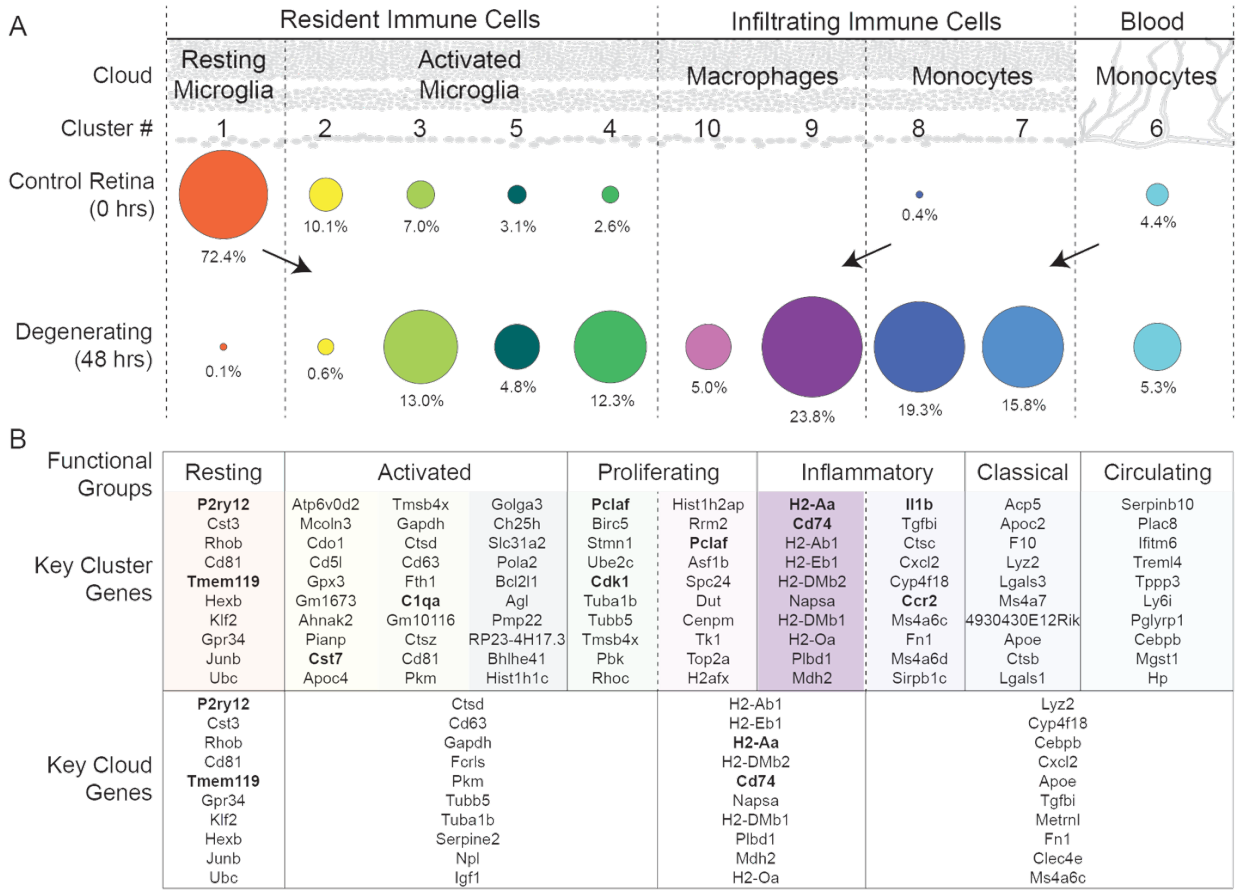

Figure 3.6. Summary of immune subpopulations identified by scRNAseq. (a) Comparison of the relative population sizes organized by cloud and cluster number for control (0 hours of light exposure) and degenerating (48 hours of light exposure) tissue. In control retina, almost all of the immune cells were resident microglia, with resting microglia being the dominant type. In degenerating tissue, most immune cells were infiltrating monocytes and monocyte-derived macrophages, while only a third were resident microglia, demonstrating that in the degenerating retina, microglia activation occurs concurrently with monocyte infiltration and differentiation into macrophages. The size of each dot corresponds to the number of cells captured; the percent of cells within each condition is given. (b) Groups based on gene expression profiles for each cluster. The top 10 significantly differentially expressed genes for each cluster and cloud are given (sorted by adjusted p-value, see Supplemental Tables 3.1 and 3.2 for an extended list,

see Methods for description of how lists were created). Expression of genes in bold are also shown graphically throughout Figures 3.3-3.5.

Supplemental materials

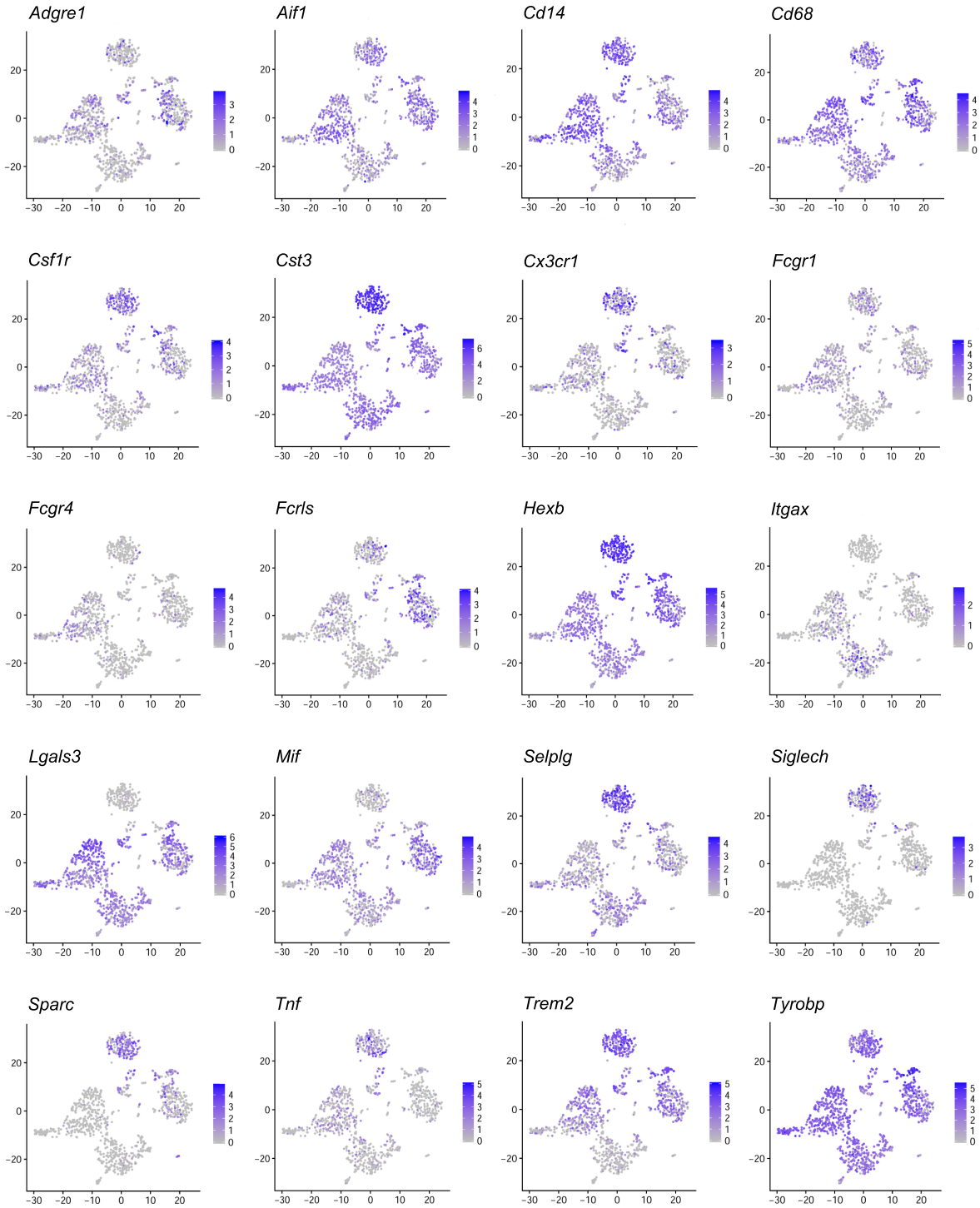

Supplemental Figure 3.1. Many commonly used marker genes of monocytes and macrophage-like cells are expressed in immune cells before and/or during retinal

degeneration. Relative expression is indicated on tSNE plots, with the highest expression in saturated color and the lowest expression in gray.

Supplemental Table 3.1. Top 35 differentially expressed genes for cells in each cloud (defined in Figure 3.3B), listed in ascending order based on adjusted p-value. Differentially expressed genes were identified using the FindMarkers function in Seurat, using a Wilcoxon rank sum test followed by Bonferroni correction. For each cloud, all cells within that cloud were compared to all other cells outside of the cloud. The log_2FC expression indicated the log_2 fold-change of the average increase in expression in cells in that cloud compared to the average expression across all other cells. Genes were only considered if they were expressed in at least 25% of the cells within that cloud. Also shown are the percent of cells within and outside of the cloud that express a given gene.

A. Cloud 1

Gene symbol	Log_2FC expression	Adjusted p-value	Cells expressing gene in Cloud (%)	All other cells expressing (%)
P2ry12	2.776	4.15E-135	98.1%	13.6%
Cst3	2.289	2.54E-82	100.0%	97.7%
Rhob	2.031	4.33E-80	92.0%	26.3%
Cd81	1.976	1.18E-78	100.0%	64.3%
Tmem119	2.012	5.45E-78	85.8%	21.4%
Gpr34	1.902	7.88E-78	77.2%	13.0%
Klf2	2.412	2.42E-77	99.4%	46.4%
Hexb	1.675	1.23E-76	100.0%	90.3%
Junb	1.774	4.02E-76	100.0%	88.3%
Ubc	1.647	1.87E-72	99.4%	89.1%
Siglech	1.521	1.36E-68	50.6%	4.0%
Jun	2.394	2.13E-67	98.1%	66.4%
Fos	2.073	5.42E-67	99.4%	79.7%
Sparc	1.552	4.72E-66	78.4%	16.2%
Jund	1.673	1.39E-65	98.8%	75.8%
Egr1	1.850	1.44E-65	94.4%	39.8%
Adrb2	2.309	8.66E-64	72.8%	16.1%
Sepp1	1.764	6.34E-59	93.8%	42.8%
Ctss	1.036	2.27E-57	100.0%	96.7%
Ccl3	2.187	3.26E-57	95.7%	67.6%
Selplg	1.787	6.87E-56	92.6%	52.3%
Ltc4s	1.341	7.61E-56	61.1%	10.3%
C1qc	1.213	1.16E-55	100.0%	79.2%
Il1a	1.803	1.69E-55	77.2%	21.9%
Dusp1	1.498	1.43E-53	99.4%	81.7%
Ier2	1.486	1.01E-48	98.8%	74.0%

C1qb	1.089	1.72E-48	100.0%	84.4%
Ccl4	2.036	2.89E-48	96.3%	73.9%
Glul	1.608	1.95E-47	86.4%	36.9%
Serinc3	1.237	4.81E-46	95.1%	61.5%
Serpine2	1.317	5.92E-46	85.8%	33.1%
Fosb	1.506	1.10E-45	81.5%	30.5%
Trem2	1.286	2.33E-45	94.4%	56.5%
C1qa	1.051	3.83E-45	100.0%	77.2%
Btg2	1.756	7.27E-43	87.7%	40.2%

B. Cloud 2

Gene Symbol	**Log_2FC expression**	**Adjusted p-value**	**Cells expressing gene in Cloud (%)**	**All other cells expressing (%)**
Ctsd	1.500	1.15E-52	94.4%	88.1%
Cd63	1.369	2.14E-51	86.7%	54.8%
Gapdh	0.839	6.29E-39	92.6%	80.1%
Fcrls	1.332	7.04E-37	59.3%	23.8%
Pkm	0.987	1.80E-34	89.2%	76.8%
Tubb5	1.118	2.21E-33	79.6%	52.4%
Tuba1b	0.948	1.79E-31	82.7%	60.8%
Serpine2	0.896	3.20E-31	67.0%	30.0%
Npl	1.041	5.91E-30	35.8%	7.6%
Igf1	1.092	2.28E-29	31.2%	5.4%
Cd81	0.368	2.42E-28	90.1%	61.1%
Fth1	0.765	6.79E-28	100.0%	99.6%
Stmn1	1.262	8.42E-27	49.7%	19.8%
Aldoa	0.874	2.80E-26	88.0%	82.5%
C1qa	0.677	4.44E-25	92.3%	75.8%
Rhoc	1.079	1.33E-24	40.7%	13.0%
Birc5	1.077	2.07E-24	28.4%	5.2%
C1qc	0.624	8.46E-24	92.9%	77.9%
Cst7	1.300	9.56E-24	33.3%	8.6%
Tmsb4x	0.692	6.36E-22	99.4%	100.0%
Syngr1	1.122	1.85E-21	60.2%	33.0%
Ctsz	0.662	1.15E-20	93.2%	94.6%
Mt1	1.345	2.32E-20	66.7%	47.4%
Prdx1	0.618	2.84E-20	91.0%	81.1%
Ctsb	0.689	1.18E-19	96.3%	96.9%
Gm10116	0.507	7.12E-18	99.1%	99.9%
C1qb	0.481	1.09E-17	96.6%	82.6%
Mif	0.915	1.48E-17	72.5%	54.1%
Ftl1	0.477	1.63E-17	99.7%	100.0%
Timp2	1.251	1.00E-16	57.1%	33.5%
2810417H13Rik	0.872	2.25E-16	30.9%	9.4%
Lpl	1.266	7.77E-16	35.5%	13.8%

Cd9	0.620	1.55E-15	88.6%	81.4%
Hmgn1	1.253	2.28E-15	51.9%	30.2%
Ctsl	0.854	3.55E-15	59.0%	36.6%

C. Cloud 3

Gene symbol	Log_2FC expression	Adjusted p-value	Cells expressing gene in Cloud (%)	All other cells expressing (%)
Lyz2	1.828	6.44E-96	100.0%	94.2%
Cyp4f18	1.378	2.79E-73	76.1%	24.6%
Cebpb	1.491	8.71E-71	97.7%	72.2%
Cxcl2	1.641	1.21E-68	92.9%	59.7%
Apoe	1.019	1.90E-67	100.0%	99.0%
Tgfbi	1.119	7.10E-60	80.4%	32.0%
Metrnl	1.324	1.83E-58	63.9%	16.5%
Fn1	1.130	1.87E-54	56.0%	12.4%
Clec4e	1.168	4.51E-49	42.9%	6.3%
Ms4a6c	0.930	1.48E-46	86.1%	43.7%
Chil3	1.489	8.77E-44	33.2%	3.0%
Lgals1	0.895	1.34E-43	84.9%	50.5%
Acp5	1.404	1.37E-43	59.7%	20.6%
Lst1	0.872	2.71E-43	54.0%	13.5%
Fcer1g	0.575	1.45E-42	99.7%	92.1%
Cyba	0.659	9.08E-42	98.3%	86.7%
Pla2g7	0.926	1.39E-40	39.5%	6.5%
Msrb1	0.982	3.76E-39	70.2%	30.2%
Prdx5	0.816	5.93E-39	92.0%	66.6%
Plaur	0.983	3.54E-37	72.4%	32.8%
Ifi27l2a	1.106	4.16E-35	71.9%	33.4%
Il1b	0.865	4.07E-34	88.4%	51.2%
Lgals3	0.863	9.74E-34	92.3%	63.7%
Ms4a7	1.039	1.03E-33	48.6%	14.2%
4930430E12Rik	0.509	5.38E-31	34.7%	6.5%
Sirpb1c	0.808	1.37E-30	39.2%	9.2%
Gm10116	0.456	5.00E-30	100.0%	99.5%
Ifitm3	0.899	1.86E-28	88.4%	51.4%
Arg1	1.450	3.25E-28	31.5%	6.2%
Ccrl2	0.771	1.32E-27	71.6%	37.3%
Psap	0.650	6.18E-27	98.9%	91.7%
Ccr2	0.628	1.35E-26	53.1%	20.1%
Thbs1	0.650	2.11E-26	26.1%	3.6%
Fcgr2b	0.604	6.04E-26	60.5%	25.8%
Sdcbp	0.562	5.10E-25	94.0%	78.9%

D. Cloud 4

Gene symbol	Log_2FC expression	Adjusted p-value	Cells expressing gene in Cloud (%)	All other cells expressing (%)
H2-Ab1	2.156	1.27E-111	100.0%	71.5%
H2-Eb1	2.170	2.00E-111	100.0%	56.2%
H2-Aa	2.101	3.80E-111	100.0%	62.2%
H2-DMb2	2.000	4.27E-111	88.3%	20.6%
Cd74	1.984	1.55E-108	100.0%	80.4%
Napsa	1.744	2.49E-99	89.1%	23.5%
H2-DMb1	1.478	1.27E-88	98.4%	45.0%
Plbd1	1.378	3.92E-81	92.6%	30.4%
Mdh2	1.560	4.93E-80	96.9%	57.6%
H2-Oa	1.606	2.11E-77	54.3%	5.0%
Cfp	1.463	5.48E-77	85.2%	27.2%
H2-DMa	1.214	1.03E-69	98.4%	56.8%
Il1r2	1.410	9.93E-69	59.4%	9.8%
Crip1	1.139	1.47E-66	97.3%	54.5%
Itgb7	1.096	3.57E-65	50.8%	5.5%
Lsp1	0.968	5.58E-60	88.3%	35.1%
Bhlhe40	1.172	5.64E-60	80.9%	28.9%
Tmsb10	0.911	1.65E-58	99.2%	76.7%
Epcam	1.092	4.64E-58	35.5%	1.5%
Qpct	1.566	2.44E-57	61.3%	14.6%
S100a11	1.255	1.16E-56	77.7%	25.1%
Gsn	1.063	6.12E-52	77.7%	28.6%
S100a6	1.066	3.38E-51	76.2%	24.8%
Ifitm2	0.928	1.19E-47	95.3%	53.3%
Syngr2	0.887	3.26E-47	89.8%	43.8%
Ifitm1	1.537	8.14E-47	39.5%	4.8%
Rpl18a	0.576	7.12E-46	100.0%	96.1%
Vasp	0.914	4.23E-45	89.1%	49.3%
Rps6	0.562	1.13E-44	100.0%	95.4%
Ifitm3	0.700	1.27E-44	96.9%	53.0%
Klrk1	0.969	1.75E-44	35.2%	3.5%
Rps27rt	0.629	1.42E-42	99.6%	85.1%
Rpl13	0.485	3.39E-42	100.0%	97.5%
Rps19	0.520	5.04E-42	100.0%	96.9%
Il1b	0.813	7.86E-42	96.1%	53.0%

Supplemental Table 3.2. Top 30 differentially expressed genes for cells in each cluster (defined in Figure 3.3C), listed in ascending order based on adjusted p-value. Differentially expressed genes were identified using the FindMarkers function in Seurat, using a Wilcoxon rank sum test followed by Bonferroni correction. For each cluster, all cells within that cluster were compared to all other cells outside of the cluster. The log_2FC expression indicated that log_2 fold-change of the average increase in expression in cells in that cluster compared to the average expression across all other cells. Genes were only considered if they were expressed in at least 25% of the cells within that cluster. Also shown are the percent of cells within and outside of the cluster that express that gene.

A. Microglia

Cluster identity	Gene symbol	Log_2FC expression	Adjusted p-value	Cells expressing gene in Cluster (%)	All other cells expressing gene (%)
Resting microglia (#1)	P2ry12	2.799	7.38e-135	97.0%	13.5%
	Cst3	2.297	7.70e-84	100.0%	97.7%
	Rhob	2.081	1.39e-83	92.2%	26.0%
	Cd81	2.004	4.39e-81	100.0%	64.2%
	Tmem119	2.026	1.72e-79	85.5%	21.2%
	Hexb	1.689	1.10e-78	100.0%	90.3%
	Klf2	2.426	1.89e-78	99.4%	46.1%
	Gpr34	1.900	3.14e-78	76.5%	12.8%
	Junb	1.765	7.28e-77	100.0%	88.2%
	Ubc	1.650	5.01e-74	99.4%	89.0%
	Fos	2.078	7.56e-69	99.4%	79.6%
	Sparc	1.631	1.30e-68	78.3%	16.0%
	Jun	2.396	1.64e-68	98.2%	66.3%
	Siglech	1.508	2.54e-68	50.0%	3.9%
	Jund	1.680	1.32e-67	98.8%	75.7%
	Adrb2	2.315	7.59e-67	73.5%	15.8%
	Egr1	1.838	1.64e-65	94.0%	39.7%
	Sepp1	1.754	2.56e-59	93.4%	42.7%
	Ccl3	2.225	8.18e-59	95.8%	67.4%
	Ctss	1.038	2.05e-58	100.0%	96.7%
	Ltc4s	1.329	7.10e-58	61.4%	10.0%
	Selplg	1.814	9.49e-58	92.8%	52.1%
	Il1a	1.858	1.21e-57	77.1%	21.7%
	C1qc	1.221	3.54e-57	100.0%	79.1%

	Dusp1	1.483	2.59e-53	99.4%	81.6%
	C1qb	1.094	9.33e-50	100.0%	84.3%
	Ccl4	2.076	2.92e-49	96.4%	73.8%
	Ier2	1.486	2.96e-49	98.8%	73.9%
	Serpine2	1.323	7.97e-48	86.1%	32.8%
	Serinc3	1.238	1.71e-47	95.2%	61.4%
Activated microglia (A) (#2)	Atp6v0d2	1.085	6.27e-83	46.4%	0.4%
	Mcoln3	0.727	1.20e-74	42.9%	0.4%
	Cdo1	1.622	5.29e-63	57.1%	1.6%
	Cd5l	2.902	2.01e-55	71.4%	3.6%
	Gpx3	3.029	2.03e-54	85.7%	6.1%
	Gm1673	1.368	7.73e-49	71.4%	4.0%
	Ahnak2	0.393	2.12e-30	28.6%	0.7%
	Pianp	0.658	2.64e-30	42.9%	2.1%
	Cst7	2.210	5.78e-28	89.3%	13.9%
	Apoc4	0.834	4.27e-27	42.9%	2.5%
	Mgll	0.496	2.27e-26	28.6%	0.9%
	Gpnmb	3.022	1.10e-24	96.4%	22.1%
	Chst2	0.276	2.24e-22	35.7%	1.9%
	Fabp3	0.827	2.14e-20	60.7%	6.8%
	Igf1	1.282	2.30e-20	75.0%	11.2%
	Ttc3	0.627	1.02e-19	35.7%	2.3%
	Pld3	2.354	4.11e-18	92.9%	29.8%
	Timp2	2.396	6.44e-18	100.0%	38.8%
	Syngr1	2.245	3.63e-17	100.0%	39.3%
	Dpp7	0.930	9.54e-17	53.6%	6.4%
	Glb1	0.810	5.98e-16	60.7%	8.3%
	Creg1	1.856	1.05e-15	100.0%	50.1%
	Lag3	1.027	1.07e-15	85.7%	17.0%
	Ctla2a	0.571	1.14e-15	35.7%	2.8%
	Cd63	1.965	1.76e-14	100.0%	63.0%
	Fabp5	1.298	3.12e-13	96.4%	28.0%
	Lyz1	0.773	3.93e-13	67.9%	11.8%
	Apoe	2.114	5.70e-13	100.0%	99.3%
	Hpse	0.675	1.50e-12	39.3%	4.3%
	Pon3	0.990	1.64e-12	60.7%	10.9%
Activated microglia (B) (#3)	Tmsb4x	0.741	3.17e-30	100.0%	99.8%
	Gapdh	0.682	3.97e-14	92.2%	82.6%
	Ctsd	0.974	1.95e-13	90.7%	89.8%
	Cd63	0.846	6.59e-13	83.7%	61.4%
	Fth1	0.636	3.64e-12	100.0%	99.7%
	C1qa	0.634	1.27e-11	97.7%	78.3%
	Gm10116	0.571	3.61e-11	100.0%	99.6%
	Ctsz	0.609	7.94e-11	95.3%	94.1%
	Cd81	0.493	1.16e-10	90.7%	66.7%
	Pkm	0.816	3.31e-10	84.5%	79.8%
	Ftl1	0.521	4.04e-10	100.0%	99.9%
	C1qc	0.571	1.63e-09	95.3%	80.5%

	Gatm	0.754	3.41e-08	79.8%	65.2%
	C1qb	0.548	3.87e-08	96.9%	85.3%
	Mif	0.861	1.16e-07	69.8%	58.1%
	Fcrls	0.898	1.95e-07	54.3%	31.4%
	Aldoa	0.678	4.38e-06	85.3%	83.9%
	Serpine2	0.641	8.57e-06	62.8%	37.8%
	Prdx1	0.512	5.76e-05	89.9%	83.2%
	Tuba1b	0.541	6.28e-05	79.1%	65.5%
	Mt1	1.024	6.34e-05	64.3%	51.5%
	Fcer1g	0.446	0.000109933	97.7%	94.1%
	Ctsb	0.486	0.000215108	97.7%	96.6%
	Cd9	0.553	0.000328161	88.4%	82.8%
	Cstb	0.512	0.000611186	77.5%	65.7%
	Rpl41	0.334	0.001352796	100.0%	98.1%
	Ppia	0.294	0.001614957	99.2%	96.5%
	Aif1	0.616	0.001615488	78.3%	70.4%
	Syngr1	0.568	0.008185932	55.0%	39.0%
	Hexb	0.315	0.018391534	93.8%	91.5%
Activated microglia, proliferating (#4)	2810417H13Rik	1.497	7.16e-51	64.6%	10.1%
	Birc5	1.450	1.49e-45	54.0%	7.2%
	Stmn1	1.409	7.66e-41	77.9%	22.8%
	Ube2c	1.555	1.68e-33	42.5%	6.0%
	Cdk1	1.381	8.85e-32	46.9%	8.4%
	Tuba1b	1.161	6.65e-31	92.9%	64.2%
	Tubb5	1.280	4.00e-30	92.0%	56.7%
	Tmsb4x	0.832	2.50e-27	98.2%	100.0%
	Pbk	1.536	4.86e-26	32.7%	4.4%
	Rhoc	1.058	1.17e-22	57.5%	16.9%
	Cdca3	0.984	4.49e-21	29.2%	4.2%
	Gapdh	0.808	1.83e-20	95.6%	82.4%
	Ccnb1	0.811	6.65e-19	27.4%	4.0%
	Pkm	0.802	1.33e-17	94.7%	78.7%
	Ppia	0.576	2.22e-17	100.0%	96.4%
	Gatm	1.167	4.32e-17	86.7%	64.7%
	Cenpa	0.821	6.43e-17	32.7%	6.4%
	Cdca8	0.980	6.40e-15	26.5%	4.7%
	Ran	0.838	2.34e-14	85.8%	66.5%
	Pttg1	0.967	4.87e-14	37.2%	9.7%
	Hmgn1	0.966	1.05e-13	65.5%	33.2%
	H2afz	0.653	3.23e-13	93.8%	86.8%
	Ranbp1	0.761	3.41e-13	89.4%	69.1%
	Tubb4b	1.139	1.06e-12	46.0%	16.3%

	Prdx1	0.663	1.09e-12	95.6%	82.7%
	Kpna2	0.897	2.96e-12	43.4%	15.0%
	Fth1	0.579	8.82e-12	100.0%	99.7%
	Tyms	0.891	9.43e-12	33.6%	9.2%
	Tacc3	0.864	9.87e-12	28.3%	6.3%
	Spc25	0.882	1.98e-11	26.5%	5.9%
Activated microglia (C) (#5)	Golga3	1.092	7.30e-20	44.9%	6.2%
	Ch25h	2.020	1.77e-18	51.0%	8.9%
	Slc31a2	1.228	8.56e-17	51.0%	9.4%
	Pola2	1.117	4.27e-16	63.3%	15.4%
	Bcl2l1	0.847	2.17e-14	32.7%	4.2%
	Agl	1.536	9.94e-14	40.8%	7.0%
	Pmp22	0.950	7.47e-12	65.3%	18.5%
	RP23-4H17.3	0.945	1.11e-11	44.9%	9.9%
	Bhlhe41	0.617	2.43e-11	28.6%	3.8%
	Hist1h1c	1.082	3.77e-11	36.7%	6.5%
	Chst1	0.550	8.06e-11	30.6%	4.5%
	Bag5	0.909	1.13e-10	34.7%	6.0%
	Tmem245	0.940	1.47e-10	46.9%	11.5%
	Agpat3	1.418	1.57e-10	28.6%	4.2%
	Trmt2a	0.415	1.66e-10	40.8%	7.8%
	Gm13075	0.564	2.14e-10	36.7%	6.9%
	Usp2	0.537	4.09e-10	38.8%	7.3%
	Timm10	0.558	8.88e-10	32.7%	5.4%
	Mid1ip1	0.948	3.46e-09	40.8%	8.8%
	Srpk1	0.706	4.22e-09	49.0%	13.1%
	Malat1	1.026	7.82e-09	98.0%	81.6%
	Lpl	1.631	1.93e-08	55.1%	18.4%
	Rab7b	1.163	2.03e-08	46.9%	13.2%
	Fam212a	0.557	3.08e-08	26.5%	4.1%
	Znrf1	0.993	4.43e-08	28.6%	4.9%
	Adamts1	0.573	4.66e-08	26.5%	4.2%
	Xist	1.053	5.72e-08	71.4%	30.5%
	Dnmt3a	0.678	6.10e-08	26.5%	4.4%
	Tns3	0.871	1.12e-07	34.7%	7.4%
	Slc2a1	0.335	2.74e-07	32.7%	6.5%

B. Monocytes and Macrophages

Cluster identity	Gene symbol	Log_2FC expression	Adjusted p-value	Cells expressing gene in Cluster (%)	All other cells expressing gene (%)
Circulating monocytes (#6)	Serpinb10	1.042	1.61e-49	26.8%	0.3%
	Plac8	2.296	1.65e-28	87.5%	27.5%
	Ifitm6	1.810	4.58e-28	57.1%	8.9%

	Treml4	1.548	5.31e-28	37.5%	3.3%
	Tppp3	1.785	9.20e-28	41.1%	4.1%
	Ly6i	1.675	3.13e-27	26.8%	1.4%
	Pglyrp1	1.690	2.20e-26	30.4%	2.1%
	Cebpb	2.114	3.98e-26	98.2%	79.2%
	Mgst1	2.121	5.79e-25	51.8%	8.1%
	Hp	1.896	9.82e-24	46.4%	6.6%
	Ifitm3	1.672	2.28e-23	98.2%	61.1%
	Clec4a3	1.682	1.50e-20	64.3%	15.6%
	H2-D1	0.944	1.50e-18	100.0%	94.1%
	Metrnl	1.890	6.41e-17	75.0%	29.0%
	Lyz2	1.363	3.00e-16	100.0%	95.8%
	Prr13	1.601	2.45e-15	89.3%	46.1%
	Ifitm2	1.168	4.09e-15	92.9%	61.3%
	Msrb1	1.448	2.82e-14	82.1%	40.6%
	Samhd1	1.564	5.50e-14	67.9%	24.9%
	Gpx1	1.092	6.02e-14	98.2%	86.9%
	Sirpb1c	1.190	1.22e-12	55.4%	16.7%
	Alox5ap	1.334	5.83e-12	87.5%	61.4%
	Clec4a1	1.163	6.41e-12	44.6%	10.5%
	Eno3	1.508	1.49e-10	26.8%	4.1%
	Dusp1	0.803	2.98e-10	98.2%	83.5%
	Plaur	1.307	1.58e-09	76.8%	43.5%
	Ly6c2	1.615	1.62e-09	33.9%	7.2%
	Adgre5	1.366	3.63e-09	35.7%	8.2%
	Gngt2	1.716	1.05e-08	75.0%	48.5%
	Ly6e	0.892	2.51e-08	92.9%	66.2%
Classical Monocytes (#7)	Acp5	1.658	6.45e-57	86.1%	25.4%
	Apoc2	0.467	1.06e-55	41.6%	2.5%
	F10	0.968	1.38e-54	39.4%	2.3%
	Lyz2	1.632	9.87e-51	100.0%	95.4%
	Lgals3	1.326	3.26e-43	99.3%	69.0%
	Ms4a7	1.193	1.91e-42	73.0%	18.3%
	4930430E12Rik	0.703	2.00e-42	56.2%	9.6%
	Apoe	1.187	6.93e-42	100.0%	99.2%
	Ctsb	1.033	4.63e-40	100.0%	96.3%
	Lgals1	1.100	6.69e-40	99.3%	56.0%
	Gm10116	0.828	9.84e-40	100.0%	99.6%
	Spp1	1.810	8.06e-38	100.0%	87.7%
	Nr1h3	0.764	5.69e-37	35.8%	3.6%
	Ftl1	0.766	2.02e-36	100.0%	99.9%
	Pla2g7	1.057	2.03e-35	54.7%	11.6%
	Msrb1	0.841	5.60e-35	92.0%	35.9%
	Cyba	0.761	9.28e-35	100.0%	89.0%
	Arg1	1.805	1.29e-34	48.2%	9.4%
	Lyz1	0.484	7.67e-30	46.7%	8.5%
	Cstb	0.990	8.98e-30	95.6%	63.1%
	Fn1	0.882	1.46e-29	67.9%	20.3%

	Cyp4f18	0.926	1.43e-27	82.5%	35.0%
	Uap1l1	0.598	3.24e-27	67.9%	20.5%
	Chil3	0.759	8.13e-27	43.1%	8.2%
	Clec4e	0.618	1.09e-26	53.3%	12.9%
	Tnfsf12	0.571	1.59e-26	38.7%	6.5%
	Tgfbi	0.842	4.28e-26	89.8%	41.2%
	Cd24a	0.822	4.42e-26	46.7%	10.3%
	Gpnmb	0.643	1.67e-24	59.1%	19.0%
	Emp1	0.447	4.50e-24	46.7%	10.4%
Inflammatory Monocytes (#8)	Il1b	1.217	3.01e-40	94.6%	57.2%
	Tgfbi	1.023	1.88e-39	89.9%	39.6%
	Ctsc	0.914	1.56e-35	98.2%	85.7%
	Cxcl2	1.328	2.19e-35	96.4%	65.5%
	Cyp4f18	0.966	3.16e-31	79.8%	33.9%
	Ccr2	0.835	3.30e-29	66.7%	24.1%
	Ms4a6c	0.772	3.95e-29	92.9%	50.6%
	Fn1	0.895	1.45e-28	61.3%	19.9%
	Ms4a6d	0.863	1.62e-28	83.9%	41.2%
	Sirpb1c	0.700	8.49e-27	50.6%	13.0%
	Klra2	0.893	9.34e-27	35.7%	6.4%
	Clec4a2	0.769	2.93e-26	51.2%	13.7%
	Prdx5	0.793	1.48e-25	94.6%	71.0%
	Ms4a4c	0.863	5.81e-25	59.5%	19.4%
	Cebpb	0.525	4.61e-23	98.2%	77.0%
	Lst1	0.738	5.40e-23	59.5%	20.3%
	Ifi27l2a	1.034	8.00e-23	78.0%	39.7%
	Clec12a	1.149	1.24e-22	50.6%	15.6%
	Ccr1	0.804	1.29e-22	66.1%	27.8%
	Ccl7	1.641	3.65e-21	61.3%	27.1%
	Apoe	0.485	3.35e-19	100.0%	99.2%
	Cd14	0.694	8.49e-18	95.2%	78.3%
	Fcer1g	0.473	8.80e-18	100.0%	93.5%
	Ly6e	0.689	3.29e-16	91.1%	63.4%
	Ifitm3	0.575	6.90e-16	92.9%	57.7%
	Ms4a6b	0.750	1.77e-15	63.1%	30.5%
	Sirpb1b	0.367	7.93e-15	36.9%	10.4%
	Lgals1	0.456	1.20e-14	89.9%	56.3%
	Pilra	0.613	7.04e-14	47.0%	18.0%
	Zbp1	0.703	1.08e-13	34.5%	10.4%
Inflammatory macrophages (#9)	H2-Aa	1.993	4.96e-97	100.0%	64.3%
	Cd74	1.906	8.40e-97	100.0%	81.5%
	H2-Ab1	2.014	6.63e-96	100.0%	73.1%
	H2-Eb1	2.024	5.13e-95	100.0%	58.6%
	H2-DMb2	1.930	7.99e-94	88.8%	24.2%
	Napsa	1.723	5.24e-81	88.3%	27.2%
	H2-DMb1	1.451	1.60e-72	98.1%	48.0%
	H2-Oa	1.641	1.39e-68	56.8%	7.1%
	Plbd1	1.378	8.78e-66	91.3%	34.1%

	Mdh2	1.459	3.76e-64	96.1%	59.9%
	H2-DMa	1.211	4.24e-62	99.0%	58.9%
	Itgb7	1.083	3.65e-59	53.9%	7.3%
	Cfp	1.317	7.22e-57	84.0%	30.6%
	Lsp1	1.007	1.73e-50	88.3%	38.0%
	Crip1	1.047	5.86e-50	96.6%	57.0%
	Bhlhe40	1.226	6.69e-50	80.1%	31.9%
	Il1r2	1.299	7.34e-48	57.3%	13.0%
	Tmsb10	0.860	6.91e-47	99.0%	78.0%
	S100a11	1.282	7.26e-45	76.7%	28.2%
	Rps27rt	0.697	2.71e-44	99.5%	85.9%
	Ifitm2	0.968	7.75e-44	96.1%	55.4%
	Rpl18a	0.612	1.98e-42	100.0%	96.3%
	Syngr2	0.964	2.85e-42	89.3%	46.4%
	Ifitm1	1.512	7.60e-42	41.7%	6.2%
	Ifitm3	0.774	6.30e-41	96.6%	55.4%
	Rpl13	0.514	4.04e-40	100.0%	97.6%
	S100a6	1.063	3.42e-39	74.3%	28.0%
	Rps27	0.684	3.61e-39	99.5%	90.4%
	Rps9	0.624	4.10e-39	100.0%	93.6%
	Epcam	0.975	6.08e-39	34.0%	3.7%
Macrophages, proliferating (#10)	Hist1h2ap	0.778	1.13e-41	41.9%	1.9%
	Rrm2	1.398	3.50e-39	72.1%	7.9%
	2810417H13Rik	1.704	2.23e-36	83.7%	12.9%
	Asf1b	1.069	2.91e-34	67.4%	7.7%
	Spc24	1.034	1.01e-31	65.1%	7.8%
	Dut	0.966	4.92e-31	79.1%	11.5%
	Cenpm	0.744	1.01e-30	44.2%	3.2%
	Tk1	1.196	2.91e-28	60.5%	7.2%
	Top2a	0.631	4.24e-28	34.9%	2.0%
	H2afx	1.455	2.03e-27	74.4%	12.7%
	Mcm7	0.877	9.64e-27	60.5%	7.7%
	Stmn1	1.469	3.19e-25	97.7%	25.6%
	Smc2	0.687	7.22e-25	39.5%	3.2%
	Cks1b	1.006	1.33e-24	86.0%	17.4%
	Cdca3	0.557	3.14e-24	48.8%	5.0%
	Nusap1	0.807	7.48e-24	41.9%	3.8%
	Birc5	1.106	8.16e-24	65.1%	9.8%
	Cks1brt	0.509	1.46e-23	65.1%	9.3%
	Dcstamp	0.644	4.47e-23	37.2%	3.0%
	Ccna2	0.671	1.24e-22	44.2%	4.3%
	Haus4	0.597	1.26e-22	48.8%	5.5%
	Tyms	0.831	9.56e-22	62.8%	9.6%
	Hmgb2	1.585	9.69e-22	100.0%	43.3%
	Plp2	0.619	1.80e-20	74.4%	13.9%
	Racgap1	0.582	2.62e-20	44.2%	4.9%
	Qpct	1.183	4.70e-20	88.4%	22.8%
	Cenph	0.472	5.81e-20	25.6%	1.5%

	Ptma	1.006	6.48e-20	100.0%	96.4%
	Apitd1	0.439	1.18e-19	30.2%	2.2%
	Rfc5	0.652	2.21e-19	58.1%	9.1%

C. Unidentified clusters

Cluster identity	Gene symbol	Log_2FC expression	Adjusted p-value	Cells expressing gene in Cluster (%)	All other cells expressing gene (%)
Unidentified 1 (#11)	Esam	2.640	4.80e-163	90.0%	0.3%
	Foxq1	1.946	4.32e-154	80.0%	0.2%
	Tmem252	2.637	2.81e-150	90.0%	0.4%
	Sox17	2.722	3.24e-150	90.0%	0.4%
	S100a16	2.488	6.74e-130	90.0%	0.5%
	Pcp4l1	2.044	2.15e-117	70.0%	0.3%
	Egfl7	3.115	2.08e-108	90.0%	0.8%
	Ramp2	1.793	2.50e-106	70.0%	0.4%
	Sparcl1	2.832	2.93e-97	70.0%	0.4%
	Ptn	2.417	5.94e-95	60.0%	0.3%
	Itm2a	3.777	2.74e-93	100.0%	1.4%
	Slc9a3r2	1.869	2.46e-92	90.0%	1.1%
	AU021092	1.774	3.59e-85	60.0%	0.4%
	Ly6c1	3.661	3.07e-78	100.0%	1.9%
	Abcb1a	1.566	1.68e-77	60.0%	0.4%
	Stra6	1.228	9.71e-77	60.0%	0.4%
	Flt1	2.399	2.89e-68	70.0%	0.9%
	Cyr61	2.590	3.42e-68	70.0%	0.9%
	Cldn5	4.314	2.04e-67	100.0%	2.3%
	Crip2	2.607	5.69e-63	80.0%	1.4%
	Hspb1	1.783	5.36e-60	70.0%	1.1%
	Ctla2a	3.308	6.67e-59	100.0%	2.8%
	Maoa	0.944	2.54e-55	60.0%	0.8%
	Lsr	1.839	2.88e-51	90.0%	2.5%
	Igfbp7	4.589	1.53e-49	100.0%	3.5%
	Ly6a	3.481	4.25e-49	100.0%	3.5%
	Gsta4	1.116	3.35e-40	40.0%	0.4%
	Vwa1	1.995	1.36e-37	70.0%	2.1%
	Vamp5	1.558	7.80e-37	60.0%	1.4%
	Pir	1.552	2.86e-36	40.0%	0.5%
Unidentified 2 (#12)	Ccr7	3.765	5.60e-82	100.0%	3.4%
	Cacnb3	1.882	1.35e-72	52.6%	0.6%
	Tbc1d4	1.816	4.12e-51	63.2%	2.0%
	Spint2	2.528	7.90e-44	84.2%	5.0%
	Serpinb6b	2.116	1.97e-41	47.4%	1.3%
	Cd200	1.975	1.70e-39	63.2%	2.8%

	Birc2	1.921	1.54e-25	63.2%	4.7%
	Zmynd15	2.519	6.50e-22	63.2%	5.7%
	Fscn1	2.769	6.79e-22	100.0%	18.1%
	Relb	3.105	2.99e-20	68.4%	7.2%
	Gypc	0.953	1.70e-19	26.3%	0.8%
	Ccl5	3.857	1.93e-19	94.7%	18.3%
	Socs2	1.540	6.70e-19	36.8%	1.9%
	Hmgn3	1.494	2.24e-18	57.9%	5.2%
	Cd1d1	1.563	3.65e-18	42.1%	2.6%
	Ramp3	1.292	2.36e-17	31.6%	1.4%
	Vsig10	1.077	1.26e-16	26.3%	1.0%
	Tmem123	3.162	1.38e-16	100.0%	27.5%
	Itga4	1.755	2.29e-15	52.6%	5.2%
	Gnb4	1.164	1.34e-14	36.8%	2.4%
	Cnn2	1.773	1.00e-13	94.7%	21.5%
	Fabp5	2.049	3.67e-13	100.0%	28.5%
	Gbp2	1.222	6.28e-13	36.8%	2.7%
	Pcgf5	1.495	7.80e-11	47.4%	5.3%
	Il4i1	1.659	1.20e-10	31.6%	2.4%
	Lsp1	2.279	1.46e-10	100.0%	46.3%
	Tspan3	2.754	2.15e-10	73.7%	16.7%
	Fam177a	1.655	2.25e-10	63.2%	10.7%
	Supt4a	1.413	1.66e-09	94.7%	30.2%
	Bhlhe40	1.666	2.96e-09	100.0%	39.7%

References

Baufeld, C., O'Loughlin, E., Calcagno, N., Madore, C., Butovsky, O., 2018. Differential contribution of microglia and monocytes in neurodegenerative diseases. J Neural Transm 125, 809–826. https://doi.org/10.1007/s00702-017-1795-7

Butler, A., Hoffman, P., Smibert, P., Papalexi, E., Satija, R., 2018. Integrating single-cell transcriptomic data across different conditions, technologies, and species. Nat. Biotechnol. 36, 411–420. https://doi.org/10.1038/nbt.4096

Calippe, B., Augustin, S., Beguier, F., Charles-Messance, H., Poupel, L., Conart, J.-B., Hu, S.J., Lavalette, S., Fauvet, A., Rayes, J., Levy, O., Raoul, W., Fitting, C., Denèfle, T., Pickering, M.C., Harris, C., Jorieux, S., Sullivan, P.M., Sahel, J.-A., Karoyan, P., Sapieha, P., Guillonneau, X., Gautier, E.L., Sennlaub, F., 2017. Complement Factor H Inhibits CD47-Mediated Resolution of Inflammation. Immunity 46, 261–272. https://doi.org/10.1016/j.immuni.2017.01.006

Chang, B., Hawes, N.L., Hurd, R.E., Davisson, M.T., Nusinowitz, S., Heckenlively, J.R., 2002. Retinal degeneration mutants in the mouse. Vision Research 42, 517–525. https://doi.org/10.1016/S0042-6989(01)00146-8

Chen, J., Simon, M.I., Matthes, M.T., Yasumura, D., LaVail, M.M., 1999. Increased susceptibility to light damage in an arrestin knockout mouse model of Oguchi disease (stationary night blindness). Invest. Ophthalmol. Vis. Sci. 40, 2978–2982.

Guillonneau, X., Eandi, C.M., Paques, M., Sahel, J.-A., Sapieha, P., Sennlaub, F., 2017. On phagocytes and macular degeneration. Prog Retin Eye Res 61, 98–128. https://doi.org/10.1016/j.preteyeres.2017.06.002

Hammond, T.R., Dufort, C., Dissing-Olesen, L., Giera, S., Young, A., Wysoker, A., Walker, A.J., Gergits, F., Segel, M., Nemesh, J., Marsh, S.E., Saunders, A., Macosko, E., Ginhoux, F., Chen, J., Franklin, R.J.M., Piao, X., McCarroll, S.A., Stevens, B., 2019. Single-Cell RNA Sequencing of Microglia throughout the Mouse Lifespan and in the Injured Brain Reveals Complex Cell-State Changes. Immunity 50, 253-271.e6. https://doi.org/10.1016/j.immuni.2018.11.004

Hao, W., Wenzel, A., Obin, M.S., Chen, C.-K., Brill, E., Krasnoperova, N.V., Eversole-Cire, P., Kleyner, Y., Taylor, A., Simon, M.I., Grimm, C., Remé, C.E., Lem, J., 2002. Evidence for two apoptotic pathways in light-induced retinal degeneration. Nat. Genet. 32, 254–260. https://doi.org/10.1038/ng984

Heng, T.S.P., Painter, M.W., Immunological Genome Project Consortium, 2008. The Immunological Genome Project: networks of gene expression in immune cells. Nat. Immunol. 9, 1091–1094. https://doi.org/10.1038/ni1008-1091

Herz, J., Filiano, A.J., Smith, A., Yogev, N., Kipnis, J., 2017. Myeloid Cells in the Central Nervous System. Immunity 46, 943–956. https://doi.org/10.1016/j.immuni.2017.06.007

Hickman, S.E., Kingery, N.D., Ohsumi, T.K., Borowsky, M.L., Wang, L., Means, T.K., El Khoury, J., 2013. The microglial sensome revealed by direct RNA sequencing. Nat. Neurosci. 16, 1896–1905. https://doi.org/10.1038/nn.3554

Jung, S., Aliberti, J., Graemmel, P., Sunshine, M.J., Kreutzberg, G.W., Sher, A., Littman, D.R., 2000. Analysis of Fractalkine Receptor CX3CR1 Function by Targeted Deletion and Green Fluorescent Protein Reporter Gene Insertion. Molecular and Cellular Biology 20, 4106–4114. https://doi.org/10.1128/MCB.20.11.4106-4114.2000

Karlen, S.J., Miller, E.B., Wang, X., Levine, E.S., Zawadzki, R.J., Burns, M.E., 2018. Monocyte infiltration rather than microglia proliferation dominates the early immune response to rapid photoreceptor degeneration. Journal of Neuroinflammation 15, 344. https://doi.org/10.1186/s12974-018-1365-4

Keren-Shaul, H., Spinrad, A., Weiner, A., Matcovitch-Natan, O., Dvir-Szternfeld, R., Ulland, T.K., David, E., Baruch, K., Lara-Astaiso, D., Toth, B., Itzkovitz, S., Colonna, M., Schwartz, M., Amit, I., 2017. A Unique Microglia Type Associated with Restricting Development of Alzheimer's Disease. Cell 169, 1276-1290.e17. https://doi.org/10.1016/j.cell.2017.05.018

Kiser, P.D., Palczewski, K., 2016. Retinoids and Retinal Diseases. Annu Rev Vis Sci 2, 197–234. https://doi.org/10.1146/annurev-vision-111815-114407

Lenz, K.M., McCarthy, M.M., 2015. A starring role for microglia in brain sex differences. Neuroscientist 21, 306–321. https://doi.org/10.1177/1073858414536468

Levine, E.S., Zam, A., Zhang, P., Pechko, A., Wang, X., FitzGerald, P., Pugh, E.N., Zawadzki, R.J., Burns, M.E., 2014. Rapid light-induced activation of retinal microglia in mice lacking Arrestin-1. Vision Res. 102, 71–79. https://doi.org/10.1016/j.visres.2014.07.011

Levy, O., Lavalette, S., Hu, S.J., Housset, M., Raoul, W., Eandi, C., Sahel, J.-A., Sullivan, P.M., Guillonneau, X., Sennlaub, F., 2015. APOE Isoforms Control Pathogenic Subretinal Inflammation in Age-Related Macular Degeneration. J. Neurosci. 35, 13568–13576. https://doi.org/10.1523/JNEUROSCI.2468-15.2015

Ma, W., Zhang, Y., Gao, C., Fariss, R.N., Tam, J., Wong, W.T., 2017. Monocyte infiltration and proliferation reestablish myeloid cell homeostasis in the mouse retina following retinal pigment epithelial cell injury. Sci Rep 7, 8433. https://doi.org/10.1038/s41598-017-08702-7

Macosko, E.Z., Basu, A., Satija, R., Nemesh, J., Shekhar, K., Goldman, M., Tirosh, I., Bialas, A.R., Kamitaki, N., Martersteck, E.M., Trombetta, J.J., Weitz, D.A., Sanes, J.R., Shalek, A.K., Regev, A., McCarroll, S.A., 2015. Highly Parallel Genome-wide Expression Profiling of Individual Cells Using Nanoliter Droplets. Cell 161, 1202–1214. https://doi.org/10.1016/j.cell.2015.05.002

McHarg, S., Clark, S.J., Day, A.J., Bishop, P.N., 2015. Age-related macular degeneration and the role of the complement system. Mol. Immunol. 67, 43–50. https://doi.org/10.1016/j.molimm.2015.02.032

McMenamin, P.G., Saban, D.R., Dando, S.J., 2019. Immune cells in the retina and choroid: Two different tissue environments that require different defenses and surveillance. Progress in Retinal and Eye Research 70, 85–98. https://doi.org/10.1016/j.preteyeres.2018.12.002

O'Koren, E.G., Mathew, R., Saban, D.R., 2016. Fate mapping reveals that microglia and recruited monocyte-derived macrophages are definitively distinguishable by phenotype in the retina. Sci Rep 6, 20636. https://doi.org/10.1038/srep20636

Ousman, S.S., Kubes, P., 2012. Immune surveillance in the central nervous system. Nat. Neurosci. 15, 1096–1101. https://doi.org/10.1038/nn.3161

R Core Team, n.d. R: A Language and Environment for Statistical Computing. R Foundation for Statistical Computing, Vienna, Austria.

Reyes, N.J., O'Koren, E.G., Saban, D.R., 2017. New insights into mononuclear phagocyte biology from the visual system. Nat. Rev. Immunol. 17, 322–332. https://doi.org/10.1038/nri.2017.13

Ronning, K.E., Allina, G.P., Miller, E.B., Zawadzki, R.J., Pugh, E.N., Herrmann, R., Burns, M.E., 2018. Loss of cone function without degeneration in a novel Gnat2 knock-out mouse. Exp. Eye Res. 171, 111–118. https://doi.org/10.1016/j.exer.2018.02.024

Saederup, N., Cardona, A.E., Croft, K., Mizutani, M., Cotleur, A.C., Tsou, C.-L., Ransohoff, R.M., Charo, I.F., 2010. Selective chemokine receptor usage by central nervous system myeloid cells in CCR2-red fluorescent protein knock-in mice. PLoS ONE 5, e13693. https://doi.org/10.1371/journal.pone.0013693

Satija, R., Farrell, J.A., Gennert, D., Schier, A.F., Regev, A., 2015. Spatial reconstruction of single-cell gene expression data. Nat. Biotechnol. 33, 495–502. https://doi.org/10.1038/nbt.3192

Schindelin, J., Arganda-Carreras, I., Frise, E., Kaynig, V., Longair, M., Pietzsch, T., Preibisch, S., Rueden, C., Saalfeld, S., Schmid, B., Tinevez, J.-Y., White, D.J., Hartenstein, V., Eliceiri, K., Tomancak, P., Cardona, A., 2012. Fiji: an open-source platform for biological-image analysis. Nat. Methods 9, 676–682. https://doi.org/10.1038/nmeth.2019

Sennlaub, F., Auvynet, C., Calippe, B., Lavalette, S., Poupel, L., Hu, S.J., Dominguez, E., Camelo, S., Levy, O., Guyon, E., Saederup, N., Charo, I.F., Rooijen, N.V., Nandrot, E., Bourges, J.-L., Behar-Cohen, F., Sahel, J.-A., Guillonneau, X., Raoul, W., Combadiere, C., 2013. CCR2(+) monocytes infiltrate atrophic lesions in age-related macular disease and mediate photoreceptor degeneration in experimental subretinal inflammation in Cx3cr1 deficient mice. EMBO Mol Med 5, 1775–1793. https://doi.org/10.1002/emmm.201302692

Shay, T., Kang, J., 2013. Immunological Genome Project and systems immunology. Trends Immunol. 34, 602–609. https://doi.org/10.1016/j.it.2013.03.004

Siegert, S., Cabuy, E., Scherf, B.G., Kohler, H., Panda, S., Le, Y.-Z., Fehling, H.J., Gaidatzis, D., Stadler, M.B., Roska, B., 2012. Transcriptional code and disease map for adult retinal cell types. Nature Neuroscience 15, 487–495. https://doi.org/10.1038/nn.3032

Ståhl, P.L., Salmén, F., Vickovic, S., Lundmark, A., Navarro, J.F., Magnusson, J., Giacomello, S., Asp, M., Westholm, J.O., Huss, M., Mollbrink, A., Linnarsson, S., Codeluppi, S., Borg, Å., Pontén, F., Costea, P.I., Sahlén, P., Mulder, J., Bergmann, O., Lundeberg, J., Frisén, J., 2016. Visualization and analysis of gene expression in tissue sections by spatial transcriptomics. Science 353, 78–82. https://doi.org/10.1126/science.aaf2403

Strell, C., Hilscher, M.M., Laxman, N., Svedlund, J., Wu, C., Yokota, C., Nilsson, M., 2019. Placing RNA in context and space – methods for spatially resolved transcriptomics. The FEBS Journal 286, 1468–1481. https://doi.org/10.1111/febs.14435

Thévenaz, P., Ruttimann, U.E., Unser, M., 1998. A pyramid approach to subpixel registration based on intensity. IEEE Trans Image Process 7, 27–41. https://doi.org/10.1109/83.650848

Wang, T., Chen, J., 2014. Induction of the unfolded protein response by constitutive G-protein signaling in rod photoreceptor cells. J. Biol. Chem. 289, 29310–29321. https://doi.org/10.1074/jbc.M114.595207

Wilden, U., Hall, S.W., Kühn, H., 1986. Phosphodiesterase activation by photoexcited rhodopsin is quenched when rhodopsin is phosphorylated and binds the intrinsic 48-kDa protein of rod outer segments. PNAS 83, 1174–1178. https://doi.org/10.1073/pnas.83.5.1174

Wilden, U., Kuehn, H., 1982. Light-dependent phosphorylation of rhodopsin: number of phosphorylation sites. Biochemistry 21, 3014–3022. https://doi.org/10.1021/bi00541a032

Wolf, S.A., Boddeke, H.W.G.M., Kettenmann, H., 2017. Microglia in Physiology and Disease. Annu. Rev. Physiol. 79, 619–643. https://doi.org/10.1146/annurev-physiol-022516-034406

Xu, J., Dodd, R.L., Makino, C.L., Simon, M.I., Baylor, D.A., Chen, J., 1997. Prolonged photoresponses in transgenic mouse rods lacking arrestin. Nature 389, 505–509. https://doi.org/10.1038/39068

Yang, J., Zhang, L., Yu, C., Yang, X.-F., Wang, H., 2014. Monocyte and macrophage differentiation: circulation inflammatory monocyte as biomarker for inflammatory diseases. Biomark Res 2, 1. https://doi.org/10.1186/2050-7771-2-1

Yu, Y.-R.A., O'Koren, E.G., Hotten, D.F., Kan, M.J., Kopin, D., Nelson, E.R., Que, L., Gunn, M.D., 2016. A Protocol for the Comprehensive Flow Cytometric Analysis of Immune Cells in Normal and Inflamed Murine Non-Lymphoid Tissues. PLoS ONE 11, e0150606. https://doi.org/10.1371/journal.pone.0150606

Zhang, P., Zam, A., Jian, Y., Wang, X., Li, Y., Lam, K.S., Burns, M.E., Sarunic, M.V., Pugh, E.N., Zawadzki, R.J., 2015. In vivo wide-field multispectral scanning laser ophthalmoscopy-optical coherence tomography mouse retinal imager: longitudinal

imaging of ganglion cells, microglia, and Müller glia, and mapping of the mouse retinal and choroidal vasculature. J Biomed Opt 20, 126005. https://doi.org/10.1117/1.JBO.20.12.126005

Ziegenhain, C., Vieth, B., Parekh, S., Reinius, B., Guillaumet-Adkins, A., Smets, M., Leonhardt, H., Heyn, H., Hellmann, I., Enard, W., 2017. Comparative Analysis of Single-Cell RNA Sequencing Methods. Mol. Cell 65, 631-643.e4. https://doi.org/10.1016/j.molcel.2017.01.023

Chapter 4

Monocyte-derived macrophages establish residence alongside bona fide microglia in the retina after degeneration

Preface

The following chapter is a manuscript that I will submit for publication following the submission of this dissertation. It has been formatted to meet the guidelines of this dissertation. The authors are Kaitryn E. Ronning, Sarah J. Karlen, and Marie E. Burns. Maire and I designed the experiments and wrote and edited the manuscript. I also performed and analyzed the *in vivo* retinal imaging, immunohistochemistry, and single-cell sequencing, and created the figures. I worked with Sarah on the design and execution of all flow cytometry and cell sorting experiments.

Abstract

Resident microglia and invading peripheral immune cells can both respond to acute injury and degeneration in the central nervous system. However, after dead and dying neurons have been cleared and homeostasis is re-established, it is unknown whether resident immune cells resume fully normal functions and to what degree the peripheral immune cells that had invaded take up residence. Previously, in a mouse model of inducible photoreceptor degeneration (*Arr1*$^{-/-}$), we found that both microglia and peripheral monocytes infiltrate the outer retina and become highly inflammatory, but the subsequent fate of these mononuclear phagocytes after degeneration has been unknown. Here, using flow cytometry, *in vivo* retinal imaging, immunohistochemistry, and single-cell mRNA sequencing, we assess changes in mononuclear phagocytes in the retina during and after the loss of photoreceptors. We find that loss of photoreceptors results in a sustained, small increase in the number of macrophages in the retina, though the population remains transcriptionally heterogeneous. Several of the subpopulations displayed gene expression patterns consistent with mildly activated phenotypes. A large subpopulation of cells was found to express markers traditionally associated with both microglial and monocytic lineages, making their etiology particularly ambiguous. Using an inducible Cre-based fluorescent lineage tracing paradigm to confirm the origins of new resident immune cells, we found approximately equal numbers of microglia and monocyte-derived macrophages in the retina well after degeneration had subsided. *In vivo* retinal imaging and immunohistochemical analysis of the migration of these populations to sites of local damage showed that both subpopulations remained functionally responsive, though the monocyte-derived cells appeared to have less migratory activity than those derived from the native resident population.

Background

Neuroinflammation has been implicated in nearly all neurodegenerative disorders. Although many of the mechanisms and details remain elusive, it is well-established that during neurodegeneration microglia can undergo dramatic transformations, including retracting their complex processes to adopt an ameboid morphology and changing their gene expression (Wolf et al., 2017). These changes are the topic of extensive investigations, with the goals of understanding these changes, determining if they may be harmful or helpful, and probing for potential therapeutic targets. Additionally, in many cases of neurodegeneration it has become clear that blood-tissue barriers can be breached, with an invasion of immune cells from the periphery joining the microglial response (Yu et al., 2020). These monocytes rapidly differentiate into microglia-like cells, which we here refer to as macrophages to distinguish these infiltrating cells from the endogenous microglia. Whether these subpopulations of microglia and macrophages consistently serve distinct functions or have different fates in the CNS is not known.

One CNS compartment commonly used to study microglia and macrophages during degeneration is the retina. Many inherited retinal degenerations as well as common forms of vision loss like age-related macular degeneration involve the loss of rod and cone photoreceptors (Karlen et al., 2020). As photoreceptors die, the remaining retina remodels, which culminates in synaptic rearrangements and, later in life, loss of other retinal neurons (Pfeiffer et al., 2020). However, between photoreceptor loss and later loss of neurons, the retina remains in a relatively stable homeostatic state. Curiously, microglia-like immune cells persist in the retina following degeneration. Whether these immune cells remain pro-inflammatory or return to a homeostatic state after the loss of photoreceptors could impact therapeutic interventions and/or late-stage retinal remodeling. Previously, we found that microglia activate and pro-inflammatory monocytic cells invade the retina in an inducible model of photoreceptor

degeneration, the *Arr1*$^{-/-}$ mouse (Karlen et al., 2018; Levine et al., 2014; Ronning et al., 2019). However, the fates of these cells after photoreceptor loss ceases were unknown.

Here, using a combination of single-cell mRNA sequencing, *in vivo* retinal imaging, and *in vitro* validations, we investigate the state of retinal immune cells after photoreceptor degeneration has waned and the retina has returned to homeostasis. Determination of the expression patterns of key genes allowed us to identify the relative activation states of subpopulations with distinct lineages and to probe the responsiveness of these subpopulations to a second retinal injury.

Methods

Animals

Mice were cared for and handled in accordance with the National Institutes of Health guidelines and under protocols approved by the UC Davis Institutional Animal Care and Use Committee. All mice were born and maintained in constant darkness before exposure to constant light (approximately 200 lux) and were approximately 3-8 months old when used for experiments. All mouse strains used for experiments were tested to confirm the absence of the *rd8* mutation. Although there are some reports of potential sex differences in microglial function (Villa et al., 2019), there were no observable sex differences in immunohistochemistry, flow cytometry, or *in vivo* imaging experiments, so both male and female mice were used for these experiments. Only female mice were used for single-cell mRNA sequencing to avoid potential confounding sex-specific differences in gene expression.

Arr1$^{-/-}$ mice (Chen et al., 1999; Xu et al., 1997) are a convenient, light-inducible model of photoreceptor degeneration. C57BL/6J mice (strain 000664), originally obtained from The Jackson Laboratory and then bred in constant dark conditions for several generations, were used as controls for some experiments. *Cx3cr1-GFP* mice (strain 005582, aka B6.129P2(Cg)-*Cx3cr1*^{tm1Litt}/J)(Jung et al., 2000) were obtained from The Jackson Laboratory and crossed with

the *Arr1*$^{-/-}$ strain to obtain *Arr1*$^{-/-}$*Cx3cr1*$^{+/GFP}$ mice. Littermate *Arr1*$^{+/+}$*Cx3cr1*$^{+/GFP}$ mice were used as controls. For lineage tracing experiments, Ai9 (strain 007909, aka B6.Cg-*Gt(ROSA)26Sor*$^{tm9(CAG\text{-}tdTomato)Hze}$/J)(Madisen et al., 2010) and *Cx3cr1-YFP-CreER* (strain 021160, aka B6.129P2(Cg)-*Cx3cr1*$^{tm2.1(cre/ERT2)Litt}$/WganJ)(Littman, 2013) mice were obtained from The Jackson Laboratory and crossed with the *Arr1*$^{-/-}$ strain to ultimately obtain *Arr1*$^{+/+\ or\ -/-}$ *Ai9*$^{KI/KI}$ *Cx3cr1*$^{+/YFP\text{-}CreER}$ mice.

In vivo retinal imaging and focal light damage

A custom-built dual scanning laser ophthalmoscopy (SLO) and optical coherence tomography (OCT) system was used to simultaneously collect structural and fluorescent information from the retina non-invasively (Zhang et al., 2015). For imaging, mice were anesthetized with 2-2.5% isoflurane and kept on a 37 °C heating pad. A micropositioner (Biptigen, Morrisville, NC) was used for rotational and translational movements of the pad to position the mouse. Pupils were dilated with tropicamide and phenylephrine (Akorn), and then hypromellose gel (GenTeal Tears Severe, Alcon) was applied to the corneal surface. This gel both prevented the cornea from drying during imaging and maintained the refractive index between the cornea and contact lens (Unicon Corporation). SLO imaging was performed with a 488nm laser, approximately 100-130 μW at the pupil, to excite GFP. Wide-field images were collected over 51° of visual angle, and increased digital sampling was used to “zoom” in on areas of interest. SLO images were processed and analyzed in FIJI (Schindelin et al., 2012), including registering images (Busse, n.d.; Thévenaz et al., 1998), averaging, and pseudo-coloring for presentation.

OCT imaging was performed with a superluminescent diode centered at 860 nm with a 132 nm bandwidth (Broadlighter T-860-HP, Superlum), at approximately 600 μW at the pupil. The FD-OCT data were processed using standard methods to transform the back-scattered light into intensity by depth information and then generate series of OCT B-scans. As in (Miller et al.,

2019) a custom Python script was used to flatten the B-scans and then register those flattened B-scans using a strip-registration algorithm to generate complete flattened OCT volumes. Focal light damage was performed by maintaining the OCT laser at a single location at full power (approximately 7-8 mW) for 2 minutes, as previously described (Miller et al., 2019).

Intraperitoneal injections

Intraperitoneal (IP) injections were used to deliver 5-ethynyl-2'-deoxyuridine (EdU) and tamoxifen for proliferation and lineage tracing experiments, respectively. For the proliferation experiments, EdU was dissolved in sterile 1x PBS at a concentration of 10 mg/mL and was delivered at a dose of 100 mg/kg (or 10 mL/kg of the EdU solution). EdU pulses were administered to both *Arr1*$^{-/-}$ and C57Bl/6J mice, approximately 2-4 months of age. In order to identify proliferating cells during degeneration, EdU pulses were delivered at 48 and 72 hours after the onset of light exposure. These are the time points that previous data (Karlen et al., 2018) indicated microglia and macrophages are mitotically active. For the lineage tracing experiments, tamoxifen was dissolved in corn oil at a concentration of 20 mg/mL. *Arr1*$^{+/+ \text{ or } -/-}$ *Ai9*$^{KI/KI}$ *Cx3cr1*$^{+/CreER\text{-}YFP}$ mice received two IP injections at a dosage of 75 mg tamoxifen/kg (or 3.67 mL/kg of the corn oil solution), separated by 1 day as previously described (O'Koren et al., 2016). These IP injections were performed when the mice were approximately 6-10 weeks of age, and dark lighting conditions were maintained during injections. Further experiments and light exposure did not proceed until at least 60 days after the tamoxifen injections to allow all the circulating monocytes to turn over, leaving only long-lived resident macrophages dual-labeled.

Immunohistochemistry

Immunohistochemistry was performed as previously described (Ronning et al., 2019). In brief, immediately after enucleation eyes were submerged in 4% paraformaldehyde at room temperature. After approximately 5 minutes of fixation, anterior segments and lenses were removed, the resulting eyecups were fixed for an additional 20-25 minutes at room temperature, and then fixed eyecups were transferred to vials of PBS at 4 °C. To remove the retinal flat

mount from the eyecup, several curvature-releasing cuts were made to the eyecup with small dissection scissors, and then small forceps were used to gently peel the retina from the rest of the eyecup. For antibody staining, retinas were incubated in 1% Triton X-100 in PBS overnight at 4 °C, blocked with normal serum for 2 hours at 37 °C, incubated in primary antibodies in PBT overnight at 4 °C, rinsed in PBT at room temperature, incubated in secondary antibodies for 1.5-2 hours at 37 °C, rinsed in PBT again at room temperature, and then mounted on glass slides using ProLong Diamond Antifade Mountant (Invitrogen). For proliferation (EdU) experiments retinal flat mounts were permeabilized in 1% Triton X-100 for 45 minutes at room temperature, followed by using the Click-iT EdU Alexafluor 488 Imaging Assay (C10337, Invitrogen) to label EdU according to manufacturer instructions. Next retinal flatmounts were blocked with normal serum and then incubated with pre-conjugated antibodies, both for approximately 2 hours at 37 °C. Finally, these flatmounts were rinsed and mounted as above. See Table 4.1 for a full list of antibodies and labeling reagents used for immunohistochemistry. All retinal flatmounts were imaged using a Nikon A1 confocal microscope. ImageJ (Schindelin et al., 2012) was used to create the pseudocolored overlay images shown in Figures 4.4A and 4.5B. Single channel images were first segmented, then overlayed, and then cells were pseudocolored orange if dual-positive or green if single-positive.

Flow cytometry and fluorescence activated cell sorting

Retina, choroid, and blood samples were prepared similarly to a previously described protocol (Karlen et al., 2018). Briefly, approximately 5 minutes before euthanasia mice received a tail vein injection of anti-mouse CD45 antibody conjugated to either PE or APC, to differentiate cells within the vasculature from those in the retinal parenchyma (O'Koren et al., 2019). Mice were then euthanized, enucleated, and then retinas isolated. Isolated retinas were placed in 1-2 mL each of digestion buffer, consisting of Hibernate medium (HBSS; 10-547F, Lonza) supplemented with 5% fetal bovine serum (FBS), 10 mM HEPES, 0.7 mg/mL calcium chloride, 1/5 mg/mL collagenase A (Roche), and 0.1 mg/mL DNase I (Roche). Tissue was incubated at

37 °C for 15-20 minutes, with mild tricheration for all samples ultimately used for single-cell sequencing, or gently disrupted with a MACS Octo Dissociator (Miltenyi Biotec) for all samples used for flow cytometry. After digestion, the cell suspension was filtered through a 70 mm cell strainer (Genesee Scientific), and resuspended in PBS. Cells were then stained for viability (Zombie NIR Fixable Viability Kit, 423106, BioLegend), blocked for 5 minutes with Fc block 1 uL/sample (eBioscience) supplemented with 5% each normal rat and mouse sera, and then incubated with antibodies diluted in Brilliant Stain Buffer (BD Biosciences) for 15-30 minutes at room temperature. Table 4.1 includes a complete list of the antibodies and cells stains used for these experiments. After staining, cell suspensions were washed in 0.5% bovine serum albumin (BSA) with 1:50 EDTA, and ultimately resuspended in either the same buffer for cell sorting experiments or Cell Staining Buffer (BioLegend) for flow cytometry experiments. Additionally, flow cytometry samples were then fixed by adding 0.5% paraformaldehyde to the final cell suspensions. Control beads were prepared using the AbC Total Antibody Compensation Bead Kit (Invitrogen) and ArC Amine Reactive Compensation Bead Kit (Invitrogen) following manufacturer guidelines.

All flow cytometry and cell sorting was performed at the UCD Flow Cytometry Shared Resource Laboratory. For the time course flow cytometry experiment, samples were run on an LSR-II Cytometer (Becton Dickinson). For quantifying cells after lineage tracing, samples were run on a Cytoflex Cytometer (Beckman Coulter). Cell sorting prior to single-cell mRNA sequencing was performed on an Astrios EQ Cell Sorter (Beckman Coulter).

Single-cell sequencing

Single-cell mRNA sequencing was performed as previously described (Ronning et al., 2019). Briefly, retinal samples were enriched for immune cells by FAC-sorting single, alive, CD45+CD11b+ cells, as described above. Cells were sorted into a solution of Dulbecco's Modified Eagle Medium (DMEM; Thermo Fischer) supplemented with 10% FBS, and then immediately used to create the expression libraries. These libraries were generated using the

10X Genomics system (Chromium) at the UC Davis DNA Technologies and Expression Core, following manufacturer recommendations. The resulting cDNA libraries were sequencing on a NovaSeq (Illumina), again following manufacturer recommendations.

After sequencing, initial processing including barcode processing, transcript alignment, and generation of gene-barcode matrices was performed using Cell Ranger (Chromium) at the UC Davis Bioinformatics Core. All further processing and analysis was performed in R, primarily using the Seurat R package (Butler et al., 2018). Following the recommended Seurat workflow, cells were filtered for quality control, and then normalized for UMI and mitochondrial counts. After principal components analysis (PCA), we performed tSNE dimensional reduction and used marker gene expression to identify general cell types. Despite the FAC sorting, there was a small amount of contamination of non-immune cells including photoreceptors. These cells were excluded, and then PCA, tSNE reduction, and clustering were performed on the remaining myeloid cells. Differentially expressed genes were identified using the FindMarkers function in Seurat. The cross-correlational analysis function in Seurat was used to combine this dataset with the previously published data from (Ronning et al., 2019). Gene enrichment analysis was performed using the Gene Ontology Panther tool (Mi et al., 2019).

Results

Ramified macrophages re-tile the retina after photoreceptor degeneration

During photoreceptor degeneration, microglia adopt an ameboid morphology and migrate to the outer nuclear layer (Silverman and Wong, 2018; Yu et al., 2020). In some cases, an influx of monocytes from the periphery and proliferation of both the resident microglia and invading monocyte-derived macrophages contribute to a dramatic increase in the number of macrophages in the degenerating retina (Karlen et al., 2020, 2018). To understand how this immune response resolves, we began by tracking Cx3CR1+ cells in the retina over time, *in vivo*. *Arr1*$^{-/-}$*Cx3cr1*$^{+/GFP}$ and control *Arr1*$^{+/+}$*Cx3cr1*$^{+/GFP}$ mice were exposed to light, and then

periodically imaged using scanning laser ophthalmoscopy to track the distribution and morphology of GFP^+ cells, and optical coherence tomography to follow the concurrent degeneration (Figure 4.1A). As previously reported (Karlen et al., 2018), we observed a dramatic increase in the number of GFP^+ cells in *Arr1*$^{-/-}$ retinas during the first few days of photoreceptor loss, and those cells were mostly ameboid in morphology (Karlen et al., 2018; Ronning et al., 2019).

Once photoreceptor loss was complete, as indicated by the disappearance of the outer nuclear layer in OCT, the density of GFP^+ cells decreased and the morphology of many of the cells became noticeably more complex and ramified (Figure 4.1A). To visualize the cell morphology at higher resolution, we amplified the GFP signal using immunohistochemistry and performed confocal imaging (Figure 4.1B, green). In retinal flatmounts, the GFP^+ cells were ramified with complex secondary and tertiary processes in both WT and KO retinas. This is in stark contrast with the ameboid shape that these cells adopt during photoreceptor cell loss (for example, see (Ronning et al., 2019)). However, the cells in the KO retinas also had noticeable differences from the normal, WT, microglia mosaic, including more variable degrees of morphological complexity. Additionally, some cells expressed MHC II proteins (Figure 4.1B, orange), which are expressed in monocyte-derived macrophages and sometimes activated microglia.

Previously, we found that subpopulations of both microglia and monocyte-derived macrophages proliferate during the first few days of photoreceptor degeneration (Ronning et al., 2019). To determine if dividing cells contribute to the retinal macrophage population after degeneration is complete, we pulsed C57 and *Arr1*$^{-/-}$ mice with EdU at days 2 and 3 of light exposure, when macrophage proliferation has been previously detected in the *Arr1*$^{-/-}$ model. Subsequently, on day 20 eyes were collected and flat mounted retinas were stained for CD11b and EdU and visualized on a confocal microscope. Many EdU^+ $CD11b^+$ cells were observed in all layers of degenerated *Arr1*$^{-/-}$ retinas, and only rarely observed in control (C57) retinas (Figure

4.1C). Cell counting from the histological images revealed approximately 45% of the $CD11b^+$ cells were also EdU^+ in the 20 day retinas (Figure 4.1D).

Sustained increase in retinal immune cells after degeneration

Even at 20 days, SLO imaging revealed qualitatively more GFP+ cells in the retina compared to healthy controls (Figure 4.1A). To further quantify myeloid cells before, during, and after photoreceptor loss we used flow cytometry. We began by using general myeloid cell gating, identifying alive, single, $CD11b^+$, $CD45^+$ cells, and then further divided these cells by their degree of CD45 expression (see Figure 4.2A for gating). Cells with relatively low CD45 expression initially increased in number, peaking at approximately 4 days of light exposure, and then gradually returned to baseline numbers (Figure 4.2B). Low CD45 expression is often a feature of tissue-resident macrophages, and so we further gated these cells using a standard microglia paradigm including $Cx3cr1^+$ and $Ly6C^{low}$ and $MHCII^{low}$ expression. These microglia followed the same temporal pattern as the larger $CD45^{low}$ gate, initially increasing and then returning to baseline cell numbers (Figure 4.2C). Myeloid cells with higher CD45 expression also increased in number during the first few days of degeneration and then later decreased but did not quite return to baseline (Figure 4.2D). Because high CD45 expression is typically a feature of peripherally-derived cells, we further differentiated these $CD45^{high}$ cells by their relative Ly6C expression, which is typically high in newly born monocytes. Cells that were $Ly6C^{high}$ increased in number early in degeneration, peaked during the very first days of light exposure, and then decreased to baseline numbers within approximately one week (Figure 4.2E, orange). In contrast, the $Ly6C^{low}$ population peaked a few days later than the $Ly6C^{high}$, and never returned to baseline cell numbers (Figure 4.2E, blue). These results suggest that the persistent increase in Cx3CR1+ cells that we observed after degeneration had waned (Figure 4.1A) was in part due to continued residence of infiltrated monocyte-derived macrophages. Thus, unlike the largely homogenous retinal macrophage population in healthy retinas, we

hypothesized that the retinal immune cell population remains heterogeneous long after the loss of photoreceptors.

Persistent transcriptional heterogeneity of retinal macrophages after loss of photoreceptors

To investigate the degree of heterogeneity of the new resident population, we performed single-cell sequencing on FACS-enriched retinal immune cells before, immediately following, and well past photoreceptor loss in *Arr1*$^{-/-}$ retinas (0, 7, and 20 days respectively). At all three time points, retinal CD45^{+} cells showed significant transcriptional similarities (Figure 4.3A), suggesting that by 1 week many cells had returned to a "resting" state similar to microglia in a healthy retina. To further probe for heterogeneity, we identified transcriptionally distinct clusters of cells (Figure 4.3B), and then evaluated expression of known marker genes (see Figure 4.3C for examples) to determine the putative identities of these clusters. This analysis identified several distinct subpopulations, including resting microglia, mildly activated microglia, and a small number of inflammatory macrophages (Figure 4.3B). Interestingly, the 7 and 20 day samples also contained another cluster, Cluster #3, of hybrid-like cells expressing some genes traditionally associated with microglia, such as *Hexb* and *Ctsd*, as well as some genes traditionally associated with a monocytic lineage, such as *CD74* and *H2-Aa* (Figure 4.3C).

When we probed the expression of common pro- and anti-inflammatory related genes, the only cluster with significant expression of either was the cluster containing a very small number of inflammatory macrophages. All other clusters lacked strong expression of both pro- and anti-inflammatory markers. This suggests that, although Clusters #2 and #3 are distinct from the traditionally "resting" microglia, these macrophages are not strongly activated. This is especially apparent when examining canonical resting microglia markers, such as *Hexb*, and activated microglial markers, such as *Lyz2* and *Sepp1*, in the mildly activated microglia cluster, Cluster #2 (Figure 4.3C). Although the expression is not quite the same as the resting microglia cluster, the differences were small in magnitude.

We next combined this dataset with a previously published dataset which included control and strongly activated macrophages at an earlier timepoint during active degeneration in this model (Ronning et al., 2019). A tSNE plot was used to graphically compare the similarities between clusters identified in these two experiments (Figure 4.3D). The control (0 days) resting microglia clusters from these two datasets largely overlapped. Especially notable in this plot is that Cluster #3 is located between the monocytic cells from the earlier timepoints, and the activated microglia from both datasets. This is in agreement with the seeming intermediate microglial and monocytic gene expression.

Monocyte-derived macrophages take up residence alongside resident microglia

Given the expression of both microglial and monocyte-derived macrophage genes in the hybrid-like cells of Cluster #3, we hypothesized that many monocyte-derived cells were adopting a microglia-like phenotype and remaining in the retina long-term. To test this hypothesis, we used an inducible fate-mapping paradigm to track the lineages of retinal immune cells after degeneration. In this lineage tracing paradigm, all *Cx3cr1*-expressing myeloid cells, including microglia and monocyte-derived cells, express YFP and a tamoxifen-inducible Cre (a Cre-ERT2 fusion protein, referred to here as CreER). Upon tamoxifen administration, Cre-mediated recombination of the Ai9 reporter results in tdTomato expression in all *Cx3cr1*-expressing cells. Then, 60+ days after tamoxifen, by which time the CreER again inactivates and all the monocytes have turned over, long-lived resident macrophages, including bona fide microglia, are YFP+ and tdTomato+, whereas the newly born cells form a monocytic lineage are only YFP+ (O'Koren et al., 2016).

We first examined retinas for dual- and single- labeled macrophages in retinas from both control and *Arr1*$^{-/-}$ retinas after 20 days of light exposure, i.e. without and after photoreceptor loss (Figure 4.4A). In healthy retinas (WT, *Arr1*$^{+/+}$*Ai9*$^{KI/KI}$ *Cx3cr1*$^{+/YFP\text{-}CreER}$ post-tamoxifen), the retinal microglia were dual-labeled, as expected. In contrast, in the degenerated retinas (KO, *Arr1*$^{-/-}$*Ai9*$^{KI/KI}$ *Cx3cr1*$^{+/YFP\text{-}CreER}$ post-tamoxifen), both single- and dual-labeled cells appeared in

the macrophage mosaic, demonstrating that monocyte-derived cells do take up residence in the retina after degeneration has resolved. These monocyte-derived macrophages had ramified morphologies, supporting the idea that these monocyte-derived cells have adopted a microglia-like phenotype (Figure 4.4A).

To quantify the relative numbers of both resident ($CD45^+YFP^+tdTomato^+$) and monocyte-derived macrophages ($CD45^+YFP^+tdTomato^-$), we performed flow cytometry before and after photoreceptor loss (for gating, see Figure 4.4B). We found that in the healthy retina, the long-lived residents ($YFP^+tdTomato^+$) were by far the dominant myeloid type, and there were negligible peripherally-derived ($YFP^+tdTomato^-$) cells. However, these peripherally derived cells were the dominant myeloid cell immediately following photoreceptor loss (Figure 4.4C, 7 day timepoint). By 20 days of light exposure, the populations of resident and peripherally derived macrophages were equivalent in size (Figure 4.4C, 20 day timepoint).

Probing the activation potential of macrophages to further retinal injury

Because we found that retinal $CD45^+$ cells are heterogeneous after degeneration, and that many have mildly activated transcriptional profiles, we next tested the ability of these "new resident" immune cells to respond to further retinal injury. We performed a focal laser injury in *Arr1*$^{-/-}$*Cx3CR1*$^{+/gfp}$ mice after photoreceptor degeneration was complete (over 20 days following light onset), and then examined retinal structure and GFP+ immune cells using OCT and SLO, respectively. Similar to the normal microglial response to local laser damage (Miller et al., 2019), the GFP+ cells in the degenerated retina migrated to and clustered at the site of damage within a few days. This cluster of cells then gradually disappeared and the GFP+ cells again spatially tiled the retina over a period of over a week (Figure 4.5A). These results demonstrate that the population of macrophages that remain in the retina after degeneration can respond to further insult.

To determine whether these responding macrophages consist of resident microglia, monocyte-derived macrophages, or both, we performed focal light damage in the fate-mapping

mice (Arr*1*$^{-/-}$*Ai9*$^{KI/KI}$ *Cx3cr1*$^{+/YFP\text{-}CreER}$) after photoreceptor loss was complete. Retinas were harvested for histology at multiple timepoints following the focal damage, and we analyzed the tissue for monocytic (YFP$^+$tdTomato$^-$) and microglial (YFP$^+$tdTomato$^+$) macrophages surrounding and at the location of the focal injury. Both microglia (YFP$^+$tdTomato$^+$) and monocyte-derived macrophages (YFP$^+$tdTomato$^-$) were visible in the tight cluster of cells that formed directly at the injury locus, but the number of monocyte-derived macrophages were far fewer (Figure 4.5B). Notably, in some instances there were monocyte-derived cells (YFP$^+$tdTomato$^-$) near the locus that did not appear to migrate as readily the neighboring microglia (YFP$^+$tdTomato$^+$) (for example, see Figure 4.5B, the day 4 timepoint). Considering that the flow cytometry had revealed that monocyte-derived macrophages comprise approximately half of the retinal macrophages at the timepoint focal damage was performed, the fact that the majority of macrophages at the damage location were microglial in origin suggests that the monocyte-derived cells residing in the retina are less responsive to further insults.

The potential difference in responsiveness between microglial and monocytic cells prompted us to look for differentially expressed gene programs between the mildly activated microglia and putative monocyte-derived macrophages in the single-cell dataset. We identified the top 35 most highly differentially expressed genes in the monocytic cells compared to the microglia and performed a gene enrichment analysis. We additionally performed a gene enrichment analysis on the top 400 most highly expressed genes in the monocytic cluster, which yielded similar results. The most enriched gene programs included macrophage activation, regulation of cell migration, antigen processing and presentation, and response to interferon-gamma. These enriched gene sets align with a monocyte-derived macrophage phenotype. However, these gene sets do not suggest that these monocyte-derived macrophages lack the ability to respond to tissue insults.

Discussion

Here we find that even well after photoreceptor degeneration is complete the retinal immune mosaic remains heterogeneous. Although some microglia do return to a resting transcriptional state, most continue to have a mildly activated phenotype even long after cell loss has subsided. Additionally, monocyte-derived macrophages take up long-lived residence alongside the microglia, adopting a microglia-like phenotype and comprising approximately half of the immune cell mosaic. Our results also suggest that these “new residents” are not as responsive to subsequent retinal insults as those that were native microglial cells.

Dramatic increase in CD45+ cells in the retina following degeneration

The large increase in myeloid cells during the initial stages of photoreceptor degeneration in the *Arr1*$^{-/-}$ mouse (Karlen et al., 2018) is the result of both infiltration of monocytes from the periphery and proliferation of microglia and monocyte-derived macrophages within the retina (Karlen et al., 2020). Although the persistent increase in retinal myeloid cells following degeneration is relatively small compared to this large increase in cells earlier during photoreceptor loss, the overall increase in the density of these immune cells is significant. Rod photoreceptors are by far the most numerous cell type in the healthy retina (Jeon et al., 1998), and so the loss of these cells results in a dramatic decrease in the volume of and total number cells in the retina. Thus, even a relatively small increase in total immune cells results in a considerable increase in the number of immune cells per total retinal neurons or retinal volume.

Monocyte-derived cells remain in the retina following degeneration

In lineage tracing experiments, here we find that of the retinal immune cells following degeneration roughly half are bona fide microglia and half are monocyte-derived. These monocyte-derived macrophages adopt a microglia-like morphology and gene expression, and spatially intermingle with the endogenous microglia (Figure 4.4). Because we find that the monocyte-derived macrophages express higher levels of MHC II genes than the microglia, the

MCH II+ cells observed in Figure 4.1B likely correspond to the monocytic cells, although MHC II expression alone is not sufficient to determine the lineage of a given cell. Additionally, our flow cytometry data here in combination with previous work suggest that these monocyte-derived macrophages arise from monocytes that invaded the retina during the first few days of degeneration, rather than resulting from continued invasion of monocytes throughout the entire course of degeneration. In particular, newly born monocytes express high levels of Ly6C, which then decreases over the cell's lifetime, especially if the monocyte differentiates into a monocyte-derived macrophage (Shi and Pamer, 2011). Thus, the lack of $CD45^{+}$ $Ly6C^{low}$ cells after the first few days of degeneration and the persistence of $CD45^{+}Ly6C^{high}$ cells (Figure 4.2E and (Karlen et al., 2018)) suggest that monocyte invasion is limited to the first few days of light exposure in the *Arr1*$^{-/-}$ model.

Monocyte-derived, or other non-microglial macrophages have been observed to similarly adopt microglia-like phenotypes and remain in the retina in the absence of continuing or active neuronal loss in previous work. However, those instances have been situations in which there is a physical damage (Paschalis et al., 2018), disruption to blood-tissue barriers (Ma et al., 2017), or even in an otherwise healthy retina but following pharmacological intervention to ablate the resident microglia (Huang et al., 2018a). Monocytic cells have been detected in other photoreceptor degenerative disorders, including widespread light damage (O'Koren et al., 2016) and age-related macular degeneration (Sennlaub et al., 2013), although it has not yet been investigated if monocytes permanently engraft into the retina in these instances. Thus, this study is important because to our knowledge this is the first demonstration of monocyte-derived macrophages taking up long-lived residence in the retina following cell autonomous degeneration. Additionally, the consistent time course of the inducible loss of neurons makes the *Arr1*$^{-/-}$ model ideal for probing these "new resident" monocytic cells in future studies.

In the *Arr1*$^{-/-}$ experiments presented here, monocyte-derived macrophages adopted a microglia-like phenotype over the course of days, consistent with evidence from other studies

that the retinal environment promotes a microglia-like phenotype for any mononuclear phagocyte. For example, after pharmaceutical ablation of retinal microglia, non-microglial immune cells from the invade and adopt morphologies and gene expression reminiscent of microglia (Huang et al., 2018a; McPherson et al., 2019; Paschalis et al., 2018). Because non-microglial repopulation following ablation has not observed in the brain thus far (Huang et al., 2018b), it remains unclear to what extent the CNS in general promotes a microglia-like phenotype for mononuclear phagocytes or if this phenomenon is specific to the microenvironment of the retina. Unexpectedly, many of the most highly-expressed genes in the putative monocyte-derived macrophage cluster in our single-cell dataset have recently been identified as key genes expressed by various macrophage subsets in peripheral CNS tissues, such as the meninges and choroid plexus (Van Hove et al., 2019). However, to what extent these conserved gene expression programs are indicative of shared functions, similar environments, or similar cell lineages remains unknown.

Heterogeneous resolution of neuroinflammation across models of acute degeneration

In the field of retinal degeneration, activation and resolution of the immune response has been investigated in a model of RPE injury that causes photoreceptor loss (Ma et al., 2017) and following a corneal alkali chemical burn that leads to retinal ganglion cell death (Paschalis et al., 2018). In both models, expression of genes associated with immune activation are detected well after cell loss ceases, suggesting that at least some of the retinal immune cells do not return to rest (Ma et al., 2017; Paschalis et al., 2018). Because neither study utilized single-cell transcriptomics the degree of heterogeneity in those post-degeneration immune populations remains unclear. The resolution of the immune response to neuronal loss has been investigated at a single-cell level in a model of facial nerve axotomy (Tay et al., 2018, 2017). Although this model does not result in as widespread of neuronal loss as the retinal *Arr1*$^{-/-}$ model, the loss of neurons does drive the activation and proliferation of nearby microglia, and then this immune response resolves approximately 30+ days after injury. In this case, single-cell sequencing

revealed that although the majority of microglia return to a resting phenotype, a small number of microglia continue to express many activation-related genes like the retinal degeneration models described above, and similar to the mildly activated microglia phenotype we observe in the single-cell dataset described here (Figure 4.3).

Curiously, this mildly activated phenotype observed in all the above models has similarities to changes observed in microglia during aging. In the aging retina, microglia accumulate in the subretinal space, increase in number, and increase their expression of activation- and inflammation-related genes (Chen et al., 2019; Ma and Wong, 2016). Curiously, aged microglia typically are not as responsive to injury as young microglia (Ma and Wong, 2016), yet here we find that microglia are still capable of robustly responding to focal injury even after all photoreceptors are lost (Figure 4.5B). The similarities of microglia in neurodegenerative disorders and those in aging are noticeable and could have implications for further immune challenges or therapeutic interventions with age, especially after potential repeated challenges throughout life.

Future directions: functional implications of the altered retinal immune state

We find that photoreceptor degeneration causes long-lasting changes to the retinal immune environment, lasting well past when neuronal loss has completed. Although we find that these retinal macrophages can still respond to further retinal insult, the retinal immune environment does not entirely return to rest, and the microglial and monocytic cells may respond differently to further injuries and insults. Differences in the response of microglial and monocytic macrophages may be dependent on the precise molecular signaling from surrounding stressed and damaged or dying retinal cells. Determining the precise molecular signals and pathways involved will be the focus of future studies. Overall, understanding the long-term and functional implications of the altered immune state following degeneration will require further investigations. Of particular interest will be investigating if this altered immune state contributes

to late-stage retinal remodeling, and if these immune cells affect therapeutic interventions such as gene therapies and cell transplants.

Table 4.1: Antibodies and labels used for immunohistochemistry and flow cytometry. IHC = immunohistochemistry; FC = flow cytometry.

Reagent	Manufacturer	Catalog Number	RRID	Application	Dilution
Goat anti-GFP antibody	Rockland	600-101-215	AB_218182	IHC	1:200
Alexa Fluor 647 anti-CD11b antibody	Biolegend	101218	AB_389327	IHC	1:300
Alexa Fluor 594 anti-I-A/I-E (MHCII) antibody	Biolegend	107650	AB_2566438	IHC	1:200
Rabbit anti-RFP antibody	Rockland	600-401-379	AB_2209751	IHC	1:750
Click-iT EdU kit for imaging, Alexa Fluor 488	Invitrogen	C10337	None	IHC	NA
Zombie NIR Viability Dye	Biolegend	423105	None	FC	1:500
APC anti-CD45 antibody	Biolegend	103112	AB_312977	FC	1:100
PE anti-CD45 antibody	Biolegend	103106	AB_312971	FC	1:100
BV605 anti-CD11b antibody	Biolegend	101257	AB_2565431	FC	1:100
BV711 anti-I-A/I-E (MHC II) antibody	Biolegend	107643	AB_2565976	FC	1:100
Alexa Fluor 488 anti-Ly6C antibody	Biolegend	128022	AB_10639728	FC	1:100
BV421 anti-CX3CR1 antibody	Biolegend	149023	AB_2565706	FC	1:100

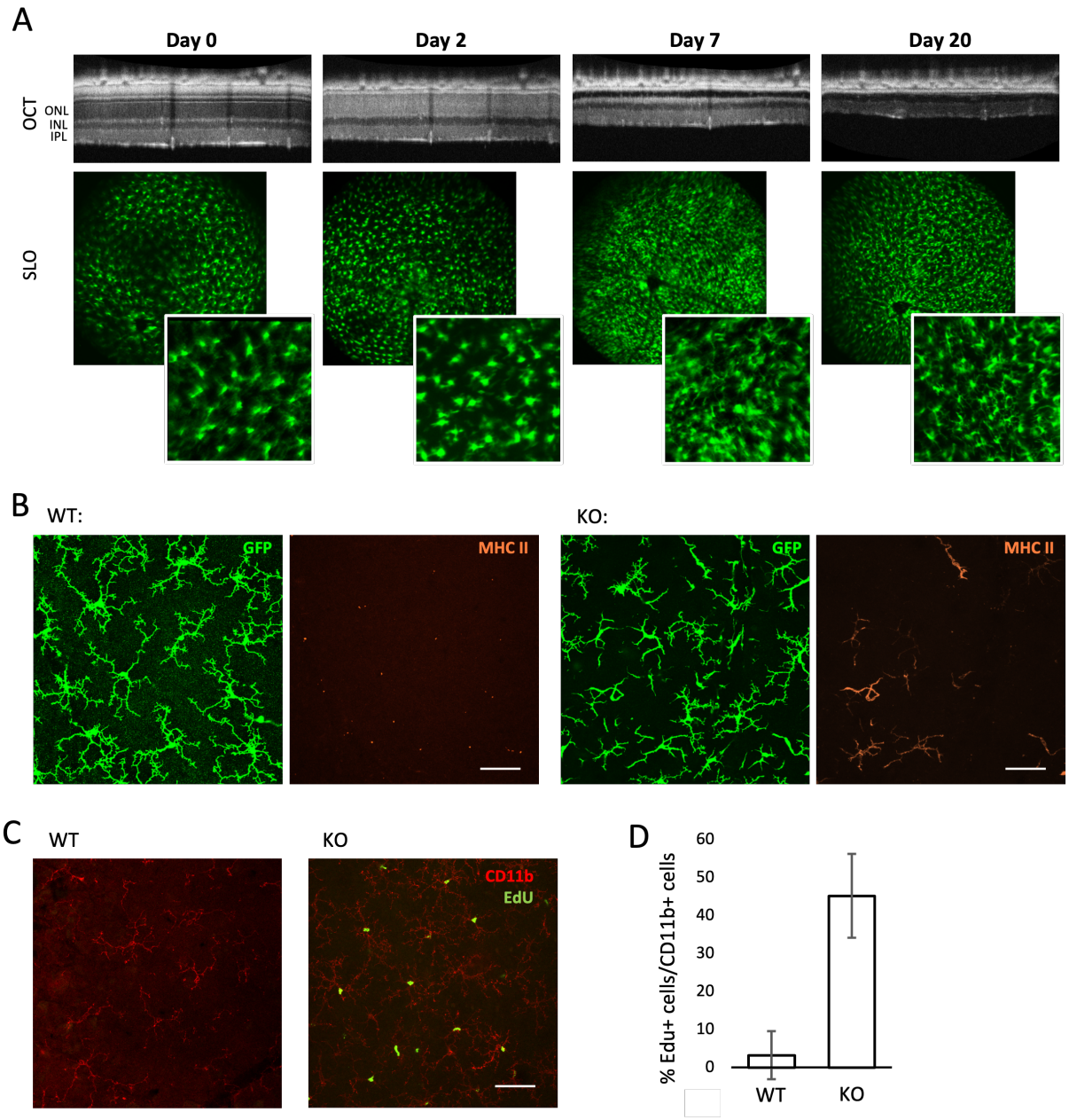

Figure 4.1. Ramified macrophages re-tile the retina after widespread photoreceptor degeneration. (A) Representative *in vivo* retinal imaging to track retinal thinning (OCT) and macrophages (SLO) in an *Arr1*$^{-/-}$*Cx3cr1*$^{+/GFP}$ mouse. (B) Maximum intensity projections through ~10 µm the inner plexiform layer of *Arr1*$^{+/+}$*Cx3cr1*$^{+/GFP}$ (WT) and *Arr1*$^{-/-}$*Cx3cr1*$^{+/GFP}$ (KO) retinas after 20 days of light exposure. Retinal flatmounts were labeled for GFP (green) and MHC II (orange). (C) Maximum intensity projections through the inner plexiform of C57Bl/6J (WT) and

Arr1$^{-/-}$ (KO) after 20 days of light exposure, pulsed with EdU at 2 and 3 days of light exposure. Macrophages are labeled with CD11b (red) and EdU^{+} nuclei are indicated in green. (D) Quantification of (C), showing the percentage of EdU^{+} CD11b^{+} cells out of all CD11b^{+} cells in the inner plexiform layers of KO and WT retinas, pulsed with EdU and 2 and 3 days, probed at 20 days of light exposure. Percentages displayed as mean +/- standard deviation. ONL = outer nuclear layer; INL = inner nuclear layer; IPL = inner plexiform layer. Scale bars indicate 50 μm.

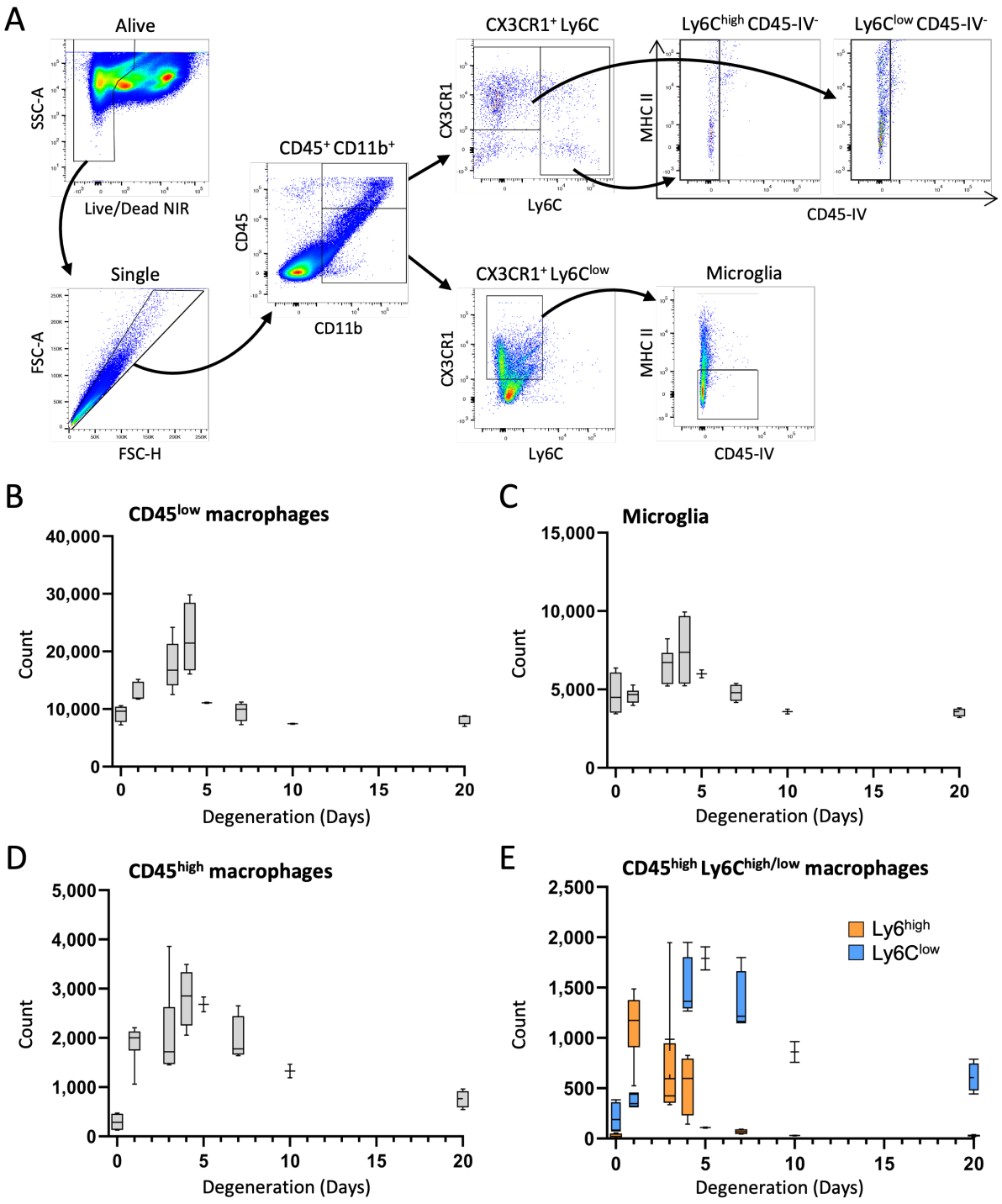

Figure 4.2. Persistent increase in CD45^{high} macrophages after degeneration. (A) Flow cytometry gating strategy. (B) Quantification of CD45^{low} macrophages, which transiently increase in number during degeneration and then return to baseline. (C) Quantification of

$CD45^{low}$ $CD11b^{+}$ $Cx3cr1^{+}$ $Ly6C^{low}$ microglia. Microglia also transiently increase in number during degeneration and then return to baseline. (D) Quantification of $CD45^{high}$ macrophages, which transiently increase in number and then decrease, but not to baseline numbers. (E) Quantification of $CD45^{high}$ $Ly6C^{high\ \&\ low}$ CD45-IV^{-} cells. $CD45^{high}$ $Ly6C^{high}$ cells increased rapidly following light onset, and then returned to baseline numbers by day 5. In contrast, $CD45^{high}$ $Ly6C^{low}$ cells increased in number more slowly, and then did not return to baseline. CD45-IV (intravenous anti-CD45 antibody) was used to exclude immune cells circulating in the retinal vasculature at tissue collection.

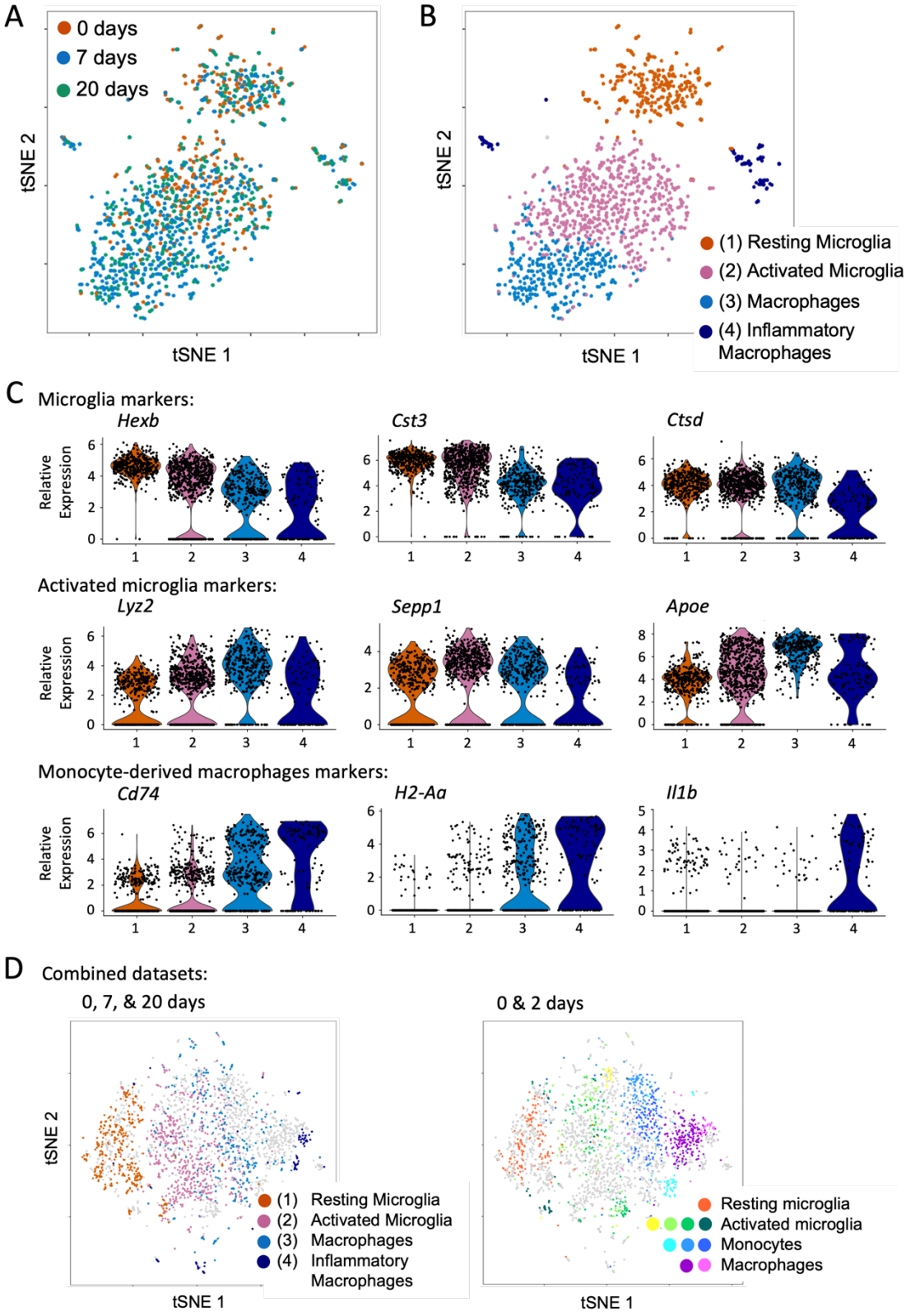
A
0 days
7 days
20 days
tSNE 2
tSNE 1
B
tSNE 2
tSNE 1
(1) Resting Microglia
(2) Activated Microglia
(3) Macrophages
(4) Inflammatory Macrophages
C
Microglia markers:
Hexb
Cst3
Ctsd
Relative Expression
Activated microglia markers:
Lyz2
Sepp1
Apoe
Monocyte-derived macrophages markers:
Cd74
H2-Aa
Il1b
D
Combined datasets:
0, 7, & 20 days
0 & 2 days
tSNE 2
tSNE 1
(1) Resting Microglia
(2) Activated Microglia
(3) Macrophages
(4) Inflammatory Macrophages
Resting microglia
Activated microglia
Monocytes
Macrophages

Figure 4.3. Single-cell mRNA sequencing reveals distinct populations of resident immune cells after degeneration. (A) tSNE plot with cells color-coded by time point. (B) tSNE plot with cells color-coded by cluster. (C) Representative gene expression of genes commonly associated microglia, activated microglia, and a monocytic lineage. (D) tSNE plot from this dataset combined with a previously published dataset of retinal macrophages before and relatively early during photoreceptor loss (Ronning et al., 2019). On the left cells are color-coded by cluster identity in (B), with grey indicating cells from the other dataset. On the right, cells from this new dataset are indicated in grey, while cells from the previous dataset are color-coded according to clusters identified in (Ronning et al., 2019). For simplicity, the cluster naming has been collapsed across general cell types.

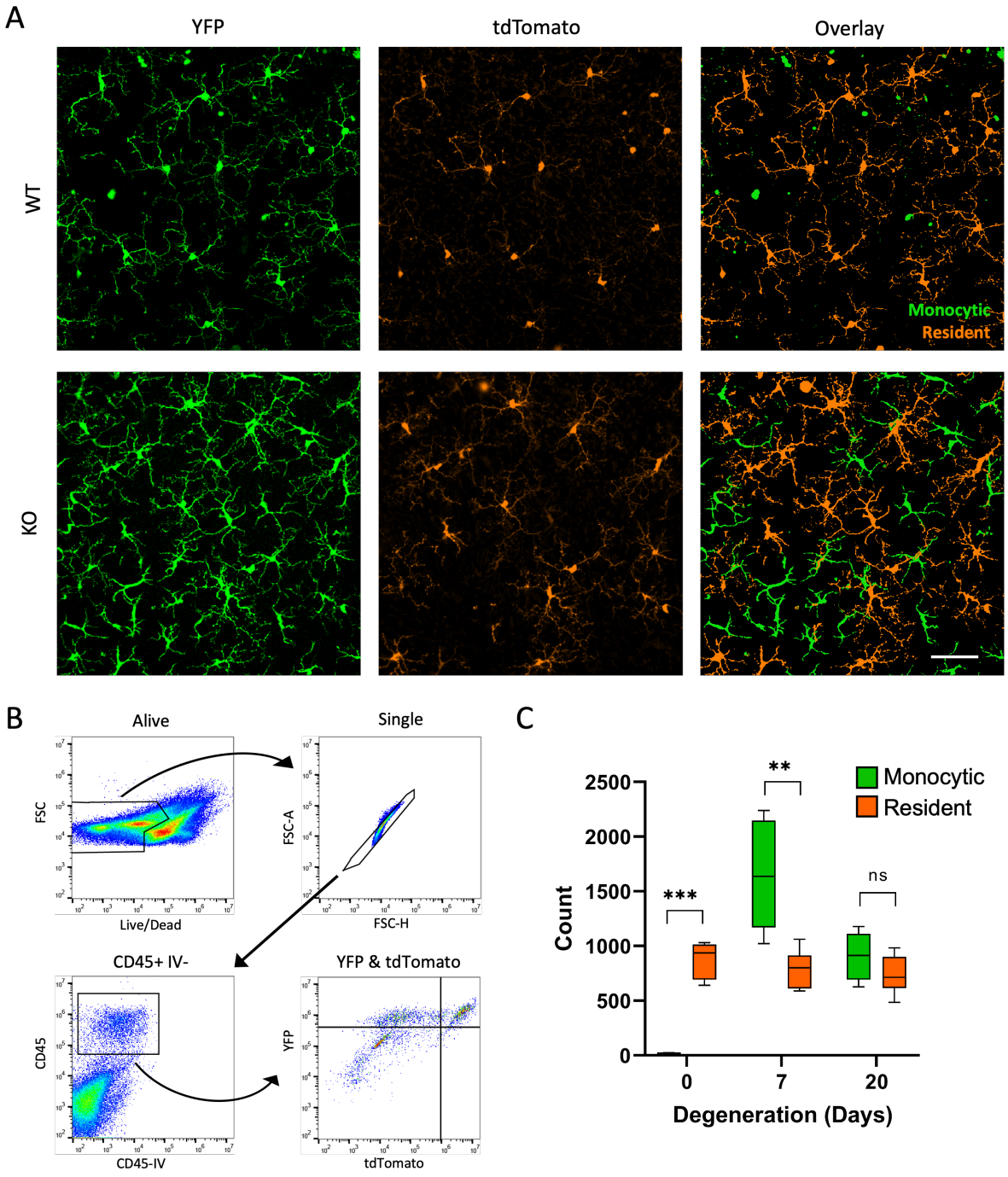

Figure 4.4. Monocyte-derived macrophages join resident microglia in the resident immune mosaic following acute photoreceptor degeneration. (A) Maximum intensity projections through the inner plexiform layers of WT and *Arr1*$^{-/-}$ (KO) retinas, after 20 days of light exposure, utilizing an inducible fluorescent lineage tracing paradigm (*Arr1*$^{+/+ \text{ or } -/-}$ *Ai9*$^{KI/KI}$

Cx3cr1$^{+/YFP\text{-}CreER}$ post-tamoxifen). Resident macrophages express both YFP and tdTomato, whereas monocyte-derived macrophages express only YFP. In overlay images, YFP^{+}tdTomato^{+} (resident) cells have been pseudocolored orange, and YFP^{+}tdTomato^{-} (monocytic) cells have been pseudocolored green. Scale bars indicate 50 μm. (B) Gating for flow cytometry to quantify resident and peripherally derived macrophages. An intravenous CD45 antibody (CD45-IV) was used to exclude immune cells in the vasculature that may have been captured during tissue dissection. (C) Quantification of resident (YFP^{+}tdTomato^{+}) and peripherally-derived (YFP^{+}tdTomato^{-}) macrophages using flow cytometry before, immediately after, and longer after photoreceptor loss.

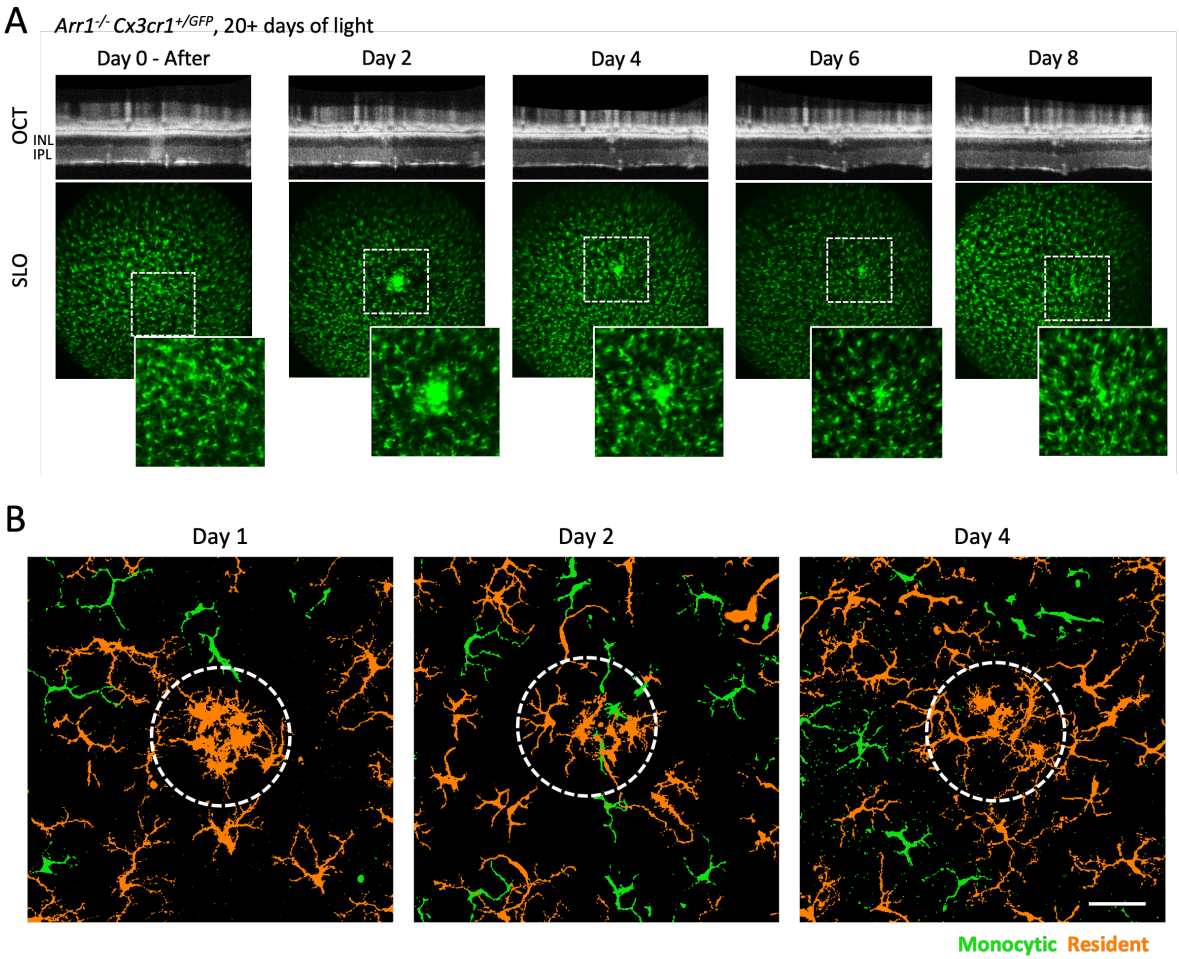

Figure 4.5. Retinal macrophages can respond to secondary, focal damage following widespread retinal degeneration. (A) Representative *in vivo* time course of an *Arr1*$^{-/-}$ *Cx3cr1*$^{+/GFP}$ retina after focal laser damage. Retinal macrophages (green, GFP^{+}) transiently respond to a focal laser damage administered over 20 days after onset of light exposure. Days indicate days post-laser injury. Top row: focal damage indicated by increased scattering in OCT. Bottom row: GFP^{+} macrophages initially migrate towards and then away from the focal damage locus. Inset locations indicated by dashed squared. (B) Representative histological images 1, 2, and 4 days following laser injury in *Arr1*$^{-/-}$ *Ai9*$^{KI/KI}$ *Cx3cr1*$^{+/YFP\text{-}CreER}$ post-tamoxifen mice. Images are pseudocolored-overlay images, as in Figure 4A, where CNS residents (predominantly microglia) are displayed in orange and peripherally-derived macrophages are indicated in green.

Dashed circles indicate approximate location of the focal damage locus, and scale bar indicates 50 μm. INL = inner nuclear layer; IPL = inner plexiform layer.

References

Busse, B., n.d. MultiStackReg.

Butler, A., Hoffman, P., Smibert, P., Papalexi, E., Satija, R., 2018. Integrating single-cell transcriptomic data across different conditions, technologies, and species. Nat. Biotechnol. 36, 411–420. https://doi.org/10.1038/nbt.4096

Chen, J., Simon, M.I., Matthes, M.T., Yasumura, D., LaVail, M.M., 1999. Increased susceptibility to light damage in an arrestin knockout mouse model of Oguchi disease (stationary night blindness). Invest. Ophthalmol. Vis. Sci. 40, 2978–2982.

Chen, M., Luo, C., Zhao, J., Devarajan, G., Xu, H., 2019. Immune regulation in the aging retina. Progress in Retinal and Eye Research 69, 159–172. https://doi.org/10.1016/j.preteyeres.2018.10.003

Huang, Y., Xu, Z., Xiong, S., Qin, G., Sun, F., Yang, J., Yuan, T.-F., Zhao, L., Wang, K., Liang, Y.-X., Fu, L., Wu, T., So, K.-F., Rao, Y., Peng, B., 2018a. Dual extra-retinal origins of microglia in the model of retinal microglia repopulation. Cell Discov 4, 9. https://doi.org/10.1038/s41421-018-0011-8

Huang, Y., Xu, Z., Xiong, S., Sun, F., Qin, G., Hu, G., Wang, J., Zhao, L., Liang, Y.-X., Wu, T., Lu, Z., Humayun, M.S., So, K.-F., Pan, Y., Li, N., Yuan, T.-F., Rao, Y., Peng, B., 2018b. Repopulated microglia are solely derived from the proliferation of residual microglia after acute depletion. Nature Neuroscience 21, 530–540. https://doi.org/10.1038/s41593-018-0090-8

Jeon, C.-J., Strettoi, E., Masland, R.H., 1998. The Major Cell Populations of the Mouse Retina. J. Neurosci. 18, 8936–8946. https://doi.org/10.1523/JNEUROSCI.18-21-08936.1998

Jung, S., Aliberti, J., Graemmel, P., Sunshine, M.J., Kreutzberg, G.W., Sher, A., Littman, D.R., 2000. Analysis of Fractalkine Receptor CX3CR1 Function by Targeted Deletion and Green Fluorescent Protein Reporter Gene Insertion. Molecular and Cellular Biology 20, 4106–4114. https://doi.org/10.1128/MCB.20.11.4106-4114.2000

Karlen, S.J., Miller, E.B., Burns, M.E., 2020. Microglia Activation and Inflammation During the Death of Mammalian Photoreceptors. Annu Rev Vis Sci 6, 149–169. https://doi.org/10.1146/annurev-vision-121219-081730

Karlen, S.J., Miller, E.B., Wang, X., Levine, E.S., Zawadzki, R.J., Burns, M.E., 2018. Monocyte infiltration rather than microglia proliferation dominates the early immune response to rapid photoreceptor degeneration. Journal of Neuroinflammation 15, 344. https://doi.org/10.1186/s12974-018-1365-4

Levine, E.S., Zam, A., Zhang, P., Pechko, A., Wang, X., FitzGerald, P., Pugh, E.N., Zawadzki, R.J., Burns, M.E., 2014. Rapid light-induced activation of retinal microglia in mice lacking Arrestin-1. Vision Res. 102, 71–79. https://doi.org/10.1016/j.visres.2014.07.011

Littman, D.R., 2013. An inducible cre recombinase driven by Cx3cr1. Mouse Genome Informatics J:190965.

Ma, W., Wong, W.T., 2016. Aging Changes in Retinal Microglia and their Relevance to Age-related Retinal Disease. Adv Exp Med Biol 854, 73–78. https://doi.org/10.1007/978-3-319-17121-0_11

Ma, W., Zhang, Y., Gao, C., Fariss, R.N., Tam, J., Wong, W.T., 2017. Monocyte infiltration and proliferation reestablish myeloid cell homeostasis in the mouse retina following retinal pigment epithelial cell injury. Sci Rep 7, 8433. https://doi.org/10.1038/s41598-017-08702-7

Madisen, L., Zwingman, T.A., Sunkin, S.M., Oh, S.W., Zariwala, H.A., Gu, H., Ng, L.L., Palmiter, R.D., Hawrylycz, M.J., Jones, A.R., Lein, E.S., Zeng, H., 2010. A robust and high-throughput Cre reporting and characterization system for the whole mouse brain. Nat. Neurosci. 13, 133–140. https://doi.org/10.1038/nn.2467

McPherson, S.W., Heuss, N.D., Lehmann, U., Roehrich, H., Abedin, Md., Gregerson, D.S., 2019. The retinal environment induces microglia-like properties in recruited myeloid cells. Journal of Neuroinflammation 16, 151. https://doi.org/10.1186/s12974-019-1546-9

Mi, H., Muruganujan, A., Ebert, D., Huang, X., Thomas, P.D., 2019. PANTHER version 14: more genomes, a new PANTHER GO-slim and improvements in enrichment analysis tools. Nucleic Acids Research 47, D419–D426. https://doi.org/10.1093/nar/gky1038

Miller, E.B., Zhang, P., Ching, K., Pugh, E.N., Burns, M.E., 2019. In vivo imaging reveals transient microglia recruitment and functional recovery of photoreceptor signaling after injury. Proc. Natl. Acad. Sci. U.S.A. 116, 16603–16612. https://doi.org/10.1073/pnas.1903336116

O'Koren, E.G., Mathew, R., Saban, D.R., 2016. Fate mapping reveals that microglia and recruited monocyte-derived macrophages are definitively distinguishable by phenotype in the retina. Sci Rep 6, 20636. https://doi.org/10.1038/srep20636

O'Koren, E.G., Yu, C., Klingeborn, M., Wong, A.Y.W., Prigge, C.L., Mathew, R., Kalnitsky, J., Msallam, R.A., Silvin, A., Kay, J.N., Bowes Rickman, C., Arshavsky, V.Y., Ginhoux, F., Merad, M., Saban, D.R., 2019. Microglial Function Is Distinct in Different Anatomical Locations during Retinal Homeostasis and Degeneration. Immunity 50, 723-737.e7. https://doi.org/10.1016/j.immuni.2019.02.007

Paschalis, E.I., Lei, F., Zhou, C., Kapoulea, V., Dana, R., Chodosh, J., Vavvas, D.G., Dohlman, C.H., 2018. Permanent neuroglial remodeling of the retina following infiltration of CSF1R inhibition-resistant peripheral monocytes. PNAS 115, E11359–E11368. https://doi.org/10.1073/pnas.1807123115

Pfeiffer, R.L., Marc, R.E., Jones, B.W., 2020. Persistent remodeling and neurodegeneration in late-stage retinal degeneration. Prog Retin Eye Res 74, 100771. https://doi.org/10.1016/j.preteyeres.2019.07.004

Ronning, K.E., Karlen, S.J., Miller, E.B., Burns, M.E., 2019. Molecular profiling of resident and infiltrating mononuclear phagocytes during rapid adult retinal degeneration using single-cell RNA sequencing. Scientific Reports 9, 4858. https://doi.org/10.1038/s41598-019-41141-0

Schindelin, J., Arganda-Carreras, I., Frise, E., Kaynig, V., Longair, M., Pietzsch, T., Preibisch, S., Rueden, C., Saalfeld, S., Schmid, B., Tinevez, J.-Y., White, D.J., Hartenstein, V., Eliceiri, K., Tomancak, P., Cardona, A., 2012. Fiji: an open-source platform for biological-image analysis. Nat. Methods 9, 676–682. https://doi.org/10.1038/nmeth.2019

Sennlaub, F., Auvynet, C., Calippe, B., Lavalette, S., Poupel, L., Hu, S.J., Dominguez, E., Camelo, S., Levy, O., Guyon, E., Saederup, N., Charo, I.F., Rooijen, N.V., Nandrot, E., Bourges, J.-L., Behar-Cohen, F., Sahel, J.-A., Guillonneau, X., Raoul, W., Combadiere, C., 2013. CCR2(+) monocytes infiltrate atrophic lesions in age-related macular disease and mediate photoreceptor degeneration in experimental subretinal inflammation in Cx3cr1 deficient mice. EMBO Mol Med 5, 1775–1793. https://doi.org/10.1002/emmm.201302692

Shi, C., Pamer, E.G., 2011. Monocyte recruitment during infection and inflammation. Nat Rev Immunol 11, 762–774. https://doi.org/10.1038/nri3070

Silverman, S.M., Wong, W.T., 2018. Microglia in the Retina: Roles in Development, Maturity, and Disease. Annu Rev Vis Sci 4, 45–77. https://doi.org/10.1146/annurev-vision-091517-034425

Tay, T.L., Mai, D., Dautzenberg, J., Fernández-Klett, F., Lin, G., Sagar, Datta, M., Drougard, A., Stempfl, T., Ardura-Fabregat, A., Staszewski, O., Margineanu, A., Sporbert, A., Steinmetz, L.M., Pospisilik, J.A., Jung, S., Priller, J., Grün, D., Ronneberger, O., Prinz, M., 2017. A new fate mapping system reveals context-dependent random or clonal expansion of microglia. Nature Neuroscience 20, 793–803. https://doi.org/10.1038/nn.4547

Tay, T.L., Sagar, null, Dautzenberg, J., Grün, D., Prinz, M., 2018. Unique microglia recovery population revealed by single-cell RNAseq following neurodegeneration. Acta Neuropathol Commun 6, 87. https://doi.org/10.1186/s40478-018-0584-3

Thévenaz, P., Ruttimann, U.E., Unser, M., 1998. A pyramid approach to subpixel registration based on intensity. IEEE Trans Image Process 7, 27–41. https://doi.org/10.1109/83.650848

Van Hove, H., Martens, L., Scheyltjens, I., De Vlaminck, K., Pombo Antunes, A.R., De Prijck, S., Vandamme, N., De Schepper, S., Van Isterdael, G., Scott, C.L., Aerts, J., Berx, G., Boeckxstaens, G.E., Vandenbroucke, R.E., Vereecke, L., Moechars, D., Guilliams, M., Van Ginderachter, J.A., Saeys, Y., Movahedi, K., 2019. A single-cell atlas of mouse brain macrophages reveals unique transcriptional identities shaped by ontogeny and tissue environment. Nat Neurosci 22, 1021–1035. https://doi.org/10.1038/s41593-019-0393-4

Villa, A., Della Torre, S., Maggi, A., 2019. Sexual differentiation of microglia. Frontiers in Neuroendocrinology 52, 156–164. https://doi.org/10.1016/j.yfrne.2018.11.003

Wolf, S.A., Boddeke, H.W.G.M., Kettenmann, H., 2017. Microglia in Physiology and Disease. Annu. Rev. Physiol. 79, 619–643. https://doi.org/10.1146/annurev-physiol-022516-034406

Xu, J., Dodd, R.L., Makino, C.L., Simon, M.I., Baylor, D.A., Chen, J., 1997. Prolonged photoresponses in transgenic mouse rods lacking arrestin. Nature 389, 505–509. https://doi.org/10.1038/39068

Yu, C., Roubeix, C., Sennlaub, F., Saban, D.R., 2020. Microglia versus Monocytes: Distinct Roles in Degenerative Diseases of the Retina. Trends in Neurosciences 43, 433–449. https://doi.org/10.1016/j.tins.2020.03.012

Zhang, P., Zam, A., Jian, Y., Wang, X., Li, Y., Lam, K.S., Burns, M.E., Sarunic, M.V., Pugh, E.N., Zawadzki, R.J., 2015. In vivo wide-field multispectral scanning laser ophthalmoscopy-optical coherence tomography mouse retinal imager: longitudinal imaging of ganglion cells, microglia, and Müller glia, and mapping of the mouse retinal and choroidal vasculature. J Biomed Opt 20, 126005. https://doi.org/10.1117/1.JBO.20.12.126005

Chapter 5

Concluding Remarks

In this dissertation, I investigated retinal microglia during health, first in a novel model of achromatopsia without photoreceptor loss (Chapter 2), and then both microglia and monocyte-derived cells during and after disease in a model of rapid, light-induced photoreceptor degeneration (Chapters 3 and 4). Throughout I used a variety of tools, including the newly created *Cx3cr1-Dendra2* mouse (Appendix), to examine the morphology, localization, gene expression, and key marker protein expression of these mononuclear phagocytes in the retina.

One key finding throughout this dissertation is the degree of heterogeneity amongst retinal immune cells during and after degeneration. The healthy retina contains a largely homogenous population of microglia (O'Koren et al., 2019). In contrast, I found that during and after photoreceptor loss there is heterogeneity within the retinal microglia, and the immune response is further complicated by a significant number of monocytic responders (Ronning et al., 2019). There have only been a few studies profiling changes in immune cell gene expression during retinal disease at the single-cell level (O'Koren et al., 2019; Ronning et al., 2019; Wieghofer et al., 2021), a gap this dissertation has in part helped to fill. Still, heterogeneous microglial activation has been observed in these studies, as well as in other models of neurodegeneration (Keren-Shaul et al., 2017; Tay et al., 2018), and many similar changes in gene expression are observed across them all. These similarities spanning central nervous system (CNS) compartments and types of neurodegeneration suggest that there is a core program of genes expressed following microglial activation, regardless of tissue or type of disease. However, the precise molecular signals or pathways that initiate this program of gene expression remain elusive and will undoubtedly be the focus of future studies.

Another key finding in this dissertation is the dramatic and prolonged response of monocytic cells. In the model of light-induced photoreceptor degeneration used in these studies,

the *Arr1*$^{-/-}$ mouse line, monocytes rapidly infiltrate the retina after the onset of light exposure (Karlen et al., 2018; Ronning et al., 2019). Monocyte invasion has also been observed in other retinal degenerative disorders, although the degree of monocytic response may vary depending on the precise type of neurodegeneration (Ma et al., 2017; O'Koren et al., 2019; Paschalis et al., 2018; Sennlaub et al., 2013). Given how robust the monocytic response is, the *Arr1*$^{-/-}$ model is ideal for studying monocytes in the retina.

In Chapter 4, I found that some monocyte-derived macrophages remain in the retina even after photoreceptor degeneration has ceased. Monocyte-derived cells have also recently been found to remain in the retina for prolonged periods after corneal and RPE injuries (Ma et al., 2017; Paschalis et al., 2018). However, to my knowledge this dissertation is the first report of monocyte-derived macrophages remaining in the retina following cell autonomous degeneration rather than direct damage that disrupts multiple cell types. Additionally, I found that these monocyte-derived cells adopt a microglia-like phenotype, including changes in gene expression and morphology. The state of a given macrophage can be strongly influenced by its surrounding microenvironment (Amit et al., 2016; Gosselin et al., 2014). However, identifying the degree to which the phenotype of monocyte-derived macrophages in the retina is determined by local environmental cues, ontogeny of the cells, and/or functions of these cells will require further study. Finally, it will also be critical to examine if the presence of these monocyte-derived cells impacts the efficacy of therapeutic interventions, such as gene therapies and cell transplants.

Future studies continuing from the work in this dissertation include investigating how the microglial response to neurodegeneration might change in the absence of monocytes. There are several ways that the number of invading monocytes can be reduced, often by inhibiting or blocking CCL2-CCR2 signaling (Chen et al., 2012; Karlen et al., 2018; Mildner et al., 2007). Depending on the type of degeneration, decreasing monocyte invasion has been observed as having helpful or harmful impacts on the course of neuronal loss (Guo et al., 2012; London et

al., 2011). In the *Arr1*$^{-/-}$ model used in this dissertation, decreasing monocyte invasion did not affect the overall course of photoreceptor loss, although this is likely due to the photoreceptor-specific mutation that leads to cell autonomous photoreceptor death in this model (Karlen et al., 2018). Regardless of the model, it is not yet known how microglial activation might be affected by the absence of monocytes. For example, I found that monocytic cells expressed the most pro-inflammatory genes relatively early during photoreceptor loss (Ronning et al., 2019). It is unknown if microglia would adopt a stronger pro-inflammatory phenotype in the absence of monocytes, or if instead the immune response would simply be less pro-inflammatory at that point during degeneration.

Along these lines, there remains ongoing debate regarding if microglial activation and monocyte invasion are helpful or harmful. In some models of degeneration mononuclear phagocytes have been implicated in exacerbating disease, whereas in other instances microglia have been identified as neuroprotective (Colonna and Butovsky, 2017; Karlen et al., 2020; Yu et al., 2020). Ultimately, whether macrophages contribute to or alleviate neuronal loss is likely dependent on the type and extent of degeneration, the rate of disease progression, the location of the immune cells, and potential underlying genetic mutations. With our newly improved understanding of the immune environment during and after neurodegeneration, a major focus of future studies will undoubtedly be identifying targets to modulate this immune environment to mitigate or prevent retinal degeneration and vision loss.

References

Amit, I., Winter, D.R., Jung, S., 2016. The role of the local environment and epigenetics in shaping macrophage identity and their effect on tissue homeostasis. Nat Immunol 17, 18–25. https://doi.org/10.1038/ni.3325

Chen, M., Zhao, J., Luo, C., Pandi, S.P.S., Penalva, R.G., Fitzgerald, D.C., Xu, H., 2012. Para-inflammation-mediated retinal recruitment of bone marrow-derived myeloid cells following whole-body irradiation is CCL2 dependent. Glia 60, 833–842. https://doi.org/10.1002/glia.22315

Colonna, M., Butovsky, O., 2017. Microglia Function in the Central Nervous System During Health and Neurodegeneration. Annu Rev Immunol 35, 441–468. https://doi.org/10.1146/annurev-immunol-051116-052358

Gosselin, D., Link, V.M., Romanoski, C.E., Fonseca, G.J., Eichenfield, D.Z., Spann, N.J., Stender, J.D., Chun, H.B., Garner, H., Geissmann, F., Glass, C.K., 2014. Environment drives selection and function of enhancers controlling tissue-specific macrophage identities. Cell 159, 1327–1340. https://doi.org/10.1016/j.cell.2014.11.023

Guo, C., Otani, A., Oishi, A., Kojima, H., Makiyama, Y., Nakagawa, S., Yoshimura, N., 2012. Knockout of ccr2 alleviates photoreceptor cell death in a model of retinitis pigmentosa. Exp Eye Res 104, 39–47. https://doi.org/10.1016/j.exer.2012.08.013

Karlen, S.J., Miller, E.B., Burns, M.E., 2020. Microglia Activation and Inflammation During the Death of Mammalian Photoreceptors. Annu Rev Vis Sci 6, 149–169. https://doi.org/10.1146/annurev-vision-121219-081730

Karlen, S.J., Miller, E.B., Wang, X., Levine, E.S., Zawadzki, R.J., Burns, M.E., 2018. Monocyte infiltration rather than microglia proliferation dominates the early immune response to rapid photoreceptor degeneration. Journal of Neuroinflammation 15, 344. https://doi.org/10.1186/s12974-018-1365-4

Keren-Shaul, H., Spinrad, A., Weiner, A., Matcovitch-Natan, O., Dvir-Szternfeld, R., Ulland, T.K., David, E., Baruch, K., Lara-Astaiso, D., Toth, B., Itzkovitz, S., Colonna, M., Schwartz, M., Amit, I., 2017. A Unique Microglia Type Associated with Restricting Development of Alzheimer's Disease. Cell 169, 1276-1290.e17. https://doi.org/10.1016/j.cell.2017.05.018

London, A., Itskovich, E., Benhar, I., Kalchenko, V., Mack, M., Jung, S., Schwartz, M., 2011. Neuroprotection and progenitor cell renewal in the injured adult murine retina requires healing monocyte-derived macrophages. J Exp Med 208, 23–39. https://doi.org/10.1084/jem.20101202

Ma, W., Zhang, Y., Gao, C., Fariss, R.N., Tam, J., Wong, W.T., 2017. Monocyte infiltration and proliferation reestablish myeloid cell homeostasis in the mouse retina following retinal pigment epithelial cell injury. Sci Rep 7, 8433. https://doi.org/10.1038/s41598-017-08702-7

Mildner, A., Schmidt, H., Nitsche, M., Merkler, D., Hanisch, U.-K., Mack, M., Heikenwalder, M., Brück, W., Priller, J., Prinz, M., 2007. Microglia in the adult brain arise from Ly-6ChiCCR2+ monocytes only under defined host conditions. Nat Neurosci 10, 1544–1553. https://doi.org/10.1038/nn2015

O'Koren, E.G., Yu, C., Klingeborn, M., Wong, A.Y.W., Prigge, C.L., Mathew, R., Kalnitsky, J., Msallam, R.A., Silvin, A., Kay, J.N., Bowes Rickman, C., Arshavsky, V.Y., Ginhoux, F., Merad, M., Saban, D.R., 2019. Microglial Function Is Distinct in Different Anatomical Locations during Retinal Homeostasis and Degeneration. Immunity 50, 723-737.e7. https://doi.org/10.1016/j.immuni.2019.02.007

Paschalis, E.I., Lei, F., Zhou, C., Kapoulea, V., Dana, R., Chodosh, J., Vavvas, D.G., Dohlman, C.H., 2018. Permanent neuroglial remodeling of the retina following infiltration of CSF1R

inhibition-resistant peripheral monocytes. PNAS 115, E11359–E11368. https://doi.org/10.1073/pnas.1807123115
Ronning, K.E., Karlen, S.J., Miller, E.B., Burns, M.E., 2019. Molecular profiling of resident and infiltrating mononuclear phagocytes during rapid adult retinal degeneration using single-cell RNA sequencing. Scientific Reports 9, 4858. https://doi.org/10.1038/s41598-019-41141-0
Sennlaub, F., Auvynet, C., Calippe, B., Lavalette, S., Poupel, L., Hu, S.J., Dominguez, E., Camelo, S., Levy, O., Guyon, E., Saederup, N., Charo, I.F., Rooijen, N.V., Nandrot, E., Bourges, J.-L., Behar-Cohen, F., Sahel, J.-A., Guillonneau, X., Raoul, W., Combadiere, C., 2013. CCR2(+) monocytes infiltrate atrophic lesions in age-related macular disease and mediate photoreceptor degeneration in experimental subretinal inflammation in Cx3cr1 deficient mice. EMBO Mol Med 5, 1775–1793. https://doi.org/10.1002/emmm.201302692
Tay, T.L., Sagar, null, Dautzenberg, J., Grün, D., Prinz, M., 2018. Unique microglia recovery population revealed by single-cell RNAseq following neurodegeneration. Acta Neuropathol Commun 6, 87. https://doi.org/10.1186/s40478-018-0584-3
Wieghofer, P., Hagemeyer, N., Sankowski, R., Schlecht, A., Staszewski, O., Amann, L., Gruber, M., Koch, J., Hausmann, A., Zhang, P., Boneva, S., Masuda, T., Hilgendorf, I., Goldmann, T., Böttcher, C., Priller, J., Rossi, F.M., Lange, C., Prinz, M., 2021. Mapping the origin and fate of myeloid cells in distinct compartments of the eye by single-cell profiling. EMBO J 40, e105123. https://doi.org/10.15252/embj.2020105123
Yu, C., Roubeix, C., Sennlaub, F., Saban, D.R., 2020. Microglia versus Monocytes: Distinct Roles in Degenerative Diseases of the Retina. Trends in Neurosciences 43, 433–449. https://doi.org/10.1016/j.tins.2020.03.012

Appendix

Tracking distinct microglia subpopulations with photoconvertible Dendra2 *in vivo*

Preface

The following appendix was submitted to *Journal of Neuroinflammation* as a manuscript titled “Tracking distinct microglia subpopulations with photoconvertible Dendra2 *in vivo*” and was accepted on September 28, 2021. The accepted version of this manuscript has been reformatted to meet the guidelines of this dissertation. The authors of the manuscript were Eric B. Miller and Sarah J. Karlen (co-first authors), Kaitryn E. Ronning, and Marie E. Burns. I performed the *ex vivo* imaging and immunohistochemistry and edited the manuscript. Additionally, I performed the *in vivo* imaging Figures A.2 and A.4 with Sarah J. Karlen and Eric B. Miller, respectively, and performed the *in vivo* photoconversions used for flow cytometry quantification in Figure A.3.

Abstract

The ability to track individual immune cells within the central nervous system has revolutionized our understanding of the roles that microglia and monocytes play in synaptic maintenance, plasticity, and neurodegenerative diseases. However, distinguishing between similar subpopulations of mobile immune cells over time during episodes of neuronal death and tissue remodeling has proven to be challenging. We recombineered a photoconvertible fluorescent protein (Dendra2; D2) downstream of the Cx3cr1 promoter commonly used to drive expression of fluorescent markers in microglia and monocytes. Like the popular *Cx3cr1–GFP* line (*Cx3cr1*$^{+/GFP}$), naïve microglia in *Cx3cr1–Dendra2* mice (*Cx3cr1*$^{+/D2}$) fluoresce green and can be noninvasively imaged in vivo throughout the CNS. In addition, individual D2-expressing cells can be photoconverted, resulting in red fluorescence, and tracked unambiguously within a field of green non-photoconverted cells for several days in vivo. Dendra2-expressing retinal microglia were noninvasively photoconverted in both ex vivo and in vivo conditions. Local in vivo D2 photoconversion was sufficiently robust to quantify cell subpopulations by flow cytometry, and the protein was stable enough to survive tissue processing for immunohistochemistry. Simultaneous in vivo fluorescence imaging of Dendra2 and light scattering measurements (Optical Coherence Tomography, OCT) were used to assess responses of individual microglial cells to localized neuronal damage and to identify the infiltration of monocytes from the vasculature in response to large scale neurodegeneration. The ability to noninvasively and unambiguously track D2-expressing microglia and monocytes in vivo through space and time makes the *Cx3cr1–Dendra2* mouse model a powerful new tool for disentangling the roles of distinct immune cell subpopulations in neuroinflammation.

Background

Microglia are the long-lived, yolk-sac derived resident immune cells of the central nervous system (CNS) that prune developing circuits, maintain healthy synaptic contacts in

adulthood, and phagocytose debris and pathogens (Silverman and Wong, 2018; Wolf et al., 2017; Yu et al., 2020). Recent work suggests the existence of microglial subpopulations, which may have important consequences for their baseline function and their response to disease (Hammond et al., 2019; O'Koren et al., 2019; Ronning et al., 2019; Wieghofer et al., 2021). In addition, damage or disease can cause the recruitment of bone-marrow derived monocytes across the blood–retinal barrier, and these monocytes can assume morphologies and expression patterns that are similar to the native microglia yet have distinct cellular functions or susceptibilities to subsequent insults (Fletcher, 2020; Karlen et al., 2018; Sennlaub et al., 2013; Yu et al., 2020; Zhang and Wong, 2021). Work in the last 5 years has sought to identify specific molecular markers for subpopulations of microglia, monocytes, and monocyte-derived macrophages, though such markers may be highly dependent on the cells' activation states and surrounding environments, making their use across models and CNS niches difficult (Eme-Scolan and Dando, 2020; Rashid et al., 2019).

Dendra2 (D2) is a monomeric, photoconvertible fluorescent protein originally cloned from the soft coral *Dendronephthya* sp. (Chudakov et al., 2007a; Gurskaya et al., 2006; Labas et al., 2002) with a similar overall structure to that of GFP (Adam et al., 2009). Like GFP, the unconverted form of D2 has a peak excitation at 490 nm and a peak emission at 507 nm; however, in D2, short wavelength light induces a structural photoconversion that shifts the spectral properties to longer wavelengths, with a peak excitation of 553 nm and a peak emission of 573 nm (Chudakov et al., 2007b; Gurskaya et al., 2006). Unlike many other photoswitchable proteins, the conversion from green (gD2) to red (rD2) is permanent, with the red signal only decaying due to protein turnover (Chudakov et al., 2007a). Thus, D2 fluorescence acts as a stable, long-lived marker that allows cells to be noninvasively tagged and tracked over space and time.

While D2 has been incorporated into several plant models (Griffiths et al., 2016) and used in cell culture work (Hasle et al., 2020), its utilization in living animals has been limited.

Examples of in vivo applications include neutrophil trafficking during inflammation in zebrafish (Yoo and Huttenlocher, 2011), quantifying protein turnover rates in vivo in *C. elegans* (Pigazzini and Kirstein, 2020), imaging vascular endothelial cell mitochondria in the mouse brain (Rutkai et al., 2020), and tagging leukocytes to track lymph node-homing in mice using fluorescence activated cell sorting (FACS) (Martens et al., 2020). The diversity of D2 applications across animal systems underscores the utility of this small, photoconvertible protein for cell identification and discrimination using current fluorescent imaging technology.

To help track individual microglia and monocyte-derived cells over space and time, we developed a mouse line expressing D2 under the Cx3cr1 promoter, the expression of which is commonly used for myeloid lineage tracing both ex vivo and in vivo (Jung et al., 2000; Yona et al., 2013). In vivo high-resolution retinal imaging of Cx3cr1-driven GFP expression allows individual microglia to be visualized at single cell resolution, but unambiguously following specific microglia over days has not been possible owing to the highly mobile nature of the cells, even in healthy tissue. Here we show that photoconversion of Cx3cr1-driven D2 expression can be used to label specific subpopulations of microglia and monocytes over several days in ex vivo and in vivo retinal imaging applications and flow cytometry assays, allowing us to track and quantify the cellular behavior of these subpopulations across the retina over time.

Methods

Animals

All animal procedures were performed in accordance with the University of California, Davis and Biocytogen's Institutional Animal Care and Use Committees and all relevant guidelines and regulations. *Cx3cr1–GFP* (*Cx3cr1*$^{GFP/GFP}$) mice were obtained from Jackson Labs (strain #005582), crossed to *C57Bl/6 J* mice (Jackson Labs strain #000664), and genotyped to ensure they did not contain either the rd8 or rd1 mutations. *Cx3cr1–Dendra2* mice (*Cx3cr1*$^{D2/D2}$) were generated as described below. Both strains were housed under 12/12 h diurnal cyclic light,

with food and water available ad libitum. *Arr1*$^{-/-}$ *Cx3cr1*$^{+/D2}$ mice were created by crossing *Arr1*$^{-/-}$ mice (Chen et al., 1999; Xu et al., 1997) with *Cx3cr1*$^{D2/D2}$ mice. Mice with the Arrestin-1 background were born and maintained in constant darkness before exposure to uniform white light of 200 lx, which initiated retinal degeneration. Both male and female adult animals were used in these studies.

Generation of the Cx3cr1-Dendra2 mutant mouse

Dendra2 knock-in mice were generated by Biocytogen, Inc. using CRISPR/Cas9 methodology. In brief, to generate the gene targeting vector, single guide RNAs were designed to target two sites of exon 2 of the *Cx3cr1* gene. For each targeting site, candidate sgRNAs were designed by the CRISPR design tool (http://crispr.mit.edu) and screened for on-target activity using UCA™ (Universal CRISPR Activity Assay), a sgRNA activity detection system developed by Biocytogen that is simpler and more sensitive than MSDase assay. The Cas9 mRNA and sgRNAs were transcribed by T7 RNA polymerase by PCR amplification, gel purified, and used as the template for in vitro transcription using the MEGAshortscript T7 kit (Life Technologies) according to the kit protocol. The Cas9 mRNA and sgRNAs were purified using the MEGAclear kit and eluted with RNase-free water. To minimize random integrations, a circular donor vector was employed. The gene targeting vector containing Dendra2–SV40-pA and 2 homology arms of left (1500 bp) and right (1500 bp) each was used as a template to repair the DSBs generated by Cas9/sgRNA. The region coding first 130 amino acids was replaced by Dendra2–SV40-pA.

C57BL/6 N female mice and KM mouse strains were used as embryo donors and pseudopregnant foster mothers, respectively. Super-ovulated female C57BL/6 N mice (3–4 weeks) were mated to C57BL/6 N stud males, and fertilized embryos were collected from the ampullae of the dams. Optimized concentrations of Cas9 mRNA, sgRNAs, and donor vector were mixed and co-injected into the cytoplasm of one-cell stage fertilized eggs. After injection, surviving zygotes were transferred into oviducts of KM albino pseudopregnant females.

Genomic DNA extracted from tails of the offspring was digested with AseI or ScaI (NEB), separated on a 1% agarose gel, and transferred to a positively charged nylon membrane (Hybond N +; Amersham International plc) for Southern Blot analysis. The blot was hybridized overnight using a DIG Easy Hyb Granules (Roche Applied Science Inc.) at 42 °C with a PCR-generated probe homologous to either the external or internal insertion sequences. Both 3'-external and internal DIG-labeled probes were prepared by PCR using Taq DNA polymerase incorporating DIG-11-dUTP (PCR DIG probe synthesis kit; Roche Applied Science Inc.) according to the manufacturer's instruction. Hybridization signals were then detected using the DIG Luminescent Detection Kit (Roche Applied Science Inc.). The following labeled primers were used to amplify the 3'-external (422 bp) probe: ACCCAGTTGGCCATGTCCCTT (forward primer) and GGCCTGGGTCTTGCCCTGAC (reverse primer). For the internal (530 bp) probe, the following primers were used: CAGACCGCCAACCTGACCGT (forward primer) and ACGGCGTGCTCGTACAGCTT (reverse primer). Mice bearing successful knock-ins were outcrossed to C57Bl/6 J mice (Jackson Labs) for several generations and genotyped to ensure they did not contain either the rd8 or rd1 mutations commonly found in inbred strains.

Immunohistochemistry

Mice were sacrificed by carbon dioxide euthanasia and eyes enucleated and submerged in 4% paraformaldehyde at room temperature. After 5 min of fixation, the cornea and lens were removed, and the eyecups were fixed for an additional 20–25 min. Retinas were removed from fixed eyecups and relieving cuts were made for flattening. Retinas were incubated in 1% Triton X-100 in 1X phosphate buffered saline (PBS) overnight at 4 °C, and then blocked with normal serum for 2 h at 37 °C. Retinas were incubated with primary antibodies overnight at 4 °C, washed 3 times in 1X phosphate buffered saline, 0.5% bovine serum albumin, with 0.5% Triton X-100 (PBT) for 15–30 min at room temperature, and incubated in secondary antibody/pre-conjugated primary solution for 1.5–2 h at 37 °C before 3 PBT washes and mounting with ProLong Diamond Antifade with DAPI (Invitrogen). Tissue was stained for GFP (1:300,

Rockland) and Iba1 (1:1000, Wako), followed by Alexa Fluor-conjugated secondary antibody (1:300; Invitrogen). Iba1 is a calcium-binding adapter protein used as a standard molecular marker used to identify microglia (Ito et al., 1998) and GFP was used to locate Dendra2, which is cross-reactive due to their similar structure (Adam et al., 2009). Tissue was imaged using a Nikon A1 confocal microscope.

Ex vivo imaging and photoconversion

Mice were euthanized by carbon dioxide narcosis and the eyes removed. Retinas were excised, cut into a clover-leaf shape for flattening, and placed into glass-bottomed Petri dish filled with Dulbecco's Modified Eagle Medium (DMEM, Sigma Aldrich) supplemented with 10% Fetal Bovine Serum (FBS; Corning) and secured with overlying mesh. The dish was then placed in an imaging chamber (Thermo Scientific) with 10% CO_2 and maintained at 37 °C. Retinas were imaged on a Nikon A1 imaging system for up to 5 h. Dendra2 was converted at the lowest 405 nm laser power setting, which corresponded to 3 μW at the imaging stage for 2 min. Converted area sizes ranged from cell soma/branches (~ 20 × 20 μm) to multiple cells (~ 320 × 320 μm). Excitation and conversion lasers were simultaneously used for some spectral imaging experiments to measure the rate of Dendra2 conversion.

Flow cytometry

Flow cytometry was performed using a protocol modified from an established method (Karlen et al., 2018; O'Koren et al., 2016). After dissection, each retina was incubated in 1 mL of digestion buffer containing: Hank's Balanced Salt Solution (10–547F, Lonza), 5% FBS, 10 mM HEPES, 0.7 mg/mL calcium chloride, 1.5 mg/mL Collagenase A (10103586001, Roche), and 0.1 mg/mL DNase I (10104159001, Roche) at 37 °C for 15 min. Following incubation, each retina was gently dissociated, and the resulting single-cell suspension was washed, filtered through a 70 μm cell strainer, centrifuged at 350×*g* for 5 min, and resuspended in PBS. Cells were stained for viability (Zombie Viability NIR, 423105, Biolegend), and blocked with Fc light chain antibodies (14016186, eBiosciences), supplemented with normal rat serum and normal

mouse serum. Cells were then incubated with Brilliant Violet 421 anti-mouse CD45 (103133, Biolegend) and Alexa Fluor 647 anti-mouse/human CD11b (101220, BioLegend). Cell suspensions were washed in PBS containing 0.5% Bovine Serum Albumin (BSA), centrifuged at 350×*g* for 5 min, and resuspended in 0.5% BSA in PBS with 1:50 EDTA. Bead controls were created using AbC Total Antibody Compensation Bead Kit (A10497, Invitrogen) and ArC Amine Reactive Compensation Bead Kit (A10628, Invitrogen). Data were acquired on a Cytoflex flow cytometer and analyzed with FlowJo software (Tree Star). Each retina was considered a single sample; 200,000 events were analyzed for each sample.

In vivo imaging and Dendra2 conversion

A custom-built, combined SLO and OCT system was used for fluorescence retinal imaging and Dendra2 conversion equipped with an OBIS LX/LS Laser Box (Coherent Inc. Santa Clara, CA, USA) with 3 laser diode modules (Zhang et al., 2015). A 488 nm laser diode module (120 μW at the mouse pupil) was used to excite green Dendra2, and a 561 nm laser diode module was used to excite red Dendra2. The 561 nm beam power varied between 130 and 200 μW at the mouse pupil. A 405 nm laser diode module was used to illuminate the retina and convert Dendra2 from green to red. The power of the 405 nm exposure ranged from 20 to 100 μW for 5–10 min, and the converted area ranged from 0.13 mm^2 to 1.2 mm^2. Consequently, the light fluence varied from 7.5 to 22.5 J/cm^2 at the cornea, resulting in 3–9 J/cm^2 radiant exposure at the retinal surface when corrected for cornea and lens transmittance (Henriksson et al., 2010).

For imaging, the mice were anesthetized with 2–2.5% isoflurane and positioned on a heating pad at 37 °C. The eyes were dilated and cyclopledged with tropicamide and phenylephrine and corneal hydration was maintained with Hypromellose gel (GenTeal Tears Severe; Alcon). Widefield SLO and OCT images spanned 51° of visual angle (2193 μm), while digitally “zoomed” images ranged between 200 μm for obtaining spectra or 728 μm for imaging the injury and response fields in the light damage model.

A superluminescent diode (860 nm, 132 nm bandwidth; Broadlighter T-860HP; Superlum) was used for OCT imaging (600 μW at pupil) and causing damage (8mW at pupil) as described previously (Miller et al., 2019). OCT images were then processed and flattened for display (Miller et al., 2019; Wojtkowski et al., 2004). En face OCT images were taken from the outer nuclear layer, while B-scans were taken from the same location for each timepoint in both models. For the near infrared (NIR) light damage model, B-scans were taken through the center of the injury field.

Spectral imaging was performed with an OceanOptics Spectrometer (QE65000 OceanOptics Inc. Dunedin, FL, USA) over a small field of view (i.e., hyperspectral images were not created as they were in ex vivo spectra). The 488 nm and 561 nm excitation sources were used separately with set of a dichroic mirrors Di01–R488/561 (Semrock, Rochester, NY), with a 503 LP emission filter for the 488 nm excitation and a 561 nm LP emission filter for the 561 nm excitation (Semrock, Rochester, NY). Conversion could not occur during spectral imaging, because different fibers were required for 405 vs 488/561 nm source delivery. For each data set, 20 spectra with 1000 ms integration time were obtained and averaged.

Fluorescence image analysis

Images from both ex vivo and in vivo experiments were analyzed with ImageJ (FIJI; NIH; (Schneider et al., 2012)) and Python (SciPy stack and Sci-Kit Image; (Van Rossum and Drake, 2009)). Ex vivo images taken on the Nikon A1 microscope were exported to tiff format using NIS elements viewer (Nikon Instruments, Inc.). For in vivo images, backgrounds were adjusted to provide similar overall contrast. To measure the SLO fluorescence signal in the injury and response field, an ROI 728 × 728 μm, centered on the center of the injury field in the widefield images, was created. The background was determined using the Rolling Ball background subtraction function was created using a radius of 50px and averaged to produce the background value. The pixel intensity was then averaged in the ROI and divided by the

background value to produce the signal strength. This normalization served to account for differences in excitation laser power or other issues that created changes in raw signal intensity.

Spectral image analysis

Spectral images were analyzed with ImageJ and Python. For hyperspectral ex vivo image and movie display, the NIS elements viewer was used to select the channels with the peak gD2 and rD2 fluorescence, then exported to tiffs and appropriate Look-Up Tables (LUTs) were applied. For analysis, the full hyperspectral image was exported as tiff and analyzed with custom-written Python code. For time series of D2 conversion, the spectra in 10 nm width bins are display for each scan. Spectra were color-coded from green to red based on scan number and each scan took ~ 1 s. Twenty scans were taken prior to 405 nm exposure and were not displayed. To determine the time course of gD2 loss and rD2 gain, the 10 nm-wide bins that included the peak gD2 and rD2 emission wavelengths were taken and displayed, including the 20 pre-405 nm exposure scans.

To quantify converted rD2, spectral data were unmixed using the theoretical rD2 and autofluorescence spectra. The theoretical spectrum was obtained from the Evrogen website https://evrogen.com and was corrected with the spectrum of the 561 nm LP filter from Semrock (see Methods section "In vivo imaging and Dendra2 conversion"). The autofluorescence spectrum was from an unconverted Dendra2 mouse with 561 nm excitation. Non-negative least squares regression was used in the linear unmixing algorithm to obtain the intensity of the rD2 fluorescence spectrum and the relevant autofluorescence spectrum. To quantify the amount of rD2 over time, the rD2 intensity was normalized to the autofluorescence intensity to control for variations in laser intensity and optical alignment of the mouse eye.

Results

Dendra2-expressing retinal microglia can be efficiently photoconverted in vivo

Cx3cr1$^{D2/D2}$ mice were generated using CRIPSR/Cas9 to knock-in the Dendra2 (D2) coding sequence behind the Cx3cr1 promoter at the same location previously used to generate *Cx3cr1*$^{GFP/GFP}$ mice (Jung et al., 2000). Immunohistochemical staining of fixed retinas of *Cx3cr1*$^{D2/D2}$ mice showed that D2 was expressed in all Iba1^{+} retinal cells, the vast majority of which are microglia (Figure A.1A). These microglia appeared at normal density with ramified morphologies, suggesting the expression of the exogenous protein had no ill effect on microglia viability or immune activation status. No other retinal cells showed expression of D2.

In live retinal explants of *Cx3cr1*$^{D2/D2}$ mice, naïve microglia fluoresced green and had a red–orange color immediately after photoconversion with 405 nm light (Figure A.1B-C, Movie A.S1). Spectral analysis of the emitted light allowed quantitative measurement of unconverted green Dendra2 (gD2) and photoconverted red Dendra2 (rD2) over time. Prior to photoconversion, the combined emission spectrum from 488 and 560 nm excitation showed a strong primary peak at 505 nm corresponding to gD2 and a small secondary peak at 571 nm corresponding to rD2 (Figure A.1D, green trace at time 0 s). During the 488 nm scanning, the 505 nm signal noticeably decreased, while the red 571 nm signal did not change, consistent with photobleaching of gD2 that did not cause photoconversion to rD2 (Figure A.1E, green trace before 405 nm onset). Following 405 nm laser exposure for 2 min (19 μW; 2175 J/cm^2 radiant exposure), the primary green peak decreased, and the secondary red peak increased, reflecting rapid photoconversion from gD2 to rD2 (Figure A.1D; yellow, orange, and red traces). Interestingly, the rate of increase of rD2 fluorescence was much greater than the rate of decrease of gD2 fluorescence (Figure A.1E, compare orange and green traces), as has also been noted by other groups (Adam et al., 2009; Gurskaya et al., 2006; Makarov et al., 2014; Pakhomov et al., 2017). The complete conversion of all D2 protein within a cell never occurred such that some gD2 protein was still detectible after 405 nm excitation in all experiments.

We next imaged the retinas of *Cx3cr1*$^{D2/D2}$ mice in vivo with combined Scanning Laser Ophthalmoscopy (SLO) to visualize the fluorescent cells and Optical Coherence Tomography

(OCT) with three-dimensional light scattering to visualize the retinal architecture. Similar to ex vivo live observations, in vivo SLO imaging with 488 nm excitation revealed a retinal microglial population that appeared qualitatively normal in density and distribution, with no obvious rD2 fluorescence (Figure A.2A, unconverted). After 405 nm exposure, there was a large increase in rD2 fluorescence and a concomitant decrease in gD2 fluorescence in the converted area (FigureA.2A, converted). Photoconverted cells could be tracked in vivo over multiple days, with rD2 fluorescence gradually decreasing over the course of a week (Figure A.2B). Spectroscopy was used to quantify in vivo changes accurately and objectively in a subset of cells across a small area (219 × 219 μm) over time (Figure A.2C). The disappearance of red fluorescence is expected based upon the gradual protein turnover of the rD2 protein, leaving only newly translated gD2 within existing cells; however, at the current resolution of our in vivo imaging, it was not possible to differentiate between loss of the rD2 protein and disappearance of red fluorescent cells themselves.

Of note, a high fluence of 405 nm light (9 J/cm^2) increased OCT light scattering in the scanned area in 3 out of 4 retinas imaged, denoting light-induced retinal damage; however, lower fluences of 405 nm light (4.5–7 J/cm^2) did not cause any detectable retinal damage, while still permitting sufficient photoconversion to readily tag individual microglia with our imaging system. In some retinas, low fluences of 405 light (4.5–7 J/cm^2; 5 min duration) that resulted in photoconversion also resulted in recruitment of microglia to the converted area. This was surprising, since there were no corresponding changes in OCT light scattering that are commonly associated with local retinal damage. In all cases, any recruited microglia returned to their normal mosaic spatial distribution within a week.

To quantify the photoconverted and non-converted microglial populations in vivo, we used fluorescence activated cell sorting (FACS). Since Cx3cr1 has been shown to have immunomodulatory and neuroprotective effects in the retina (Rashid et al., 2019; Wolf et al., 2013; Zabel et al., 2016), for this and all subsequent experiments, heterozygous mice

(e.g., *Cx3cr1*$^{+/D2}$) were used to ensure microglia possessed a functional copy of Cx3cr1 and a single copy of the D2 label. We converted four large areas in one eye of a *Cx3cr1*$^{+/D2}$ mouse, creating a large subpopulation of rD2 microglia across the retina (Figure A.3A). Within 24 h after conversion, mice were euthanized and the retinas removed; *Cx3cr1*$^{+/GFP}$ retinas were processed in parallel for comparison. Retinas were dissociated and all live, single cells expressing CD45^{+} Cd11b^{+} with high Cx3cr1 expression (as measured by GFP fluorescence) were quantified with flow cytometry, using the gating shown in Figure A.3B. As expected, the *Cx3cr1*$^{+/GFP}$ mouse retina contained GFP-expressing cells but no red fluorescence (Figure A.3C, left). The unconverted control eye of the *Cx3cr1*$^{+/D2}$ mouse was similar, with only a few rD2 cells detected (Figure A.3C, middle). However, the converted eye in the *Cx3cr1*$^{+/D2}$ mouse showed fewer gD2 microglia and a greatly increased number of rD2 microglia (Figure A.3C, right). Interestingly, the green fluorescence was noticeably brighter in the *Cx3cr1*$^{+/D2}$ mice compared to the *Cx3cr1*$^{+/GFP}$ mice (Figure A.3C). These results demonstrate that expression from a single copy of D2 and its photoconversion in vivo are sufficient to be used for flow cytometry and cell sorting.

Photoconverted Dendra2 to identify resident microglia during widespread retinal degeneration

Having shown that flow cytometry could be performed immediately after in vivo photoconversion, we next used FACS to quantify photoconverted cells over time in a model of neurodegeneration. Mice lacking Arrestin-1 (Arr1, also known as visual arrestin) were used to noninvasively induce photoreceptor degeneration. Arr1 is a photoreceptor-specific cytosolic protein that deactivates photoexcited rhodopsin, shutting down the rod phototransduction cascade (Wilden and Kuehn, 1982; Xu et al., 1997). In *Arr1*$^{-/-}$ mice, rods become extraordinarily sensitive to light but continue to be healthy as long as the animals are dark-reared; prolonged exposure to room light induces photoreceptor degeneration (Chen et al., 1999; Hao et al., 2002; Levine et al., 2014; Wang and Chen, 2014), resulting in the loss of half of the photoreceptors within 48 h (Karlen et al., 2018). *Arr1*$^{-/-}$ *Cx3cr1*$^{+/D2}$ mice were dark-reared and their microglia

photoconverted in four large areas in one eye of each mouse, either prior to ("Healthy Retina", Figure A.4A) or after 4 days of light-induced photoreceptor degeneration ("Degenerating Retina", Figure A.4B-D). Quantification of gD2 and rD2 cells in the retina by FACS revealed that the population of photoconverted rD2 microglia was remarkably stable regardless of the health status of the retina for up to 48 h (Figure A.4A-C). As before, the unconverted control eyes showed negligible rD2 cells (Figure A.4D). Together, these data demonstrate that subpopulations of retinal microglia can be reliably quantified in a degenerating retina for at least 48 h after photoconversion, and that there is no detectable microglial cell loss during this time of profound photoreceptor clearance.

Next, we used this degeneration model to monitor cell subpopulations during retinal degeneration in vivo using SLO retinal imaging. In healthy mice (prior to inducing degeneration), we photoconverted resident microglia across the full area of the visible retina using the 405 nm laser (Figure A.4E). Both control (*Arr1*$^{+/+}$ *Cx3cr1*$^{+/D2}$) and experimental mice (*Arr1*$^{-/-}$ *Cx3cr1*$^{+/D2}$) were then exposed to continuous room light, initiating retinal degeneration in the *Arr1*$^{-/-}$ mouse. Within 24 h, green cells that had not been photoconverted were visible within and near retinal vessels only in the degenerating retinas (Figure A.4F, white arrows). In contrast, retinas of WT mice 24 h after conversion contained only a population of yellow/orange cells and no green cells (Figure A.4G). Since resident microglia contained both gD2 and rD2, giving them a yellow/orange appearance in the composite image, the bright green cells that were easily distinguishable from the rD2-containing population in the degenerating *Arr1*$^{-/-}$ retinas likely originated from outside the retinal field of view, presumably having extravasated from the retinal vasculature as previously described (Karlen et al., 2018).

Microglia with converted Dendra2 can be tracked during a response to localized photoreceptor damage

One of the great promises of this mouse line is the ability to track individual microglia over space and time in vivo. Thus, we used local laser damage in the retinas of *Cx3cr1*$^{+/D2}$ mice

to study how cells move to and from a local site of injury as the damaged cells are removed and the tissue reorganizes. Microglia were first photoconverted in a small retinal region (Figure A.5A, conversion site) without causing damage (Figure A.5E, pre-damage OCT). Subsequently, photoreceptors within the rD2 field were damaged using a high intensity near-infrared (NIR) laser (Figure A.5A, injury site), causing an immediate increase in OCT light scattering indicative of tissue damage (Figure A.5E) that could be monitored over time (Figure A.5F).

After NIR damage, all rD2-labeled microglia migrated to the injury field and progressively formed a dense, bright cluster of cells over 3 days (Figure A.5A, zoom A.5D). Initially the rD2 cells accumulated on the side of the injury field closest to the region from which they had migrated. Over a period of days, the rD2 cells became dispersed throughout the injury field. After 1 week, the structural damage visible by OCT was less distinct and most of the microglia had left the injury locus; only a small cluster of fluorescent cells occupied the core damaged region (Figure A.5A, zooms A.5C, D). By this time, the rD2 label had become difficult to detect, with only a few faint flocculent red-fluorescent bodies visible (Figure A.5D, 1 week timepoint). Finally, at 2 and 3 weeks after NIR damage, no rD2 label was at all detectable and the green microglia distribution had largely returned to normal, with only a small cluster of gD2 cells remaining in the core of the injury field (Figure A.5A, zooms A.5C, D).

To track the microglial response and the change in rD2 fluorescence over time, we quantified the intensity of gD2 and rD2 fluorescence from the SLO images, following an established protocol (Miller et al., 2019). The SLO gD2 signal was initially prominent but lost nearly twofold intensity after 405 nm conversion (Figure A.5B, 488 nm Ex). This gD2 signal subsequently increased over time, peaking at 72 h presumably due to the accumulation of cells at the injury locus. From 1 to 3 week post-damage, the gD2 signal decreased, returning nearly to baseline by 3 weeks. Image analysis of the emitted light showed an immediate loss of gD2 and gain of rD2 signal after 405 nm exposure, consistent with photoconversion (Figure A.5B, 561 nm Ex). After 24 h, the rD2 signal began to gradually fall, presumably as protein levels in

the cell turned over, reaching baseline around 7 days (Figure A.5B). Overall, these results show that distinct microglial populations can be reliably tracked over space and time as they respond to neuronal injury and degeneration.

Discussion

Here we show that the *Cx3cr1–Dendra2* mouse (*Cx3cr1*$^{+/D2}$) is a useful model for labeling resident microglia and unambiguously tracking immune subpopulations for several days during neuronal injury and tissue remodeling.

In the *Cx3cr1*$^{D2/D2}$ homozygous mouse, the endogenous Cx3cr1 alleles have been replaced by knock-ins of the fluorescent protein Dendra2, the same strategy employed in the commonly used *Cx3cr1*$^{GFP/GFP}$ mouse [(Jung et al., 2000) Jackson Labs strain 005582]. Healthy neurons express the receptor's ligand, Cx3CL1, which helps maintain microglia in a normal basal state, and studies indicate that mice heterozygous for *Cx3cr1*$^{+/GFP}$ have microglia that function normally in the retina (Beli et al., 2016; Paolicelli et al., 2014; Wolf et al., 2013). For our study, we likewise used heterozygous *Cx3cr1*$^{+/D2}$ mice and did not observe any qualitative abnormalities in microglia form or function. Histology and in vivo SLO imaging of retinal microglia showed a ramified morphology and spatial distribution that is typical for cells in healthy CNS retina. Following photoreceptor damage, these microglia underwent a morphological change and migrated to the affected photoreceptors, a functional response indistinguishable from observations in wild-type (C57BL/6 J) and *Cx3cr1*$^{+/GFP}$ mice [(Yu et al., 2020), reviewed in (Karlen et al., 2020; Rashid et al., 2019)]. Together, these data indicate that microglia in the *Cx3cr1*$^{+/D2}$ mouse retain their ability to respond to neurodegeneration and function comparably to those in the *Cx3cr1–GFP* mouse.

While naïve *Cx3cr1*$^{+/D2}$ cells continually produce green GFP-like fluorescence, photoconversion in cells of interest can be efficiently driven by noninvasive 405 nm light exposure, converting selected cells to a permanent RFP-like fluorescence that lasts up to a

week (Figures A.1, A.2, A.5). Once photoconverted, rD2 can be tracked both ex vivo and in vivo in healthy and degenerating retinas, and the D2 protein is stable enough to survive tissue processing for flow cytometry (Figures A.3, A.4). In principle, the *Cx3cr1*$^{+/D2}$ mouse should also be useful for studying rates of protein turnover, though we did not use it for this purpose. In our in vivo studies that imaged the same cell populations across several days, cell crowding and intermixing did not allow quantitative interpretation of the rD2 and gD2 ratio to estimate protein turnover rates. Overall, the ability to track, sort, and quantify naïve gD2 and photoconverted rD2 microglia simultaneously is a powerful tool for disentangling the roles of mixed immune cell populations.

A variety of other tools have been developed to fluorescently label resident microglia and infiltrating macrophages and visualize their dynamics during health and disease (Bennett et al., 2016; Goldmann et al., 2013; Jung et al., 2000; Lückoff et al., 2017; McKinsey et al., 2020; Parkhurst et al., 2013; Reyes et al., 2017); however, very few of these are able to target and track spatially distinct subsets of microglia that are known to exist (Hammond et al., 2019; O'Koren et al., 2019; Ronning et al., 2019; Wieghofer et al., 2021). One exception is the *Cx3cr1–CreER* mouse that has been used to develop the "Microfetti" mouse in which individual long-lived macrophages are labeled with one of four fluorophores (Tay et al., 2017). This mouse allows subsets of microglia to be distinctly labeled and has been useful for better understanding microglia proliferation at rest and during activation. However, in this line the fluorophore expression after tamoxifen administration is random, and thus spatially distinct subsets of microglia cannot be purposefully targeted. In contrast, the *Cx3cr1*$^{+/D2}$ mouse described here allows individual, spatially distinct subsets of microglia, at varying scales, to be specifically tagged and followed over time using a variety of in vivo, ex vivo, and histological techniques.

In this study, we utilized the *Cx3cr1–Dendra2* mouse to noninvasively tag and track subpopulations of cells in the retina. Specifically, in response to widespread degeneration,

photoconverted rD2 resident microglia were joined by naïve gD2 circulating Dendra2-expressing cells that exited the retinal vasculature and infiltrated the parenchyma (Figure A.4E, white arrows). Furthermore, following local laser damage, a subpopulation of photoconverted microglia clustered at the injury locus (Figure A.5, rD2 at 1–3 days) then redistributed as the tissue recovered (Figure A.5B, 1–3 weeks). This ability to specifically label subsets of cells could also permit functional comparisons between distinct populations of macrophages using a variety of downstream techniques that typically do not include spatial information, such as single-cell RNAseq and ATAC-seq. Thus, this mouse can be used both to track distinct macrophages over time in the tissue and to probe specific roles of unique immune populations during injury and degeneration.

Conclusion

Distinguishing between subpopulations of microglia and other immune cells within the CNS during episodes of neuronal death and tissue remodeling has proven to be challenging. Here we describe the novel *Cx3cr1–Dendra2* mouse (*Cx3cr1*$^{+/D2}$) in which subpopulations of microglia can be photoconverted from green to red and tracked unambiguously for several days during neuronal injury and tissue remodeling. Naïve and photoconverted Dendra2 signal can also be used for flow cytometry and cell sorting of distinct microglia populations. This mouse line has additional uses beyond retinal microglia studies, such as tracking resident immune cells in other CNS compartments, quantifying protein turnover within microglia, and studying the function of Cx3cr1-expressing myeloid cells outside the CNS.

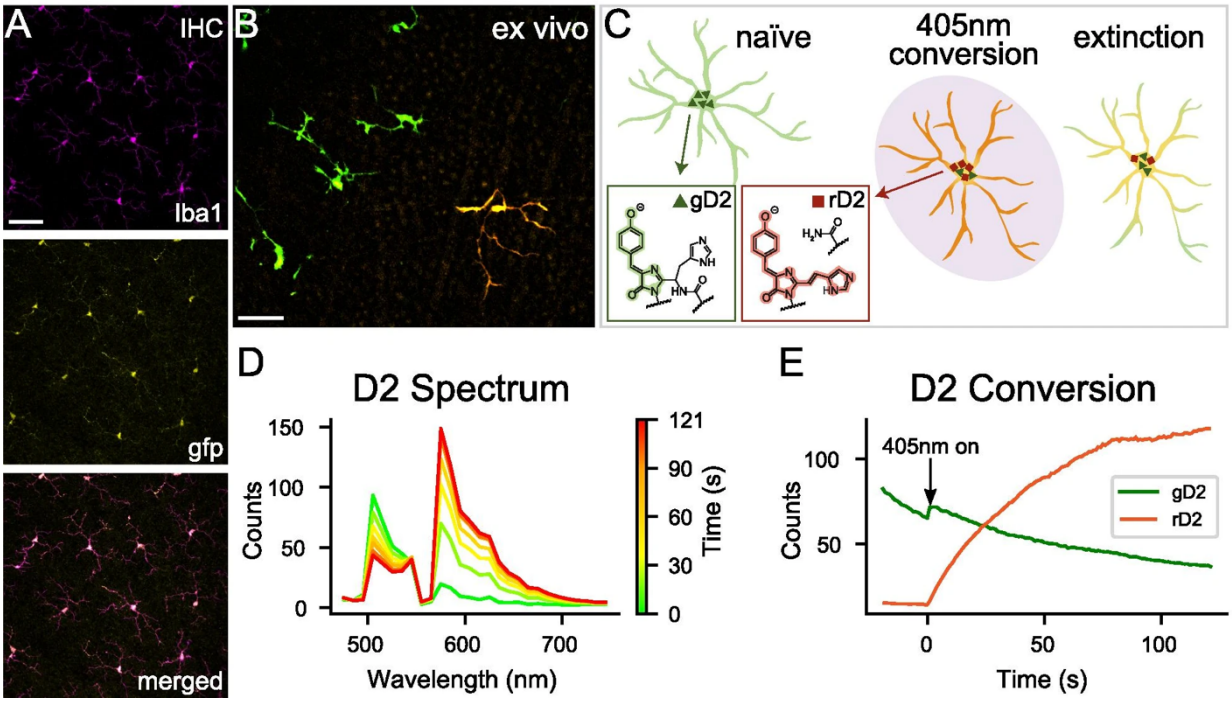

Figure A.1. Characterization of the *Cx3cr1–Dendra2* mouse. (A) Immunohistochemistry of *Cx3cr1*$^{D2/D2}$ retina showing Iba1^{+} microglia staining (top) is concurrent with Cx3cr1–Dendra2 expression (amplified using anti-GFP antibody, middle) and displays normal microglia morphology. Scale 500 μm; from a female mouse, $n = 3$ retina (3 mice). (B) Merged image of live retinal explants from a male *Cx3cr1*$^{D2/D2}$ mouse showing microglia with intrinsic unconverted gD2 fluorescence under 488 nm light (left) and a single photoconverted cell expressing rD2 under 560 nm light (right). Scale 100 μm, $n = 6$ retinas (5 mice). (C) Schematic of photoconversion. Naïve microglia shown in green; triangles indicate gD2. Following noninvasive 405 nm light exposure (center), gD2 permanently converts to rD2 (red squares), shifting microglia fluorescence to a red/orange color. Over time, protein turnover causes an extinction of rD2 and gain of gD2 (right). Insets show gD2 and rD2 structure. (D) D2 spectral analysis of the photoconverted cell in (B) shows that prior to photoconversion, the combined emission spectrum from 488 and 560 nm excitation has a strong gD2 primary peak at 505 nm and a slight rD2 secondary peak at 571 nm (green trace, time 0 s). Exposure to 2 min of 405 nm light decreases the gD2 peak and sharply increases the rD2 peak (red trace), reflecting rapid

photoconversion (time course shown in multicolored traces). (E) D2 conversion rates of the photoconverted cell in (B) indicate that the 488 nm laser caused gD2 photobleaching prior to 405 nm onset but did not cause appreciable photoconversion (green trace). Onset of the 405 nm laser at $t = 0$ caused a rapid rise in rD2 (red trace) and a decrease in gD2.

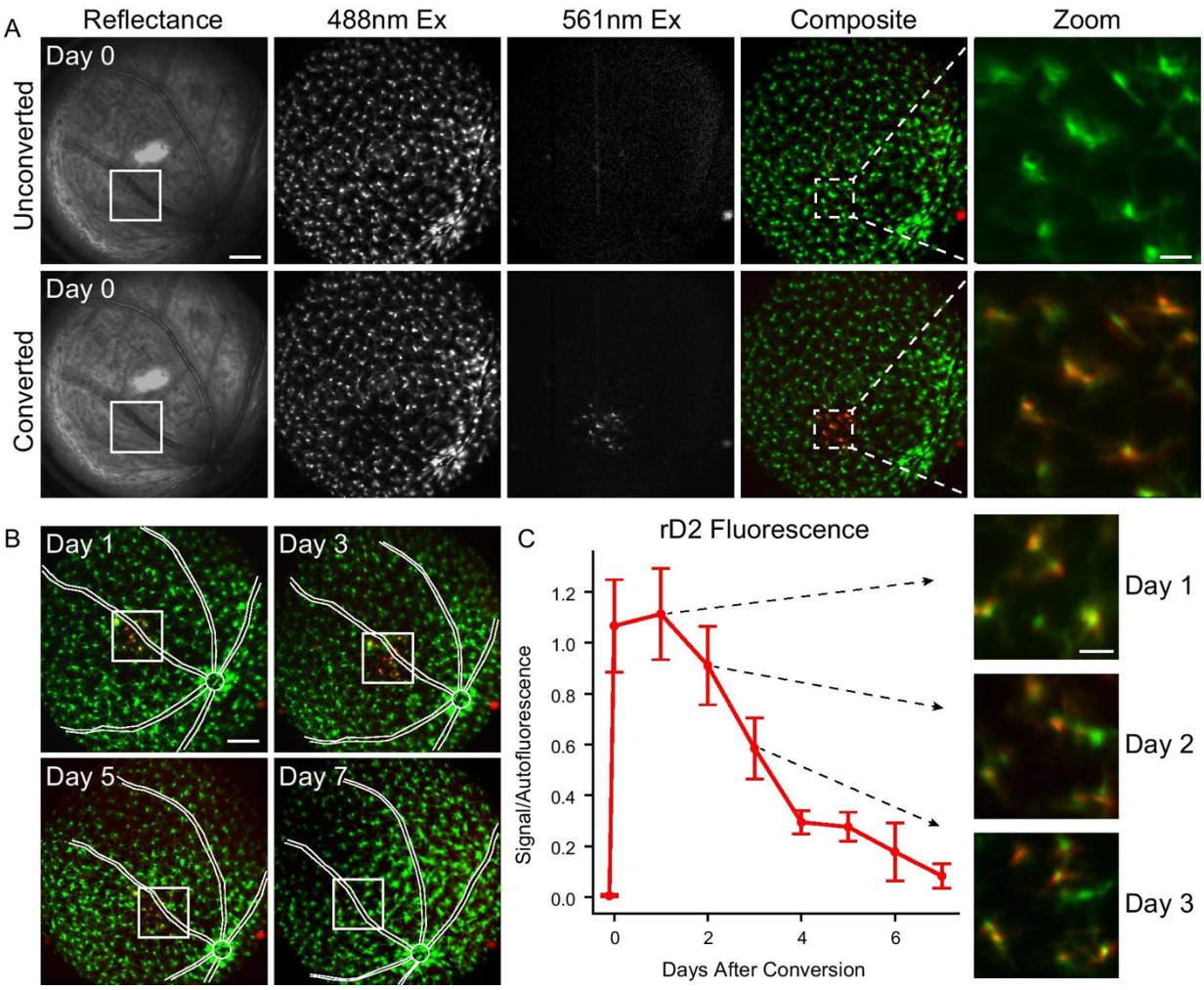

Figure A.2. In vivo imaging of Cx3cr1–Dendra2 in healthy retina. (A) Retinal microglia in a *Cx3cr1*$^{D2/D2}$ retina from a female mouse appeared qualitatively normal in density and distribution using in vivo SLO under 488 nm excitation both before (unconverted) and immediately after (converted) exposure of a small retinal area to 405 nm light (75 μW, 365 × 365 μm area, 9 J/cm2 radiant exposure). The 405 nm exposure resulted in a clearly defined region of rD2 fluorescence; rD2 was not observed in surrounding regions or in the unconverted eye. Composite image shows a pseudo-colored merge of the 488 nm and 561 nm images; zoomed region denoted by dashed lines. Scale 300 μm; zoom scale 50 μm, n = 8 retinas (5 mice). (B) Changes in rD2 fluorescence over the course of 1 week taken from the same eye as shown in (A). Converted region denoted with a white box; blood vessels drawn for

reference. Scale 300 μm. (C) Quantification of rD2 using spectral analysis taken over 7 days (mean ± SEM, *n* = 5 retinas). Insets show zoomed images taken from the same mouse as in (A) at days 1–3 after photoconversion. Scale 50 μm.

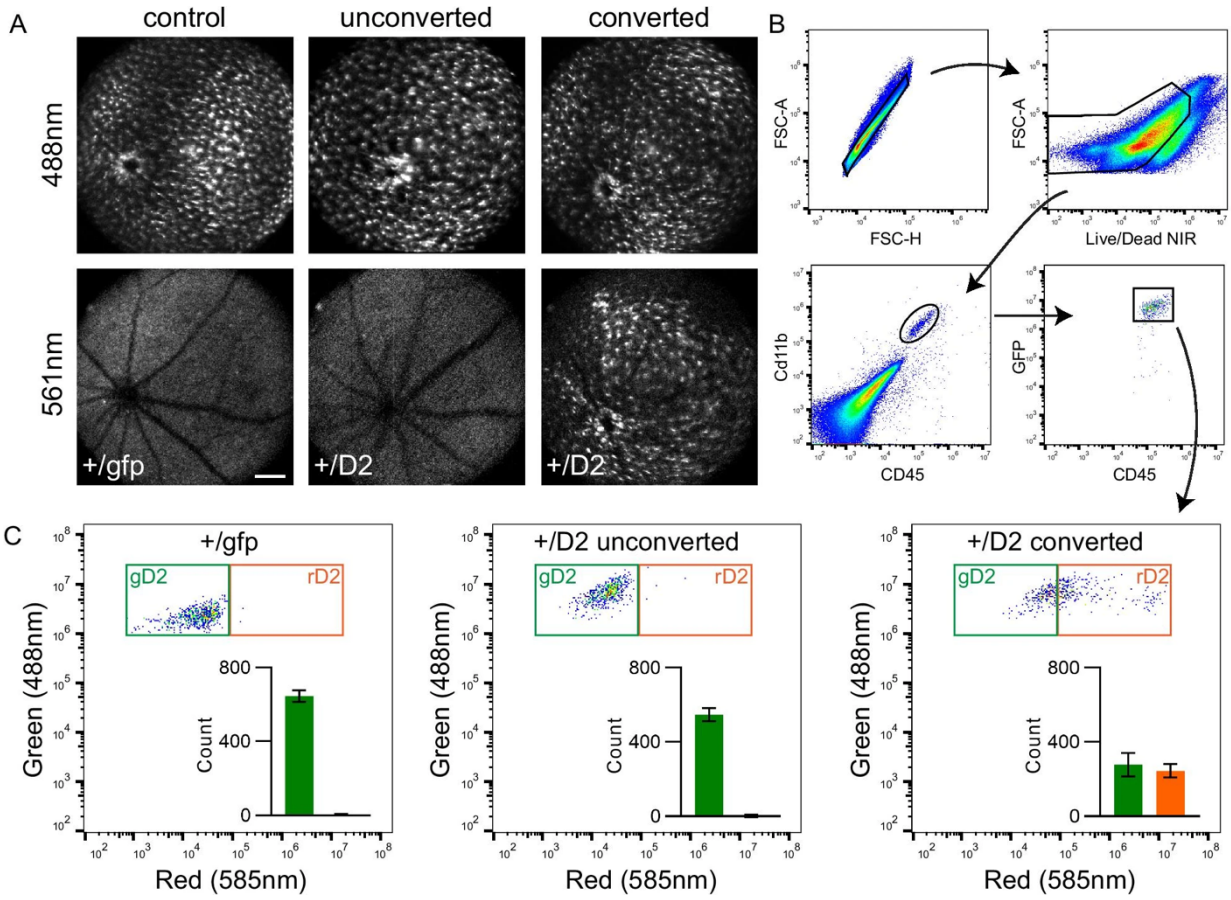

Figure A.3. Quantification of photoconverted D2 cells using flow cytometry. (A) *In vivo* SLO imaging of a *Cx3cr1*$^{+/GFP}$ retina, a naive *Cx3cr1*$^{+/D2}$ retina (unconverted), and a photoconverted *Cx3cr1*$^{+/D2}$ retina that was exposed to 405 nm light across the entire retinal surface (110 μW, 780 × 780 μm per quadrant, 3.5–5 J/cm^2 radiant exposure). Scale 300 μm. (B) Flowcytometry gates used to identify single cells, alive, double positive for Cd11b$^+$ CD45$^+$, and with high expression of Cx3cr1, as measured by green fluorescence to exclude peripheral monocytes. (C) Quantification of green gD2 cells and green and red double positive rD2 cells from each condition. The *Cx3cr1*$^{+/GFP}$ retina was composed entirely of green, GFP$^+$ microglia, similar to the *Cx3cr1*$^{+/D2}$ unconverted retina which was nearly all green gD2 microglia, with a negligible population of rD2 fluorescence. Conversely, the *Cx3cr1*$^{+/D2}$ photoconverted retina had

fewer gD2 cells and a large population of rD2 cells. Error bars are SE, n = 3 retinas per group (5 mice), all retinas were from male mice.

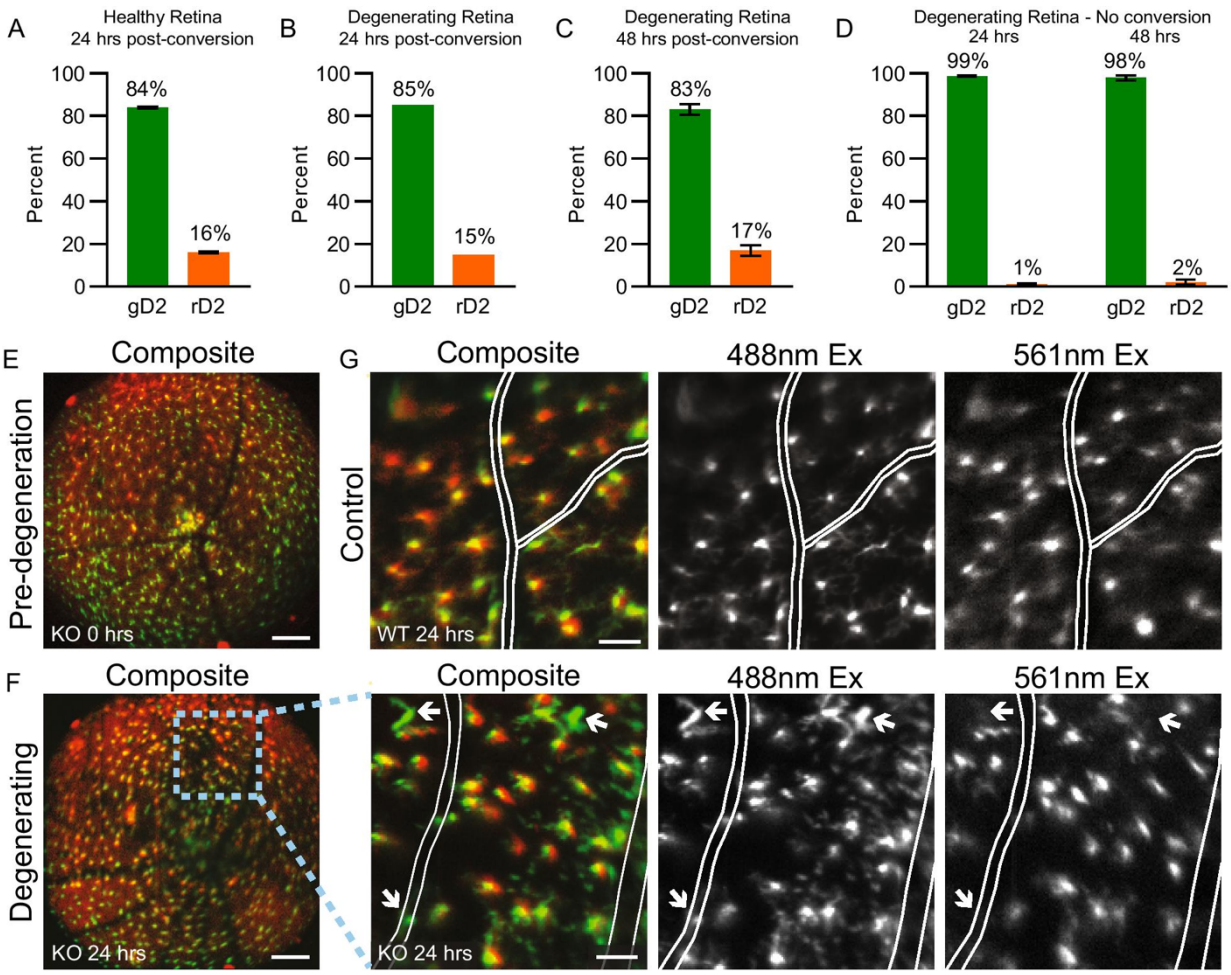

Figure A.4. Photoconversion is stable for several days and can differentiate subpopulations of microglia in healthy and degenerating retina. (A) In healthy, dark reared *Arr1*$^{-/-}$ *Cx3cr1*$^{+/D2}$ mice, 24 h after a large portion of retina was photoconverted in vivo (150 µW, 780 × 780 µm, 6 J/cm^2 radiant exposure), 16% of flow cytometry-isolated cells were rD2 positive. (B-C) Similar numbers were found in degenerating *Arr1*$^{-/-}$ *Cx3cr1*$^{+/D2}$ retina after 24 h (B) and 48 h (C) of light exposure, demonstrating stability of the photoconverted microglia population over multiple days in degenerating retina. (D) In degenerating retinas that were not subjected to photoconversion, only 1–2% of cells were rD2 positive, which is similar to unconverted controls in healthy retina. Error bars are SE, n = 2 retinas, 1 male/1 female for each experimental condition. (E-G) In *Arr1*$^{-/-}$ *Cx3cr1*$^{+/D2}$ (KO) and *Arr1*$^{+/+}$ *Cx3cr1*$^{+/D2}$ (WT control) mice, resident microglia in the imaging area were photoconverted (6 J/cm^2) prior to light

exposure. Comparison of pre-degenerating (E) and degenerating (F) retina in the same mouse revealed that after 24 h of light exposure, bright green cells that had not been photoconverted were visible within and near retinal vessels only in degenerating retina (F, white arrows in zoomed images) and were clearly distinguishable from resident microglia that appeared yellow/orange and contained gD2 and rD2. Similar bright green, single labeled cells were not observed in *Arr1* wildtypes (G). Images (E,F) from same female mouse, (G) from a male mouse; panels to the right of (F) are digitally magnified images from the dashed box area in the full imaging field to the left; white lines denote vasculature in zoomed images. Widefield scale 300 μm, zoomed scale 100 μm.

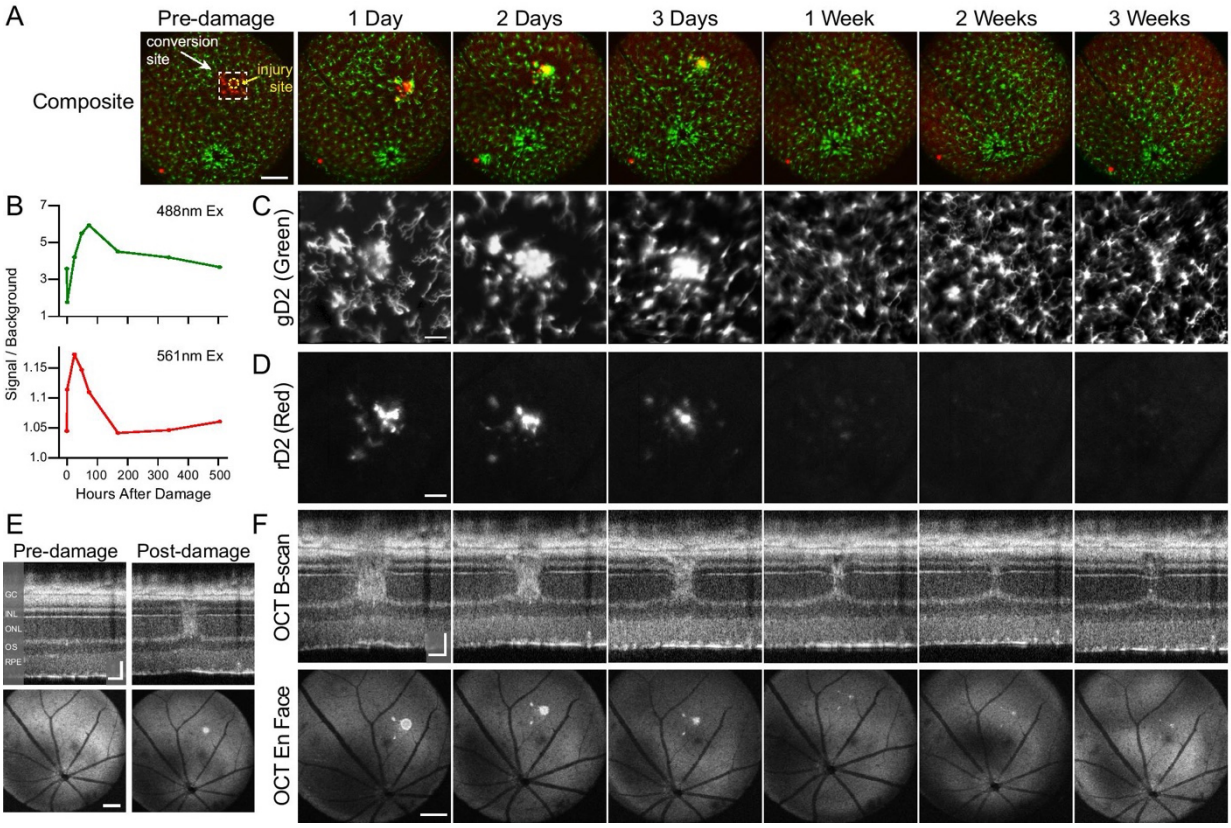

Figure A.5. Microglial response to localized damage. (A) Composite widefield images showing naïve microglia (green) and photoconverted microglia (red) in the retina prior to focal NIR damage (pre-damage) and the subsequent 1 day to 3 weeks in the same female mouse ($n = 1$ retina). Cells were photoconverted in an area of ~ 365 × 365 μm (9 J/cm^2, dashed white line); retinal damage was induced at the injury site (yellow, ~ 150 μm diameter). All detectable rD2 microglia migrated to the injury field within 24 h, progressively forming a dense, bright cluster of cells over the first 3 days. Scale 300 μm. (B) Quantified intensity of gD2 (green, top trace) and rD2 (red, bottom trace) fluorescence in the injury site shown in (A) over time. The gD2 signal was initially bright against the background but lost nearly twofold intensity after photoconversion (lower point at $t = 0$); conversely, the rD2 signal increased nearly threefold after photoconversion (upper point at $t = 0$), peaking 24 h after damage, then falling to baseline levels by 1 week. (C,D) Magnified views of the gD2 (488 nm excitation) and rD2 (561 nm excitation) fluorescent images at each timepoint within the injury locus. Scale 100 μm. (E) OCT imaging

was performed simultaneously to monitor the integrity of retinal layers and the changes in light scattering characteristic of retinal damage in the same mouse as (A). Both OCT B-scans (top, optical sections) and *en face* images (bottom) through the injury locus reveal the increase in light scattering in the outer nuclear layer (ONL) evoked by the NIR laser damage (Post-damage). Note that prior to NIR laser exposure (Pre-damage) retinal layers appeared normal, confirming that the prior 405 nm light exposure used for D2 photoconversion did not cause photoreceptor damage. (F) OCT B-scans (top) and *en face* images (bottom) for subsequent timepoints matched to corresponding SLO in (A). The localized damage from the NIR exposure was most extensive at 1 day and nearly resolved by 3 weeks. B-scan scale 100 μm horizontal, 50 μm vertical; *en face* scale 300 μm. *GC* ganglion cell layer, *INL* inner nuclear layer, *OS* outer segments, *RPE* retinal pigment epithelium.

Supplementary information

Movie A.S1. Zoomed image of a ex vivo microglia during 405 nm laser photoconversion. There is an immediate decrease in 488 nm green fluorescence and an increase in 561 nm red fluorescence, which increased upon each subsequent scan of the 405 nm laser. Images from a male *Cx3cr1*$^{D2/D2}$ mouse.

This additional multimedia file can be found at:

https://jneuroinflammation.biomedcentral.com/articles/10.1186/s12974-021-02285-x#Sec17

References

Adam, V., Nienhaus, K., Bourgeois, D., Nienhaus, G.U., 2009. Structural basis of enhanced photoconversion yield in green fluorescent protein-like protein Dendra2. Biochemistry 48, 4905–4915. https://doi.org/10.1021/bi900383a

Beli, E., Dominguez, J.M., Hu, P., Thinschmidt, J.S., Caballero, S., Li Calzi, S., Luo, D., Shanmugam, S., Salazar, T.E., Duan, Y., Boulton, M.E., Mohr, S., Abcouwer, S.F., Saban, D.R., Harrison, J.K., Grant, M.B., 2016. CX3CR1 deficiency accelerates the development of retinopathy in a rodent model of type 1 diabetes. J Mol Med 94, 1255–1265. https://doi.org/10.1007/s00109-016-1433-0

Bennett, M.L., Bennett, F.C., Liddelow, S.A., Ajami, B., Zamanian, J.L., Fernhoff, N.B., Mulinyawe, S.B., Bohlen, C.J., Adil, A., Tucker, A., Weissman, I.L., Chang, E.F., Li, G., Grant, G.A., Hayden Gephart, M.G., Barres, B.A., 2016. New tools for studying microglia in the mouse and human CNS. Proc Natl Acad Sci U S A 113, E1738-1746. https://doi.org/10.1073/pnas.1525528113

Chen, J., Simon, M.I., Matthes, M.T., Yasumura, D., LaVail, M.M., 1999. Increased susceptibility to light damage in an arrestin knockout mouse model of Oguchi disease (stationary night blindness). Invest. Ophthalmol. Vis. Sci. 40, 2978–2982.

Chudakov, D.M., Lukyanov, S., Lukyanov, K.A., 2007a. Tracking intracellular protein movements using photoswitchable fluorescent proteins PS-CFP2 and Dendra2. Nat Protoc 2, 2024–2032. https://doi.org/10.1038/nprot.2007.291

Chudakov, D.M., Lukyanov, S., Lukyanov, K.A., 2007b. Using photoactivatable fluorescent protein Dendra2 to track protein movement. Biotechniques 42, 553, 555, 557 passim. https://doi.org/10.2144/000112470

Eme-Scolan, E., Dando, S.J., 2020. Tools and Approaches for Studying Microglia In vivo. Front. Immunol. 11. https://doi.org/10.3389/fimmu.2020.583647

Fletcher, E.L., 2020. Contribution of microglia and monocytes to the development and progression of age related macular degeneration. Ophthalmic Physiol Opt 40, 128–139. https://doi.org/10.1111/opo.12671

Goldmann, T., Wieghofer, P., Müller, P.F., Wolf, Y., Varol, D., Yona, S., Brendecke, S.M., Kierdorf, K., Staszewski, O., Datta, M., Luedde, T., Heikenwalder, M., Jung, S., Prinz, M., 2013. A new type of microglia gene targeting shows TAK1 to be pivotal in CNS autoimmune inflammation. Nat Neurosci 16, 1618–1626. https://doi.org/10.1038/nn.3531

Griffiths, N., Jaipargas, E.-A., Wozny, M.R., Barton, K.A., Mathur, N., Delfosse, K., Mathur, J., 2016. Photo-convertible fluorescent proteins as tools for fresh insights on subcellular interactions in plants. J Microsc 263, 148–157. https://doi.org/10.1111/jmi.12383

Gurskaya, N.G., Verkhusha, V.V., Shcheglov, A.S., Staroverov, D.B., Chepurnykh, T.V., Fradkov, A.F., Lukyanov, S., Lukyanov, K.A., 2006. Engineering of a monomeric green-to-red photoactivatable fluorescent protein induced by blue light. Nat Biotechnol 24, 461–465. https://doi.org/10.1038/nbt1191

Hammond, T.R., Dufort, C., Dissing-Olesen, L., Giera, S., Young, A., Wysoker, A., Walker, A.J., Gergits, F., Segel, M., Nemesh, J., Marsh, S.E., Saunders, A., Macosko, E., Ginhoux, F., Chen, J., Franklin, R.J.M., Piao, X., McCarroll, S.A., Stevens, B., 2019. Single-Cell RNA Sequencing of Microglia throughout the Mouse Lifespan and in the Injured Brain Reveals Complex Cell-State Changes. Immunity 50, 253-271.e6. https://doi.org/10.1016/j.immuni.2018.11.004

Hao, W., Wenzel, A., Obin, M.S., Chen, C.-K., Brill, E., Krasnoperova, N.V., Eversole-Cire, P., Kleyner, Y., Taylor, A., Simon, M.I., Grimm, C., Remé, C.E., Lem, J., 2002. Evidence for two apoptotic pathways in light-induced retinal degeneration. Nat. Genet. 32, 254–260. https://doi.org/10.1038/ng984

Hasle, N., Cooke, A., Srivatsan, S., Huang, H., Stephany, J.J., Krieger, Z., Jackson, D., Tang, W., Pendyala, S., Monnat, R.J., Trapnell, C., Hatch, E.M., Fowler, D.M., 2020. High-throughput, microscope-based sorting to dissect cellular heterogeneity. Mol Syst Biol 16, e9442. https://doi.org/10.15252/msb.20209442

Henriksson, J.T., Bergmanson, J.P.G., Walsh, J.E., 2010. Ultraviolet radiation transmittance of the mouse eye and its individual media components. Exp Eye Res 90, 382–387. https://doi.org/10.1016/j.exer.2009.11.004

Ito, D., Imai, Y., Ohsawa, K., Nakajima, K., Fukuuchi, Y., Kohsaka, S., 1998. Microglia-specific localisation of a novel calcium binding protein, Iba1. Brain Res Mol Brain Res 57, 1–9. https://doi.org/10.1016/s0169-328x(98)00040-0

Jung, S., Aliberti, J., Graemmel, P., Sunshine, M.J., Kreutzberg, G.W., Sher, A., Littman, D.R., 2000. Analysis of Fractalkine Receptor CX3CR1 Function by Targeted Deletion and Green Fluorescent Protein Reporter Gene Insertion. Molecular and Cellular Biology 20, 4106–4114. https://doi.org/10.1128/MCB.20.11.4106-4114.2000

Karlen, S.J., Miller, E.B., Burns, M.E., 2020. Microglia Activation and Inflammation During the Death of Mammalian Photoreceptors. Annu Rev Vis Sci 6, 149–169. https://doi.org/10.1146/annurev-vision-121219-081730

Karlen, S.J., Miller, E.B., Wang, X., Levine, E.S., Zawadzki, R.J., Burns, M.E., 2018. Monocyte infiltration rather than microglia proliferation dominates the early immune response to rapid photoreceptor degeneration. Journal of Neuroinflammation 15, 344. https://doi.org/10.1186/s12974-018-1365-4

Labas, Y.A., Gurskaya, N.G., Yanushevich, Y.G., Fradkov, A.F., Lukyanov, K.A., Lukyanov, S.A., Matz, M.V., 2002. Diversity and evolution of the green fluorescent protein family. Proc Natl Acad Sci U S A 99, 4256–4261. https://doi.org/10.1073/pnas.062552299

Levine, E.S., Zam, A., Zhang, P., Pechko, A., Wang, X., FitzGerald, P., Pugh, E.N., Zawadzki, R.J., Burns, M.E., 2014. Rapid light-induced activation of retinal microglia in mice lacking Arrestin-1. Vision Res. 102, 71–79. https://doi.org/10.1016/j.visres.2014.07.011

Lückoff, A., Scholz, R., Sennlaub, F., Xu, H., Langmann, T., 2017. Comprehensive analysis of mouse retinal mononuclear phagocytes. Nat Protoc 12, 1136–1150. https://doi.org/10.1038/nprot.2017.032

Makarov, N.S., Cirloganu, C., Perry, J.W., Lukyanov, K.A., Solntsev, K.M., 2014. Steady-state and time-resolved spectroscopic studies of green-to-red photoconversion of fluorescent protein Dendra2. Journal of Photochemistry and Photobiology A: Chemistry 280, 5–13. https://doi.org/10.1016/j.jphotochem.2014.02.001

Martens, R., Permanyer, M., Werth, K., Yu, K., Braun, A., Halle, O., Halle, S., Patzer, G.E., Bošnjak, B., Kiefer, F., Janssen, A., Friedrichsen, M., Poetzsch, J., Kohli, K., Lueder, Y., Gutierrez Jauregui, R., Eckert, N., Worbs, T., Galla, M., Förster, R., 2020. Efficient homing of T cells via afferent lymphatics requires mechanical arrest and integrin-supported chemokine guidance. Nat Commun 11, 1114. https://doi.org/10.1038/s41467-020-14921-w

McKinsey, G.L., Lizama, C.O., Keown-Lang, A.E., Niu, A., Santander, N., Larpthaveesarp, A., Chee, E., Gonzalez, F.F., Arnold, T.D., 2020. A new genetic strategy for targeting microglia in development and disease. Elife 9, e54590. https://doi.org/10.7554/eLife.54590

Miller, E.B., Zhang, P., Ching, K., Pugh, E.N., Burns, M.E., 2019. In vivo imaging reveals transient microglia recruitment and functional recovery of photoreceptor signaling after injury. Proc. Natl. Acad. Sci. U.S.A. 116, 16603–16612. https://doi.org/10.1073/pnas.1903336116

O'Koren, E.G., Mathew, R., Saban, D.R., 2016. Fate mapping reveals that microglia and recruited monocyte-derived macrophages are definitively distinguishable by phenotype in the retina. Sci Rep 6, 20636. https://doi.org/10.1038/srep20636

O'Koren, E.G., Yu, C., Klingeborn, M., Wong, A.Y.W., Prigge, C.L., Mathew, R., Kalnitsky, J., Msallam, R.A., Silvin, A., Kay, J.N., Bowes Rickman, C., Arshavsky, V.Y., Ginhoux, F., Merad, M., Saban, D.R., 2019. Microglial Function Is Distinct in Different Anatomical Locations during Retinal Homeostasis and Degeneration. Immunity 50, 723-737.e7. https://doi.org/10.1016/j.immuni.2019.02.007

Pakhomov, A.A., Martynov, V.I., Orsa, A.N., Bondarenko, A.A., Chertkova, R.V., Lukyanov, K.A., Petrenko, A.G., Deyev, I.E., 2017. Fluorescent protein Dendra2 as a ratiometric genetically encoded pH-sensor. Biochem Biophys Res Commun 493, 1518–1521. https://doi.org/10.1016/j.bbrc.2017.09.170

Paolicelli, R.C., Bisht, K., Tremblay, M.-È., 2014. Fractalkine regulation of microglial physiology and consequences on the brain and behavior. Front Cell Neurosci 8, 129. https://doi.org/10.3389/fncel.2014.00129

Parkhurst, C.N., Yang, G., Ninan, I., Savas, J.N., Yates, J.R., Lafaille, J.J., Hempstead, B.L., Littman, D.R., Gan, W.-B., 2013. Microglia promote learning-dependent synapse formation through brain-derived neurotrophic factor. Cell 155, 1596–1609. https://doi.org/10.1016/j.cell.2013.11.030

Pigazzini, M.L., Kirstein, J., 2020. In Vivo Quantification of Protein Turnover in Aging C. Elegans using Photoconvertible Dendra2. J Vis Exp. https://doi.org/10.3791/61196

Rashid, K., Akhtar-Schaefer, I., Langmann, T., 2019. Microglia in Retinal Degeneration. Frontiers in Immunology 10, 1975. https://doi.org/10.3389/fimmu.2019.01975

Reyes, N.J., O'Koren, E.G., Saban, D.R., 2017. New insights into mononuclear phagocyte biology from the visual system. Nat. Rev. Immunol. 17, 322–332. https://doi.org/10.1038/nri.2017.13

Ronning, K.E., Karlen, S.J., Miller, E.B., Burns, M.E., 2019. Molecular profiling of resident and infiltrating mononuclear phagocytes during rapid adult retinal degeneration using single-cell RNA sequencing. Scientific Reports 9, 4858. https://doi.org/10.1038/s41598-019-41141-0

Rutkai, I., Evans, W.R., Bess, N., Salter-Cid, T., Čikić, S., Chandra, P.K., Katakam, P.V.G., Mostany, R., Busija, D.W., 2020. Chronic imaging of mitochondria in the murine cerebral vasculature using in vivo two-photon microscopy. Am J Physiol Heart Circ Physiol 318, H1379–H1386. https://doi.org/10.1152/ajpheart.00751.2019

Schneider, C.A., Rasband, W.S., Eliceiri, K.W., 2012. NIH Image to ImageJ: 25 years of image analysis. Nat Methods 9, 671–675. https://doi.org/10.1038/nmeth.2089

Sennlaub, F., Auvynet, C., Calippe, B., Lavalette, S., Poupel, L., Hu, S.J., Dominguez, E., Camelo, S., Levy, O., Guyon, E., Saederup, N., Charo, I.F., Rooijen, N.V., Nandrot, E., Bourges, J.-L., Behar-Cohen, F., Sahel, J.-A., Guillonneau, X., Raoul, W., Combadiere, C., 2013. CCR2(+) monocytes infiltrate atrophic lesions in age-related macular disease and mediate photoreceptor degeneration in experimental subretinal inflammation in Cx3cr1 deficient mice. EMBO Mol Med 5, 1775–1793. https://doi.org/10.1002/emmm.201302692

Silverman, S.M., Wong, W.T., 2018. Microglia in the Retina: Roles in Development, Maturity, and Disease. Annu Rev Vis Sci 4, 45–77. https://doi.org/10.1146/annurev-vision-091517-034425

Tay, T.L., Mai, D., Dautzenberg, J., Fernández-Klett, F., Lin, G., Sagar, Datta, M., Drougard, A., Stempfl, T., Ardura-Fabregat, A., Staszewski, O., Margineanu, A., Sporbert, A., Steinmetz, L.M., Pospisilik, J.A., Jung, S., Priller, J., Grün, D., Ronneberger, O., Prinz, M., 2017. A new fate mapping system reveals context-dependent random or clonal expansion of microglia. Nature Neuroscience 20, 793–803. https://doi.org/10.1038/nn.4547

Van Rossum, G., Drake, F.L., 2009. Python 3 Reference Manual. CreateSpace, Scotts Valley, CA.

Wang, T., Chen, J., 2014. Induction of the unfolded protein response by constitutive G-protein signaling in rod photoreceptor cells. J. Biol. Chem. 289, 29310–29321. https://doi.org/10.1074/jbc.M114.595207
Wieghofer, P., Hagemeyer, N., Sankowski, R., Schlecht, A., Staszewski, O., Amann, L., Gruber, M., Koch, J., Hausmann, A., Zhang, P., Boneva, S., Masuda, T., Hilgendorf, I., Goldmann, T., Böttcher, C., Priller, J., Rossi, F.M., Lange, C., Prinz, M., 2021. Mapping the origin and fate of myeloid cells in distinct compartments of the eye by single-cell profiling. EMBO J 40, e105123. https://doi.org/10.15252/embj.2020105123
Wilden, U., Kuehn, H., 1982. Light-dependent phosphorylation of rhodopsin: number of phosphorylation sites. Biochemistry 21, 3014–3022. https://doi.org/10.1021/bi00541a032
Wojtkowski, M., Srinivasan, V., Ko, T., Fujimoto, J., Kowalczyk, A., Duker, J., 2004. Ultrahigh-resolution, high-speed, Fourier domain optical coherence tomography and methods for dispersion compensation. Opt Express 12, 2404–2422. https://doi.org/10.1364/opex.12.002404
Wolf, S.A., Boddeke, H.W.G.M., Kettenmann, H., 2017. Microglia in Physiology and Disease. Annu. Rev. Physiol. 79, 619–643. https://doi.org/10.1146/annurev-physiol-022516-034406
Wolf, Y., Yona, S., Kim, K.-W., Jung, S., 2013. Microglia, seen from the CX3CR1 angle. Frontiers in Cellular Neuroscience 7, 26. https://doi.org/10.3389/fncel.2013.00026
Xu, J., Dodd, R.L., Makino, C.L., Simon, M.I., Baylor, D.A., Chen, J., 1997. Prolonged photoresponses in transgenic mouse rods lacking arrestin. Nature 389, 505–509. https://doi.org/10.1038/39068
Yona, S., Kim, K.-W., Wolf, Y., Mildner, A., Varol, D., Breker, M., Strauss-Ayali, D., Viukov, S., Guilliams, M., Misharin, A., Hume, D.A., Perlman, H., Malissen, B., Zelzer, E., Jung, S., 2013. Fate Mapping Reveals Origins and Dynamics of Monocytes and Tissue Macrophages under Homeostasis. Immunity 38, 79–91. https://doi.org/10.1016/j.immuni.2012.12.001
Yoo, S.K., Huttenlocher, A., 2011. Spatiotemporal photolabeling of neutrophil trafficking during inflammation in live zebrafish. J Leukoc Biol 89, 661–667. https://doi.org/10.1189/jlb.1010567
Yu, C., Roubeix, C., Sennlaub, F., Saban, D.R., 2020. Microglia versus Monocytes: Distinct Roles in Degenerative Diseases of the Retina. Trends in Neurosciences 43, 433–449. https://doi.org/10.1016/j.tins.2020.03.012
Zabel, M.K., Zhao, L., Zhang, Y., Gonzalez, S.R., Ma, W., Wang, X., Fariss, R.N., Wong, W.T., 2016. Microglial phagocytosis and activation underlying photoreceptor degeneration is regulated by CX3CL1-CX3CR1 signaling in a mouse model of retinitis pigmentosa. Glia 64, 1479–1491. https://doi.org/10.1002/glia.23016
Zhang, P., Zam, A., Jian, Y., Wang, X., Li, Y., Lam, K.S., Burns, M.E., Sarunic, M.V., Pugh, E.N., Zawadzki, R.J., 2015. In vivo wide-field multispectral scanning laser ophthalmoscopy-optical coherence tomography mouse retinal imager: longitudinal imaging of ganglion cells, microglia, and Müller glia, and mapping of the mouse retinal and choroidal vasculature. J Biomed Opt 20, 126005. https://doi.org/10.1117/1.JBO.20.12.126005
Zhang, Y., Wong, W.T., 2021. Innate Immunity in Age-Related Macular Degeneration, in: Chew, E.Y., Swaroop, A. (Eds.), Age-Related Macular Degeneration: From Clinic to Genes and Back to Patient Management, Advances in Experimental Medicine and Biology. Springer International Publishing, Cham, pp. 121–141. https://doi.org/10.1007/978-3-030-66014-7_5